Extended Boundary Element Method approach for Direct and Accurate Evaluation of Stress Intensity Factors

Ibrahim Alatawi

Thesis submitted towards the
degree of Doctor of Philosophy

Mechanics Research Group
School of Engineering and Computing Sciences
Durham University
United Kingdom

January 2016

Extended Boundary Element Method approach for Direct and Accurate Evaluation of Stress Intensity Factors

Ibrahim Alatawi

Abstract

This thesis introduces an alternative method to evaluate Stress Intensity Factors (SIFs) in computational fracture mechanics directly, using the Extended Dual Boundary Element Method (XBEM) for 2D problems. A novel auxiliary equation introduced which enforces displacement continuity at the crack tip to yield a square system. Additionally, the enrichment method has been extended to 3D, so that the J-integral with XBEM and a direct technique are used to evaluate SIFs. This includes a complete description of the formulation of enrichment functions, a substitution of the enriched form of displacement into boundary integral equations, treatment of singular integrals, assembly of system matrices and the introduction of auxiliary equations to solve the system directly. The enrichment approach utilizes the Williams expansions to enrich crack surface elements for accurate evaluation of stress intensity factors. Similar to other enrichment methods, the new approach can yield accurate results on coarse discretisations, and the enrichment increases the 2D problem size by only two degrees of freedom per crack tip. In the case of 3D, the number of the new degrees of freedom depends on the desired number of crack front points where SIFs need to be evaluated. The auxiliary equations required to yield a square system are derived by enforcing continuity of displacement at the crack front. The enrichment approach provides the values of singular coefficients K_I , K_{II} and K_{III} directly in the solution vector; without any need for postprocessing such as the J-integral. Numerical examples are used to compare the accuracy of these directly computed SIFs to the J-integral processing of both conventional and XBEM approximations.

Declaration

The work in this thesis is based on research carried out in the Computational Mechanics Group, School of Engineering and Computing Sciences, Durham University. No part of this report has been submitted elsewhere for any other degree or qualification and it is all my own work unless referenced to the contrary in the text.

Parts of this work have been published in the following:

Journals

Alatawi, I.A. & Trevelyan, J.
A direct evaluation of stress intensity factors using the Extended Dual Boundary Element Method. *Engineering Analysis with Boundary Elements* , 52(0), 56-63, 2015.

Conferences

I.A. Alatawi, & J. Trevelyan
A Direct Method to Evaluate Stress Intensity Factors Using Extended BEM, *Proceedings of the 22nd UK National Conference of the Association for Computational Mechanics in Engineering.* Exeter, 101-104, 2014.

I.A. Alatawi, G. Hattori & J. Trevelyan
Analysis of 3D Crack Problems by the Extended Boundary Element Method (XBEM), *Proceedings of the 23rd UK National Conference of the Association for Computational Mechanics in Engineering.* Swansea, 287-290, 2015.

I.A. Alatawi, & J. Trevelyan
Direct evaluation of Stress Intensity Factors for crack problems by Extended Boundary Element Method 3D, *Proceedings of The Tenth UK Conference on Boundary Integral Methods*, Brighton, 100-104, 2015

Gabriel Hattori, I.A. Alatawi, & J. Trevelyan
A direct SIF approach for anisotropic materials using the Boundary Element Method, *Proceedings of the 23rd UK National Conference of the Association for Computational Mechanics in Engineering.* Swansea, 279-282, 2015.

Acknowledgements

Grateful appreciation and deepest gratitude for their help and support are extended to the following persons; who, in one way or another, have contributed to making this study achievable.

It is a great pleasure to acknowledge my sincere gratitude to my supervisor Professor Jon Trevelyan, who kindly supervised me during my doctoral studies at Durham University.

Thanks must also be extended towards my second supervisor, and the head of the Mechanics Research Group Professor Charles Augarde who was always ready to help.

I also acknowledge the suggestions I received from Dr. Gabriel Hattori, Dr. Mohammed Seaid, Dr. M Shadi Mohamed, and Dr. Robert Simpson which helped to complete this thesis.

Deep thanks to all my friends at Durham - Zahur, Baseer, Tim, Jonathan, Michael and Ganesh who made studying at Durham extraordinary.

This thesis would not have been accomplished without generous funding from the Education Ministry of Saudi Arabia.

Last but not least, I would like to take this opportunity to thank my large family for their support and encouragement; I also appreciate the patience shown by my wife and my sons during my studies.

Ibrahim Alatawi
Durham, January 2016

Contents

List of Figures

List of Tables

Nomenclature & Abbreviations

Abbreviations

BEM	Boundary Element Method
BIE	Boundary Integral Equation
CPV	Cauchy Principal Value
DBEM	Dual Boundary Element Method
DBIE	Displacement Boundary Integral Equation
DoF	Degree of Freedom
FEM	Finite Element Method
FMM	Fast Multipole Method
GL	Gauss-Legendre
LEFM	Linear Elastic Fracture Mechanics
PDE	Partial Differential Equation
PUM	Partition of Unity Method
SIF	Stress Intensity Factor
TBIE	Traction Boundary Integral Equation
XBEM	Extended Boundary Element Method
XFEM	Extended Finite Element Method

Symbols

α_{ij}	Jump term
$\bar{a}$	Node number
$\bar{n}$	Field element
$\fint$	Cauchy Principal Value Integral

$-\!\!\!\!\!\!\int$	Hadamard finite part Integral
$\Delta(X - X')$	Dirac delta
δ_{ij}	Kronecker delta
ϵ_{ij}	Strain components
κ	Kolosov's constant
λ	Lamé constant
$\mathcal{G}$	Energy Release Rate
$\mathcal{G}_c$	Critical Energy Release Rate
μ	Shear modulus
∇^2	Laplacian operator
ν	Poisson's ratio
ν'	Modified Poisson's ratio
Φ	Airy stress function
ρ, θ	Polar coordinate system
σ_{ij}	Stress components
ξ, η	Local coordinates
a	Crack length for 2D edge crack and radius for penny shaped crack in 3D
b_i	Body force components
C_{ij}	Free-term
D_{kij}	differentiated displacement fundamental solution
E	Young's modulus
E'	Modified Young's modulus
$J^{\bar{n}}(\xi)$	2D Jacobian of transformation for element $\bar{n}$
$J^{\bar{n}}(\xi_1, \xi_2)$	3D Jacobian of transformation for element $\bar{n}$
J_I,J_{II}, J_{III}	J-integral components for mode I, II and III
K_I,K_{II}, K_{III}	stress intensity factor for mode I, II and III
m	Number of nodes
n, b, t	Crack local coordinate system

$N^{\bar{a}}$	Shape function for node $\bar{a}$
N_e	Number of elements
n_i	Normal components
S	Domain boundary
S_{kij}	Differentiated traction fundamental solution
t_i	Traction components
T_{ij}	Traction fundamental solution
u_i	Displacement components
U_{ij}	Displacement fundamental solution
V	Volume domain
W	Strain energy density
X	Field point in domain
x	Field point on boundary
X'	Source point in domain
x'	Source point on boundary
x, y, z	Cartesian coordinate system
x_i	Coordinate components

Chapter 1

Introduction

We must acknowledge that fracture is a significant issue in industrial applications, and that improved design theories to counter fracture are needed. The fundamental question each theory tries to answer is: what crack size is allowable within an existing structure, while still ensuring safe operation? With regard to this issue, which is also referred to as *damage tolerance*, Zenhder comments:

> "Perhaps you would say that any crack, any flaw, is not allowable in the jet aircraft that carries your family across the ocean. Unfortunately such an aircraft does not exist. We must face reality square-on; recognize that flaws exist and to the very best of our ability, design our structures, monitoring protocols and maintenance procedures to ensure a low probability of failure by fracture" [6]
>
> (Fracture Mechanics, Alan Zehnder, 2012)

The aim of designing structures to resist fractures is not new. The capability of engineers and architects to do so was exhibited in the ancient constructions erected by the Egyptians and the Romans. However, modern construction techniques mean that structures are more susceptible to damage and failure than during previous eras when more simple constructions dominated. The analysis and design of structural materials in various fields of engineering are driven by the aim to prevent crack propagation, which can ultimately give rise to a catastrophic failure. Such failure (e.g. Aloha Airline flight 243 Fig. (1.1)) is considered seriously in the aerospace industry. While safety is in the premier place in terms of importance, an overdesigned airframe can also result in excessive weight, so is to be avoided. Likewise, in power plant design, engineers place considerable importance on methods to prevent catastrophic failure, especially for processes involving the generation of nuclear power. The theory of fracture mechanics has been developed to quantify the effects on performance of cracks present in materials. To a certain extent, all structures have cracks. Their existence results from basic defects in the constituent materials, or the induced in the course of long service. Such cracks are assessed in terms of stability, requiring a basic theory in fracture mechanics. The stability of a crack, and its critical length at which unstable rapid propagation occurs, may be characterised by a parameter known as the energy release rate [7]. Later, Stress Intensity Factors (SIFs) were introduced by [8], as an essential coefficients to measure the magnitude of stress. The load pattern, crack length and geometry of a structure determine the SIFs for each problem. The implementation of SIFs to examine crack stability requires appropriate knowledge of stress fields near the crack tip. It is unfortunate that analytical solutions are only available for relatively simple and selected cases. However, SIFs can be determined numerically for cases with complex geometry and boundary conditions, by applying computational techniques such as the Boundary Element Method (BEM) and Finite Element Method (FEM). However, using conventional FEM or BEM formulations is a challenge when handling the singularity occurs at the crack tip [9].

Refining the mesh is a simple approach for capturing the behaviour of singular field around the crack tip, yet the computational time is the price to be paid for this simplicity. More complicated developments and adaptations are essential for the numerical methods to solve fracture problems efficiently. These adjustments include basic procedures using crack tip SIFs, as well as methods that are more complex constructing special crack elements that model the stresses throughout the entire crack zone [10]. Significant progress has been observed in the field using enrichment, with the introduction of the Partition

Figure 1.1: Damaged Aloha airline flight 243 [1]

of Unity Method (PUM) [11]. An enriched basis can be formed by combining prior knowledge of the solution space (e.g. Williams expansions [12]) and the nodal shape functions associated with the mesh. This construction allows for accurate evaluation of SIFs in crack problems. Additionally, enrichment can only be added to a local element where the domain needs to be enriched. The finite element method was the first to utilise the implementation of enrichment technique [13]. This allowed for accurate evaluation of crack problems while using a coarse mesh. On the other hand, the boundary element method has gained more attention as a useful technique for obtaining numerical solutions to fracture problems, which (i) are dominated by effects on the boundary (i.e. the crack surfaces), and (ii) involve a discontinuous stress and strain field. It also offered good accuracy for solutions on the domain boundary, whereas finite element methods offered greatest accuracy at integration points within the element. This enrichment technique has recently been extended to BEM by [14], which has been used successfully to study crack behaviour.

In this thesis, the Williams expansions for displacement are used to enrich the boundary element method, giving an enriched method which is henceforth called the Extended Boundary Element Method (XBEM). The use of enrichment has improved accuracy when using a coarse mesh. The implementation of enrichment adds a small number of new degrees of freedom to the system. Sufficient numbers of equations are generated using a new method for enforcing the displacement continuity at the crack tip. A unique technique is used to solve for added degrees of freedom, allowing for the direct evaluation of SIFs without the need for a postprocessing method, such as the J-integral. The enrichment is only applied to crack surface elements offering greater flexibility for the same code when used for both enriched and unenriched problems.

Generally, the context of this thesis begin with the coverage of fracture mechanics, and gradually builds towards the boundary element method, leading to a greater focus on the Dual Boundary Element Method (DBEM) and finally introducing the enrichment of DBEM for 2D then 3D. In more details, the second chapter begins with a historical review of fracture mechanics. The chapter then is extended to include the modes of crack, Linear Elastic Fracture Mechanics (LEFM) and SIFs. The aim of the third chapter is to present the advancement of numerical fracture mechanics achieved through FEM, meshless methods and the boundary element method. In the fourth chapter, attention is turned to the dual boundary element method to demonstrate the concepts associated with the method beside the treatment of mathematical difficulties that arise when the method is implemented. Following this, chapter five and six present the implementation of enriched DBEM with examples. Overall, these chapters examine the advantages of enriching DBEM, and reveal the main factors that affect efficiency and computing time. Finally, the conclusion includes a summary of the results achieved, and observations and recommendations for future research.

The novel contribution of the thesis will be presented in Chapters 5 and 6. Enrichment of two-dimensional crack problems will be introduced in Chapter 5, where a novel auxiliary equation to enforce displacement continuity at the crack tip is proposed to yield a square system. This creates a system that can solve the unknown of additional degrees of freedom directly. After this, a complete guide to enrich the Dual Boundary Element Method in 3D will be presented in Chapter 6, including the formulation of enrichment functions. In addition, it investigates the substitution of enriched displacement into the boundary integral equations, the treatment of singular integrals and assembly of the system matrices. Finally, the enforcement of crack front displacement yields the necessary auxiliary equations required to solve the unknown, added degrees of freedom.

Chapter 2

Fracture Mechanics

2.1 Introduction

The development of the study of fracture mechanics begins with analysis of the flaws and imperfections within materials that are often considered the primary causes of the onset of fractures. The effects of concentrated stresses, adjacent to imperfections or irregularities have long been acknowledged. The concentration of stresses around a circular hole in an infinite plate under uniaxial tension was first evaluated by Kirsch [15], who showed that the maximum normal stress on the hole exceeds the applied far-field stress by a factor of 3, i.e. a stress concentration factor of 3 applies. Inglis [16] extended the investigation of stress concentration to the more general case of an elliptical hole, where maximum stress can be found by $(1 + 2a/b)\sigma$. This solution reveals the stress concentration factor is an increasing function of the ellipse aspect ratio. Figure 2.1 shows when $a \gg b$ a crack forms, while a stress singularity develops near the crack tip. As a legacy of these developments, the major axis of ellipse a is still used as a symbol to represent crack length. It is clear that a direct application of Inglis solution will yield a singular value, since $\sigma_c \to \infty$ when $b \to 0$.

The complexity and size of modern structures has generated numerous design issues, including famous fracture mechanics failures, such as those that occurred in the Liberty ships during World War II. Later the Aloha Airline flight 243 accident highlighted fatigue

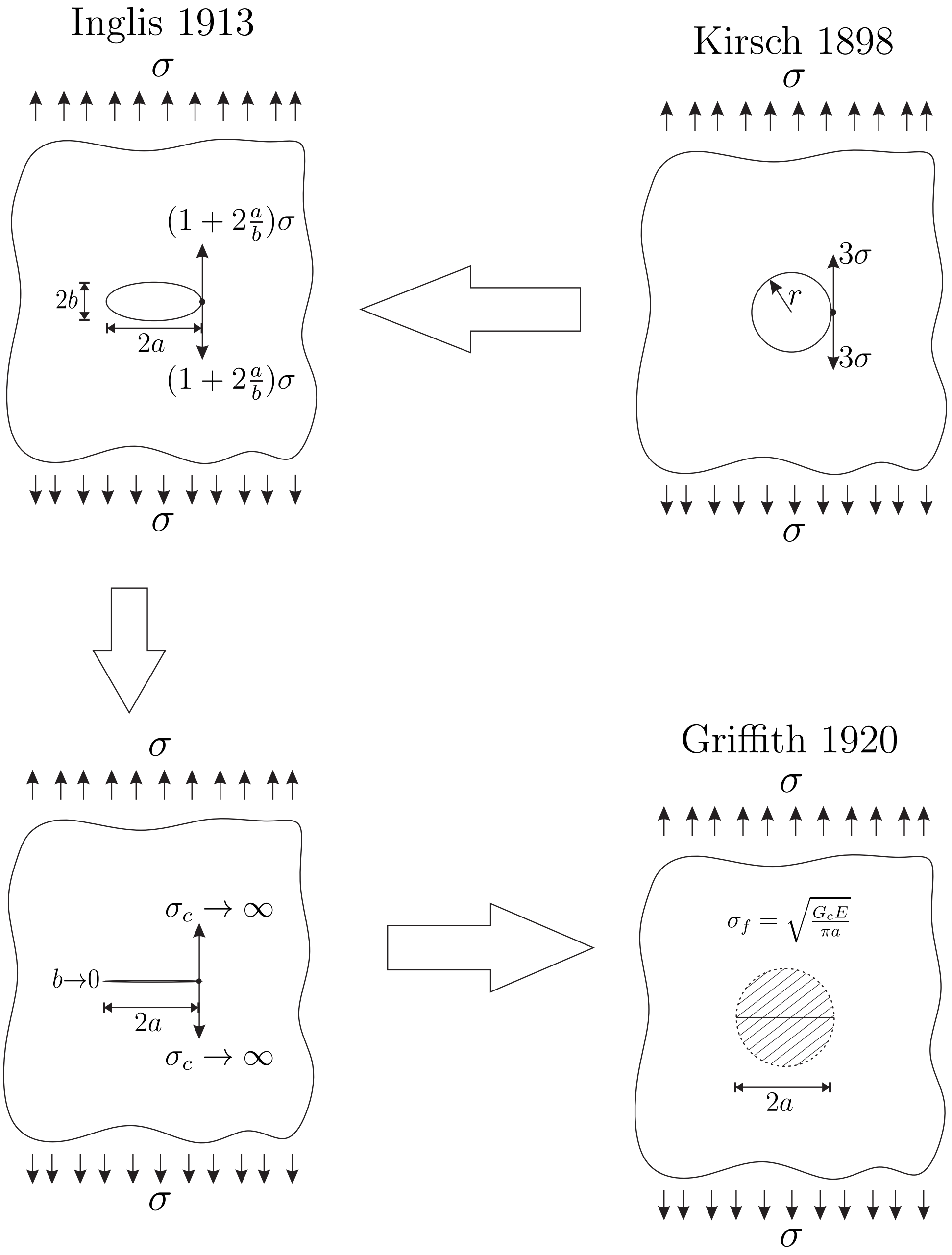

Figure 2.1: The development of fracture mechanics

Figure 2.2: Liberty ships [2]

failure and associated public safety concerns motivating a desire to create optimum designs to promote fracture mechanics from a scientific perspective as a fundamental engineering tool. With this in mind, Griffith [7] proposed an energy based approach to overcoming the mathematical difficulties associated with the presence of a physical singularity near the crack tip. However, the Griffith Critical Energy Release Rate $\mathcal{G}_c$ only accounts for energy required to break atomic bonds per unit surface area. Therefore, the method was limited to estimating the critical crack length of brittle materials. Subsequently, Irwin [8] extended Griffith's work to tackle the energy associated with the plastic deformation of ductile materials.

The solutions proposed by Griffith and Irwin were designed to answer the simple question of whether failure would occur or not in response to applied stresses. However, Irwin [17] also introduced stress intensity factors to describe the magnitude of the crack tip singularities in a specific direction. Soon, Williams proposed expansions [12] that were the first to express stresses and displacements in the field near the crack tip. These theories offer the asymptotic stresses and displacements at the crack tip, including infinite stress. These solutions indicate that the distribution of stresses and displacements are similar, but that the magnitudes of these solutions would vary between geometries. In fact, change in geometries affects the magnitude of the stress intensity factors denoted by K_I, K_{II} and K_{III}.

When making fracture assessments and, in particular, when predicting crack propagation, it is of great importance to have an accurate understanding of the field of stress in the vicinity of the crack tip. In linear elastic fracture mechanics, the stress intensity factors play a major role in the description of the stress and displacement. The exact value of SIFs can be calculated analytically in the case of a few special problems. However, SIFs can be determined for a wider range of problems, including a different combination of geometry and loading conditions by experiments or utilising numerical methods.

The present chapter tracks the early developments leading to analytical solutions. We recall that this thesis is focused on the accurate valuation of SIFs by using an asymptotic solution as an enrichment function. With LEFM in mind, the following sections illustrate the progress toward finding an approach offering a generalised analytical solution. Subsequently, a section will be added to detail the use of 2D expansions to enrich 3D problems.

2.2 Linear Elastic Fracture Mechanics

Theoretically, linear elastic fracture mechanics is the fundamental form of fracture mechanics, assuming that linear elastic material behaviour is essential. The assumptions associated with the theory of LEFM state that the body material is elastic in the large domain, although, at the same time, a vanishingly small inelastic region, known as the plastic zone at the crack tip is neglected. Considering the linear behaviour of materials, the stress state can be the basis of a crack growth criterion, whereas the stress field can be determined analytically. The resulting crack growth criteria are considered locally, since a small material volume at the crack tip is being examined. LEFM solutions contain stress and displacement fields asymptotically close to the crack tip. The stress and strain fields from the LEFM are no longer valid when there is a large plastic crack tip zone, nor when materials exhibit nonlinear elastic behaviour. In this case, stress fields cannot be used to describe the properties of crack growth. However, many engineering problems are considered to be linear elastic, since the majority of materials exhibit linear behaviour under normal operating service loads. The early development of fracture theories is demonstrated in the following sections, which rely on the concept of LEFM.

2.3 Energy approach

Griffith [7] laid the foundations of his research in the analysis of the fracture mechanics of glass. Based on previous studies by Inglis [16], about calculating stress concentrations around elliptical holes, Griffith proposed a method for estimating fracture strength. However, the Inglis solution poses a mathematical difficulty, in that the implementation of $(1 + 2a/b)\sigma$ yields singular stress. This leads to the conclusion that materials have zero strength, such that, even a small application of stress would result in material failure, as stresses become infinite causing bonds to break. Therefore, Griffith shifted the focus of his work from crack tip stresses to an energy balance calculation, which has since been considered a critical advancement in materials science. The strain energy per unit volume of a stressed material is given by,

$$U^* = \frac{1}{V}\int f dx = \int \frac{f}{A}\frac{dx}{L} = \int \sigma d\epsilon \tag{2.1}$$

considering $\sigma = E\epsilon$ for linear materials, the strain energy per unit volume given as,

$$U^* = \frac{E\epsilon^2}{2} = \frac{\sigma^2}{2E} \tag{2.2}$$

After the crack has propagated to a depth of a in the material, the field surrounding the crack surfaces is unloaded which results in a release of strain energy. Griffith employed this concept to calculate the precise value of the released energy.

As shown in Fig. 2.3 the released strain energy can be illustrated by considering two triangles adjacent to crack surfaces, with a width of a and a height of βa, as being free from stresses, while the remainder of the material under full stress σ. Using the Inglis solution for stresses around elliptic holes, Griffith was able to determine the value of the

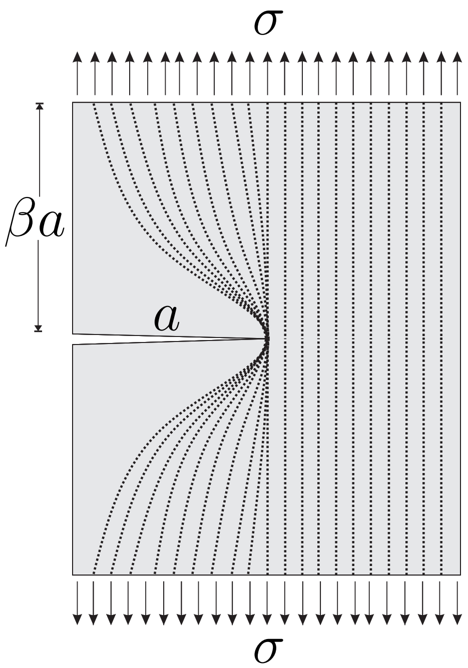

Figure 2.3: Stresses field adjacent to crack free surfaces

parameter $\beta = \pi$. The released strain energy U is equivalent to the strain energy per unit volume multiplied by the volume of both triangles,

$$U = -\frac{\sigma^2}{2E}\pi a^2 \tag{2.3}$$

here U refers to the strain energy released per unit thickness of a specimen. The strain energy is released in response to crack propagation. However, crack propagation requires bonds to be broken when the required energy is essentially absorbed by the material. The surface energy $\mathbb{S}$ for a crack of length a with a unit depth is given by,

$$\mathbb{S} = 2\gamma_s a \tag{2.4}$$

where γ_s denotes surface energy, and the factor 2 is included as two free surfaces are created. Fig. 2.4 shows the total energy of the crack which is the sum of the energy required to form the new surfaces [7].

With the continuous propagation of the crack, the strain energy becomes increasingly dependent on the quadratic nature of a. After the crack reaches critical length a_c the

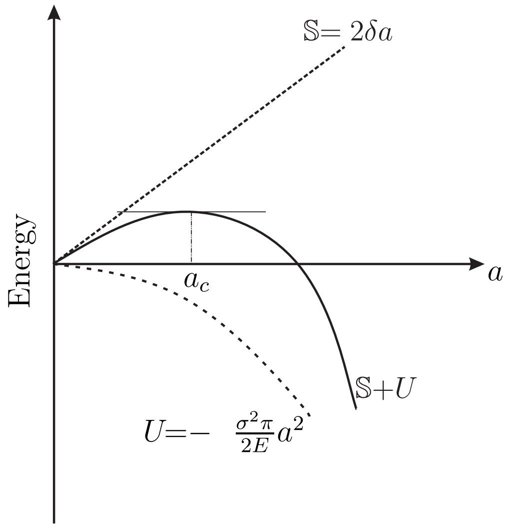

Figure 2.4: Energy balance in the presence of cracks

system reduces its energy by allowing the crack to grow further. The increment of applied stress is necessary for crack growth until it reaches a critical length when $a = a_c$; after this point it propagates spontaneously and rapidly. Unless care is taken, this can result in rapid, unexpected and catastrophic failure. The critical crack length value is obtained by setting the derivative of the total energy to zero,

$$\frac{\partial(\mathbb{S}+U)}{\partial a} = 2\gamma_s - \frac{\sigma_f^2}{E}\pi a = 0 \tag{2.5}$$

When the above condition is satisfied, the crack becomes unstable, and the critical stress, denoted by σ_f can be found as,

$$\sigma_f = \sqrt{\frac{2E\gamma_s}{\pi a}} \tag{2.6}$$

Griffith conducted his initial research on brittle materials, in particular glass rods. As a result, the energy release rate presented by Griffith only contains surface energy γ_s. However, for ductile materials, it is not possible to accurately model the fracture based on just the consideration of surface energy. The effect of the plastic zone near the crack tip was studied by Irwin which is demonstrated in the next section.

2.4 Stress Intensity Factors

In a ductile material the region around the crack tip cannot sustain an infinite stress and a plastic zone develops. Therefore, the energy required to extend the crack is greater than the surface energy. This was initially considered by Irwin [8]. By including a term known as the plastic work per unit area γ_p and replacing γ_s in Eqn. (2.6) with the combined term $\gamma_p + \gamma_s$ the critical stress evaluation of a crack can be extended to metals in a plane strain by,

$$\sigma_f = \sqrt{\frac{2E(\gamma_s + \gamma_p)}{\pi a}} \tag{2.7}$$

using the energy release rate notation Eqn. (2.7) can be rewritten as,

$$\sigma_f = \sqrt{\frac{E\mathcal{G}}{\pi a}} \tag{2.8}$$

where the energy release rate $\mathcal{G} = 2(\gamma_s + \gamma_p)$. Also Irwin identified the universality of the crack tip singular stress field, showing that the stress intensity factors may be used to determine the stress magnitudes. In addition, SIFs are able to differentiate between the mode of the applied load. Moreover, SIFs describe the modes of loads by singular coefficients, denoted as K_I, K_{II} and K_{III} associated with mode I, II and III, respectively, as shown in Fig 2.5. Considering the directions of applied loads, a cracked body deforms in three ways, depending on the movements of the crack surfaces in relation to each other. These are commonly known as, opening mode (mode I), in which two crack surfaces are drawn away from each other. Shearing or sliding mode (mode II), in which there is sliding of two cracked surfaces over each other in line with the crack; and finally, tearing mode (mode III), in which there is a sliding of the crack surfaces over each other in a direction perpendicular to the crack line. When considering a crack in an infinite plate

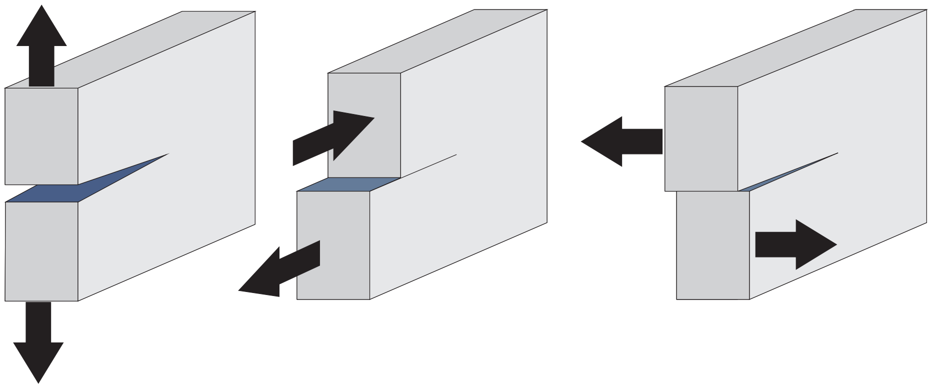

Mode$I$

ModeII

ModeIII

Figure 2.5: Crack deformation modes

under uniform tensile stress the singular coefficients relate to applied stress by,

$$\begin{Bmatrix} K_I \\ K_{II} \\ K_{III} \end{Bmatrix} = \sqrt{\pi a} \begin{Bmatrix} \sigma_{zz} \\ \sigma_{xz} \\ \sigma_{yz} \end{Bmatrix} \tag{2.9}$$

where a is half the crack length for a crack in an infinite plate, σ_{ij} are the components of the applied stress tensor (in the far field) and x, y, z are the cartesian coordinates system (in cases when the crack local coordinates are different from global, then the crack local coordinates are set to be n, b, t; see Fig. 2.6). These three basic modes are normally studied when examining crack propagation. However, it is possible to use mixed-mode growth, as crack growth may take place in a complicated stress field. SIFs are cumulative for similar loadings, which implies that the SIF for an intricate system of loads may be obtained by adding the SIFs obtained for each load separately.

2.5 Relationship between K_I and $\mathcal{G}$

Until now, two parameters describing crack behaviours have been presented. These are the stress intensity factors and the energy release rate. The energy release rate defines global behaviour, whereas K_I is specific to the local parameter. A unique relationship between K_I and $\mathcal{G}$ exists in the case of linear elastic materials. Equation (2.8) expresses $\mathcal{G}$ when the crack is in a plate of infinite dimension and subjected to uniform tensile

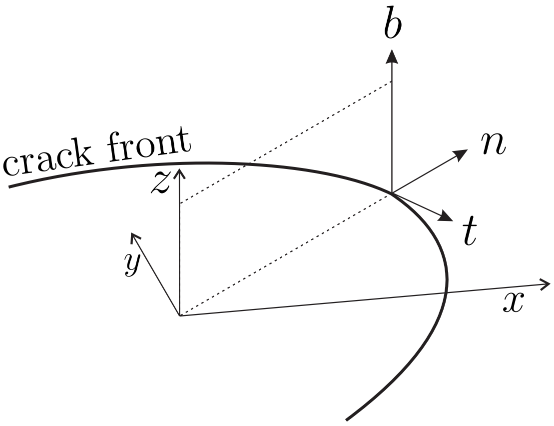

Figure 2.6: Relationship between the global coordinates and the crack local coordinates

stress. K_I for the same situation is expressed by equation (2.9). Substitution of the two equations for plane stress gives,

$$\mathcal{G} = \frac{K_I^2}{E} \tag{2.10}$$

Throughout this thesis, we will use the notation E' to avoid writing distinct expressions to defined plane strain and plane stress (where E' is the modified Young's modulus as defined in Eqn. (A.1.12)). Hence, the relation between $\mathcal{G}$ and K_I for plane stress, as well as plane strain can be written as,

$$\mathcal{G} = \frac{K_I^2}{E'} \tag{2.11}$$

As already stated the two equations, (2.8) and (2.9) are applicable only to cracks in an infinite plate; hence, we need to prove that the equation (2.11) states a general relationship applicable to problems in any dimension. A proof can be found for this in the crack closure technique performed by Irwin [17]. The analysis has been presented in detail in Appendix C.1. For practical application, the SIFs for different geometry and loading are given by,

$$K_I = Y\sigma\sqrt{\pi a} \tag{2.12}$$

where Y is a dimensionless geometrical factor. There are references containing multiple

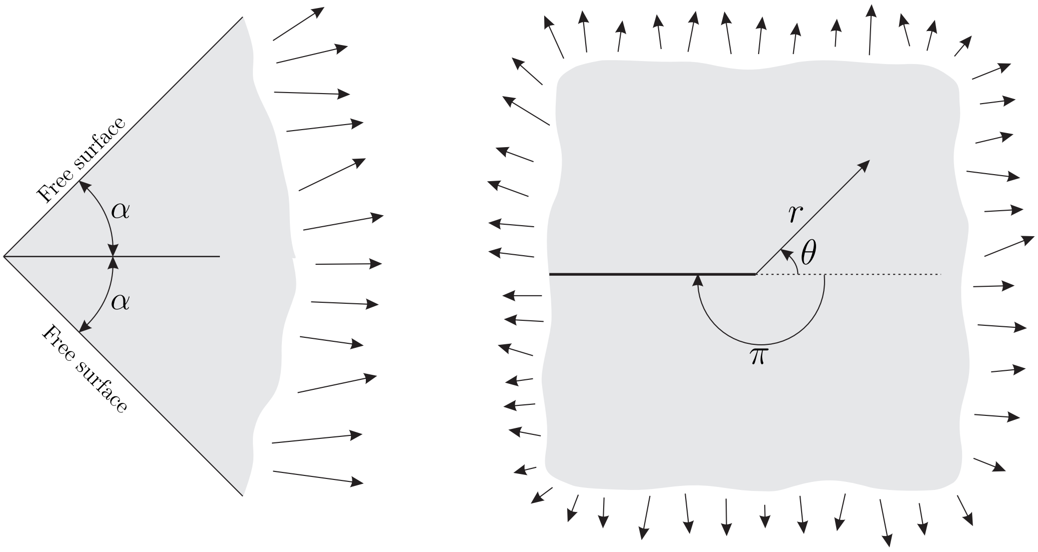

Figure 2.7: Williams configuration of a wedge and the special case to the right

values of Y for different cases [5]. A common case is $Y = 1.12$ for a small edge crack of length a in a large plate. Energy release rate and SIFs are primarily used for examining the crack stability. However, several methods have been proposed to analyse the distribution of stresses around cracks. The following two sections demonstrate methods proposed earlier by Williams [12] and Westergaard [18]; both approaches consider the local stress field under certain global boundary conditions and configurations.

2.6 Williams expansions

Pioneering research by Williams shows the universal distribution of crack singularity for elastic crack problems. Initial studies focus on stresses at the corner of a plate in different boundary conditions and at various enclosed angles. The crack is a special case of Williams problem, wherein the crack enclosed angle α equals π and the surfaces are considered traction-free as presented in Fig. 2.7. Utilising Airy stress function Williams was able to derive the stress expansions that describe stresses behaviour in the vicinity of the crack tip. A complete representation of the derivation process can be found in Appendix C.2. These, stress expansions near the crack tip can be written as,

$$\begin{aligned}\sigma_{nn} &= \sum_{n=}^{\infty} \frac{n}{2} r^{\frac{n}{2}-1} \left\{ C_{1n}\left[\left(2+\frac{n}{2}+(-1)^n\right)\cos\left(\frac{n}{2}-1\right)\theta+\left(\frac{n}{2}-1\right)\cos\left(\frac{n}{2}-3\right)\theta\right]\right.\\ &- \left. C_{2n}\left[\left(2+\frac{n}{2}-(-1)^n\right)\sin\left(\frac{n}{2}-1\right)\theta-\left(\frac{n}{2}-1\right)\sin\left(\frac{n}{2}-3\right)\theta\right]\right\} \qquad (2.13a)\end{aligned}$$

$$\begin{aligned}\sigma_{bb} &= \sum_{n=}^{\infty} \frac{n}{2} r^{\frac{n}{2}-1} \left\{ C_{1n}\left[\left(2-\frac{n}{2}-(-1)^n\right)\cos\left(\frac{n}{2}-1\right)\theta+\left(\frac{n}{2}-1\right)\cos\left(\frac{n}{2}-3\right)\theta\right]\right.\\ &- \left. C_{2n}\left[\left(2-\frac{n}{2}+(-1)^n\right)\sin\left(\frac{n}{2}-1\right)\theta+\left(\frac{n}{2}-1\right)\sin\left(\frac{n}{2}-3\right)\theta\right]\right\} \qquad (2.13b)\end{aligned}$$

$$\begin{aligned}\sigma_{nb} &= \sum_{n=}^{\infty} \frac{n}{2} r^{\frac{n}{2}-1} \left\{ C_{1n}\left[\left(\frac{n}{2}-1\right)\sin\left(\frac{n}{2}-3\right)\theta+\left(\frac{n}{2}+(-1)^n\right)\sin\left(\frac{n}{2}-1\right)\theta\right]\right.\\ &+ \left. C_{2n}\left[\left(\frac{n}{2}-1\right)\cos\left(\frac{n}{2}-3\right)\theta-\left(\frac{n}{2}-(-1)^n\right)\cos\left(\frac{n}{2}-1\right)\theta\right]\right\} \qquad (2.13c)\end{aligned}$$

where n and b denote the local coordinates with the origin at the crack tip. In this system the n axis lies in the crack plane and the b axis is perpendicular to the crack plane. Finally, Hooke's law can be used to obtain strains, which then are integrated to find displacements. The resulting expressions for the crack tip displacements can then be written as,

$$\begin{aligned}u_n &= \sum_{n=}^{\infty} \frac{r^{\frac{n}{2}}}{2\mu} \left\{ C_{1n}\left[\left(\kappa+\frac{n}{2}+(-1)^n\right)\cos\frac{n}{2}\theta-\frac{n}{2}\cos\left(\frac{n}{2}-2\right)\theta\right]\right.\\ &- \left. C_{2n}\left[\left(\kappa+\frac{n}{2}-(-1)^n\right)\sin\frac{n}{2}\theta-\frac{n}{2}\sin\left(\frac{n}{2}-2\right)\theta\right]\right\} \qquad (2.14a)\end{aligned}$$

$$\begin{aligned}u_b &= \sum_{n=}^{\infty} \frac{r^{\frac{n}{2}}}{2\mu} \left\{ C_{1n}\left[\left(\kappa-\frac{n}{2}-(-1)^n\right)\sin\frac{n}{2}\theta+\frac{n}{2}\sin\left(\frac{n}{2}-2\right)\theta\right]\right.\\ &- \left. C_{2n}\left[\left(\kappa-\frac{n}{2}+(-1)^n\right)\cos\frac{n}{2}\theta+\frac{n}{2}\cos\left(\frac{n}{2}-2\right)\theta\right]\right\} \qquad (2.14b)\end{aligned}$$

where μ is the shear modulus and κ is Kolosov's constant defined as $\kappa = 3 - 4\nu$ and $\kappa = (3-\nu)/(1+\nu)$ for plane strain and plane stress, respectively; ν being the Poisson's ratio. In the context of linear elastic fracture mechanics, the solutions for stresses and displacements given by (2.14) and (2.13) are fundamental; since these yield an asymptotic

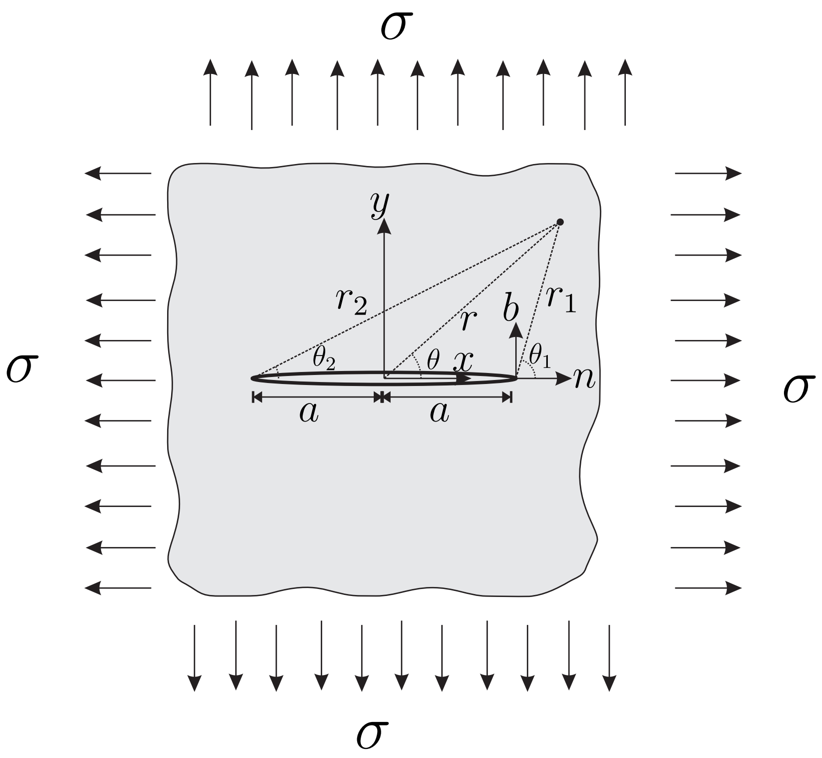

Figure 2.8: Westergaard centred crack with two polar coordinate systems

analytical solution in the region close to the crack tip which other methods can use to investigate accuracy.

2.7 Westergaard solution

Another technique was that proposed by Westergaard [18] to tackle crack problems and provide solutions. This procedure uses the biharmonic equation, as an automatic satisfaction guarantee when complex equations show analytical behaviour. Therefore, this involves applying the complex analysis technique formerly submitted by Muskhelishvili [19]. Here we consider a centred crack with two local polar crack tip coordinate systems, as presented in Fig. 2.8.

The complex analysis technique utilises the complex variable z which is expressed as,

$$z - a = (x - a) + iy = r_1 e^{i\theta_1} \tag{2.15a}$$

$$z + a = (x + a) + iy = r_2 e^{i\theta_2} \tag{2.15b}$$

The steps of Westergaard's solution begin by formulating a complex function as,

$$F(z) = \mathbb{R}\mathrm{e}\,\hat{\hat{Z}}(z) + y\left[\mathbb{I}\mathrm{m}\,\hat{Z}(z) + \mathbb{I}\mathrm{m}\,\hat{Y}(z)\right] \tag{2.16}$$

here $Z(z)$ and $Y(z)$ are complex functions which will be described subsequently, while the symbol ($\hat{}$) denotes integration with respect to the complex variable z. Hence,

$$\frac{d\hat{\hat{Z}}}{dx} = \hat{Z}, \qquad \frac{d\hat{Z}}{dz} = Z, \qquad \frac{d\hat{Y}}{dz} = Y \tag{2.17}$$

As a result of the Cauchy-Riemann equations, it is possible to achieve the following derivative expressions,

$$\frac{\partial F}{\partial x} = \mathbb{R}\mathrm{e}\,\hat{Z} + y\,[\mathbb{I}\mathrm{m}\,Z + \mathbb{I}\mathrm{m}\,Y] \tag{2.18a}$$

$$\frac{\partial F}{\partial y} = \mathbb{I}\mathrm{m}\,\hat{Y} + y\,[\mathbb{R}\mathrm{e}\,Z + \mathbb{R}\mathrm{e}\,Y] \tag{2.18b}$$

These equations need to be differentiated once again, and then substituted into expressions relating the stresses to the Airy stress function (A.2.16); this will yield,

$$\sigma_{xx} = \mathbb{R}\mathrm{e}\,Z - y\,[\mathbb{I}\mathrm{m}\,Z' + Y'] + 2\,\mathbb{R}\mathrm{e}\,Y \tag{2.19a}$$

$$\sigma_{yy} = \mathbb{R}\mathrm{e}\,Z + y\,[\mathbb{I}\mathrm{m}\,Z' + \mathbb{I}\mathrm{m}\,Y'] \tag{2.19b}$$

$$\sigma_{xy} = -\,\mathbb{R}\mathrm{e}\,Y - y\,[\mathbb{I}\mathrm{m}\,Z' + \mathbb{I}\mathrm{m}\,Y'] \tag{2.19c}$$

These expressions can be used to derive strains by utilising the elastic constitutive equations and then displacements using integration. Next, by using the semi-inverse method, a convenient selecting from the complex functions Z and Y is required to satisfy the problem's boundary conditions. Westergaard chose the following complex functions by considering the problem of the centred crack in an infinite plate.

$$Z(x) = \frac{\sigma_z}{\sqrt{z^2 - a^2}}\,, \qquad Y(z) = 0 \tag{2.20}$$

The substitution of expressions (2.20) into the functions that relate stress to the Airy stress function (A.2.16), the solution for stresses in a centre crack can be written as,

$$\sigma_{xx} = \frac{\sigma r}{\sqrt{r_1 r_2}} \cos\left(\theta - \frac{\theta_1+\theta_2}{2}\right) - \frac{\sigma a^2}{(r_1 r_2)^{\frac{3}{2}}} r_1 \sin(\theta_1) \sin\left(\frac{3}{2}[\theta_1+\theta_2]\right) \quad (2.21a)$$

$$\sigma_{yy} = \frac{\sigma r}{\sqrt{r_1 r_2}} \cos\left(\theta - \frac{\theta_1+\theta_2}{2}\right) + \frac{\sigma a^2}{(r_1 r_2)^{\frac{3}{2}}} r_1 \sin(\theta_1) \sin\left(\frac{3}{2}[\theta_1+\theta_2]\right) \quad (2.21b)$$

$$\sigma_{xy} = \frac{\sigma a^2}{(r_1 r_2)^{\frac{3}{2}}} r_1 \sin(\theta_1) \cos\left(\frac{3}{2}[\theta_1+\theta_2]\right) \quad (2.21c)$$

If a point that lies close to one of the crack tips is selected, then the following relationship can be assumed,

$$r_2 \approx 2a, \quad r \approx a, \quad \theta_2 \approx \theta \approx 0 \quad (2.22)$$

When Eqn.(2.22) is substituted into Eqns. (2.21), this gives the following expressions in the vicinity of either of the crack tips,

$$\sigma_{nn} = \frac{\sigma\sqrt{\pi a}}{\sqrt{2\pi r}} \cos\left(\frac{\theta}{2}\right) \left[1 - \sin\left(\frac{\theta}{2}\right) \sin\left(\frac{3\theta}{2}\right)\right] \quad (2.23a)$$

$$\sigma_{bb} = \frac{\sigma\sqrt{\pi a}}{\sqrt{2\pi r}} \cos\left(\frac{\theta}{2}\right) \left[1 + \sin\left(\frac{\theta}{2}\right) \sin\left(\frac{3\theta}{2}\right)\right] \quad (2.23b)$$

$$\sigma_{nb} = \frac{\sigma\sqrt{\pi a}}{\sqrt{2\pi r}} \cos\left(\frac{\theta}{2}\right) \sin\left(\frac{\theta}{2}\right) \cos\left(\frac{3\theta}{2}\right) \quad (2.23c)$$

where (n, b) are the crack local coordinates with the origin at the crack tip, see Fig. 2.8. The term $\sigma\sqrt{2\pi}$ is a constant for a particular geometry and loading; hence, it is replaced with the constant K_I. By recalling the first order terms of the Williams expansion for an edge crack (2.13), and comparing the expressions in (2.23), we observe that the two equations are identical. This further proves that regardless of geometry or loading equations relating stresses and displacement around a crack are the same. Also the constant K_I is the key parameter governing the magnitudes of stresses and displacements. In a similar manner, the singular coefficient for mode II can be determined, and then substituted into (2.21), to generate expressions for stresses around the crack tip, which are given by,

$$\begin{aligned}\sigma_{nn} &= \frac{K_I}{\sqrt{2\pi r}}\cos\left(\frac{\theta}{2}\right)\left[1-\sin\left(\frac{\theta}{2}\right)\sin\left(\frac{3\theta}{2}\right)\right] \\ &- \frac{K_{II}}{\sqrt{2\pi r}}\sin\left(\frac{\theta}{2}\right)\left[1-\cos\left(\frac{\theta}{2}\right)\cos\left(\frac{3\theta}{2}\right)\right]+\dots \end{aligned} \tag{2.24a}$$

$$\begin{aligned}\sigma_{bb} &= \frac{K_I}{\sqrt{2\pi r}}\cos\left(\frac{\theta}{2}\right)\left[1+\sin\left(\frac{\theta}{2}\right)\sin\left(\frac{3\theta}{2}\right)\right] \\ &+ \frac{K_{II}}{\sqrt{2\pi r}}\sin\left(\frac{\theta}{2}\right)\left[1-\cos\left(\frac{\theta}{2}\right)\cos\left(\frac{3\theta}{2}\right)\right]+\dots \end{aligned} \tag{2.24b}$$

$$\begin{aligned}\sigma_{nb} &= \frac{K_I}{\sqrt{2\pi r}}\cos\left(\frac{\theta}{2}\right)\sin\left(\frac{\theta}{2}\right)\cos\left(\frac{3\theta}{2}\right) \\ &+ \frac{K_{II}}{\sqrt{2\pi r}}\sin\left(\frac{\theta}{2}\right)\cos\left(\frac{\theta}{2}\right)\sin\left(\frac{3\theta}{2}\right)+\dots \end{aligned} \tag{2.24c}$$

Hooke's law is used to obtain strains, which are then integrated. This allows for writing the displacements surrounding the crack tip as,

$$\begin{aligned}u_n &= \frac{K_I}{2\mu}\sqrt{\frac{r}{2\pi}}\cos\left(\frac{\theta}{2}\right)\left[\kappa-1+2\sin^2\left(\frac{\theta}{2}\right)\right] \\ &+ \frac{K_{II}}{2\mu}\sqrt{\frac{r}{2\pi}}\sin\left(\frac{\theta}{2}\right)\left[\kappa+1+2\cos^2\left(\frac{\theta}{2}\right)\right] \end{aligned} \tag{2.25a}$$

$$\begin{aligned}u_b &= \frac{K_I}{2\mu}\sqrt{\frac{r}{2\pi}}\sin\left(\frac{\theta}{2}\right)\left[\kappa+1-2\cos^2\left(\frac{\theta}{2}\right)\right] \\ &- \frac{K_{II}}{2\mu}\sqrt{\frac{r}{2\pi}}\cos\left(\frac{\theta}{2}\right)\left[\kappa-1-2\sin^2\left(\frac{\theta}{2}\right)\right] \end{aligned} \tag{2.25b}$$

where μ is the shear modulus of the material. These expressions can be used to determined the stress and displacement at any point around the crack, once parameters K_I and K_{II} are evaluated. The stress intensity factor defines strains and stress as well as displacements in the vicinity of the crack tip; on the other hand, the net change in the potential energy caused by extension of the crack length is defined by the energy release rate. Finally, the antiplane shearing mode which is the third mode in fracture mechanics (mode III), does

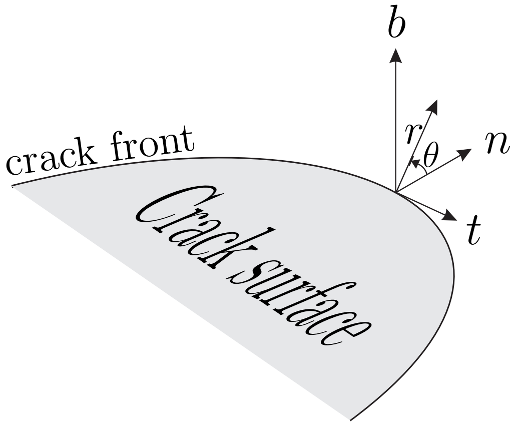

Figure 2.9: Local coordinates at a 3D the crack front

not occur in the plane of the problem.

2.8 Singular field problems in anti-plane mode

A crack in a three-dimensional geometry is an essential component of fracture analysis and fracture toughness examination, as it appears frequently when assessing failures. However, we must present mode III before considering stress intensity factors in three-dimensions. The antiplane shearing or tearing mode (mode III) does not appear in planar elasticity, which explains why this mode was not included in the studies of Williams and Westergaard. A cracked body subjected to antiplane loading always yields similar form of stress singularity distribution at the crack tip as shown by [20]. The evaluation of mode III needs to be considered in a cylindrical coordinate r, θ, t; such that r is measured from the crack front, and $0 < \theta < \pm\pi$ in the plane $n - b$ which is perpendicular to the crack surface, while t is perpendicular to the $n - b$ plane, as presented in Fig. 2.9. Its useful to introduce all the components associated with the new added axis t for mode I and II. Firstly, stress and displacement components in the antiplane shearing for mode I are given by,

$$\sigma_{tt} = \nu(\sigma_{nn} + \sigma_{bb}) \quad \text{plane strain} \tag{2.26a}$$

$$\sigma_{tt} = 0 \quad \text{plane stress} \tag{2.26b}$$

$$\sigma_{nt} = \sigma_{bt} = 0 \tag{2.26c}$$

$$u_t = 0; \tag{2.26d}$$

and for mode II,

$$\sigma_{tt} = \nu(\sigma_{nn} + \sigma_{bb}) \tag{2.27a}$$

$$\sigma_{nt} = \sigma_{bt} = 0 \tag{2.27b}$$

$$u_t = 0; \tag{2.27c}$$

where σ and u are the local stresses and displacements. The asymptotic stresses for mode III can be expressed as

$$\sigma_{nn} = \sigma_{bb} = \sigma_{tt} = \sigma_{nb} = 0 \tag{2.28a}$$

$$\sigma_{nt} = -\frac{K_{III}}{\sqrt{2\pi r}} \sin\frac{\theta}{2} \tag{2.28b}$$

$$\sigma_{bt} = \frac{K_{III}}{\sqrt{2\pi r}} \cos\frac{\theta}{2} \tag{2.28c}$$

Also the asymptotic displacements for mode III are,

$$u_n = u_b = 0 \tag{2.29a}$$

$$u_t = \frac{K_{III}}{2\mu}\sqrt{\frac{r}{2\pi}} \sin\frac{\theta}{2} \tag{2.29b}$$

where μ is the shear modulus of the material. A crack three-dimensional body can be treated as two-dimensions, since the field containing the crack front singularity is approximately two-dimensional. An investigation by [21] found the crack tip stress singularity is identical to the form of the two-dimensional singularity. In addition, a study by [22] demonstrated that the distribution of asymptotic stresses around a penny shaped crack is similar to the two-dimensional result. The analytical stress intensity factor for a penny shaped crack in an infinite domain under mode I conditions [23]; is given by,

$$K_I = \frac{2}{\pi}\sigma\sqrt{\pi a} \tag{2.30}$$

where K_I is the singular coefficient for mode I, σ the applied stress, and a the radius of the penny shaped crack. The use of two-dimensional SIFs for three-dimensional problems requires special care, since SIFs depend on the location of the point at the crack front, at which the stresses are evaluated. Furthermore, for 3D problems a body is modelled by volume and a crack by a smooth surface while the front of a crack by a smooth curve. Taking any point as the origin of the local coordinates include an n-axis pointing along the direction of the propagation of the front, a b-axis perpendicular to the plane of the crack, and a t-axis tangent to the crack front, as presented in Fig. 2.9.

In applications, a fracture toughness of materials can be used to determine the critical value of SIFs. In general fracture toughness is used to indicate the resistance of materials to propagate a pre-existing flaw. Standard engineering procedures assume that flaws of various sizes are present to some extent in all materials, since they cannot be certain if a material is defect free. However, engineers have made use of LEFM theory to obtain fracture toughness, as denoted by K_{Ic}, K_{IIc} and K_{IIIc} for mode I, II and III, respectively. In this approach, the flaw shape, material geometry, boundary conditions and material fracture toughness are considered to assess the ability of materials to resist fracture.

2.9 Stress Intensity Factors in Fatigue

Fatigue is damage that occurs as sub-critical crack growth under a cyclical load. Fatigue cracks continue to propagate under this cyclical load until they either retard or reach a critical length at which rapid and catastrophic failure occurs. Since, cracks are accepted to exist in structures under the concept of damage tolerance. It is vital that engineers are able to predict the crack growth rate subject to cycle load, not only for aircraft but also other structures. Therefore, the part in question can then be replaced or repaired before the crack reaches a critical length. A fundamental yet simple equation, which might often be used to determine the crack growth rate is the Paris law [24]. By examining a number of alloys he realised that a log-log scale gives a straight line when the crack growth rate is plotted against the range of SIF, as presented in Fig.2.10. Mathematically this can be written as,

$$\frac{da}{dN} = C(\Delta K)^m \tag{2.31}$$

where a denotes the crack length, and N is the number of cycles. C and m are constants dependent on the material properties, whereas ΔK represents the range of the stress intensity factor. Unquestionably, SIFs are the most significant parameters used for calculations of the rate of crack growth, with large accuracy dependence.

Table 2.1: Effect of SIFs error on the evaluation of N using Paris Law

Alloy	m	C	N_E		
			0.5% ΔK_{IE}	1% ΔK_{IE}	1.5% ΔK_{IE}
A533 Steel [25]	2.2	2×10^{-11}	1.09	2.17	3.22
40H Steel [25]	2.97	3.96×10^{-12}	1.47	2.91	4.33
1045 [26]	3.5	8.2×10^{-13}	1.73	3.42	5.08
A1 PA7 [25]	4	7×10^{-11}	1.98	3.9	5.78

It has been shown that in the vicinity of the crack exhibits singular stresses at the

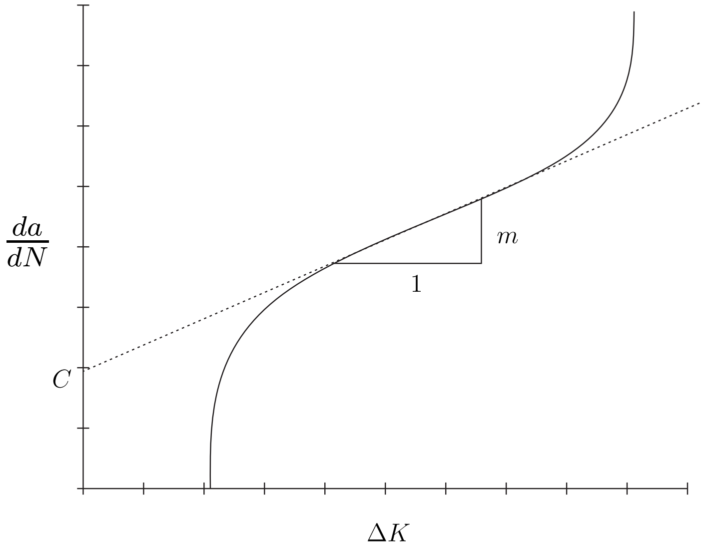

Figure 2.10: A log − log graph shows SIFs and fatigue relationship

point of the crack tip. Furthermore, the presence of singularity and the need for accurate evaluation of SIFs combination creates a challenge for any numerical method. Therefore, it is of great importance to evaluate SIFs accurately to allow Paris law to yield accurate results. To demonstrate this, we have considered a flat sheet under mode I cycling load with various material properties. Table 2.1 shows the sensitivity of N to error in the evaluation of K_I. Errors of 0.5%, 1% and 1.5% respectively, were imposed on the SIFs, then we calculated N using correct ΔK and ΔKs with the imposed errors. The results demonstrate that the percentage error in N is a function of m and can be written as,

$$N_E \approx m\Delta K_{IE} \tag{2.32}$$

where N_E and ΔK_{IE} are the percentage error in N and ΔK_I, respectivly. Therefore, it is clear that the inaccuracy of K_I will be amplified by m in the crack growth rate estimation. It should be noted that the material property m can be considerably higher for other materials, which lead to higher errors in the estimation of fatigue life. This error may lead to a failure to replace the damaged parts, or to set a precise schedule for inspections.

Chapter 3

Numerical Fracture Mechanics

3.1 Numerical Methods

Numerical methods form the most commonly used practical techniques for obtaining SIFs for two-dimensional and three-dimensional cracked bodies subjected to complex loading conditions. In fact, numerical simulation is a valid substitute tool for scientific experiments (particularly in relation to complex engineering problems) that can be expensive, time consuming, and in some cases dangerous. The following section presents the latest developments in popular methods that have been used for solving crack problems in LEFM.

3.1.1 Finite element method

The finite element method is a numerical technique used to compute solutions associated with boundary value problems in engineering analysis. The finite element approach is currently applied to a comprehensive range of engineering fields. The method has been extensively employed in the analysis of structures, solids, fluids and heat transfer. Although it is difficult to date exactly the invention of FEM [27–31], it is clear the development of finite element methods for solving practical engineering problems was accelerated by the advent of the digital computer .

The FEM governing equations are generally expressed as partial differential equations.

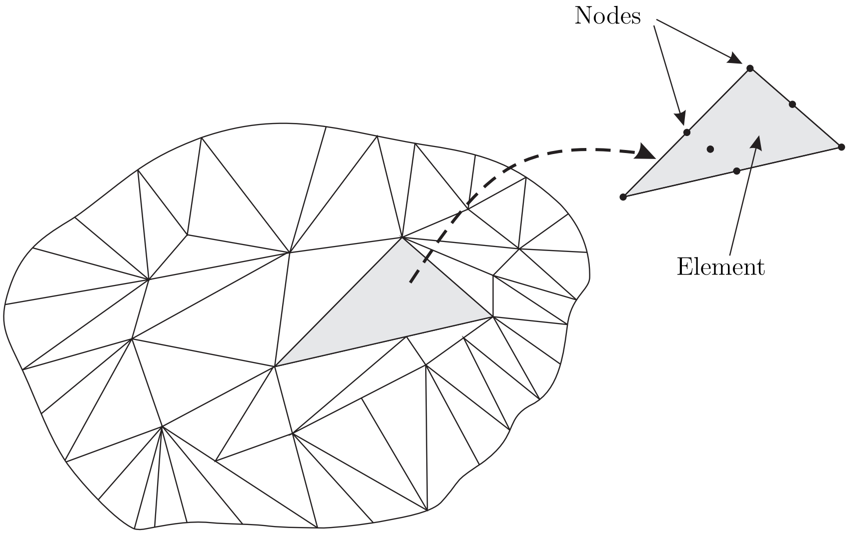

Figure 3.1: Finite element method with triangular mesh

These equations are written in a weak form through utilising domain integration to satisfy the governing equations in an average manner [32]. The virtual work of a domain V with boundary S subject to body force b_i and traction t_i can be expressed as,

$$\int_V \sigma_{ij} \delta\epsilon_{ij} dV = \int_V b_i \delta u_i dV + \int_S t_i \delta u_i dS \tag{3.1}$$

where σ_{ij} and $\delta\epsilon_{ij}$ are components of stress and virtual strain respectively, and u_i and δu_i represent the components of displacements and virtual displacement. The integration of the domain is approximated by summation over a finite number of elements that discretise the domain. Fig. 3.1 represents a two-dimensional domain in which triangular elements are used for discretisation. The variables are defined and determined at the nodal points, and the assessment of the domain variables is obtained by interpolation over an individual element. Shared nodes allow for the assembly of elements into a global system of equations capable of being represented in matrix form as,

$$[K]\{u\} = \{f\} \tag{3.2}$$

where K is the stiffness matrix, u is the primary variable that needs to be determined, and f is the applied load. The stiffness matrix for a structural finite element holds the material

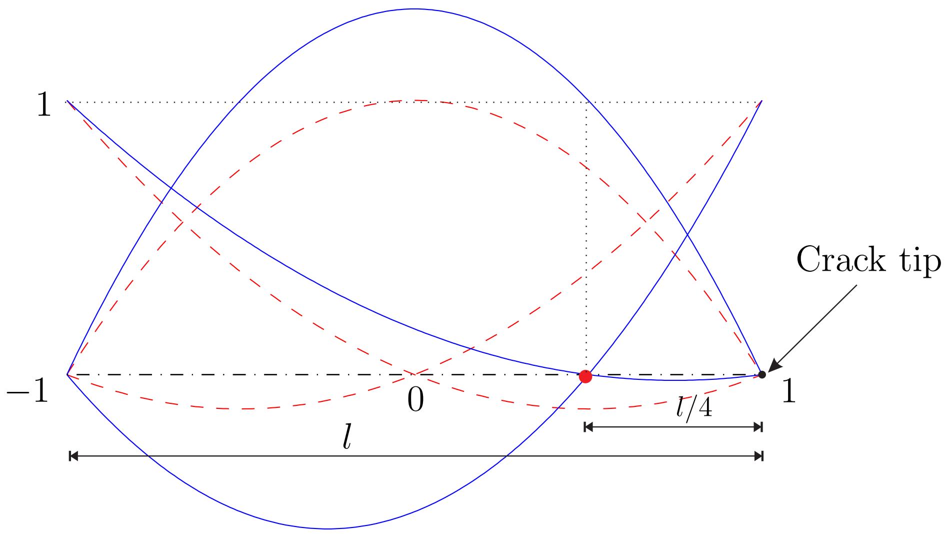

Figure 3.2: Quarter point element

and geometrical information which expresses the element resistance to deformation under loading conditions. These deformations can include axial tension, shear, bending, and torsional effects. The term *stiffness matrix* is also employed with non-structural analyses including fluid flow and heat transfer, since this matrix expresses the resistance of the element to change when external influences are applied [33].

The application of FEM to resolving crack problems involves significant difficulties, which arise when determining the singular field near the crack tip. Standard finite element methods only use regular polynomial functions for u_i, ϵ_{ij} and σ_{ij}. Therefore, they present a poor representation of the crack singularity as illustrated by [34]. Mesh refinement can be used at the crack tip, but a large number of elements can be required to achieve the required accuracy, and this has obvious consequences on computational efficiency. It is the genre experience that determines whether the mesh is optimal, or sufficient, for the problem under analysis. However, accuracy needs to be balanced with computational time and difficulties in relation to smooth mesh generation.

The use of a specialised element with the ability to capture the singularity (e.g. quarter-point) is considered, in order to avoid the refinement of the mesh. The quarter-point fundamental concept consists of modifying an isoparametric element with quadratic shape functions such that the mid-node position is changed [35]. Therefore, the coordinates of this node are shifted from the middle to the position of the quarter-point toward the crack tip see Fig. 3.2. The element displacement and stress fields are transformed into a form that precisely presents the radial function of the crack tip field. The non-linear mapping between the natural and local coordinates (known as nodal-distorted shape functions) produces the singular $1/\sqrt{r}$ behaviour. The two-dimensional quarter-point element can be generated from either a triangular, or a quadrilateral element, through changing the mid-nodes along two edges [36]. For instance, a quarter-point method has been employed by [37] for two-dimensional and three-dimensional problems in LEFM. Although, various techniques used to extract SIFs in a postprocessing step, including stress field, displacement field, and J-integrals. Furthermore, the presented two-dimensional edge crack results show that the best accuracy was achieved by the J-integral with an absolute error of 0.32%. For three-dimesnsons, the results for a central penny shaped crack show improve accuracy when the quarter-point element is employed with the J-integral. In addition, the quarter-point element was used for anisotropic by [38], whereas M-integral is used for extracting the SIFs. The submitted results demonstrate that an absolute error of 0.03% can be obtained with refined mesh for a two-dimensional edge crack. However, curved crack modelling requires particular attention. Alternatively, enriched FEM can be used to add singularity behaviour to the displacement approximations.

3.1.2 Extended Finite Element Method

Based on the FEM, the Extended Finite Element Method (XFEM) is a numerical approach designed specifically for treating discontinuities. Two types of discontinuity are generally considered, including weak discontinuities and strong discontinuities. Whereas weak discontinuities are found within the solution variable derivatives, strong discontinuities appear in the problem solution variables. The development of enriched elements has been established by Benzley [13], followed by the identification of the partition of unity approach, which was introduced by Melenk & Babuška [11]. In 1999, the concept of

XFEM was first introduced by [39], followed by the method gaining additional attention [40–45].

The utilisation of the partition of unity functions whose values adds up to unity at every point in the domain, is the primary concept behind the partition of unity methods. In general, the incorporation of a non-polynomial function is obtained through the concept of the partition of unity, and it is then possible to combine any set of functions to express the field locally [39]. It is important to note that, these non-polynomial functions are undistorted by the multiplication by shape functions because the shape functions exhibit the partition of unity property. Moreover, these functions may include any priori knowledge of the solution by experimental results or any analytical solution of the problem while the extended finite element method enables the inclusion of the local enrichment of approximation spaces.

The two-dimensional crack asymptotic displacement field enrichment can be achieved by employing a set of crack tip displacement functions incorporating the radial and angular behaviour as presented by [11]; and can be written as follows,

$$\Psi(x) = \{\Psi_1, \Psi_2, \Psi_3, \Psi_4\} = \left[\sqrt{r}\cos\frac{\theta}{2}, \sqrt{r}\sin\frac{\theta}{2}, \sqrt{r}\sin\theta\cos\frac{\theta}{2}, \sqrt{r}\sin\theta\cos\frac{\theta}{2}\right] \tag{3.3}$$

where r and θ denote the local coordinates with the origin at the crack tip. It should be noted that the partition of unity for finite element method [11] is similar to the extended finite element method [39], apart from the fact that XFEM is a local partition of unity method. *Locally* refers to the fact that only a region adjacent to the cracks is enriched with enrichment functions, employing the concept of the partition of unity. However, the introduction of additional degrees of freedom renders it problematic to implement the XFEM into pre-existing commercial finite element codes.

In general, XEFM is utilised to model crack propagation without the need for remeshing. Also, the implementation of enrichment improves the SIFs accuracy, results presented by [39], show an accurate evaluation of SIFs when using a local enrichment approach. For two-dimensional edge crack in a rectangular plate under shear load the absolute error of

K_I and K_{II} were 0.5% and 1.6%, respectively. In thee-dimensions, central penny shaped crack in a cube under uniaxial load considered by [41]. The presented results reveal an error of 1.4% when a sufficient number of elements are used. The XFEM has been under continuous development as a tool for fracture mechanics [46]. Hence, it exhibits accurate determination of SIFs while using coarse mesh.

3.1.3 Phase Field method

The concept of the phase field method consists of the introduction of a phase field that tracks the location of defects and cracks implicitly. The crack is expressed by a new added field variable, which is *one* if it is intact and *zero* if the material is fully cracked and cracking is considered as a phase transition problem [47]. In phase field crack models are expressed by a regularization parameter which controls the width of the transition zone, in which the developing damage field is interpolated between 1 and 0.

The phase field approach is attractive due to its ability to evaluate elegantly complicated fracture procedures, including crack initiation, propagation and branching, both in general situations and for three-dimensional geometries, without the need to use additional specialised approaches. A number of different phase field approaches have been investigated for fracture mechanics over the previous decade [48]. Based on Griffith theory a number of phase field models for quasi-static brittle fracture have been independently submitted, extended from the variational formulation and the associated regularised formulation for brittle fracture by [49, 50]. Furthermore, the complete process for quasi-static crack initiation, propagation and branching is governed by minimising the energy functional; which can be written as,

$$E(\mathbf{u}, \Gamma) = E_d(\mathbf{u}) + E_s(\Gamma) = \int_\Omega \varphi_0(\varepsilon(\mathbf{u}))\, d\Omega + G_c \int_\Gamma ds \tag{3.4}$$

where $E_d(\mathbf{u})$ denotes the elastic energy and $E_s(\Gamma)$ represents the energy required to create the crack. G_c is the material fracture toughness and φ_0 is the elastic energy density in relation to Griffith's theory. The approach has been extended by [49] to enable an efficient numerical treatment of Eqn. (3.4) by utilising a regularised form. Therefore, the regularised energy functional $E_\epsilon(\mathbf{u}, s)$ can be written as,

$$E_\epsilon(\mathbf{u}, s) = \int_\Omega (s^2 + \eta)\psi_0(\varepsilon(\mathbf{u}))\ d\Omega + G_c \int_\Omega \left(\frac{1}{4\epsilon}(1 - s^2) + \epsilon|\nabla s|^2 \right) \tag{3.5}$$

where s is a field variable, known as the crack field parameter. The value of s varies smoothly from $s = 1$ for undamaged material to $s = 0$ for fully separated material. An artificial residual stiffness of a totally broken phase, $s = 0$, is modelled by the small dimensionless parameter η which is essential to prevent numerical difficulties. Alternate minimisation and back-tracking algorithms are employed to determined the solution of Eqn. (3.5) as revealed in [49].

However, the use of the phase field to model crack problems imposes a number of restrictions on the mesh. Moreover, the finite element discretisation needs to be sufficiently fine in comparison to the length of the regularization parameter, where the parameter needs to be sufficiently fine to obtain reasonable results and determine singular field appearing near the crack. A study carried out by [51] suggests that the appropriate value of the regularisation parameter is 1% of the global geometric dimension of the specimen.

The phase field method has been utilised to model various types of interfaces. These include electromagnetic wave propagation [52], contact of liquid and solid problems [53], study of crystal structures [54] and applications that related to medicine [55] . In addition, there has been a continuous investigation of phase field methods for cracks for two-dimensions [47]. However, a small number of studies have been extended to the three-dimensional [56], in which crack front instabilities subjected to mixed mode conditions were examined. The computational cost of three-dimensional modelling is very high, leading to the use of grid adaptivity and highly parallelised techniques, being essential to the provision of efficient algorithms (consult [47] for further information).

3.1.4 Configurational Forces method

The method of configurational forces, also known as material forces, represents a robust technique for examining various types of material defects. The approach is utilised to investigate defects and track material deformation. Phase transformations and fracture mechanics are also among its applications. The configurational forces method was established by Eshelby [57, 58] to study internal forces acting on a crack tip singularity. Based on restrictive constitutive equations by [59], Gurtin [60] presented a general configurational force balance, outlined as follows (in keeping with the notation of [60]),

$$\int_{\partial R} Dm\, da + \int_{R} f da + \int_{\partial \mathcal{B}} Cv\, ds + \int_{\mathcal{B}} \mathbf{e} da = 0 \tag{3.6}$$

where R is a three-dimensional domain that intersects with the phase interface, and m is an outward unit normal to ∂R. $\mathcal{B}$ is the interface surface in R, and n is a normal to this surface and v is the outward unit normal to the curve $\partial\mathcal{B}$, as illustrated in Fig. 3.3. The configurational fields presented in Eqn.(3.6) comprise the following: D is bulk stress, which operates in response to the exchange of the material surface at the boundary of R. Generalised surface tension C is stress within the interface that acts in response to the increment in the interfacial region and the changes in the orientation of the interface. In addition, $\mathbf{e}$ and f are the internal forces distributed over the interface and the bulk volume, respectively.

Moreover, several formulations have been proposed, including fracture initiation defects for a brittle fracture [50, 61], and numerical evaluation of material configurational forces at static fracture fronts [62–65]. For instance, a numerical implementation using finite element method was introduced by [66], considering a variational formulation of brittle fracture in elastic solids. The presented results for a two-dimensional edge crack in rectangular plate under tensile stress show that, an accuracy of 8.8% can be achieved when a refined mesh is used. In addition, the configurational forces method has been implemented successfully in fracture propagation with the finite element, extended finite

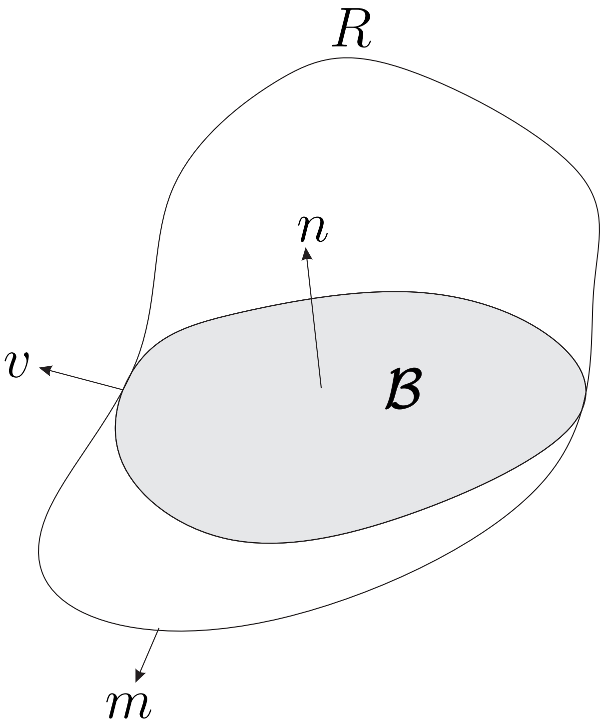

Figure 3.3: The interface contained within the control volume

element and discontinuous Galerkin method by [67–69]. Recently, configurational force has been applied to fracture mechanics by [70], in order to consider large, isotropic and hyperelastic problems in three-dimensions. Furthermore, this approach can be easily extended to deal with anisotropic materials. However, the configurational forces method is currently incapable of handling non-smooth crack kinking [71]. Additionally, further limitations include crack branching and multiple crack coalescence, which have not been considered or formulated.

3.1.5 Meshless methods

The FEM has been implemented in a large number of fields of research, with considerable success. However, the use of FEM places limitations and restrictions on the quality of the mesh. As a result of mesh interpolation, distorted and low quality mesh leads to the increment of errors, and the subsequent requirement for remeshing is time consuming for both humans and machines, particularly when dealing with complex three-dimensional geometries as shown by [72]. Additionally, classical mesh based techniques are not fully suited to addressing an issue of discontinuity that fails to align with the element edges,

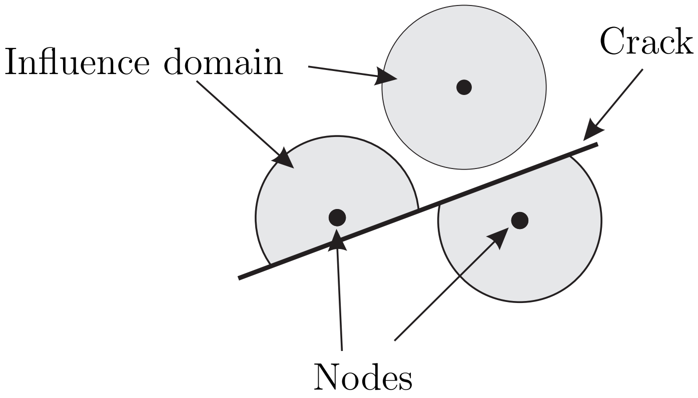

Figure 3.4: Visibility criterion of meshfree nodes

leading to discontinuities being handled by remeshing or discontinuous enrichment. Commonly, costly remeshing can generally be avoided by the enrichment of the approximation functions, thus adding new degrees of freedom to the system.

The fundamental concept behind meshfree methods is to provide an accurate solution to an integral equation through a set of nodes arbitrarily distributed in the domain, and without defining a mesh that relates these nodes to one another [73]. In a similar concept, a number of meshfree techniques have been proposed to date, with the earliest being submitted simultaneously by Lucy [74], and Gingold and Monaghan [75] who introduced smoothed particle hydrodynamics.

An element free Galerkin method was proposed by [76] to handle linear elastic fracture problems. The approach uses a visibility criterion to model crack discontinuity, such that the domain of influence for a node near the crack is truncated when intersecting with the crack surface as in Fig. 3.4. It based on the fact that a node on one side of the crack surface will not affect points on the opposite side of the crack surface. However, the implementation of visibility criterion creates difficulties when dealing with nodes near the crack tip. An improved continuous meshless approximations utilising the diffraction and transparency method submitted by [77] to treat near crack tip nodes.

An enrichment of the element free Galerkin method has been introduced by [78, 79], where the linear elastic fracture mechanics approximation is enriched both extrinsically and intrinsically. An example of method enriched by the analytical solution in an extrinsic manner is presented by [80], as,

$$u(x) = \sum N^p u(x)^p + \sum_{n=1}^{n_k} \hat{K}_I^n \psi_I^n + \hat{K}_{II} \psi_{II}^n \tag{3.7}$$

where n_k is the total number of cracks, u^p is the nodal displacement and N is the usual polynomial basis. $\hat{K}_I$ and $\hat{K}_{II}$ denotes the additional degrees of freedom for mode I and II, respectively. The functions ψ_I^n and ψ_{II}^n are the leading order terms of Williams displacement expansions. Recently, an element free Galerkin method has been employed to evaluate stress intensity factors for cracks in composite material [81]. In the proposed approach, the integral interaction technique has been extended to the element free Galerkin method, and the newly developed interaction integrals have been introduced for the analysis of mixed mode fracture problems. The submitted results show that, the obtained K_I by the proposed EFGM agree with the analytical results for various combinations of E_2/E_1 and a/W ratios.

Noted in element free Galerkin, polynomial shape functions are replaced by functions based on moving least squares expression [82]. Moreover, the integration of the weak form integral equation is obtained over a regular background grid (making it to some extent not truly meshless). Utilising this formulation coupled with an enriched basis in two-dimesnsions, [83] were able to obtain an accurate evaluation of SIFs with an absolute error of 0.3%. However, in the Meshless Local Petrov Galerkin (MLPG) method [84], the integration is considered over multiple overlapping sub-domains centred on the nodes. The assumption being that if the equation is satisfied over these sub-domains, then it will also be satisfied over the volume as a whole. The method has been successfully applied to model elastoplastic fracture problem of moderately thick plate by [85].

In general, meshfree methods benefit from higher order continuity and yield a smoother stress distribution near the crack fronts [72]. Although meshfree methods have been implemented in most fields of structure and fracture mechanics, difficulties remain in the development of efficient computational algorithms with sufficient nodal integration and scalable application of essential boundary conditions [86].

3.1.6 Boundary Element Method

The boundary element method is a numerical technique applied to solve Partial Differential Equations (PDEs). PDEs, expressing the behaviour of the unknown both inside and on the boundary of a domain, are transformed into an integral equation over the boundary. Subsequently, the numerical solution to this equation is calculated at the boundary only, while internal stresses and strains can be evaluated through a post-process step. Based on the formulation proposed by Green [87], Jaswon [88] used a direct boundary integral equation formulation to solve potential problems numerically. Furthermore, Rizzo [89] extended the method to elastostatics, and this was later adapted to solve 3D problems by [90].

The use of the BEM in linear elastic fracture mechanics has now become well established, and is commonly implemented in practice. The ability to accurately evaluate the stress intensity factors is the main reason for using the BEM over other methods, such as the FEM [91]. Therefore, many approaches have been submitted to estimate SIFs using the BEM. However, the direct application of the BEM to coplanar surfaces (i.e., two crack surfaces lying on the same plane) leads to mathematical degeneration [92]. On the other hand, this difficulty can be overcome for symmetrical geometries by imposing the symmetry of the boundary conditions and then considering only one crack surface.

A more general and widely applied technique for non-symmetrical cracks was submitted by [93]. This approach uses the formulation of multi-domains which can be implemented for anti-symmetrical as well as symmetrical crack problems in both two-dimensional and three-dimensional configurations. The method splits the body into multi-domains; each domain has artificial boundaries, with the consequence that a domain has only one crack surface. However, the use of sub-domain method introduces extra degrees of freedom and is difficult to automate for crack propagation modelling. Alternatively, the dual boundary element method presented by [94–96] has been confirmed as a general and efficient method for modelling cracks. Indeed, the DBEM can model coplanar surfaces problems in a single domain formulation by applying the displacement boundary integral equation to one surface and the traction boundary integral equation to the opposite surface. However, the main difficulty arising from the formulation of the DBEM is the requirement to evaluate of Cauchy and Hadamard principal value integrals, occurring in the traction BIE [97]. Thus, the derivation of the DBEM has considered the required conditions for the existence of these singular integrals; however, certain restrictions are imposed on the selection of the shape functions for elements on the crack surfaces [94]. The method has been applied successfully to model cracks in two-dimensions whereas the values of SIFs are extracted by the J-integral [94]. The results show that accuracy of 0.4% when the ideal J-integral path is selected. The DBEM was also extended to three-dimensions [95] and the J-integral is used to obtain the SIFs for inclined crack in a cylinder.

Commonly, adaptive techniques are applied to the boundary element method in order to overcome the singular behaviour associated with the crack tip. The most frequently used approach including the subtraction of singularity method and the weight function method, as presented in [98]. However, in most postprocessing procedure is needed to evaluate the stress intensity factors, which can be achieved using path independent contour integrals.

3.1.7 Extended Boundary Element Method

The finite element method has been used as a framework for a large number of modified techniques that have been formulated for fracture analysis. However, the use of the boundary element method as a framework has increased, due to the ability to capture discontinuous functions and to provide accurate results on the boundary, which is where the crack lies. The method proposed by [99] introduced the formulation of special singular shape functions including Williams expansion, which expresses a crack tip singularity. Embedded unknowns are added in the formulation of the shape functions, hence, there is a need to employ auxiliary boundary integral equations.

Furthermore, Williams expansions have been used with the BEM by Portela et al. [97] to subtract the singularity by dividing the domain into singular and regular fields.

The technique was able to evaluate K_I and K_{II} directly. Recently, the partition of unity approach was used by Simpson and Trevelyan [14], who presented an enriched boundary element method in a similar manner to the XFEM. Moreover, this work extended the benefits of XFEM to provide high accuracy of the SIFs from a coarse and boundary-only discretisations. Indeed, they extended the application of the enrichment method to curved cracks [100]. However, both implementations relied on the use of the J-integral [101] to calculate the SIFs. A similar approach for anisotropic materials was submitted by [102] to explore the use of enrichment functions embedded into the boundary element method formulation. The main advantage of this approach was the reduction in the additional degrees of freedom generated opposed to the classical partition of the unity approach. The enrichment functions were obtained using the Stroh formalism [103]; a concise formulation that is dependent only on material properties.

The use of the square root behaviour for enrichment is not new; an earlier approach in which the square root was introduced into the shape functions for special crack tip elements was proposed by Li, *et al.* [104], and applied to the relative crack face displacements in a symmetric Galerkin BEM based on weak form integral equations. The current thesis describes an new enriched XBEM algorithm for fracture mechanics. The starting point of this work, as presented in Alatawi and Trevelyan [105], is to develop a new method for writing the auxiliary equations and thereby recover the SIFs directly from the solution vector, precluding the need for a postprocessing stage like the J-integral.

3.2 Assessment of Stress Intensity Factors

In making fracture assessments, particularly the prediction of crack propagation, it is important to have an accurate understanding of the stress field in the vicinity of the crack tip. In the context of linear elastic fracture mechanics, SIFs together with the Williams expansions, play a major role in the determination of stresses and displacements that distributed over the singular field. Studies on the calculation of SIFs have yielded various approaches that include analytical and numerical techniques. Essentially, analytical methods are only suitable for specifically defined crack geometries and boundary conditions.

Thus, in the case of a wide range of problems with simple geometry and loading, the SIFs can be determined from handbooks (e.g. [23]). However, when dealing with complicated shapes and boundary conditions, engineers must make use of numerical methods in order to resolve the stress fields and thereby, reveal the SIFs.

Generally, the evaluation of SIFs can be classified into either direct or postprocessing methods. Direct methods offer the speed and flexibility to evaluate higher order terms. The direct value of SIFs are extracted by manipulating the calculation of displacements and stresses related to elements adjacent the crack tip. In the main, two methods are most commonly used to obtain SIFs directly, which include the enriched element [13] and the hybrid element [106]. The difference between these approaches is evident in the treatment of the displacement compatibility. In the case of the hybrid element approach, displacement compatibility is enforced by minimising a functional that contains displacements and added unknowns. Whereas, in the case of enriched element formulation, displacement compatibility is exactly satisfied through applying a transition element, which connects the regular element and the enriched element at the crack tip. An example of hybrid element use is the work by Xiao and Karihaloo [4], which aimed to evaluate SIFs and the coefficients higher order terms. Whereas, enrichment by a square root was introduced into the shape functions for special crack tip elements in an earlier study by Li, *et al.* [104]. On the other hand, the J-integral is a postprocessing approach taken over a closed independent integral path and based on energy approach. Furthermore, the J-integral is the most popular postprocessing technique and is available to general purpose FEM and BEM codes that do not have any particular formulations injected in order to deal directly with the stress singularity.

The increasing applications of composite and non-linear materials in many engineering fields has motivated researchers to consider the resistance of these materials to crack initiation and propagation, which requires the determination of the SIFs. Recently, several approaches have been added, including fractal hybrid finite elements [107] and fractal-like FEM [108] for handling bi-material problems. The fractal finite element method, which divides the domain into a regular and a singular region, where the crack tip is the centre of similarity for the singular region was introduced by [109, 110]. Furthermore, several generalised stress intensity factor methods have been proposed to handle composite material accurately, as presented in [111, 112].

The Gauss Chebyshev method was modified by [113] in such a way as to directly evaluate the stress intensity factors at the crack tips. Moreover, the extrapolation of displacements or stresses [114] can be used to evaluate SIFs with acceptable accuracy. Further examples of the successful application of the direct evaluation of stress intensity factors can be found in [115, 116]. In the context of LEFM, many analytical techniques have been developed which involve the direct and postprocess evaluation of SIFs [117]. However, for the purposes of this thesis, the J-integral (a postprocessing method) has been employed to verify numerical results and demonstrate the effect of the use of the enriched boundary element method. Therefore, it is essential to present the J-integral decomposition for both two-dimensional and three-dimensional problems.

3.2.1 J-integral

The J-integral was introduced by Rice [101] as a general approach to detrmine the energy release rate. Rice demonstrated that the J-integral is a path independent approach, since the evaluation of the integral in a far field around a crack tip is related to the deformation near the crack tip. The advantages of using the J-integral method are that it can be computed numerically along a path around the crack tip, and can be employed for linear and non-linear problems. Several numerical techniques [118–121] have been developed utilising the J-Integral to evaluate the components of SIFs for various type of cracks using both the BEM and the FEM, and including two-dimensional and three-dimensional problems. Two techniques used to extract the SIFs from a mixed mode J-integral for 2D and 3D crack problems will be presented shortly.

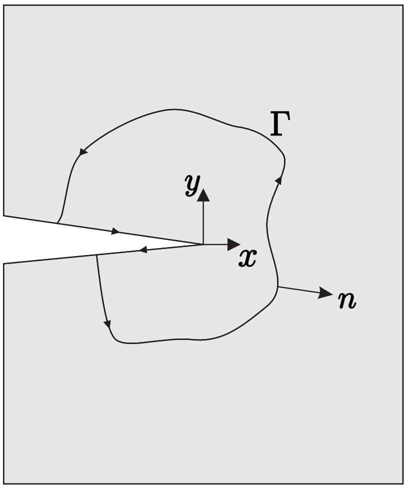

Figure 3.5: J-integral path in 2D domain

3.2.1.1 Decomposition of the 2D J-integral

Consider a path Γ surrounding a 2D flat crack with local coordinates x, y originating at the crack tip, so that the path starts at a point on the lower crack surface and ends at a point on the upper crack surface, as shown in Fig. 3.5. The J-integral can be defined as,

$$J = \int_{\Gamma} \left(W n_x - t_i \frac{\partial u_i}{\partial x} \right) d\Gamma \tag{3.8}$$

where u_i and t_i are the displacement and traction components, respectively. In addition, n_x is the outward normal in x-direction to the path Γ. The integral path Γ is a closed contour around the crack tip that includes parts from the upper and lower crack faces. It is sufficient not to include the portion of the path along the crack surfaces when analysing traction-free crack problems, since $n_x = t_i = 0$. Finally, W as it appears in equation (3.8) represents the strain energy density and can be defined as,

$$W = \frac{1}{2} \sigma_{ij} \epsilon_{ij} \tag{3.9}$$

where σ_{ij} and ϵ_{ij} are the stress and strain components, respectively. In order to gain a better understanding of the crack behaviour, it is necessary to express the J-integral in terms of the SIFs. Since the J-integral is equivalent to the energy release rate, it can be

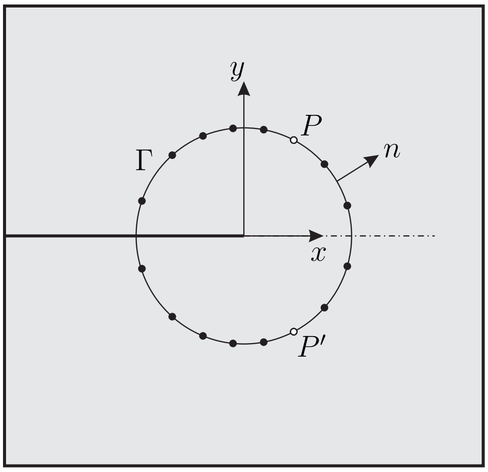

Figure 3.6: J-integral with symmetrical internal points

expressed in terms of the SIFs for the 2D plane stress (see Eqn. (C.1.7)); as,

$$J = \frac{K_I^2}{E'} + \frac{K_{II}^2}{E'} \tag{3.10}$$

where E' is the modified Young's Modulus for plane stress and plane strain as presented in Eqns. (A.1.12). Consider a special case, when K_{II} equals zero (pure mode I), then a simple rearrangement of Eqn. (3.10) will yield the value of K_I directly. However, very often cracks in actual geometry are subjected to mixed mode crack conditions. Thus, it is important to decouple the J-integral into the two components of mode I and II in the case of mixed mode cracks. Indeed, several approaches have been submitted to decompose the J-integral into its components, including [122, 123]. A simple technique suggested by Ishikawa, *et al.* [124] is to separate the J-integral into mode I and II. They demonstrated that the components on the J-integral path, which include strain, displacement, stress and traction, can be decoupled analytically if a symmetrical mesh is placed around the crack tip. Consider two symmetrical points $P(x, y)$ and $P'(x, -y)$ around the crack line as presented in Fig. 3.6. Here, σ_{ij}, ϵ_{ij}, u_i and t_i are the field components of the point $P(x, y)$, and similarly σ'_{ij}, ϵ'_{ij}, u'_i and t'_i are the field components of the point $P'(x, -y)$; then the symmetrical and anti-symmetrical parameters can be written as,

$$\sigma_{ij} = \sigma_{ij}^{I} + \sigma_{ij}^{II} \tag{3.11a}$$

$$\epsilon_{ij} = \epsilon_{ij}^{I} + \epsilon_{ij}^{II} \tag{3.11b}$$

$$u_i = u_i^{I} + u_i^{II} \tag{3.11c}$$

where

$$\begin{Bmatrix} \sigma_{xx}^{I} \\ \sigma_{yy}^{I} \\ \sigma_{xy}^{I} \end{Bmatrix} = \frac{1}{2}\begin{Bmatrix} \sigma_{xx} + \sigma'_{xx} \\ \sigma_{yy} + \sigma'_{yy} \\ \sigma_{xy} - \sigma'_{xy} \end{Bmatrix}, \quad \begin{Bmatrix} \sigma_{xx}^{II} \\ \sigma_{yy}^{II} \\ \sigma_{xy}^{II} \end{Bmatrix} = \frac{1}{2}\begin{Bmatrix} \sigma_{xx} - \sigma'_{xx} \\ \sigma_{yy} - \sigma'_{yy} \\ \sigma_{xy} + \sigma'_{xy} \end{Bmatrix} \tag{3.12a}$$

$$\begin{Bmatrix} \epsilon_{xx}^{I} \\ \epsilon_{yy}^{I} \\ \epsilon_{xy}^{I} \end{Bmatrix} = \frac{1}{2}\begin{Bmatrix} \epsilon_{xx} + \epsilon'_{xx} \\ \epsilon_{yy} + \epsilon'_{yy} \\ \epsilon_{xy} - \epsilon'_{xy} \end{Bmatrix}, \quad \begin{Bmatrix} \epsilon_{xx}^{II} \\ \epsilon_{yy}^{II} \\ \epsilon_{xy}^{II} \end{Bmatrix} = \frac{1}{2}\begin{Bmatrix} \epsilon_{xx} - \epsilon'_{xx} \\ \epsilon_{yy} - \epsilon'_{yy} \\ \epsilon_{xy} + \epsilon'_{xy} \end{Bmatrix} \tag{3.12b}$$

$$\begin{Bmatrix} u_{x}^{I} \\ u_{y}^{I} \end{Bmatrix} = \frac{1}{2}\begin{Bmatrix} u_{x} + u'_{x} \\ u_{y} - u'_{y} \end{Bmatrix}, \quad \begin{Bmatrix} u_{x}^{II} \\ u_{y}^{II} \end{Bmatrix} = \frac{1}{2}\begin{Bmatrix} u_{x} - u'_{x} \\ u_{y} + u'_{y} \end{Bmatrix} \tag{3.12c}$$

Since, the J-integral path is symmetrical around the crack plane when $y = 0$, then the outward normals associated with the points $P(x, y)$ and $P'(x, -y)$ hold the following relationship,

$$(n'_x, n'_y) = (n_x, -n_y) \tag{3.13}$$

The substitution of Eqns. (3.11) into Eqn. (3.8) bearing the relationship with Eqn. (3.13) in mind, means that the J-integral can be presented as,

$$J = J_I + J_{II} \tag{3.14}$$

where J_I and J_{II} are defined as,

$$J_l = \int_{\Gamma} \left(\frac{1}{2}\sigma_{ij}^{l}\epsilon_{ij}^{l} n_x - t_i^{l}\frac{\partial u_i^{l}}{\partial x} \right) d\Gamma \quad l = I, II \tag{3.15}$$

The J-integral is widely implemented in both the FEM and the BEM to determine the SIFs with high accuracy. In the case of three-dimensions, the decomposition of the J-integral yields the SIFs for modes I, II and III, which will be represented in the next section.

3.2.1.2 Decomposition of the 3D J-integral

In a similar manner to the decomposition of the J-integral in 2D, the individual SIF components of the J-integral are obtained from the field parameters that are combined from symmetrical points around the crack plane. The implementation of the J-integral to three-dimensional crack problems has been presented by [125–128]. Subsequently, Rigby and Aliabadi [129] applied the correct decomposition to the three-dimensional problems, where the J-integral is presented as,

$$\begin{aligned} J(\eta) &= \int_{\Gamma_\epsilon} \left(W n_n - t_i \frac{\partial u_i}{\partial x_n} \right) d\Gamma \\ &= \int_{C+\gamma} \left(W n_n - t_i \frac{\partial u_i}{\partial x_n} \right) d\Gamma - \int_{\Omega(C)} \frac{\partial}{\partial x_t} \left(\sigma_{it} \frac{\partial u_i}{\partial x_n} \right) d\Omega \end{aligned} \tag{3.16}$$

where $i = n, t, b$ and W represents the strain energy density and n_n is the unit normal in n-direction. Whereas, t_i and u_i are the traction and displacement components, respectively. The contour Γ_ϵ is identical to C_ϵ; however it proceeds in an anticlockwise direction. The value of the integrand is dependent on the location η at the crack front as shown in Fig. 3.7. In the case of traction-free cracks, the contour integral over the crack faces is zero. Furthermore, Rigby and Aliabadi demonstrated that the J-integral can be split into two parts to yield symmetrical and anti-symmetrical parts, which can be written as,

$$J = J^S + J^{AS} \tag{3.17}$$

where J^S and J^{AS} denote the symmetrical and anti-symmetrical parts, respectively. The symmetrical part is identical to mode I, whilst the anti-symmetrical part consists of modes

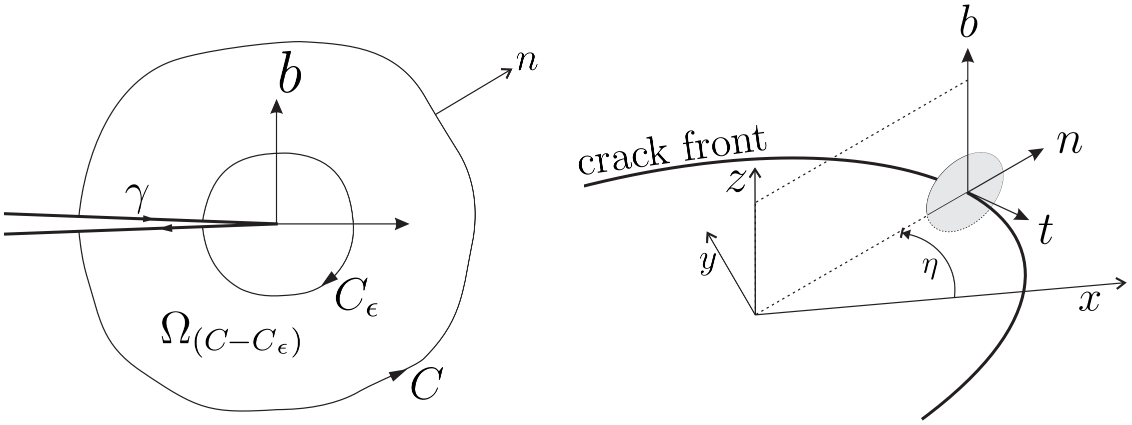

Figure 3.7: J-integral definition in 3D domain

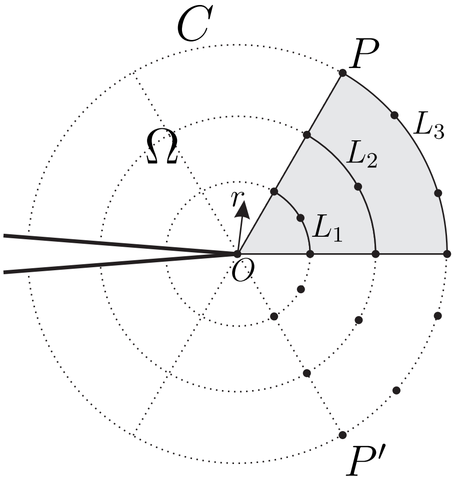

Figure 3.8: J-integral with symmetrical internal points on surface

II and III, represented as,

$$J^S = J^I \quad \text{and} \quad J^{AS} = J^{II} + J^{III} \tag{3.18}$$

where J^I, J^{II} and J^{III} are the J-integral components for modes I, II and III. Under further analysis, the decomposition approach separates the components of modes II and III. The three components are related to the J-integral by,

$$J(\eta) = J^I(\eta) + J^{II}(\eta) + J^{III}(\eta) \tag{3.19}$$

Consider a symmetrical contour around the crack plane (see Fig. 3.8) such that for any pair of symmetrical points P and P', the normals n and n' are related as,

$$n(n_n, n_b, 0) = n'(n_n, -n_b, 0) \tag{3.20}$$

Then the decomposition of the stresses can be represented by,

$$\begin{aligned} \sigma_{ij} &= \sigma_{ij}^{I} + \sigma_{ij}^{II} + \sigma_{ij}^{III} \\ &= \frac{1}{2}\begin{Bmatrix} \sigma_{nn} + \sigma'_{nn} \\ \sigma_{nb} - \sigma'_{nb} \\ \sigma_{nt} + \sigma'_{nt} \\ \sigma_{bb} + \sigma'_{bb} \\ \sigma_{bt} - \sigma'_{bt} \\ \sigma_{tt} + \sigma'_{tt} \end{Bmatrix} + \frac{1}{2}\begin{Bmatrix} \sigma_{nn} - \sigma'_{nn} \\ \sigma_{nb} + \sigma'_{nb} \\ 0 \\ \sigma_{bb} - \sigma'_{bb} \\ 0 \\ \sigma_{tt} - \sigma'_{tt} \end{Bmatrix} + \frac{1}{2}\begin{Bmatrix} 0 \\ 0 \\ \sigma_{nt} - \sigma'_{nt} \\ 0 \\ \sigma_{bt} + \sigma'_{bt} \\ 0 \end{Bmatrix} \end{aligned} \tag{3.21}$$

The decomposition of the strain is obtained from the stress decomposition by applying Hooke's law. The strain components can be written as,

$$\begin{aligned} \epsilon_{ij} &= \epsilon_{ij}^{I} + \epsilon_{ij}^{II} + \epsilon_{ij}^{III} \\ &= \frac{1}{2}\begin{Bmatrix} \epsilon_{nn} + \epsilon'_{nn} \\ \epsilon_{nb} - \epsilon'_{nb} \\ \epsilon_{nt} + \epsilon'_{nt} \\ \epsilon_{bb} + \epsilon'_{bb} \\ \epsilon_{bt} - \epsilon'_{bt} \\ \epsilon_{tt} + \epsilon'_{tt} \end{Bmatrix} + \frac{1}{2}\begin{Bmatrix} \epsilon_{nn} - \epsilon'_{nn} \\ \epsilon_{nb} + \epsilon'_{nb} \\ 0 \\ \epsilon_{bb} - \epsilon'_{bb} \\ 0 \\ \epsilon_{tt} - \epsilon'_{tt} \end{Bmatrix} + \frac{1}{2}\begin{Bmatrix} 0 \\ 0 \\ \epsilon_{nt} - \epsilon'_{nt} \\ 0 \\ \epsilon_{bt} + \epsilon'_{bt} \\ 0 \end{Bmatrix} \end{aligned} \tag{3.22}$$

The displacement can be obtained from Eqn.(3.22) by employing the relationship between strains and displacements (see Eqn. (A.1.3)) as,

$$\frac{\partial u_i}{\partial x_j} = \frac{\partial u_i^{I}}{\partial x_j} + \frac{\partial u_i^{II}}{\partial x_j} + \frac{\partial u_i^{III}}{\partial x_j} \tag{3.23}$$

The substitution of the decomposed field parameters in equations (3.23), (3.22) and (3.21) into equation (3.16), yields the J-integral components in terms of mode I, II and III, and can be written as,

$$\begin{aligned} J(\eta)^l &= \int_C \left(W^l n_n - \sigma_{ij}^l \frac{\partial u_i^l}{\partial x_n} n_j \right) d\Gamma \\ &+ \int_{\Omega(C)} \left(\frac{\partial \sigma_{in}^l}{\partial x_n} + \frac{\partial \sigma_{ib}^l}{\partial x_b} \right) \frac{\partial u_i^l}{\partial x_n} d\Omega - \int_{\Omega(C)} \sigma_{it}^l \frac{\partial^2 u_i^l}{\partial x_n \partial x_t} d\Omega \end{aligned} \tag{3.24}$$

where $l = I, II, III$. The integration value over the domain $\Omega(C)$ can be obtained in two steps. First, we evaluate the line integral of L_1, L_2 and L_3 using Simpson's Rule. Then, Newton-Cotes can be used, since the arcs (L_1, L_2, L_3) are equally spaced (see Fig. 3.8); for illustration a four points Newton-Cotes can be written as,

$$J_A = \frac{r}{8}(3L_1 + 3L_2 + L_3) \tag{3.25}$$

where J_A is the integral over the shaded segment. Likewise, we can obtain the integration value for all other segments. Since the J-integral components are obtained separately for each mode, then the SIFs can be determined (see Eqn.(C.1.7)) at any crack front position as,

$$J(\eta) = \frac{K_I^2(\eta)}{E'} + \frac{K_{II}^2(\eta)}{E'} + \frac{K_{III}^2(\eta)}{2\mu} \tag{3.26}$$

where E' denotes modified Young's modulus and μ is the shear modulus. The J-integral can be sufficiently evaluated using the BEM, since the required parameters at the internal points on the integration path are accurately determined. The calculation of internal points is obtained by employing boundary integral equations (see Sec. 4.1.6), which can be achieved without the need for discretising the domain. Moreover, the J-integral is evaluated by integrating the parameters of internal points (stress, strain and derivative of strain) along the integration path in a plane that is perpendicular to the crack plane. Consequently, the J-integral is able to yield highly accurate results without modifying the boundary mesh.

3.3 Conclusion

Over the past three decades, the methods described in this chapter have been used to solve many crack problems [33, 39, 47, 70, 83, 97, 104]. However, many of these methods are still under development, whereas some methods have already been confirmed to be more suitable for particular types of problems. Undeniably, the finite element method is the most popular. Nevertheless the limitations of the method have prompted researchers to explore alternative approaches. Several techniques have been introduced to modify the FEM, to obtain the singular behaviour around the crack tip, including the quarter-point element, the XFEM, phase field methods and the configurational forces method. Likewise, restrictions on mesh quality have encouraged the community to investigate meshfree methods. In contrast, the boundary element method has now become established as a robust numerical procedure for solving cracks in fracture mechanics problems. The reduction in the dimensionality and the yielding of accurate SIFs for two-dimensional and three-dimensional problems are the important advantages of the BEM over the FEM. The following chapters in this thesis will focus mainly on the boundary element method, including the formulation and numerical implementation for fracture mechanics.

Chapter 4

Boundary Element Method

4.1 Formulation of BEM

Key advancements in the historical development of the boundary element method were introduced in Section 3.1.6, and further details can be found in [130]. The BEM is now established as a numerical tool made available to engineers and scientists. The superiority of the method over other approaches can be demonstrated, if implemented to model appropriate applications. Currently, BEM is not as popular as FEM, for several reasons. Mainly, this is because of the difficulties associated with the mathematical formulation and treatment of singularity. In addition, FEM is very versatile since a weak form can be written for any PDE and a corresponding formulation can be developed, so that the FEM can be applied to a wide variety of problems found in science and engineering. By contrast, the BEM is limited to problems for which a Green's function is available. The FEM is also far more straightforward to apply for non-linear problems.

The BEM solution is calculated at the boundaries, and it is not required to evaluate the required function through the domain. The solution at internal points is given by direct evaluation in a postprocessing step, since the unknown boundary distribution is determined. Therefore, the solution space dimensions are reduced by one unit in comparison to the problem physical domain. Consequently, BEM has far fewer degrees of freedom and therefore a much smaller system matrix. Furthermore, BEM offers accurate results for crack problems; hence cracks lay on the boundaries.

This chapter presents the formulation of BEM, by constructing a system of equations, which can be implemented numerically. The formulation of the boundary element method can be obtained directly or indirectly, however both techniques yield similar results. The integral equation is formulated in the case of direct formulation, in terms of unknown boundary source functions. Moreover, the derivation of the direct integral equation starts by either applying the Betti-reciprocal theory or the weighted residual method. The following section demonstrates the use of the reciprocal theorem to derive the direct integral equation.

4.1.1 Betti-reciprocal theory

The development of the reciprocal theorem is attributed to Maxwell, Betti and Rayleigh [131]; it is a robust theory for analysing linear elastic problems. Here, the Boundary Integral Equation (BIE) is derived by utilising the reciprocal theorem under conditions of equilibrium. We start by considering two systems, (a) and (b) in which the stresses and strains corresponding to each system are $(\sigma_{ij}, \epsilon_{ij})$ and $(\sigma^*_{ij}, \epsilon^*_{ij})$, respectively. According to the reciprocal theorem the work done by the stresses of system (a) on the strains of system (b) is identical to the work done by the stresses of system (b) on the strains of system (a). This can be presented in the form of an integral relationship As shown by [131] and can be written as,

$$\int_V \sigma_{ij}\epsilon^*_{ij} dV = \int_V \sigma^*_{ij}\epsilon_{ij} dV \tag{4.1}$$

where V is an arbitrary volume domain. When using the strain-displacement relationship from Eqn. A.1.3, the strains in (4.1) can be expressed in terms of displacements as,

$$\int_V \frac{1}{2}\sigma_{ij}\left(u^*_{i,j} + u^*_{j,i}\right) dV = \int_V \frac{1}{2}\sigma^*_{ij}\left(u_{i,j} + u_{j,i}\right) dV \tag{4.2}$$

By utilising symmetrical terms σ_{ij} and σ^*_{ij}, Eqn. (4.2) can be simplified to,

$$\int_V \sigma_{ij} u^*_{i,j} dV = \int_V \sigma^*_{ij} u_{i,j} dV \tag{4.3}$$

where

$$\begin{aligned}\frac{1}{2}\sigma_{ij}\left(u^*_{i,j} + u^*_{j,i}\right) &= \frac{1}{2}\left(\sigma_{ij} u^*_{i,j} + \sigma_{ij} u^*_{j,i}\right) \\ &= \frac{1}{2}\left(\sigma_{ij} u^*_{i,j} + \sigma_{ji} u^*_{j,i}\right) \\ &= \sigma_{ij} u^*_{i,j} \qquad (4.4)\end{aligned}$$

The first term in the Eqn.(4.3) can be expressed as,

$$\int_V \sigma_{ij} u^*_{i,j} dV = \int_V \left[(\sigma_{ij} u^*_i)_{,j} - \sigma_{ij,j} u^*_i\right] dV \tag{4.5}$$

It is convenient to note that, Eqn.(4.5) was derived by considering the product rule of the first term on the right hand side. The term $\sigma_{ij,j}$ is associated with the body force term b_i by the equilibrium Equation (A.1.2), and can be substituted into (4.5) to give,

$$\int_V \sigma_{ij} u^*_{i,j} dV = \int_V (\sigma_{ij} u^*_i)_{,j} \, dV + \int_V b_i u^*_i dV \tag{4.6}$$

Now, we must consider transforming the domain integrals into boundary integrals. This can be achieved by employing the divergence theorem. Consider an arbitrary 3D domain V with a smooth surface S, and a function f which holds continuous derivatives with respect to the coordinates (x, y, z). Then the volume integral can be expressed on the surface as,

$$\int_V f_{i,i} dV = \int_S f_i n_i dS \tag{4.7}$$

where n_i is the unit outward normal (see Fig. 4.1). When applying the divergence theorem to the first term on the right hand side of Eqn.(4.6); this gives,

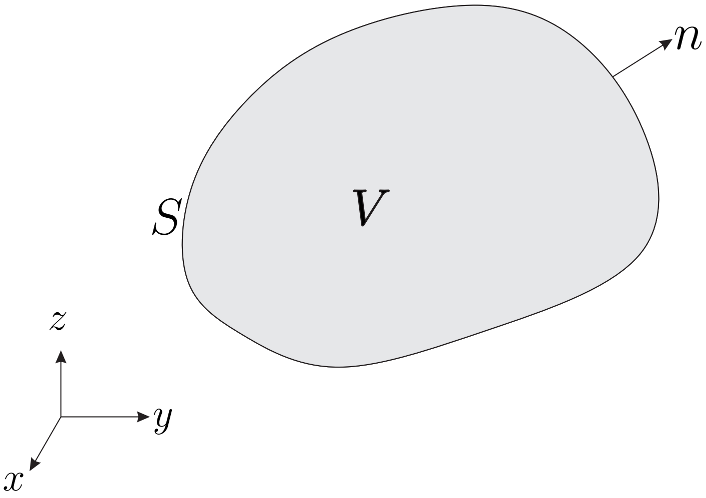

Figure 4.1: A 3D arbitrary domain V with boundary S

$$\int_V \sigma_{ij} u^*_{i,j} dV = \int_S \sigma_{ij} u^*_i n_j dS + \int_V b_i u^*_i dV \tag{4.8}$$

By utilising the traction-stress relationship, Equation (4.8) can be rewritten as,

$$\int_V \sigma_{ij} u^*_{i,j} dV = \int_S t_i u^*_i dS + \int_V b_i u^*_i dV \tag{4.9}$$

By returning to equation (4.3) and applying identical procedures to the right hand side, the final expression can be presented as,

$$\int_S t_i u^*_i dS + \int_V b_i u^*_i dV = \int_S t^*_i u_i dS + \int_V b^*_i u_i dV \tag{4.10}$$

Equation (4.10) is known as Betti's reciprocal work theorem. This is a system of linear equations with a unique solution that can be achieved by utilising Betti's theorem to obtain a boundary integral equation, which links two sets of tractions and displacements for systems (a) and (b), such that system (a) consists of unknown displacements and tractions and system (b) contains known displacements and tractions. Therefore, in the following sections, we derive the displacement boundary integral equation, before introducing the fundamental solution.

4.1.2 Somigliana's identity for displacement

Betti's Reciprocal work theorem, which has been demonstrated in the previous section, can be used to derive the boundary integral equation for elastostatic problems. Therefore, the body force b_i in Eqn. (4.10) can be assumed to correspond to a point force at a location X' in an infinite sheet. By using the Dirac delta function $\Delta(X - X')$, the body force b_i can be presented as,

$$b_i^* = \Delta(X - X')e_i \tag{4.11}$$

where e_i denotes a unit vector, representing a unit positive force in the i direction applied at X'. We can then introduce a useful Dirac delta function property, which can be written as,

$$\int_V f(X)\Delta(X - X')dV = f(X') \tag{4.12}$$

The substitution of Eqn. (4.11) into the last integral term in Eqn. (4.10) using the property in Eqn. (4.12), yields,

$$\int_V b_i^* u_i dV = \int_V \Delta(X - X')e_i u_i dV = u_i(X')e_i \tag{4.13}$$

The displacement fields corresponding to the point force solution can be expressed as,

$$u_i^* = U_{ij}(X', X)e_j \tag{4.14}$$

Likewise, the traction solution can be written as,

$$t_i^* = T_{ij}(X', X)e_j \tag{4.15}$$

The use of (4.14), (4.15) and (4.13) with some rearrangement and cancellation of the unit vector e_i, allows the Eqn. (4.10) to be written as,

$$u_i(X') = \int_S U_{ij}(X', x)t_j(x)dS - \int_S T_{ij}(X', x)u_j(x)dS + \int_V U_{ij}(X', X)b_j(X)dV \tag{4.16}$$

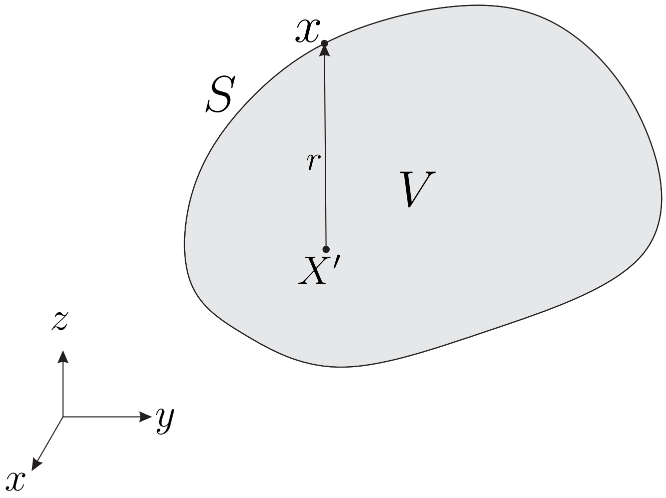

Figure 4.2: Point force applied at X' in domain V with surface S

where $x \in S$. Eqn. (4.16) is known as the Somigliana's identity for displacements [131], which relates the displacement value at any internal point X' within domain V to boundary S displacements and tractions (see Fig. 4.2). However, the solution for a point on the boundary S, can be obtained by considering the limit as $X' \to x'$ (where $x' \in S$). Since, the fundamental solutions show singular behaviour when $r \to 0$, we therefore must introduce them before proceeding with the derivation.

4.1.3 Fundamental solutions

The term *fundamental solution* is commonly used to describe the solution of governing equations due to a point force [132]. Moreover, a fundamental solution can simply be defined as a representation of the response of an infinite homogeneous domain to a point load. It is therefore essential to be able to obtain the individual fundamental solution for a particular differential equation in a 2D or 3D domain.

Generally, the derivation of fundamental solutions relies on the existence of the point force solution. Here, Navier's equation has been used to express the unit point force applied at point X'; which can be written as,

$$\mu u_{i,jj} + \frac{\mu}{1-2\nu} u^*_{j,jj} + \Delta(X - X')e_i = 0 \tag{4.17}$$

The use of the Galerkin vector is the most common technique for deriving a fundamental solution [131]. Therefore, through the utilisation of the Galerkin vector, displacement u_i^* can be expressed as,

$$u_i^* = G_{i,kk} - \frac{1}{1-2\nu} G_{k,ik} \tag{4.18}$$

The substitution of Eqn. (4.18) into Eqn. (4.17) yields,

$$\mu G_{i,kkjj} - \frac{\mu}{2(1-\nu)} G_{k,ikjj} + \frac{\mu}{1-\nu} \left[G_{j,kkij} - \frac{1}{2(1-\nu)} G_{k,jkij} \right] + \Delta(X - X')e_i = 0 \tag{4.19}$$

since $G_{k,ikjj} = G_{k,jjki} = G_{j,kkjj} = G_{k,jjki}$, then Eqn. (4.19) can be simplified to;

$$\mu G_{i,kkjj} + \Delta(X - X')e_i = 0 \tag{4.20}$$

and using the Laplace operator, the term $G_{i,kkjj}$ can be expressed by $\nabla^2(\nabla^2 G_i)$, and equation (4.20) can be written as,

$$\mu \nabla^2(\nabla^2 G_i) + \Delta(X - X')e_i = 0 \tag{4.21}$$

At this point, let $F_i = \nabla^2 G_i$, therefore Eqn. (4.21) can be expressed as,

$$\nabla^2 F_i + \frac{1}{\mu} \Delta(X - X')e_i = 0 \tag{4.22}$$

The solution for Eqn. (4.22) can be obtained from potential theory and is also known as Kelvin's point force solution [133]. The three-dimensional solution is written as,

$$F_i = \frac{1}{4\pi\mu r} e_i \tag{4.23}$$

and the Galerkin vector for three-dimensional problems is expressed as,

$$G_i = \frac{1}{8\pi\mu} r e_i \tag{4.24}$$

The substitution of the derivative of Eqn. (4.24) into Eqn. (4.18) yields,

$$u_i^* = \frac{1}{8\pi\mu}\left(r_{,kk}e_i - \frac{1}{2(1-\nu)}r_{,ik}e_k\right) \tag{4.25}$$

By noting that $r_{,kk} = 2/r$ and $r_{,ik} = (\delta_{ik} - r_{,i}r_{,k})/r$, Eqn. (4.25) therefore can be represented as,

$$u_i^* = \frac{1}{16\pi\mu(1-\nu)r}\left[(3-4\nu)\delta_{ij} + r_{,i}r_{,j}\right]e_j \tag{4.26}$$

The substitution of Eqn. (4.26) into (4.14) gives,

$$U_{ij}(x', x) = \frac{1}{16\pi\mu(1-\nu)r}\left[(3-4\nu)\delta_{ij} + r_{,i}r_{,j}\right] \tag{4.27}$$

where $U_{ij}(x', x)$ is the displacement fundamental solution for 3D elasticity problems, representing the displacement in the direction j at point x due to unit point load acting in the i direction at x'. The traction fundamental solution can be determined by utilising the relationship between displacement and strain, and then between strain and stress.Therefore, the traction can be written as,

$$t_i^* = \frac{-1}{8\pi(1-\nu)r^2}\left\{\frac{\partial r}{\partial n}\left[(1-2\nu)\delta_{ij} + 3r_{,i}r_{,j}\right] - (1-2\nu)(n_j r_{,i} - n_i r_{,j})\right\}e_j \tag{4.28}$$

where n_i is the outward normal acting at the field point. The substitution of Eqn. (4.28) into (4.15) gives,

$$T_{ij}(x', x) = \frac{-1}{8\pi(1-\nu)r^2}\left\{\frac{\partial r}{\partial n}\left[(1-2\nu)\delta_{ij} + 3r_{,i}r_{,j}\right] - (1-2\nu)(n_j r_{,i} - n_i r_{,j})\right\} \tag{4.29}$$

where $T_{ij}(x', x)$ is the traction fundamental solution for elasticity problems, which represents traction in the direction j at point x due to unit point load acting in the i direction at x'. Differentiation of (4.27) with respect to x' in the k direction yields,

$$U_{ij,k}(x', x) = \frac{1}{16\pi\mu(1-\nu)r^2}\left[(3-4\nu)\delta_{ij}r_{,k} + 3r_{,i}r_{,j}r_{,k} - r_{,i}\delta_{jk} - r_{,j}\delta_{ki}\right] \tag{4.30}$$

Similarly, the differentiation of Eqn. (4.29) with respect to x' in the k direction yields,

$$\begin{aligned} T_{ij,k}(x',x) =& \frac{1}{16\pi(1-\nu)r^3}\left\{3\frac{\partial r}{\partial n}\left[(1-2\nu)\delta_{ij}r_{,k} + \nu(\delta_{ik}r_{,j} + \delta_{jk}r_{,i}) - 5r_{,i}\, r_{,j}\, r_{,k}\right]\right. \\ & + 3\nu(n_i r_{,j}\, r_{,k} + n_j r_{,i}\, r_{,k}) + (1-2\nu)(3n_k r_{,i}\, r_{,j} + n_j\delta_{ik} + n_i\delta_{jk}) \\ & \left. - (1-4\nu)n_k\delta_{ij}\right\} \end{aligned} \tag{4.31}$$

By utilising the relationship between stress and strain, Eqn. (4.30) can be written as,

$$D_{kij} = \frac{1}{8\pi(1-\nu)r^2}\left[(1-2\nu)(r_{,j}\delta_{ki} + r_{,i}\delta_{jk} - \delta_{ij}r_{,k}) + 3r_{,i}r_{,j}r_{,k}\right] \tag{4.32}$$

and likewise equation (4.31) can be expressed as,

$$\begin{aligned} S_{kij} =& \frac{\mu}{4\pi(1-\nu)r^3}\left\{3\frac{\partial r}{\partial n}\left[(1-2\nu)\delta_{ij}r_{,k} + \nu(\delta_{ik}r_{,j} + \delta_{jk}r_{,i}) - 5r_{,i}\, r_{,j}\, r_{,k}\right]\right. \\ & + 3\nu(n_i r_{,j}\, r_{,k} + n_j r_{,i}\, r_{,k}) + (1-2\nu)(3n_k r_{,i}\, r_{,j} + n_j\delta_{ik} + n_i\delta_{jk}) \\ & \left. - (1-4\nu)n_k\delta_{ij}\right\} \end{aligned} \tag{4.33}$$

Similar procedures can be used to obtain the fundamental solution for two-dimensional problems. Therefore, the solution for Eqn. (4.22) for two-dimensional problems can be written as,

$$F_i = -\frac{1}{2\pi\mu}\ln(r)e_i \tag{4.34}$$

and the Galerkin vector for two-dimensional problems is given by,

$$G_i = -\frac{1}{8\pi\mu}r^2\ln(r)e_i \tag{4.35}$$

By following the same steps as required for three-dimensions, the two-dimensional fundamental solution for displacement is expressed as,

$$U_{ij}(x',x) = \frac{1}{8\pi\mu(1-\nu)}\left[(3-4\nu)\ln\left(\frac{1}{r}\right)\delta_{ij} + r_{,i}r_{,j}\right] \tag{4.36}$$

and the two-dimensional fundamental solution for traction is given by,

$$T_{ij}(x',x) = \frac{-1}{4\pi(1-\nu)r}\left\{\frac{\partial r}{\partial n}\left[(1-2\nu)\delta_{ij} + 2r_{,i}r_{,j}\right] - (1-2\nu)(n_j r_{,i} - n_i r_{,j})\right\} \tag{4.37}$$

Differentiation of Eqn. (4.36) with respect to x' in the k direction gives the the fundamental solution for the strain integral equation, which can be written as,

$$U_{ij,k}(x',x) = \frac{1}{4\pi\mu(1-\nu)r}\left[(3-4\nu)\delta_{ij}r_{,k} + 2r_{,i}r_{,j}r_{,k} - r_{,i}\delta_{jk} - r_{,j}\delta_{ki}\right] \tag{4.38}$$

Likewise, differentiation of Eqn. (4.37) with respect to x' in the k direction yields,

$$\begin{aligned} T_{ij,k}(x',x) =& \frac{\mu}{4\pi(1-\nu)r^3}\left\{3\frac{\partial r}{\partial n}\left[(1-2\nu)\delta_{ij}r_{,k} + \nu(\delta_{ik}r_{,j} + \delta_{jk}r_{,i}) - 5r_{,i}r_{,j}r_{,k}\right]\right. \\ & + 3\nu(n_i r_{,j}r_{,k} + n_j r_{,i}r_{,k}) + (1-2\nu)(3n_k r_{,i}r_{,j} + n_j\delta_{ik} + n_i\delta_{jk}) \\ & \left. - (1-4\nu)n_k\delta_{ij}\right\} \end{aligned} \tag{4.39}$$

By addressing the relationship between stress and strain, Eqn. (4.38) can be written as,

$$D_{kij} = \frac{1}{4\pi(1-\nu)r}\left[(1-2\nu)(r_{,j}\delta_{ki} + r_{,i}\delta_{jk} - \delta_{ij}r_{,k}) + 2r_{,i}r_{,j}r_{,k}\right] \tag{4.40}$$

and similarly Eqn. (4.39) can be expressed as,

$$\begin{aligned} S_{kij} =& \frac{\mu}{4\pi(1-\nu)r^2}\left\{2\frac{\partial r}{\partial n}\left[(1-2\nu)\delta_{ij}r_{,k} + \nu(\delta_{ik}r_{,j} + \delta_{jk}r_{,i}) - 4r_{,i}r_{,j}r_{,k}\right]\right. \\ & + 2\nu(n_i r_{,j}r_{,k} + n_j r_{,i}r_{,k}) + (1-2\nu)(2n_k r_{,i}r_{,j} + n_j\delta_{ik} + n_i\delta_{jk}) \\ & \left. - (1-4\nu)n_k\delta_{ij}\right\} \end{aligned} \tag{4.41}$$

The fundamental solutions presented above are suitable for plane strain implementation. However for plane stress problems, fundamental solutions can be obtained by using the modified Young's modulus and Poisson's ratio as defined in Eqns. (A.1.12) and (A.1.13). Since the fundamental solutions have been now established, we can proceed

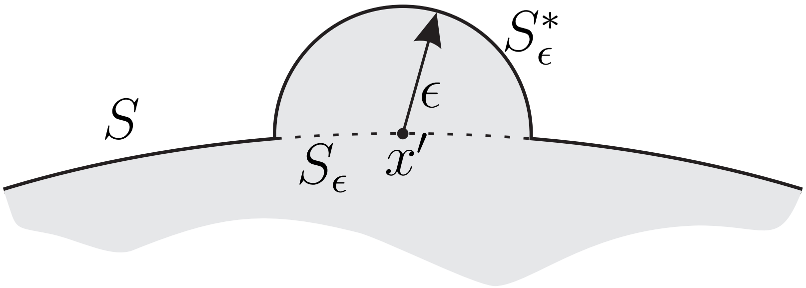

Figure 4.3: Semi-circular added domain on the boundary

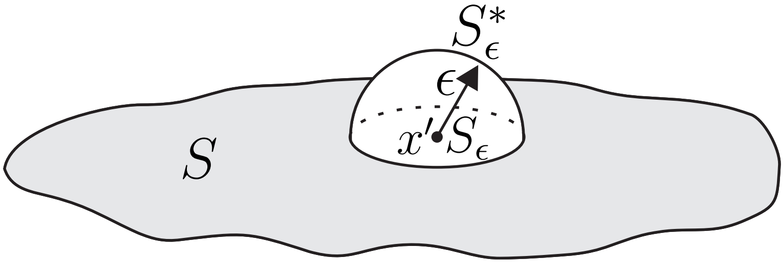

Figure 4.4: Hemispherical added domain on the boundary

with the formulation to move the source point X' to the boundary.

4.1.4 Displacement BIE

The Displacement Boundary Integral Equation (DBIE) is the final step in the derivation of the boundary integral equation. Next, we recall Eqn. (4.16), which can be used to evaluate any source points inside domain V. Since, the fundamental solutions $U_{ij}(x, x)$ and $T_{ij}(x, x)$ are a function of r, they become singular as $r \to 0$. Therefore, considering the limit as $X' \to x'$ is essential to obtain a solution for the points on the boundary. Moreover, to avoid the singular behaviour, the integration domain can be split into a singular and regular integral [131]. This can be achieved by considering a vanishing domain around the singular point x'. In the case of two-dimensional problems the vanishing domain can be defined as a semi-circular region with a radius ϵ and centred at point x' as illustrated in Fig 4.3. Whereas, with three-dimensional problems, the vanishing domain is defined as a hemispherical region with radius ϵ and centred at point x', as presented in Fig. 4.4. Now, the problem boundary S^* can be defined as,

$$S^* = (S - S_\epsilon) + S_\epsilon^* \tag{4.42}$$

where S_ϵ is the segment which has been removed from the boundary S. Next, we apply the limit to the first term on the right hand side of Eqn. (4.16), which can be written as,

$$\int_S U_{ij}(X',x)t_j(x)dS = \lim_{\epsilon\to 0}\int_{(S-S_\epsilon)} U_{ij}(x',x)t_j(x)dS + \lim_{\epsilon\to 0}\int_{S_\epsilon^*} U_{ij}(x',x)t_j(x)dS \quad (4.43)$$

It is important to observe that, the first term on the right hand side of (4.43) is integrable and can be evaluated numerically using an appropriate scheme. Whereas, the second term on the right hand side of (4.43) contains a singularity of the order $O(\ln(1/r))$ in two-dimensions and $O(r^{-1})$ in three-dimensions. However, the value of the integral is bounded; in fact, it tends to zero when $\epsilon \to 0$, further details can be found in [134].

Now, consider the second term on the right hand side of Eqn. (4.16). When applying the limit it can be written as,

$$\int_S T_{ij}(X',x)u_j(x)dS = \lim_{\epsilon\to 0}\int_{(S-S_\epsilon)} T_{ij}(x',x)u_j(x)dS + \lim_{\epsilon\to 0}\int_{S_\epsilon^*} T_{ij}(x',x)u_j(x)dS \quad (4.44)$$

where both terms on the right hand side of Eqn. (4.44) contain singularity of the order $O(r^{-1})$ in two-dimensions and $O(r^{-2})$ in three-dimensions. In this case, the Cauchy Principal Value (CPV) is used to evaluate the first term on the right hand side of Eqn. (4.44). Whereas, the second term on the right hand side can be regularised by expanding the displacement (i.e. the displacement $u_j(x)$ is differentiable) about the source point, using the first term in the Taylor series expansion; which can be written as,

$$\begin{aligned}\lim_{\epsilon\to 0}\int_{S_\epsilon^*} & T_{ij}(x',x)u_j(x)dS \\ &= \lim_{\epsilon\to 0}\left[\int_{S_\epsilon^*} T_{ij}(x',x)[u_j(x)-u_j(x')]dS\right] + u_j(x')\lim_{\epsilon\to 0}\left[\int_{S_\epsilon^*} T_{ij}(x',x)dS\right] \quad (4.45)\end{aligned}$$

The first term on the right hand side of Eqn. (4.45) is equal to zero, since the displacements must be continuous. Whereas, the second term can be expressed as,

$$u_j(x')\lim_{\epsilon\to 0}\left[\int_{S_\epsilon^*} T_{ij}(x',x)dS\right] = \alpha_{ij}(x')u_j(x') \quad (4.46)$$

where α_{ij} represents a jump term. By substituting the outcome of the limiting processes into Eqn. (4.16), then the displacement boundary integral can be written as,

$$C_{ij}u_j(x') + \fint_S T_{ij}(x', x)u_j(x)dS = \int_S U_{ij}(x', x)t_j(x)dS + \int_V U_{ij}(x', X)b_j(X)dV \quad (4.47)$$

where $\fint$ denotes the CPV integral, and the free term is defined as $C_{ij}(x') = \delta_{ij}(x') + \alpha_{ij}(x')$. Commonly, the free term C_{ij} is evaluated using rigid body motion, however the derivation of the jump term α_{ij} can be found in Appendix B.1. It is important to note that, the last term in Eqn.(4.47) still needs to be integrated over domain V. However, in many cases (i.e. thermoelastic, centrifugal loading) these can be transformed into boundary integrals, or alternatively, can be neglected in the case of zero body forces.

4.1.5 Numerical implementation of BIE

The analytical integration of Eqn. (4.47) in the present form is difficult, unless the boundary of a domain can be expressed using a simple equation such as a circular curve. In order to implement the boundary integral equation for any geometry, it is essential to consider numerical integration. The numerical edition of the boundary integral equation is referred to as the boundary element method. The numerical integration procedure involves dividing the integral boundary S into small segments $\bar{n}$, also known as elements, as illustrated in Fig 4.5. Furthermore, the geometry x_j, displacement u_j and traction t_j parameters can be described over individual elements by utilising arbitrary functions, which can be expressed mathematically for 2D (illustrated in [131]) as,

$$\begin{aligned} x_j &= \sum_{\bar{a}=1}^{m} N^{\bar{a}}(\xi)x_j^{\bar{a}} \\ u_j &= \sum_{\bar{a}=1}^{m} N^{\bar{a}}(\xi)u_j^{\bar{a}} \\ t_j &= \sum_{\bar{a}=1}^{m} N^{\bar{a}}(\xi)t_j^{\bar{a}} \end{aligned} \quad (4.48)$$

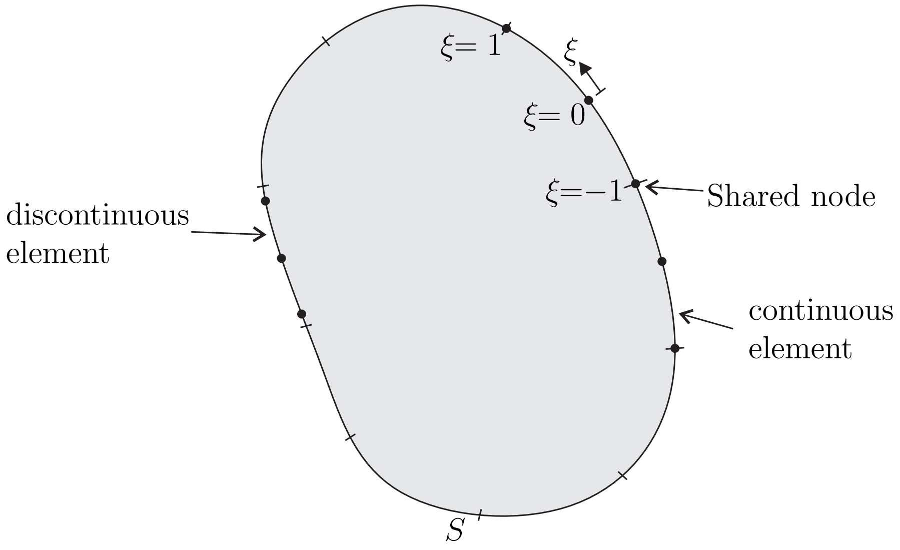

Figure 4.5: Discretisation of 2D boundary into elements

where m is the total number of nodes on the element and $\bar{a}$ is the node number. Shape functions N are polynomials of degree $m-1$, and each shape function is equal to 1 at the associated node $\bar{a}$, and zero at all other nodes. Here, ξ is a non-dimensional coordinate and is defined over the element as $-1 \leq \xi \leq 1$ as shown in Fig 4.5. A discretised boundary element can be achieved by substituting Eqns. (4.48) into Eqn. (4.47), which can be written in the absence of body forces as,

$$C_{ij}(x')u_j(x') + \sum_{\bar{n}=1}^{N_e}\sum_{\bar{a}=1}^{m} P_{ij}^{\bar{n}\bar{a}} u_j^{\bar{n}\bar{a}} = \sum_{\bar{n}=1}^{N_e}\sum_{\bar{a}=1}^{m} Q_{ij}^{\bar{n}\bar{a}} t_j^{\bar{n}\bar{a}} \tag{4.49}$$

where N_e is the total number of elements, and $P_{ij}^{\bar{n}\bar{a}}$ and $Q_{ij}^{\bar{n}\bar{a}}$ can be expressed as,

$$P_{ij}^{\bar{n}\bar{a}} = \int_{-1}^{1} N^{\bar{a}}(\xi) T_{ij}\left[x', x(\xi)\right] J^{\bar{n}}(\xi) d\xi \tag{4.50a}$$

$$Q_{ij}^{\bar{n}\bar{a}} = \int_{-1}^{1} N^{\bar{a}}(\xi) U_{ij}\left[x', x(\xi)\right] J^{\bar{n}}(\xi) d\xi \tag{4.50b}$$

where $J^{\bar{n}}(\xi)$ denotes the Jacobian of transformation, which relates the global Cartesian coordinates to the local coordinate ξ, and is given by:

$$J^{\bar{n}}(\xi) = \sqrt{\left(\frac{dx}{d\xi}\right)^2 + \left(\frac{dx}{d\xi}\right)^2} \tag{4.51}$$

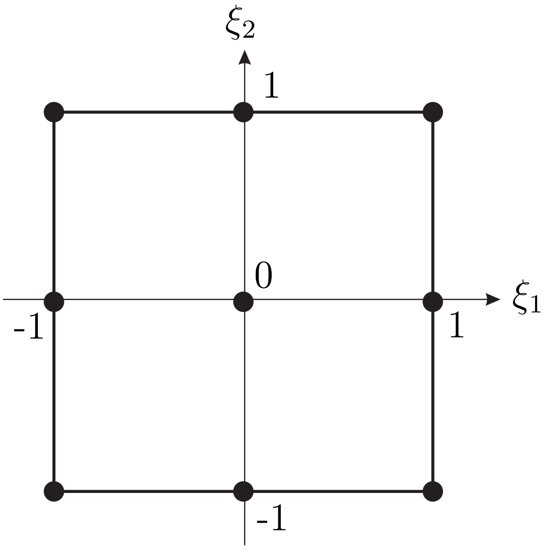

Figure 4.6: Nine node continuous element

Similarly, the three-dimensional geometry x_j, displacement u_j and traction t_j parameters can be approximated over each element using shape functions, and can be written as,

$$
\begin{aligned}
x_j &= \sum_{\bar{a}=1}^{m} N^{\bar{a}}(\xi_1,\xi_2)x_j^{\bar{a}} \\
u_j &= \sum_{\bar{a}=1}^{m} N^{\bar{a}}(\xi_1,\xi_2)u_j^{\bar{a}} \\
t_j &= \sum_{\bar{a}=1}^{m} N^{\bar{a}}(\xi_1,\xi_2)t_j^{\bar{a}}
\end{aligned}
\tag{4.52}
$$

where ξ_1 and ξ_2 local variables are defined as $-1 \leq \xi_1, \xi_2 \leq 1$, as illustrated in Fig. 4.6. The three-dimensional discretised boundary element can be obtained by substituting Eqns. (4.52) into Eqn. (4.47), which can be written in the case of zero body forces as,

$$
C_{ij}(x')u_j(x') + \sum_{\bar{n}=1}^{N_e}\sum_{\bar{a}=1}^{m} P_{ij}^{\bar{n}\bar{a}}u_j^{\bar{n}\bar{a}} = \sum_{\bar{n}=1}^{N_e}\sum_{\bar{a}=1}^{m} Q_{ij}^{\bar{n}\bar{a}}t_j^{\bar{n}\bar{a}} \tag{4.53}
$$

where $P_{ij}^{\bar{n}\bar{a}}$ and $Q_{ij}^{\bar{n}\bar{a}}$ are defined for 3D problems as,

$$P_{ij}^{\bar{n}\bar{a}} = \int_{-1}^{1}\int_{-1}^{1} N^{\bar{a}}(\xi_1,\xi_2)T_{ij}\left[x', x(\xi_1,\xi_2)\right] J^{\bar{n}}(\xi_1,\xi_2)d\xi_1 d\xi_2 \tag{4.54a}$$

$$Q_{ij}^{\bar{n}\bar{a}} = \int_{-1}^{1}\int_{-1}^{1} N^{\bar{a}}(\xi_1,\xi_2)U_{ij}\left[x', x(\xi_1,\xi_2)\right] J^{\bar{n}}(\xi_1,\xi_2)d\xi_1 d\xi_2 \tag{4.54b}$$

where $J^{\bar{n}}(\xi_1,\xi_2)$ is the Jacobian of transformation, which describes the relationship between the global Cartesian coordinates and the local coordinates ξ_1 and ξ_2, and is defined as,

$$J^{\bar{n}}(\xi_1,\xi_2) = \sqrt{J_1^2 + J_2^2 + J_3^2} \tag{4.55}$$

where

$$J_1 = \frac{\partial x_y}{\partial \xi_1}\frac{\partial x_z}{\partial \xi_2} - \frac{\partial x_z}{\partial \xi_1}\frac{\partial x_y}{\partial \xi_2} \tag{4.56}$$

$$J_2 = \frac{\partial x_z}{\partial \xi_1}\frac{\partial x_x}{\partial \xi_2} - \frac{\partial x_x}{\partial \xi_1}\frac{\partial x_z}{\partial \xi_2} \tag{4.57}$$

$$J_3 = \frac{\partial x_x}{\partial \xi_1}\frac{\partial x_y}{\partial \xi_2} - \frac{\partial x_y}{\partial \xi_1}\frac{\partial x_x}{\partial \xi_2} \tag{4.58}$$

It is important to note that, the shape functions change for the same type of element if the nodes layout on the element is changed. In terms of elements, these can be selected from various types of elements including straight lines, quadratic curves or cubic splines. In fact crucially, the accuracy of any boundary element method programme depends on the type and the size of selected elements.

At this point, the system of generated equations must be assembled into a system of matrices in order to use a numerical solver. This can be achieved by using nodal collocation which is the most commonly used method in the implementation of BEM. In this process, the discretised integral Eqns. (4.49) and (4.53) are evaluated by placing the source point x' at each nodal point. Here, the location of the collocation point is considered to be x^c, thus the discretised integral equations can be written as,

$$C_{ij}(x^c)u_j(x^c) + \sum_{\bar{n}=1}^{N_e}\sum_{\bar{a}=1}^{m} P_{ij}^{\bar{n}\bar{a}}(x^c)u_j^{\bar{n}\bar{a}} = \sum_{\bar{n}=1}^{N_e}\sum_{\bar{a}=1}^{m} Q_{ij}^{\bar{n}\bar{a}}(x^c)t_j^{\bar{n}\bar{a}} \qquad c = 1, M \tag{4.59}$$

where M represents the total number of collocation nodes. However, before evaluating the double summation in Eqn. (4.59), it is necessary to consider the displacement continuity requirement over the boundary. Therefore, the displacement of shared nodes in the case of a continuous element must be combined, which allows the second term in Eqn. (4.59) to be expressed as,

$$\sum_{\bar{n}=1}^{N_e}\sum_{\bar{a}=1}^{m} P_{ij}^{\bar{n}\bar{a}}(x^c)u_j^{\bar{n}\bar{a}} = \sum_{\bar{\gamma}=1}^{M} \bar{H}_{ij}^{c\bar{\gamma}}u_j^{\bar{\gamma}} \tag{4.60}$$

where $\bar{\gamma}$ is the global node number. In Eqn. (4.60), shared nodes are combined and the summation can now be computed over nodes denoted by $\bar{\gamma}$. As tractions on shared nodes can differ, the summation term on the right hand side can be computed without combining, to give,

$$\sum_{\bar{n}=1}^{N_e}\sum_{\bar{a}=1}^{m} Q_{ij}^{\bar{n}\bar{a}}(x^c)t_j^{\bar{n}\bar{a}} = \sum_{\bar{n}=1}^{N_e}\sum_{\bar{a}=1}^{m} G_{ij}^{c\bar{n}\bar{a}}(x^c)t_j^{\bar{n}\bar{a}} \tag{4.61}$$

The substitution of Eqns. (4.60) and (4.61) into Eqn. (4.59) yields,

$$C_{ij}(x^c)u_j(x^c) + \sum_{\bar{\gamma}=1}^{M} \bar{H}_{ij}^{c\bar{\gamma}}u_j^{\bar{\gamma}} = \sum_{\bar{n}=1}^{N_e}\sum_{\bar{a}=1}^{m} G_{ij}^{c\bar{n}\bar{a}}(x^c)t_j^{\bar{n}\bar{a}} \tag{4.62}$$

Since free term C_{ij} arises when $x' = x$, it is possible to express the free term using Kronecker delta as,

$$C_{ij}(x^c)u_j(x^c) + \sum_{\bar{\gamma}=1}^{M} \bar{H}_{ij}^{c\bar{\gamma}}u_j^{\bar{\gamma}} = C_{ij}(x^c)\delta_{c\bar{\gamma}} + \sum_{\bar{\gamma}=1}^{M} \bar{H}_{ij}^{c\bar{\gamma}}u_j^{\bar{\gamma}} = \sum_{\bar{\gamma}=1}^{M} H_{ij}^{c\bar{\gamma}}u_j^{\bar{\gamma}} \tag{4.63}$$

This allows Eqn. (4.62) to be rewritten as,

$$\sum_{\bar{\gamma}=1}^{M} H_{ij}^{c\bar{\gamma}}u_j^{\bar{\gamma}} = \sum_{\bar{n}=1}^{N_e}\sum_{\bar{a}=1}^{m} G_{ij}^{c\bar{n}\bar{a}}(x^c)t_j^{\bar{n}\bar{a}} \tag{4.64}$$

Eqn. (4.64) can now be expressed in matrix notation as,

$$[\boldsymbol{H}]\{\boldsymbol{u}\} = [\boldsymbol{G}]\{\boldsymbol{t}\} \tag{4.65}$$

where $\boldsymbol{H}$ is a square matrix of the size $2M \times 2M$ containing the integration values of $P_{ij}^{\bar{n}\bar{a}}$ and the jump term (see Appendix B.1), and $\boldsymbol{G}$ is a $2M \times 2N_e m$ matrix containing the integration values of $Q_{ij}^{\bar{n}\bar{a}}$. The vector $\boldsymbol{u}$ has $2M$ components and $\mathbf{t}$ has $2N_e m$ components, holding unknown and prescribed conditions for displacement and traction, respectively. However, swapping the columns of both the $\boldsymbol{H}$ and $\boldsymbol{G}$ matrices to transfer unknowns to the left hand side and prescribed conditions to the right hand side allows the system of Eqn. (4.65) to be written as,

$$[\boldsymbol{A}]\{\boldsymbol{x}\} = \{\boldsymbol{y}\} \tag{4.66}$$

where $\boldsymbol{x}$ is a vector holding all unknown boundary conditions, $\boldsymbol{y}$ is a vector containing the multiplication results of prescribed boundary conditions and associated coefficient and the coefficients matrix $\boldsymbol{A}$ contains the unknown related coefficients.

4.1.6 Internal points

The system of linear equations has now been solved, and the values of displacements and tractions determined for all nodes on the boundary. Therefore, it is a straightforward matter to compute displacement at any internal point by utilising the displacement boundary integral equation [135]. Moreover, the displacement at the internal point can be obtained by considering the interior point to be x' and substituting all the boundary displacements and tractions into (4.47), where the fundamental solutions U_{ij} and T_{ij} can be obtained from (4.36) and (4.37) for two-dimensional and (4.27) and (4.29) for three-dimensional problems.

The strain at an interior point can be evaluated by taking the derivative of the displacement boundary integral equation. Here, zero body forces are considered, thus the derivation of (4.47) with respect to x' can be written as,

$$u_{j,k}(x') + \int_S T_{ij,k}(x', x) u_j(x) dS = \int_S U_{ij,k}(x', x) t_j(x) dS \tag{4.67}$$

where the derivative of the fundamental solutions $U_{ij,k}$ and $U_{ij,k}$ can be determined from (4.38) and (4.39) for two-dimensional, and (4.30) and (4.31) for three-dimensional problems. Moreover, due to the differentiation, the order of the singularity in equation (4.67) increased to a hypersingularity. However, the singularity does not appear, since the interior point never lies on the boundary. Therefore, the free term C_{ij} has also been dropped in the derivation processes.

The stress for internal points can be obtained by applying Hooke's law to equation (4.67) to give,

$$\sigma_{j,k}(x') + \int_S S_{kij}(x', x) u_j(x) dS = \int_S D_{kij}(x', x) t_j(x) dS \tag{4.68}$$

where D_{kij} and S_{kij} can be evaluated using (4.40) and (4.41) for two-dimensional, and (4.32) and (4.33) for three-dimensional problems.

As there is no singularity behaviour observed in the evaluation of internal points, all integrations can be evaluated using the standard Gaussian-Legendre (GL) quadrature method. However, should the interior point lies very close to the boundary, it would be important to consider using near singular integral schemes.

4.2 Modelling of crack coplanar surfaces

In the context of linear elastic fracture analysis, BEM has established itself as one of the most accurate numerical methods [131]. However, direct implementation of the BEM to crack problems gives rise to mathematical degeneration. Earlier, Cruse [92] reported the mathematical difficulty that emerges when using the displacement boundary integral equation to model crack problems. Rows associated with crack surface nodes in matrices $\boldsymbol{H}$ and $\boldsymbol{G}$ become identical leading to a singular system; therefore no reasonable solution

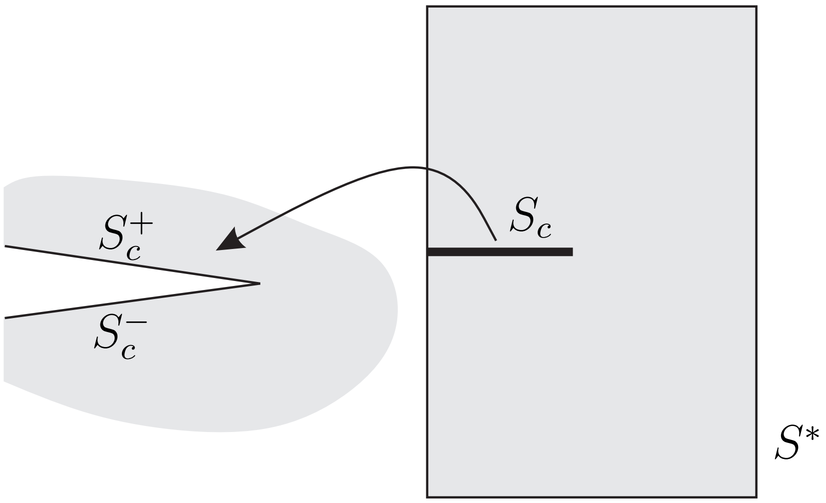

Figure 4.7: Coplanar surfaces for edge crack

can be obtained.

Several methods have been proposed to overcome the indeterminate system of equations including symmetrical simplification, multi-domain and the DBEM approach. Furthermore, the reader can find advantages and limitations associated with each method in Sec. 3.1.6. However, this section aims to introduce the approach used to model the crack surfaces in this thesis. Therefore, the derivation of the dual boundary element method for the coplanar crack is presented next.

4.2.1 Displacement integral equation

The formulation of the displacement boundary integral equation for the coplanar crack surfaces begins by recalling Eqn. (4.16), which can be written for internal points X' as presented by [94], and in the absence of body forces as,

$$u_i(X') = \int_{S^*+S_c^++S_C^-} U_{ij}(X',x)t_j(x)dS - \int_{S^*+S_c^++S_C^-} T_{ij}(X',x)u_j(x)dS \tag{4.69}$$

where S_c^- and S_c^+ denote the lower and upper crack surfaces, respectively. The remaining boundary is denoted by S^*, as shown in Fig. 4.7. It can be seen, from the outward normal relationship that $n_i(x^-) = -n_i(x^+)$ the fundamental solutions (see Sec. 4.1.3) on the lower crack surface relate to those on the upper crack surface by,

$$\begin{aligned} U_{ij}(X', x^+) &= U_{ij}(X', x^-) \\ T_{ij}(X', x^+) &= -T_{ij}(X', x^-) \end{aligned} \tag{4.70}$$

where x^+ and x^- are the field points associated with the upper and lower crack surfaces, respectively. Combining the two crack surfaces, such that $S_c = S_c^- = S_c^+$ allows Eqn. (4.69) to be written as,

$$\begin{aligned} u_i(X') = \int_{S^*} U_{ij}(X', x)t_j(x)dS - \int_{S^*} T_{ij}(X', x)u_j(x)dS \\ + \int_{S_c} U_{ij}(X', x)\Sigma t_j(x)dS - \int_{S_C} T_{ij}(X', x)\Delta u_j(x)dS \end{aligned} \tag{4.71}$$

where Δu_j and Σt_j are given by

$$\begin{aligned} \Delta u_j &= u_j(x^+) - u_j(x^-) \\ \Sigma t_j &= t_j(x^+) + t_j(x^-) \end{aligned} \tag{4.72}$$

From the traction relationship in Eqn. (4.70), we can see $\Sigma t_j = 0$, when applying equal and opposite tractions to the crack surfaces. Additionally, $\Sigma t_j = 0$ when a traction-free crack is considered. Now, the domain source point X' can be placed on the upper crack surface S_c^+ as x^+, by following the BIE derivation illustrated in Sec. 4.1.4, and Eqn. (4.71) can be written for traction-free cracks as,

$$\begin{aligned} C_{ij}(x^+)u_j(x^+) + C_{ij}(x^-)u_j(x^-) = \int_{S^*} U_{ij}(x', x)t_j(x)dS \\ - \int_{S^*} T_{ij}(x', x)u_j(x)dS + \fint_{S_C} T_{ij}(x', x)\Delta u_j(x)dS \end{aligned} \tag{4.73}$$

The coincidence of the source point x^+ with x^- on the opposite crack surface S_c^- gives rise to the extra free term $C_{ij}(x^-)u_j(x^-)$. Moreover, the use of Eqn. (4.73) to collocate on x^- will yield a set of identical rows to those generated by collocating on x^+. Therefore, Eqn. (4.73) will be used for collocation on one of the crack surfaces, and an additional integral equation will be introduced now for collocating on the other crack surface.

4.2.2 Traction integral equation

The formulation of the stress integral equation can be achieved in a similar manner to the displacement integral equation as seen in [94]. Therefore, the stress integral equation for collocation points x^- on the lower crack surface S_c^- can be written as,

$$\begin{aligned}\frac{1}{2}\sigma_{ij}(x^-) - \frac{1}{2}\sigma_{ij}(x^+) = & -\!\!\!\!\!\!\int_S D_{kij}(x^-, x)t_k(x)dS \\ & - = \!\!\!\!\!\!\!\!\int_S S_{kij}(x^-, x)u_k(x)dS \end{aligned} \tag{4.74}$$

where $=\!\!\!\!\!\!\int$ denotes the Hadamard finite part integral. Multiplying Eqn. (4.74) by the outward unit normal $n_i(x)$ at the source point x^-, allows the traction boundary equation to be written as,

$$\begin{aligned}\frac{1}{2}t_j(x^-) - \frac{1}{2}t_j(x^+) = & \; n_i(x^-) -\!\!\!\!\!\!\int_S D_{kij}(x^-, x)t_k(x)dS \\ & - n_i(x^-) =\!\!\!\!\!\!\!\!\int_S S_{kij}(x^-, x)u_k(x)dS \end{aligned} \tag{4.75}$$

The fundamental solutions D_{kij} and S_{kij} hold the following relationship:

$$\begin{aligned} D_{kij}(x', x^+) &= D_{kij}(x', x^-) \\ S_{kij}(x', x^+) &= -S_{kij}(x', x^-) \end{aligned} \tag{4.76}$$

Using the relationships (4.76), the first term on the right hand side of Eqn. (4.75) can be expressed as,

$$\begin{aligned} & -\!\!\!\!\!\!\int_S D_{kij}(x^-, x)t_k(x)dS \\ = & -\!\!\!\!\!\!\int_{S_c^-} D_{kij}(x^-, x)t_k^-(x)dS + -\!\!\!\!\!\!\int_{S_c^+} D_{kij}(x^-, x)t_k^+(x)dS + -\!\!\!\!\!\!\int_{S^*} D_{kij}(x^-, x)t_k(x)dS \\ = & -\!\!\!\!\!\!\int_{S_c^-} D_{kij}(x^-, x)\left[t_k^-(x) + t_k^+(x)\right] dS + -\!\!\!\!\!\!\int_{S^*} D_{kij}(x^-, x)t_k(x)dS \end{aligned} \tag{4.77}$$

Similarly, the second term on the right hand side of Eqn. (4.75) can be expressed as,

$$
\begin{aligned}
&\int\!\!\!\!\!=_{S} S_{kij}(x^-,x)u_k(x)dS \\
&= \int\!\!\!\!\!=_{S_c^-} S_{kij}(x^-,x)u_k^-(x)dS + \int\!\!\!\!\!=_{S_c^+} S_{kij}(x^-,x)u_k^+(x)dS + \int\!\!\!\!\!=_{S^*} S_{kij}(x^-,x)u_k(x)dS \\
&= \int\!\!\!\!\!=_{S_c^+} S_{kij}(x^-,x)\Delta u_k(x)dS + \int\!\!\!\!\!=_{S^*} S_{kij}(x^-,x)u_k(x)dS
\end{aligned}
\tag{4.78}
$$

The substitution of Eqns. (4.77) and (4.78) into Eqn. (4.75) yields,

$$
\begin{aligned}
&\frac{1}{2}t_j(x^-) - \frac{1}{2}t_j(x^+) = -n_i(x^-)\int\!\!\!\!\!=_{S_c^+} S_{kij}(x^-,x)\Delta u_k(x)dS - n_i(x^-)\int\!\!\!\!\!=_{S^*} S_{kij}(x^-,x)u_k(x)dS \\
&+n_i^-(x)n_i(x^-)\int\!\!\!\!\!-_{S_c^-} D_{kij}(x^-,x)\left[t_k^-(x) + t_k^+(x)\right]dS + n_i(x^-)\int\!\!\!\!\!-_{S^*} D_{kij}(x^-,x)t_k(x)dS
\end{aligned}
\tag{4.79}
$$

In the case when equilibrium traction $t_j(x^-) = -t_j(x^-)$ is assumed, Eqn. (4.79) can be rewritten as,

$$
\begin{aligned}
&t_j(x^-) + n_i(x^-)\int\!\!\!\!\!=_{S_c^+} S_{kij}(x^-,x)\Delta u_k(x)dS \\
&+n_i(x^-)\int\!\!\!\!\!=_{S^*} S_{kij}(x^-,x)u_k(x)dS = n_i(x^-)\int\!\!\!\!\!-_{S^*} D_{kij}(x^-,x)t_k(x)dS
\end{aligned}
\tag{4.80}
$$

Now, the Traction Boundary Integral Equation (TBIE) can be used for collocation on the lower crack surface without regenerating identical rows to the displacement boundary integral equation.

4.2.3 Dual Boundary Element Method (DBEM)

Chen [136] and Portela *et al.* [94] independently introduced the DBEM to resolve two-dimensional problems and later Mi and Aliabadi [95] extended the approach to three-dimensional problems. The dual boundary element method is an easy to implement and computationally efficient technique for modelling crack problems in BEM. The method employs of two independent boundary integral equations; where the displacement boundary integral equation is used when collocating on one crack surface, and the traction

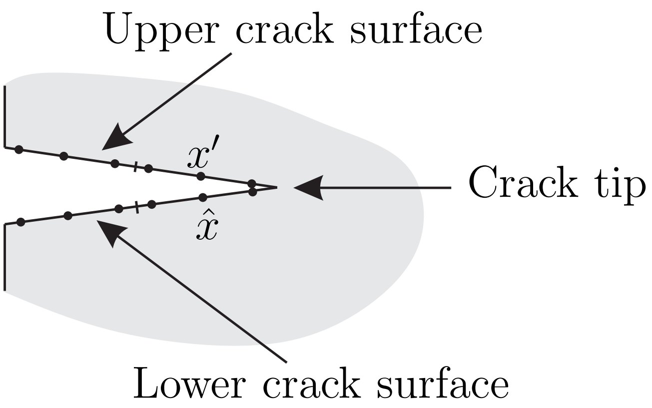

Figure 4.8: Crack characteristics when using the DBEM

boundary integral equation is used on the other surface. When the DBIE is used for collocation on x' on the upper crack surface, Eqn. (4.73) can be represented as,

$$C_{ij}(x')u_j(x') + C_{ij}(\hat{x})u_j(\hat{x}) + \fint_S T_{ij}(x', x)u_j(x)dS = \int_S U_{ij}(x', x)t_j(x)dS \tag{4.81}$$

where $\hat{x}$ is the point coincident with the source x', but lying on the opposing crack surface as shown in Fig. 4.8. When using TBIE to collocate at x' on the lower crack surface, Eqn. (4.80) can be expressed as,

$$\frac{1}{2}t_j(x') - \frac{1}{2}t_j(\hat{x}) = \fint_S D_{ij}(x', x)t_j(x)dS - \fint\!\!\!\!=_S S_{kij}(x', x)u_j(x)dS \tag{4.82}$$

The main challenge with DBEM implementation is the evaluation of the Cauchy principal value integral which arises in DBIE and TBIE, and the Hadamard finite part integral observed in TBIE. Certainly, the existence of strongly singular and hypersingular integrals requires particular attention when choosing shape functions for the crack surfaces. The application of the displacement integral equation imposes continuity of the displacement components at the collocation nodes. Whereas, the traction integral equation requires displacement derivatives that are continuous at the collocation points. These conditions can be satisfied automatically by using discontinuous quadratic elements. The implementation of DBEM and the treatment of singular integrals will be shown in the following section.

4.3 Evaluation of the DBEM integrals

This section concentrates on evaluating the dual boundary element method integrals, since BEM integrals are implicitly included in DBEM. In fact, the accuracy of BEM and the DBEM results rely on an accurate evaluation of boundary integral equations, which mainly consist of fundamental solutions. It was demonstrated earlier that fundamental solutions are singular, and that this singularity depends on the distance r between the source point x' and the field point x. Therefore, integrals can be categorised into regular and singular integrals. In the case of a regular integral, a numerical quadrature method can be used to directly obtain the integral value. Whereas, singular integrals can be classified into weakly singular, strongly singular and hypersingular, and can be treated according to the order of the singularity. In addition, particular attention needs to be directed toward the near singular integral when the source point is very close to the field element. In order to evaluate these singularities several techniques have been developed; it is the aim of this section to address the methods used in this thesis.

4.3.1 Regular integrals

Non-singular integration is the simplest type of integral and occurs when the source point is at a distance from the element containing the field point. Commonly, regular integrals can be computed using a numerical quadrature method, such as the Gauss-Legendre quadrature. The use of GL permits numerical integration of a function defined over an interval between -1 and $+1$. Therefore, for example the integrand $P_{ij}^{\bar{n}\bar{a}}$, as it appears in Eqn. (4.50a) can be calculated using the Gauss-Legendre scheme as,

$$P_{ij}^{\bar{n}\bar{a}} = \int_{-1}^{1} N^{\bar{a}}(\xi) T_{ij}\left[x', x(\xi)\right] J^{\bar{n}}(\xi) d\xi \approx \sum_{g=1}^{N_g} N^{\bar{a}}(\xi_g) T_{ij}\left[x', x(\xi_g)\right] J^{\bar{n}}(\xi_g) w_g \tag{4.83}$$

where ξ_g and w_g are Gauss points and associated weights respectively (these points and related weight can be found in any textbook e.g. [131]), and N_g describes the total number of Gauss points. Similarly, the three-dimensional integrand $P_{ij}^{\bar{n}\bar{a}}$, appears in Eqns. (4.54a)

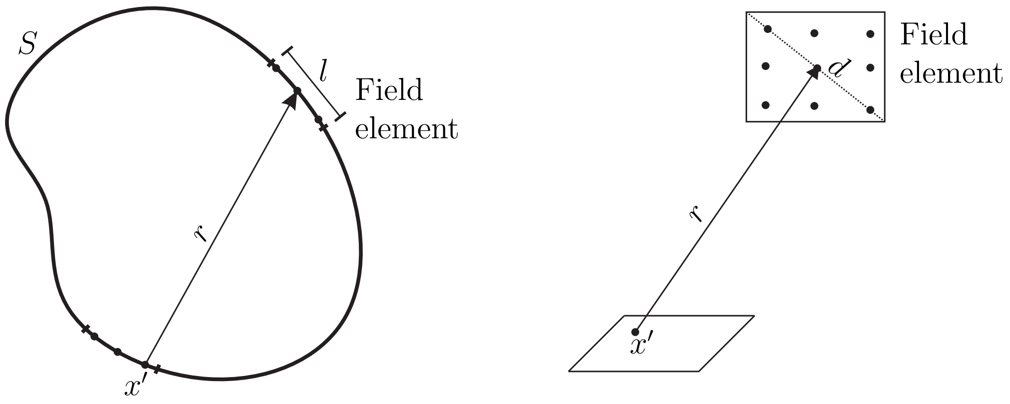

Figure 4.9: Adaptive method to determine the required number of integration points

and can be obtained numerically as,

$$
\begin{aligned}
P_{ij}^{\bar{n}\bar{a}} &= \int_{-1}^{1}\int_{-1}^{1} N^{\bar{a}}(\xi_1,\xi_2)T_{ij}\left[x', x(\xi_1,\xi_2)\right] J^{\bar{n}}(\xi_1,\xi_2)d\xi_1 d\xi_2 \\
&\approx \sum_{g_2=1}^{N_{g_2}}\sum_{g_1=1}^{N_{g_1}} N^{\bar{a}}(\xi_{g_1},\xi_{g_2})T_{ij}\left[x', x(\xi_{g_1},\xi_{g_2})\right] J^{\bar{n}}(\xi_{g_1},\xi_{g_2})w_{g_1}w_{g_2} \qquad (4.84)
\end{aligned}
$$

where ξ_{g_1} and ξ_{g_2} represent the GL points and the associated weights w_{g_1} and w_{g_2}. It is necessary to increase the number of integration points when the source point x' is positioned closer to the field element. However, the increment of the integration points directly effects the computational cost. Therefore, it is convenient to consider an adaptive technique to improve the efficiency of the numerical integration. This can be achieved using the ratio of the size of the field element and the distance r, that is l/r, (where l is the element size), as proposed by [137]. In the case of three-dimensional problems, l can be replaced with the field element diagonal d, as illustrated in Fig. 4.9. However, near singular integration methods can be used, when a higher number of integration points is required.

4.3.2 Near singular integrals

Gauss-Legendre quadrature can be used to obtain the value of regular integrals when the collocation point is distant from the field element. However, the accuracy of any integration is significantly affected by the singularity observed in fundamental solutions when the source point is close to the field element. This effect is proportional to the kernels order of singularity. In the case of low order singularity, it is sufficient to use higher orders of integration. However, kernels containing strongly singular and hypersingular require alternative treatment.

4.3.2.1 Element sub-division

An effective approach with which to evaluate the near singular involves dividing the field element into sub-elements [135]. Moreover, instead of increasing the integration points across the element, the division of elements allows the integration points to be concentrated where they are most needed. The use of a sub-element technique imposes calculation of transformation Jacobian associated with local sub-element coordinates. Alternatively, the Telles transformation method [138] can be used for near singular integrals, as will be introduced shortly in relation to the treatment of weakly singular integrals.

4.3.3 Weakly singular integrals

When the collocation point lies inside the field element, the form of numerical integration required depends on the order of the singularity. In this case, the use of a higher order of integration is insufficient, and can result in increasing the error when a large number of integration points are used.

4.3.3.1 Logarithmic Gaussian quadrature

In the case of two-dimensional weakly singular integrals (see Table 4.1), a particular type of Gauss-Legendre can be used to achieve the integration. Commonly, the first choice when evaluating integrals comprising a logarithmic singularity is the logarithmic Gaussian quadrature routine, which allows evaluation of the integral in a similar manner to the GL quadrature. Therefore, the logarithmic integral appears in the 2D weakly singular kernels

Table 4.1: Degree of singularity for 2D and 3D kernels

Kernel	**Two-dimensions**		**Three-dimensions**	
	Order	**Singularity type**	**Order**	**Singularity type**
U_{ij}	$O(\ln(1/r))$	Weakly singular	$O(1/r)$	Weakly singular
T_{ij}	$O(1/r)$	Strongly singular	$O(1/r^2)$	Strongly singular
D_{kij}	$O(1/r)$	Strongly singular	$O(1/r^2)$	Strongly singular
S_{kij}	$O(1/r^2)$	hypersingular	$O(1/r^3)$	hypersingular

as defined in Eqns. (4.50b) and can be obtained as,

$$\begin{aligned} Q_{ij}^{\bar{n}\bar{a}} &= \int_{-1}^{1} N^{\bar{a}}(\xi) U_{ij}\left[x', x(\xi)\right] J^{\bar{n}}(\xi) d\xi \\ &= \int_{0}^{1} N^{\bar{a}}(\xi_l) U_{ij}\left[x', x(\xi_l)\right] J^{\bar{n}}(\xi) d\xi_l \\ &\approx \sum_{g_l=1}^{N_{g_l}} N^{\bar{a}}(\xi_{g_l}) U_{ij}\left[x', x(\xi_{gl})\right] J^{\bar{n}}(\xi_{gl}) w_{g_l} \end{aligned} \tag{4.85}$$

where ξ_{g_l} and w_{g_l} are logarithmic Gauss points and weights respectively. It is critical to consider the transformation of integration limits, since the logarithmic Gauss-Legendre is expressed by the limits 0 to 1 instead of -1 to $+1$. In the case of a continuous element, the linear transformation can be computed as $\xi_l = 0.5(1+\xi)$ and $\xi_l = 0.5(1-\xi)$ when collocating on the first and last points respectively. Whereas, the element needs to be divided into sub-elements when collocating on the middle point or when a discontinuous element is used.

4.3.3.2 Variable transformation in 2D

Alternatively, the Telles transformation [139] can be employed to evaluate weakly singular integrals. This approach has also been validated for the evaluation of near singular integrals. The transformation is formulated to allow the Jacobian to eliminate the singularity, this then means the integral can be accurately evaluated using Gauss-Legendre quadrature. Consider a weakly singular function $f(\xi)$ at a point ξ' where $-1 \leq \xi' \leq 1$, this can be expressed in Telles form as,

$$\int_{-1}^{1} f(\xi) d\xi = \int_{-1}^{1} f\left\{\frac{(\eta-\bar{\eta})^3 + \bar{\eta}(\bar{\eta}^2+3)}{1+3\bar{\eta}^2}\right\} \frac{3(\eta-\bar{\eta})^2}{1+3\bar{\eta}^2} d\eta \tag{4.86}$$

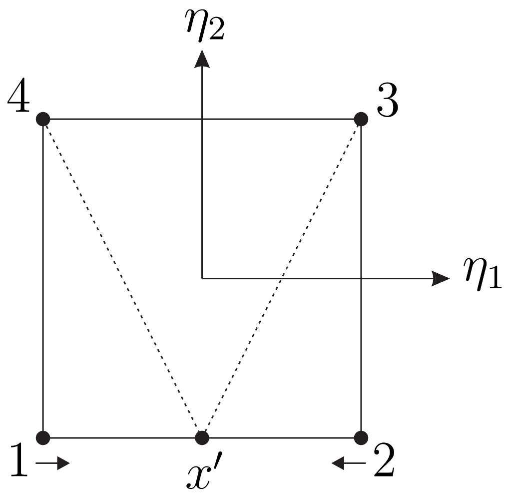

Figure 4.10: Collapsed quadrilateral element

where $\bar{\eta}$ is given by

$$\bar{\eta} = \sqrt[3]{\xi'\xi^* + |\xi^*|} + \sqrt[3]{\xi'\xi^* - |\xi^*|} + \xi' \tag{4.87}$$

and ξ^* is defined as,

$$\xi^* = \xi'^2 - 1 \tag{4.88}$$

where η is the new local coordinate. It can be seen from Eqn. (4.86) that the Jacobian presented by $(\eta - \bar{\eta})$ is equal to zero at singular point ξ'. This simple technique provides an accurate evaluation for weakly singular integrals, and reduces the computational cost in cases involving near singular integrals. It is convenient to mention that, the Telles transformation can be applied to the double integrals that appear in three-dimensional problems.

4.3.3.3 Variable transformation in 3D

Alternatively, the transformation of variables in three-dimensions can be obtained by mapping a triangle element into a square elements; such that the Jacobian of transformation is equal to zero at the singular point. This can be achieved in the case of a quadrilateral element by subdividing the element into triangular sub-elements, as suggested by [140]. Next, we define new local coordinates η_1 and η_2 as illustrated in Fig. 4.10 and a new linear shape functions as,

$$\begin{aligned}\xi_1(\eta_1,\eta_2) &= L_1(\eta_1,\eta_2)\xi_{11} + L_2(\eta_1,\eta_2)\xi_{12} + L_3(\eta_1,\eta_2)\xi_{13} + L_2(\eta_1,\eta_2)\xi_{14} \\ \xi_2(\eta_1,\eta_2) &= L_1(\eta_1,\eta_2)\xi_{21} + L_2(\eta_1,\eta_2)\xi_{22} + L_3(\eta_1,\eta_2)\xi_{23} + L_2(\eta_1,\eta_2)\xi_{24} \qquad (4.89)\end{aligned}$$

where ξ_{11} and ξ_{21} are the local coordinates ξ_1 and ξ_2 for point 1. The linear rectangular shape functions L_1, L_2, L_3 and L_4 are defined as,

$$\begin{aligned}L_1(\eta_1,\eta_2) &= \frac{1}{4}(1-\eta_1)(1-\eta_2) \\ L_2(\eta_1,\eta_2) &= \frac{1}{4}(1+\eta_1)(1-\eta_2) \\ L_3(\eta_1,\eta_2) &= \frac{1}{4}(1+\eta_1)(1+\eta_2) \\ L_4(\eta_1,\eta_2) &= \frac{1}{4}(1-\eta_1)(1+\eta_2) \qquad (4.90)\end{aligned}$$

At the singular point x' the rectangle collapses, and points 1 and 2 are joined as,

$$\xi_{11} = \xi_{21} \quad \text{and} \quad \xi_{12} = \xi_{22} \qquad (4.91)$$

The transformation Jacobian for transferring local coordinates from ξ_1 and ξ_2 to η_1 and η_2, can be calculated as,

$$J(\eta_1,\eta_2) = \frac{\partial\xi_1}{\partial\eta_1}\frac{\partial\xi_2}{\partial\eta_2} - \frac{\partial\xi_2}{\partial\eta_1}\frac{\partial\xi_1}{\partial\eta_2} \qquad (4.92)$$

where the derivative of ξ_1 and ξ_2 with respect to η_1 can be calculated as,

$$\begin{aligned}\frac{\partial\xi_1}{\partial\eta_1} &= \frac{\partial L_1}{\partial\eta_1}\xi_{11} + \frac{\partial L_2}{\partial\eta_1}\xi_{21} + \frac{\partial L_3}{\partial\eta_1}\xi_{31} + \frac{\partial L_4}{\partial\eta_1}\xi_{41} \\ \frac{\partial\xi_2}{\partial\eta_1} &= \frac{\partial L_1}{\partial\eta_1}\xi_{12} + \frac{\partial L_2}{\partial\eta_1}\xi_{22} + \frac{\partial L_3}{\partial\eta_1}\xi_{32} + \frac{\partial L_4}{\partial\eta_1}\xi_{42} \qquad (4.93)\end{aligned}$$

The derivative of ξ_1 and ξ_2 with respect to η_2 is calculated similarly. Finally, the three-dimensional weakly singular integral in (4.54b) can be written as,

$$Q_{ij}^{\bar{n}\bar{a}} = \int_{-1}^{1}\int_{-1}^{1} N^{\bar{a}}(\xi_1,\xi_2)U_{ij}\left[x', x(\xi_1,\xi_2)\right] J^{\bar{n}}(\xi_1,\xi_2)d\xi_1 d\xi_2 \tag{4.94}$$

$$= \int_{-1}^{1}\int_{-1}^{1} N^{\bar{a}}(\eta_1,\eta_2)U_{ij}\left[x', x(\eta_1,\eta_2)\right] J^{\bar{n}}(\xi_1,\xi_2)J^{\bar{n}}(\eta_1,\eta_2)d\eta_1 d\eta_2 \tag{4.95}$$

The transformation technique can be used for near singular integrals by projecting the source point to the nearest point on the field element and treating it as a singular point.

4.3.4 Strongly singular and hypersingular integrals

Evaluating strongly singular and hypersingular integrals (see Table 4.1) is considered to be a difficult task in the implementation of DBEM, since Gauss-Legendre quadrature is not applicable. Several techniques have been developed to handle these type of integrals [96], including indirect, analytical and semi-analytical integration. In the case of a strongly singular integral, the most commonly used method is rigid body motion. This indirect method allows the evaluation of singular terms corresponding to the Cauchy principal value. However, rigid body motion cannot be used with DBEM. Alternatively, an analytical integration method is available for DBEM when a particular type of element is used. Moreover, if a flat discontinuous element is considered, then strongly singular and hypersingular integrals can be reduced to simple expressions. However, the assumption made for analytical integration restricts the geometry of the problem. In addition, since the aim of this thesis is to enrich the DBEM, a more general method should be considered. Therefore, a semi-analytical integration technique is demonstrated below for the treatment of enriched 2D and 3D singularities.

4.3.4.1 Singularity subtraction technique

The approach used to evaluate strongly singular and hypersingular integrals is a semi-numerical technique known as the subtraction of singularity method [141]. In this approach, integrands are expanded using the Taylor series, which allows singular terms to be removed from the integrand, and leaves only regular terms that can be computed directly using a standard GL quadrature. The singular terms can then be integrated analytically and returned to the integral. This is a general approach that can be applied to any displacement approximation, enabling the enrichment function to be included as part of the singular integral.

2D semi-analytical integral

Guiggiani and Casalini [141] introduced a direct evaluation of the Cauchy principle value. The approach contains a complete treatment of singular integrals in two-dimensions, including all free-terms associated with the limiting process. The method can be demonstrated for 2D problems by considering the hypersingular kernel S_{kij}, which appears in the traction boundary integral Eqn. (4.82), and can be written as,

$$I = \oint_{-1}^{1} S_{kij}(\xi', x(\xi)) N^{\bar{a}}(\xi) J(\xi) d\xi \tag{4.96}$$

Let $F(\xi', \xi)$ be defined as,

$$F(\xi', \xi) = S_{kij}(\xi', x(\xi)) N^{\bar{a}}(\xi) J(\xi) \tag{4.97}$$

The aim now is to expand $F(\xi', \xi)$ into a form that allows non-singular and singular terms to be separated easily. Therefore, using the Laurent series $F(\xi', \xi)$ is expanded as,

$$F(\xi', \xi) = \frac{F_{-2}(\xi')}{(\xi - \xi')^2} + \frac{F_{-1}(\xi')}{(\xi - \xi')} + O(1) \tag{4.98}$$

where $F_{-2}(\xi')$ and $F_{-1}(\xi')$ are local terms that depend on the first and second derivatives of the Kernel, Jacobian and shape functions $N^{\bar{a}}$, which are evaluated at a singular point ξ'. The singularities are now expressed by $(\xi - \xi')^2$ and $(\xi - \xi')$ to allow easy analytical integration. The remaining terms are not singular and can be integrated numerically. The focus then is on the integration of singular terms which need to be added to the integral once integrated.

By following a similar process to the limiting procedure introduced in Sec. 4.1.4, we

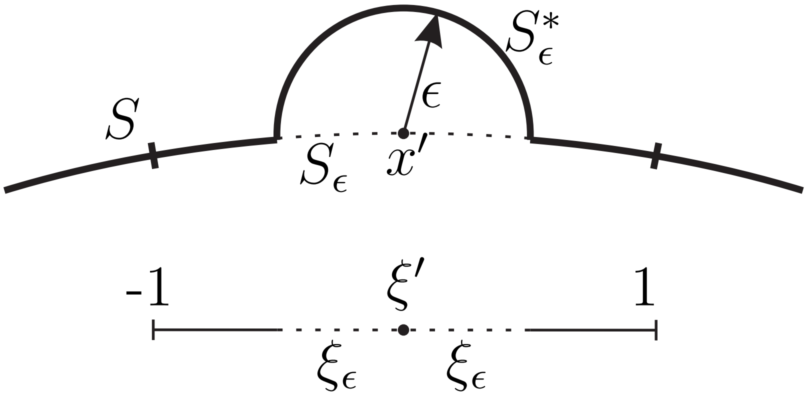

Figure 4.11: Limiting procedure with local coordinate system

consider a semicircle vanishing domain centred at source point ξ'. However, here the limit is taken with respect to the local coordinate as $\xi_\epsilon \to 0$, where the integral is split into two intervals $[-1, \xi' - \xi_\epsilon]$ and $[\xi' + \xi_\epsilon, 1]$ as illustrated in Fig. 4.11. Since, the integration intervals are defined, it is now possible to express the integral including the singular parts as,

$$\begin{aligned} I &= \int_{-1}^{1} \left[F(\xi', \xi) - \left(\frac{F_{-2}(\xi')}{(\xi - \xi')^2} + \frac{F_{-1}(\xi')}{(\xi - \xi')} \right) \right] d\xi \\ &+ \lim_{\epsilon \to 0} \left\{ \int_{-1}^{\xi' - \xi_\epsilon} \frac{F_{-1}(\xi')}{(\xi - \xi')} d\xi + \int_{\xi' + \xi_\epsilon}^{1} \frac{F_{-1}(\xi')}{(\xi - \xi')} d\xi \right. \\ &+ \left. \int_{-1}^{\xi' - \xi_\epsilon} \frac{F_{-2}(\xi')}{(\xi - \xi')^2} d\xi + \int_{\xi' + \xi_\epsilon}^{1} \frac{F_{-2}(\xi')}{(\xi - \xi')^2} d\xi + N^{\bar{a}}(\xi) \frac{b_{kij}(\xi)}{\epsilon} \right\} \\ &= I_0 + I_{-1} + I_{-2} \end{aligned} \tag{4.99}$$

where the first term I_0 consists of a regularised integral and can be computed directly using Gauss Legendre quadrature. The second term I_{-1} includes the singular integral related to F_{-1}, which can be integrated analytically.

The singular terms are integrated analytically with consideration of the limit as $\xi_\epsilon \to 0$. Therefore, the relationship between ϵ and the infinitesimal boundary ξ_ϵ can be expressed about the source point ξ' using the Taylor series as,

$$\epsilon = J(\xi')\xi_\epsilon + O(\xi_\epsilon) \tag{4.100}$$

If the higher order terms are ignored, ξ_ϵ can be obtained as,

$$\xi_\epsilon = \frac{\epsilon}{J(\xi')} \tag{4.101}$$

The substitution of (4.101) into I_{-1}, and analytical integration yields,

$$\begin{aligned} I_{-1} &= \lim_{\epsilon \to 0} \left\{ \int_{-1}^{\xi' - \frac{\epsilon}{J(\xi')}} \frac{F_{-1}(\xi')}{(\xi - \xi')} d\xi + \int_{\xi' + \frac{\epsilon}{J(\xi')}}^{1} \frac{F_{-1}(\xi')}{(\xi - \xi')} d\xi \right\} \\ &= F_{-1}(\xi') \ln \left| \frac{1 - \xi'}{-1 - \xi'} \right| \end{aligned} \tag{4.102}$$

The third term I_{-2} containing the free-term emerges from the limiting process and the singular integrals related to F_{-2}. Similarly, analytical integration can be obtained after substituting (4.101) into I_{-2}, which gives,

$$\begin{aligned} I_{-2} &= \lim_{\epsilon \to 0} \left\{ \int_{-1}^{\xi' - \frac{\epsilon}{J(\xi')}} \frac{F_{-2}(\xi')}{(\xi - \xi')^2} d\xi + \int_{\xi' + \frac{\epsilon}{J(\xi')}}^{1} \frac{F_{-2}(\xi')}{(\xi - \xi')^2} d\xi + N^{\bar{a}}(\xi) \frac{b_{kij}(\xi)}{\epsilon} \right\} \\ &= F_{-2}(\xi') \left[\frac{1}{-1 - \xi'} - \frac{1}{1 - \xi'} \right] \end{aligned} \tag{4.103}$$

The final form of the integral can be written as,

$$\begin{aligned} I &= \int_{-1}^{+1} \left[F(\xi', \xi) - \left(\frac{F_{-2}(\xi')}{(\xi - \xi')^2} + \frac{F_{-1}(\xi')}{(\xi - \xi')} \right) \right] d\xi \\ &+ F_{-1}(\xi') \ln \left| \frac{1 - \xi'}{-1 - \xi'} \right| + F_{-2}(\xi') \left[\frac{1}{-1 - \xi'} - \frac{1}{1 - \xi'} \right] \end{aligned} \tag{4.104}$$

Now, the hypersingular integral can be evaluated easily, having obtained the values of F_{-2} and F_{-2}. Conveniently, in the case of strongly singular integrals, the term I_{-2} is equal to zero which simplifies the problem further.

3D semi-analytical integrals

The semi-analytical treatment of the strongly singular and hypersingular was extended by Guiggiani and Gigante [134] for use with three-dimensional problems. The singular integral is expanded using the Taylor series to allow the subtraction of singular terms in

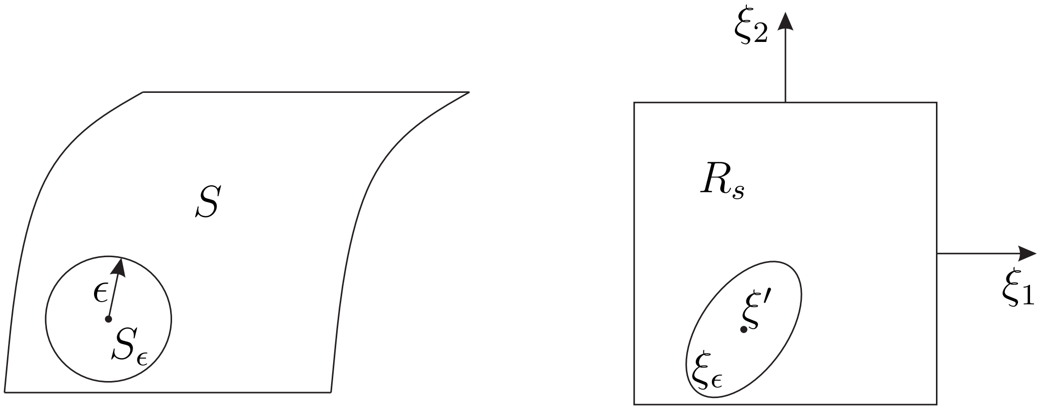

Figure 4.12: limiting procedure for three-dimensional problems

a similar manner to that used with the two-dimensional treatment. The method can be illustrated for 3D problems by considering the hypersingular kernel S_{kij} as an example; this can be written as,

$$I = \int_{-1}^{1}\int_{-1}^{1} S_{kij}(x', x) N^{\bar{a}}(\xi_1, \xi_2) J(\xi_1, \xi_2) d\xi_1\xi_2 \tag{4.105}$$

The limiting procedure for three-dimensional problems begins by considering discontinuous elements and denoting a portion of the boundary S containing the source point x' by S_ϵ. However, to make the analytical integrals simple, the limit is considered with respect to local coordinates as illustrated in Fig. 4.12. Applying the limit to Eqn. (4.105), gives,

$$I = \lim_{\epsilon \to 0}\left\{\int_{R_s - \xi_\epsilon} S_{kij}(x', x) N^{\bar{a}}(\xi_1, \xi_2) J(\xi_1, \xi_2) d\xi_1\xi_2 + N^{\bar{a}}(\xi')\frac{b_{ikj}(x')}{\epsilon}\right\} \tag{4.106}$$

where the last term in Eqn. (4.106) represents the free-term that emerges because of the limiting process. Following common practice in BEM, the polar coordinate system (ρ, θ) centred at ξ' relates to the local coordinate as,

$$\begin{aligned} \xi_1 &= \xi_1' + \rho\cos\theta \\ \xi_2 &= \xi_2' + \rho\sin\theta \end{aligned} \tag{4.107}$$

By noticing that $d\xi_1 d\xi_2 = \rho d\rho d\theta$, the combination of (4.105) and (4.107), yields,

$$I = \lim_{\epsilon \to 0} \left\{ \int_0^{2\pi} \int_{\alpha(\epsilon,\theta)}^{\hat{\rho}(\theta)} S_{kij}(x', x) N^{\bar{a}}(\rho, \theta) J(\xi_1, \xi_2) \rho d\rho d\theta + N^{\bar{a}}(\xi') \frac{b_{ikj}(x')}{\epsilon} \right\} \tag{4.108}$$

Now, let $F(\rho, \theta)$ be defined as,

$$F(\rho, \theta) = S_{kij}(x', x) N^{\bar{a}}(\rho, \theta) J(\xi_1, \xi_2) \rho \tag{4.109}$$

Since the function $F(\rho, \theta)$ is a singular of order ρ^{-2}, the use of Laurent series expansion with respect to ρ, gives,

$$F(\rho, \theta) = \frac{F_{-2}(\theta)}{\rho^2} + \frac{F_{-1}(\theta)}{\rho} + O(1) \tag{4.110}$$

where F_{-2} and F_{-1} are real functions of θ. It is crucial for these functions to depend on θ to represent the asymptotic behaviour of $F(\rho, \theta)$ when $\rho \to 0$. Additionally, it is necessary to introduce $\alpha(\epsilon, \theta)$ in the form of the Taylor series expansion with respect to ϵ, which can be expressed as,

$$\rho = \alpha(\epsilon, \theta) = \epsilon \beta(\theta) + \epsilon^2 \gamma(\theta) + O(\epsilon^3) \tag{4.111}$$

where $\beta(\theta)$ and $\gamma(\theta)$ are related to the kernel being integrated and can be easily evaluated. By adding and subtracting the first two terms of the series expansion (4.110) in expression (4.108), we obtain,

$$\begin{aligned} I &= \lim_{\epsilon \to 0} \left\{ \int_0^{2\pi} \int_{\alpha(\epsilon,\theta)}^{\hat{\rho}(\theta)} \left[F(\rho, \theta) - \left(\frac{F_{-2}(\theta)}{\rho^2} + \frac{F_{-1}(\theta)}{\rho} \right) \right] d\rho d\theta \right. \\ &+ \int_0^{2\pi} \int_{\alpha(\epsilon,\theta)}^{\hat{\rho}(\theta)} \frac{F_{-1}(\theta)}{\rho} d\rho d\theta \\ &+ \left. \int_0^{2\pi} \int_{\alpha(\epsilon,\theta)}^{\hat{\rho}(\theta)} \frac{F_{-2}(\theta)}{\rho^2} d\rho d\theta + N^{\bar{a}}(\xi') \frac{b_i(x')}{\epsilon} \right\} \\ &= I_0 + I_{-1} + I_{-2} \end{aligned} \tag{4.112}$$

where the first term I_0 is regular and can be evaluated using standard quadrature rules. The second term I_{-1} includes the singular integral related to F_{-1}, which can be integrated as,

$$\begin{aligned} I_{-1} &= \lim_{\epsilon \to 0} \int_0^{2\pi} \int_{\alpha(\epsilon,\theta)}^{\hat{\rho}(\theta)} \frac{F_{-1}(\theta)}{\rho} d\rho d\theta \\ &= \lim_{\epsilon \to 0} \int_0^{2\pi} F_{-1}(\theta) \left[\ln|\hat{\rho}| - \ln|\alpha(\epsilon,\theta)| \right] d\theta \\ &= \int_0^{2\pi} F_{-1}(\theta) \ln|\hat{\rho}| \, d\theta - \lim_{\epsilon \to 0} \int_0^{2\pi} F_{-1}(\theta) \ln|\alpha(\epsilon,\theta)| \, d\theta \\ &= \int_0^{2\pi} F_{-1}(\theta) \ln\left|\frac{\hat{\rho}}{\beta(\theta)}\right| d\theta - \lim_{\epsilon \to 0} \left\{ \ln\epsilon \int_0^{2\pi} F_{-1}(\theta) d\theta \right\} \\ &= \int_0^{2\pi} F_{-1}(\theta) \ln\left|\frac{\hat{\rho}}{\beta(\theta)}\right| d\theta \end{aligned} \tag{4.113}$$

We consider the property $\int_0^{2\pi} F_{-1}(\theta) d\theta = 0$, since F_{-1} has a property such that $F_{-1}(\theta) = -F_{-1}(\theta + \pi)$; further detail on this can be found in [134]. Eqn. (4.113) shows that I_{-1} is equivalent to a one-dimensional regular integral. Similar treatment can be applied to I_{-2} such that,

$$\begin{aligned} I_{-2} &= \lim_{\epsilon \to 0} \left\{ \int_0^{2\pi} \int_{\alpha(\epsilon,\theta)}^{\hat{\rho}(\theta)} \frac{F_{-2}(\theta)}{\rho^2} d\rho d\theta + N^{\bar{a}}(\xi') \frac{b_i(x')}{\epsilon} \right\} \\ &= \lim_{\epsilon \to 0} \left\{ \int_0^{2\pi} F_{-2}(\theta) \left[-\frac{1}{\hat{\rho}(\theta)} + \frac{1}{\alpha(\epsilon,\theta)} \right] d\theta + N^{\bar{a}}(\xi') \frac{b_i(x')}{\epsilon} \right\} \\ &= \lim_{\epsilon \to 0} \left\{ \int_0^{2\pi} \frac{F_{-2}(\theta)}{\epsilon\beta(\theta)} \left(1 - \epsilon \frac{\gamma(\theta)}{\beta(\theta)} \right) d\theta + N^{\bar{a}}(\xi') \frac{b_i(x')}{\epsilon} \right\} - \int_0^{2\pi} \frac{F_{-2}(\theta)}{\hat{\rho}(\theta)} d\theta \\ &= \lim_{\epsilon \to 0} \frac{1}{\epsilon} \left\{ \int_0^{2\pi} \frac{F_{-2}(\theta)}{\beta(\theta)} d\theta + N^{\bar{a}}(\xi') b_i(x') \right\} - \int_0^{2\pi} F_{-2}(\theta) \left[\frac{\gamma(\theta)}{\beta(\theta)} + \frac{1}{\hat{\rho}(\theta)} \right] d\theta \\ &= -\int_0^{2\pi} F_{-2}(\theta) \left[\frac{\gamma(\theta)}{\beta(\theta)} + \frac{1}{\hat{\rho}(\theta)} \right] d\theta \end{aligned} \tag{4.114}$$

It is convenient to observe that I_{-2} is equivalent to a one-dimensional regular integral. In this case, since a higher order singularity is considered, both terms $\epsilon\beta(\theta)$ and $\epsilon 2\gamma(\theta)$ must be retained in the expansion (4.114) for $\alpha(\epsilon, \theta)$. By collecting the previous results, the final expression for the evaluation of hypersingular integrals in three-dimensions can be written as,

$$\begin{aligned} I &= \int_0^{2\pi}\int_0^{\hat{\rho}(\theta)} \left[F(\rho,\theta) - \left(\frac{F_{-2}(\theta)}{\rho^2} + \frac{F_{-1}(\theta)}{\rho}\right)\right] d\rho d\theta \\ &+ \int_0^{2\pi} \left\{F_{-1}(\theta)\ln\left|\frac{\hat{\rho}}{\beta(\theta)}\right| d\theta - F_{-2}(\theta)\left[\frac{\gamma(\theta)}{\beta(\theta)} + \frac{1}{\hat{\rho}(\theta)}\right]\right\} d\theta \end{aligned} \tag{4.115}$$

The Eqn. (4.115) shows that the quantity I, which is initially given via a limiting process, including a hypersingular integral and an unbounded term, is equal to a regular double integral in addition to a regular one-dimensional integral. It essential to note that the integral must have a finite value since the integral equation that it sits in relates to a real physical problem [134]. Moreover, the limiting process is considered to have been performed exactly, since all singular integrations have been carried out analytically. In the case of strongly singular integrals, further simplification can be made to Eqn. (4.115), since the term F_{-2} is equal to zero.

4.4 Conclusion

The BEM is a robust method applied to analyse fracture mechanics and evaluate SIFs [91]. The formulation of BEM presented in this chapter was obtained directly, by constructing a system of equations that can be implemented numerically. This began by utilising Betti-reciprocal theorem under conditions of equilibrium to derive the BIE. Next, Somigliana's identity for displacements was implemented to relate the displacement value at any internal point within the domain to displacements and tractions located at the boundary. The displacement boundary integral equation can then be achieved by applying the limit as the internal point approach to the boundary. Consequently, the jump terms that emerge from the limitation process are evaluated analytically. The domain is then discretised to allow for the numerical evaluation of integrals. Utilising the collocation method, the system of generated equations can be assembled into a system of matrices to be solved numerically. However, in cases where the source point is located in the same or close to the field element, a proper approach must be used to determine the value of the integrals accurately. Furthermore, the treatment of singular and nearly singular integrals depends on the degree of singularity. A subtraction technique [134] was presented in the chapter to tackle strongly singular and hypersingular integrals; whereas, a transformation approach can be used to evaluate near singular integrals.

In cases of modelling crack problems with coplanar surfaces (i.e. two crack surfaces lying on the same plane), a mathematical difficulty emerges, which leads to a singular matrix. This occurs as the rows associated with crack surface nodes in the system become identical. However, the DBEM approach can be implemented to overcome this difficulty. In addition, the singular field in the vicinity of the crack tip/front required spatial treatment. Hence, conventional basis functions are insufficient for capturing the displacement behaviour. The next chapter introduces the enrichment of DBEM in 2D to improve the ability of the basis functions to obtain displacements accurately.

Chapter 5

Enrichment of 2D Dual Boundary Element Method

5.1 Introduction

In linear elastic fracture mechanics, SIFs play a significant role in the evaluation of stresses and displacements in the vicinity of the crack tip. However, it is well known that because of the singularity that appears at the crack tip, obtaining SIFs using numerical methods without modification is inefficient. Moreover, the need to use a very refined mesh near the crack tip was first noted by [9]. Since then, research into numerical fracture mechanics has involved developing algorithms that can offer a more efficient solution. The reader can find reviews of common methods utilised to obtain accurate results using a coarse mesh in Sec. 3.1.

It can be seen that the application of XFEM reduced the need for mesh refinement, and also separated the mesh from the crack path enabling crack propagation analysis to proceed without the need for remeshing. For these reasons it has spawned a considerable volume of literature. The enrichment technique was extended to BEM to take advantage of methodological features, including the ability to capture discontinuous functions and to support accurate solutions offered on the domain boundary. Various enrichment techniques have been proposed [104, 142] to resolve two-dimensional problems; since a wide range of fracture problems can be simplified into plane stress or plane strain. Recently, the partition of unity approach was used in a manner similar to XFEM by Simpson and Trevelyan [143], who presented an enriched boundary element method, naming it as XBEM. The proposed approach demonstrates the application of two types of formulation: *local* and *global* enrichment. In the case of local formulation, the enrichment functions were derived from the first-order terms of the Williams expansion, enabling the enriched displacement to be written as,

$$u_j^{\bar{n}} = \sum_{\bar{a}=1}^{m} N^{\bar{a}}(\xi) u_j^{\bar{n}\bar{a}} + \sum_{\bar{a}=1}^{m} \sum_{l=1}^{L} N^{\bar{a}} \Psi_l^u(\xi) A_{jl}^{\bar{n}\bar{a}} \tag{5.1}$$

where m and $N^{\bar{a}}$ are the number of nodes on the element and the shape functions, respectively; and $\bar{n}$ denotes the element number. $A_{jl}^{\bar{n}\bar{a}}$ denotes the enrichment coefficient, and $\Psi_l^u(\xi)$ the set of L basis functions obtained from the first-order terms of the Williams expansion, as given by Eqn. (3.3). The use of Eqn. (5.1) in the case of flat element introduces two additional Degrees Of Freedom (DOFs) per node, and in the case of a curved element eight DOFs were added to the system per node. Simpson and Trevelyan noted that a large number of enriched elements or the application to a curved crack had a negative effect on the conditioning of the system; in many cases this led to a poor quality solution. Therefore, a small number of elements were enriched to minimise the number of added degrees of freedom, and an appropriate number of additional collocation points were used to yield a square system. These additional collocation points have been allocated over the enriched elements. It is essential to note that this method was used to improve the estimation of the displacement near the crack, and that SIFs were obtained in a postprocess step using the J-integral.

As an alternative, the global formulation submitted by Simpson and Trevelyan [14, 143] permits direct evaluation of SIFs, and reduces additional unknowns to only two degrees of freedom. This approach enables the formulation of enrichment functions from Williams expansions (2.25), in a similar manner to that applied by Benzley [13]; hence the enriched displacement is given by

$$u_j = \sum_{\bar{a}=1}^{m} N^{\bar{a}}(\xi) u_j^{\bar{a}} + \tilde{K}_I \psi_{Ij}^u + \tilde{K}_{II} \psi_{IIj}^u \tag{5.2}$$

where $\tilde{K}_I$ and $\tilde{K}_{II}$ denote enrichment coefficients for modes I and II, that can correspond to SIFs when the required displacement continuity is provided. The enrichment functions ψ_{Ij}^u and ψ_{IIj}^u are defined as,

$$\psi_{Ix}^u = \frac{1}{2\mu}\sqrt{\frac{r}{2\pi}} \cos\left(\frac{\theta}{2}\right)\left[\kappa - 1 + 2\sin^2\left(\frac{\theta}{2}\right)\right] \tag{5.3a}$$

$$\psi_{IIx}^u = \frac{1}{2\mu}\sqrt{\frac{r}{2\pi}} \sin\left(\frac{\theta}{2}\right)\left[\kappa + 1 + 2\cos^2\left(\frac{\theta}{2}\right)\right] \tag{5.3b}$$

$$\psi_{Iy}^u = \frac{1}{2\mu}\sqrt{\frac{r}{2\pi}} \sin\left(\frac{\theta}{2}\right)\left[\kappa + 1 - 2\cos^2\left(\frac{\theta}{2}\right)\right] \tag{5.3c}$$

$$\psi_{IIx}^u = -\frac{1}{2\mu}\sqrt{\frac{r}{2\pi}} \cos\left(\frac{\theta}{2}\right)\left[\kappa - 1 - 2\sin^2\left(\frac{\theta}{2}\right)\right] \tag{5.3d}$$

It can be noted that $u_j^{\bar{a}}$ in Eqn. (5.2) is a nodal coefficient; it does not represent nodal displacement. Instead, the real displacement can be obtained by combining the three terms. Alternatively, real displacements and stress intensity factors can be evaluated directly by subtracting the nodal values of the enrichment functions. This can be achieved by interpolating displacements as,

$$u_j = \sum_{\bar{a}=1}^{m} N^{\bar{a}}(\xi) u_j^{\bar{a}} + \tilde{K}_I \sum_{\bar{a}=1}^{m} N^{\bar{a}}(\psi_{Ij}^u - \bar{\psi}_{Ij}^u) + \tilde{K}_{II} \sum_{\bar{a}=1}^{m} N^{\bar{a}}(\psi_{IIj}^u - \bar{\psi}_{IIj}^u) \tag{5.4}$$

where $\bar{\psi}_{Ij}^u$ and $\bar{\psi}_{IIj}^u$ represent the value of the enrichment functions ψ_{Ij}^u and ψ_{IIj}^u at node $\bar{a}$. The use of the interpolation functions $N^{\bar{a}}(\psi_{Ij}^u - \bar{\psi}_{Ij}^u)$ and $N^{\bar{a}}(\psi_{IIj}^u - \bar{\psi}_{IIj}^u)$, which equal zero at all nodal points on the element allows for real displacements to be obtained. Moreover, to yield a square system, additional boundary integral equations are formulated from the crack tip solution. However, the use of the new boundary integral equations restricts the method to model problems that consist of only a single crack tip. The use of this technique was capable of yielding the SIFs with an approximate error of 2.5%. In addition, the enrichment shows superior improvement in the J-integral results. Subsequently, the approach was extended to assess curved cracks [100], since this adds only two extra degrees of freedom per crack tip to the system.

In this thesis, the XBEM approach is extended using a modified form of enrichment (similar to the global enrichment functions used by Simpson and Trevelyan [14]) in combination with crack tip displacement constraint equations, to provide the values of SIFs directly. The aim of the method demonstrated here is to provide solutions to problems by achieving a considerable reduction in the number of degrees of freedom required to determine results with prescribed accuracy. The discussion begins by presenting the formulation of the method while outlining the enrichment of the dual boundary element method. Next, the implementation and the treatment of the singularity are introduced. Finally, verification of the method is given, by comparing the direct SIFs against the J-integral, and in addition the effect on the J-integral results when using XBEM is shown.

5.2 Formulation

The main purpose of enrichment is to introduce auxiliary functions to provide a better estimation of the required variation, which would present difficulties when using standard polynomial functions. With this in mind, the most convenient choice for capturing the singular field that appears in the vicinity of the crack tip, is the leading order terms of Williams expansions (as represented by Eqns. 2.13). Moreover, the use of Williams expansions was confirmed to have improved the approximation of displacement in earlier work by Simpson and Trevelyan. The same strategy of enrichment is used here to yield identical expression for enriched displacements, which are then applied to the boundary integral equations.

5.2.1 Enrichment of Displacement

A considerable volume of literature demonstrated that the singular field near the crack tip cannot be captured using standard quadratic interpolation of displacements in BEM unless highly refined meshes are used. Alternatively, the use of an asymptotic analytical expression for displacements around the crack tip, within the BIE, exhibits an improvement in accuracy when using coarse meshes. The well-known Williams expansion for near crack tip displacement as expressed in Eqn. (2.25) as presented by [100], which can be written in terms of K_I and K_{II} as,

$$u_j = K_I \psi_{Ij}(r,\theta) + K_{II} \psi_{IIj}(r,\theta) \tag{5.5}$$

The enrichment function implemented and used here is identical to that introduced by [14]. However, the enrichment function is rewritten here with a slight change in notation, since the current formulation permits the modelling of more than one crack tip. In addition, a rotation matrix is introduced to the enrichment function, as the displacement evaluated via enriched terms is associated with crack local coordinates, which originated at the crack tip. Therefore, Eqn. (5.5) can be used to enrich an otherwise classical piecewise polynomial shape function approximation, of displacement near the crack tip, in a fashion similar to that described in early work by Benzley, as follows,

$$\begin{aligned}\{u_x^\lambda \; u_y^\lambda\}^T = [\boldsymbol{u}^{\bar{a}}(x)]\{N^{\bar{a}}(\xi)\} \quad &+ \quad \tilde{K}_I^\lambda [R_{jq}(\alpha)]\{\psi_{In}^\lambda(r,\theta) \;\; \psi_{Ib}^\lambda(r,\theta)\}^T \\ &+ \quad \tilde{K}_{II}^\lambda [R_{jq}(\alpha)]\{\psi_{IIn}^\lambda(r,\theta) \;\; \psi_{IIb}^\lambda(r,\theta)\}^T \end{aligned} \tag{5.6}$$

where $\boldsymbol{u}^{\bar{a}}(x)$ is given by

$$\boldsymbol{u}^{\bar{a}}(x) = \begin{bmatrix} u_{x1} & u_{x2} & u_{x3} \\ u_{y1} & u_{y2} & u_{y3} \end{bmatrix} \tag{5.7}$$

where u_{x1} and u_{y1} denote the displacements in x and y-direction for node 1 on element $\bar{a}$. The coefficients $\tilde{K}_I^\lambda$ and $\tilde{K}_{II}^\lambda$ describe the unknown amplitudes of the enrichment functions ψ_{Iq}^λ and ψ_{IIq}^λ, as related to the crack tip λ, and are found as terms in the XBEM solution vector. The rotation matrix R is used to transfer displacements from the crack's local coordinates (n, b) to global coordinates (x, y) (see Appendix A.3), as presented in Fig. 5.1. It was mentioned earlier that $u_j^{\bar{a}}$ is no longer the nodal displacement (as in the conventional

BEM), but instead is to be viewed simply as a coefficient scaling the Lagrangian shape function $N^{\bar{a}}$ for node $\bar{a}$. It is noted that Eqn. (5.5) predicts the displacement components to vanish at the crack tip, i.e. at $r = 0$. Therefore, an important role of the first term in (5.6) is to capture non-zero displacement of the crack tip. Using the new notation the terms $\psi_{Iq}(r,\theta)$ and $\psi_{IIq}(r,\theta)$ can be written as,

$$\psi^{\lambda}_{In} = \frac{1}{2\mu}\sqrt{\frac{r}{2\pi}}\cos\frac{\theta}{2}\left[\kappa - 1 + 2\sin^2\frac{\theta}{2}\right] \tag{5.8a}$$

$$\psi^{\lambda}_{IIn} = \frac{1}{2\mu}\sqrt{\frac{r}{2\pi}}\sin\frac{\theta}{2}\left[\kappa + 1 + 2\cos^2\frac{\theta}{2}\right] \tag{5.8b}$$

$$\psi^{\lambda}_{Ib} = \frac{1}{2\mu}\sqrt{\frac{r}{2\pi}}\sin\frac{\theta}{2}\left[\kappa + 1 - 2\cos^2\frac{\theta}{2}\right] \tag{5.8c}$$

$$\psi^{\lambda}_{IIb} = \frac{-1}{2\mu}\sqrt{\frac{r}{2\pi}}\cos\frac{\theta}{2}\left[\kappa - 1 - 2\sin^2\frac{\theta}{2}\right] \tag{5.8d}$$

where r and θ are polar coordinates centred at the crack tip, μ is the shear modulus and κ is a parameter defined as $\kappa = 3 - 4\nu$ and $\kappa = \frac{3-\nu}{1+\nu}$ for plane strain and plane stress, respectively; ν being the Poisson's ratio. Since, the formulation introduces an accurate expression for the crack tip displacement behaviour, a more accurate result is anticipated for crack problems when the enriched expression is substituted into boundary integral equations.

5.2.2 Extended Dual Boundary Element Method

As shown in Sec. 4.2.3, applying the classical direct collocation BEM to problems containing cracks results in rank deficiency, since duplicate equations are formed when collocating on coincident nodes on opposing crack surfaces. The dual boundary element method [94] overcomes this difficulty, and is also an efficient technique for modelling crack problems in BEM. The method consists of two independent boundary integral equations; where DBIE is used when collocating on one crack surface, and TBIE is used on another. Therefore, the enriched form of the displacement is substituted into the DBIE equation, as given by

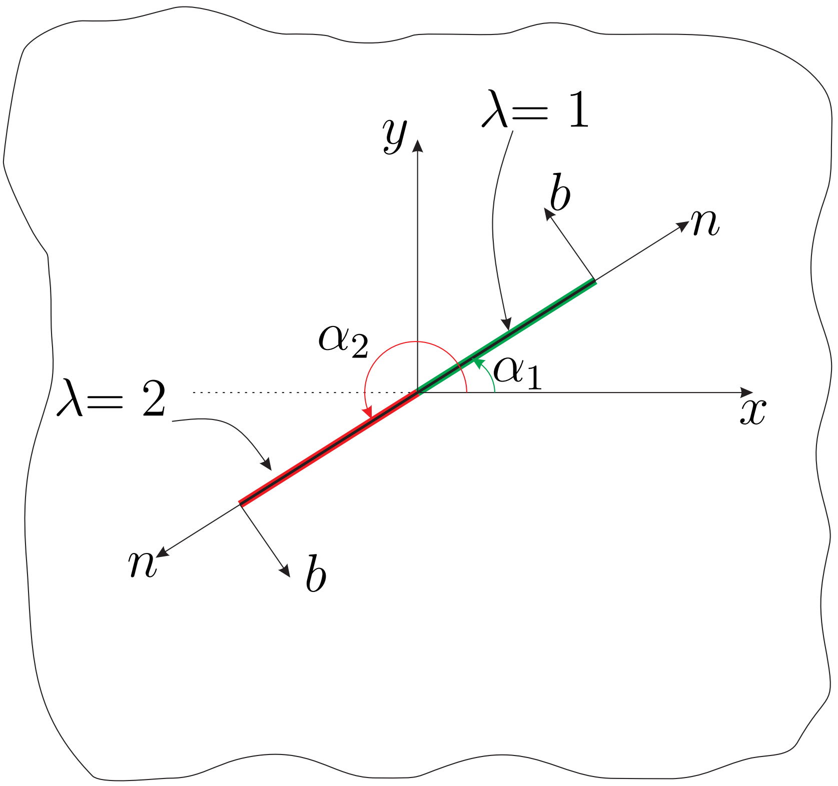

Figure 5.1: Crack local coordinates and elements related to each crack tip

(4.81). The resultant equation can be expressed in discretised form as,

$$C_{ij}(x')u_j(x') + C_{ij}(\hat{x})u_j(\hat{x}) + \sum_{\bar{n}=1}^{N_e}\sum_{\bar{a}=1}^{m} P_{ij}^{\bar{n}\bar{a}} u_j^{\bar{n}\bar{a}} + \sum_{\bar{n}=1}^{Ne} \tilde{P}_{iI}^{\bar{n}\lambda} \tilde{K}_I^{\lambda} + \sum_{\bar{n}=1}^{N_e} \tilde{P}_{iII}^{\bar{n}\lambda} \tilde{K}_{II}^{\lambda} = \sum_{\bar{n}=1}^{N_e}\sum_{\bar{a}=1}^{m} Q_{ij}^{\bar{n}\bar{a}} t_j^{\bar{n}\bar{a}} \tag{5.9}$$

where N_e and m are the total number of elements and number of nodes per element, respectively. The free terms C_{ij} emerge from the strongly singular integral of the traction kernel. x and x' denote the usual field and source point in boundary element methods, and $\hat{x}$ is the point coincident with the source, but lying on the opposing crack surface. It is important to note that the second jump term is zero for cases when collocating on the exterior boundary, as there is no coincident point with x'. The values for $P_{ij}^{\bar{n}\bar{a}}$ and $Q_{ij}^{\bar{n}\bar{a}}$ are given by Eqns. (4.50a) and (4.50b) respectively, and the new terms $\tilde{P}_{jI}^{\bar{n}\lambda}$ and $\tilde{P}_{jII}^{\bar{n}\lambda}$ are defined as,

$$\tilde{P}_{iI}^{\bar{n}\lambda} = \int_{-1}^{1} [T_{ij}(x', x(\xi))][R_{jq}(\alpha)]\{\psi_{In}^{\lambda}(\xi) \;\; \psi_{Ib}^{\lambda}(\xi)\}^T J^{\bar{n}}(\xi) d\xi \tag{5.10a}$$

$$\tilde{P}_{iII}^{\bar{n}\lambda} = \int_{-1}^{1} [T_{ij}(x', x(\xi))][R_{jq}(\alpha)]\{\psi_{IIn}^{\lambda}(\xi) \;\; \psi_{IIb}^{\lambda}(\xi)\}^T J^{\bar{n}}(\xi) d\xi \tag{5.10b}$$

where $\xi \in (-1, 1)$ is the local parametric coordinate used to describe the element, $J^n(\xi)$ is the Jacobian for the coordinate transformation, and T_{ij} represents the traction fundamental solutions. Enrichment is only applied to elements on the crack surfaces, and in the vicinity of the crack tips; therefore, for most elements displacement is expressed in the usual shape function form. If element $\bar{n}$ is unenriched, then $\tilde{P}_{jI}^{\bar{n}\lambda} = 0$ and $\tilde{P}_{jII}^{\bar{n}\lambda} = 0$. In addition, as $\theta = \pm\pi$ at the crack surfaces for a flat crack, ψ_{Iq}^{λ} and ψ_{IIq}^{λ} are only functions of r. It should be noted that the free terms that emerge from the limiting procedure have not been affected by the enrichment, since the terms related to enriched integrals are cancelled out during implementation.

The substitution of enriched displacement into the traction boundary integral equation as given by (4.82); means the resultant equation can be written in a discretised form as,

$$\begin{aligned} n_i(x') \sum_{\bar{n}=1}^{N_e} \sum_{\bar{a}=1}^{m} E_{kij}^{\bar{n}\bar{a}} u_k^{\bar{n}\bar{a}} + n_i(x') \sum_{\bar{n}=1}^{N_e} \tilde{E}_{Iij}^{\bar{n}\lambda} \tilde{K}_I^{\lambda} \\ + n_i(x') \sum_{\bar{n}=1}^{N_e} \tilde{E}_{IIij}^{\bar{n}\lambda} \tilde{K}_{II}^{\lambda} = n_i(x') \sum_{\bar{n}=1}^{N_e} \sum_{\bar{a}=1}^{m} F_{kij}^{\bar{n}\bar{a}} t_k^{\bar{n}\bar{a}} \end{aligned} \tag{5.11}$$

In this work we consider traction-free cracks, so that $t_j(x')$ and $t_j(\hat{x})$ in (4.82) vanish. This means they can then be dropped in the description of the enriched form. The regular terms $E_{kij}^{\bar{n}\bar{a}}$ and $F_{kij}^{\bar{n}\bar{a}}$ are given by

$$E_{kij}^{\bar{n}\bar{a}} = \int_{-1}^{1} N^{\bar{a}}(\xi) S_{kij}(x', x(\xi)) J^{\bar{n}}(\xi) d\xi \tag{5.12a}$$

$$F_{kij}^{\bar{n}\bar{a}} = \int_{-1}^{1} N^{\bar{a}}(\xi) D_{kij}(x', x(\xi)) J^{\bar{n}}(\xi) d\xi \tag{5.12b}$$

where S_{kij} and D_{kij} denote the derivative of the fundamental solution for traction and displacement and are given by Eqns. (4.41) and (4.40). In cases when the element $\bar{n}$ is unenriched, then $\tilde{E}^{\bar{n}\lambda}_{Iij} = 0$ and $\tilde{E}^{\bar{n}\lambda}_{IIij} = 0$, or otherwise are given by

$$\tilde{E}^{\bar{n}\lambda}_{Iij} = \int_{-1}^{1} [S_{kij}(x', x(\xi))][R_{jq}(\alpha)]\{\psi^{\lambda}_{In}(\xi) \;\; \psi^{\lambda}_{Ib}(\xi)\}^T J^{\bar{n}}(\xi) d\xi \tag{5.13a}$$

$$\tilde{E}^{\bar{n}\lambda}_{IIij} = \int_{-1}^{1} [S_{kij}(x', x(\xi))][R_{jq}(\alpha)]\{\psi^{\lambda}_{IIn}(\xi) \;\; \psi^{\lambda}_{IIb}(\xi)\}^T J^{\bar{n}}(\xi) d\xi \tag{5.13b}$$

It is clear after introducing the enrichment equations (5.9) and (5.11) that new degrees of freedom arise. The main advantage of formulating the enrichment, as stated above, is that the number of extra degrees of freedom is limited to two per crack tip. Thus, increasing the number of enriched elements does not affect the size of the system. In order to achieve a square system of equations, an additional collocation point can be used, and this makes it possible obtain $\tilde{K}^{\lambda}_{I}$ and $\tilde{K}^{\lambda}_{II}$ as part of the solution vector. However, as will be shown in the numerical examples, the additional collocation point does not yield accurate SIFs directly in situations when the crack tip has non-zero displacement.

5.2.3 Crack Tip Tying Constraint

DBEM involves a hypersingular integral equation which imposes requirements on the continuity of displacement derivatives at the collocation point. Continuity cannot normally be achieved because of the C^0 continuity of shape functions at nodes shared by adjacent elements. Therefore, most DBEM implementations utilise discontinuous elements. In this type of element, the nodes are located within the body of the element as shown in Fig. 5.2. As a result of discontinuous element is that a displacement discontinuity is frequently observed at the crack tip. While this does not preclude attainment of accurate SIFs, it does provide an opportunity to design a simple set of auxiliary equations while at the same time enforcing a displacement continuity as observed in the physical problem being modelled.

Crack tip displacement can be approximated by extrapolating over the adjacent elements on the upper and lower crack surfaces. This allows for the use of a new tying constraint that (i) provides a very simple form for the additional equations required to

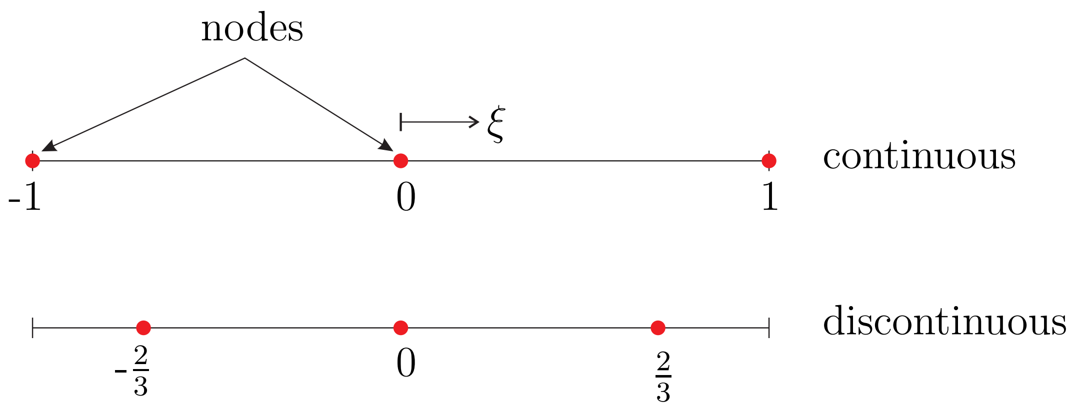

Figure 5.2: Two-dimensional continuous and discontinuous element

accommodate the extra enrichment degrees of freedom, (ii) allows the enrichment amplitudes $\tilde{K}_I^\lambda$ and $\tilde{K}_{II}^\lambda$ to approximate closely the stress intensity factors K_I and K_{II}, and thereby (iii) removes the need for J-integral computations. This can be achieved by the simple method of constraining against a displacement discontinuity at the crack tip.

We define element A, as parameterised by local variable ξ_A, the element on the upper crack surface and touching the crack tip at $\xi_A = 1$, and further define element B, as parameterised by the local variable ξ_B, the element on the lower crack surface and touching the crack tip at $\xi_B = -1$. Applying the expression (5.6) to give the displacement at the crack tip which is denoted as point y, and equating the values from the elements A and B, yields,

$$\begin{aligned} &\{N^a(1)\}^T\{u_{Aj}^{a\lambda}\} + \tilde{K}_I^\lambda[R_{jq}(\alpha)]\{\psi_{In}^\lambda(y)\ \psi_{Ib}^\lambda(y)\}^T + \tilde{K}_{II}^\lambda[R_{jq}(\alpha)]\{\psi_{IIn}^\lambda(y)\ \psi_{IIb}^\lambda(y)\}^T \\ = &\{N^b(-1)\}^T\{u_{Bj}^{b\lambda}\} + \tilde{K}_I^\lambda[R_{jq}(\alpha)]\{\psi_{In}^\lambda(y)\ \psi_{Ib}^\lambda(y)\}^T + \tilde{K}_{II}^\lambda[R_{jq}(\alpha)]\{\psi_{IIn}^\lambda(y)\ \psi_{IIb}^\lambda(y)\}^T \end{aligned} \tag{5.14}$$

where $N_A^a(\xi_A)$ and $N_B^b(\xi_B)$ denote the shape functions for nodes a and b of elements A and B respectively. Terms u_{Aj}^a, u_{Bj}^b present the coefficients multiplying the respective shape functions for these nodes (these are not nodal displacements, which they would be in conventional BEM, but are no longer because of the injection of the enrichment functions). It should be noted that, the enrichment terms cancel at the crack tip since

$r = 0$. Therefore, constraint Eqn. (5.14) can be simplified and rearranged as,

$$\{N^a(1)\}^T\{u_{Aj}^{a\lambda}\} - \{N^b(-1)\}^T\{u_{Bj}^{b\lambda}\} = 0 \tag{5.15}$$

The use of constraint Eqn. (5.15) for displacements in both directions x and y, provides two additional equations for each crack tip. These equations are appended to the BEM system formed by collocation at the nodes, creating a square system. Solving the system for unknowns allows $\tilde{K}_I^\lambda$ and $\tilde{K}_{II}^\lambda$ to be revealed in the solution column with high accuracy.

5.3 Implementation

Implementation of TBIE and DBIE requires much care when evaluating the hypersingular and strongly singular integrals. It should be noted that the use of enrichment functions does not change the order of the singularity. Meanwhile, the use of TBIE imposes certain conditions on the selection of the elements used for the discretisation of crack surfaces. These conditions require the tangential derivative of the solution to be continuous because the existence of Cauchy and Hadamard principal value integrals. It is routine to overcome this problem while still using collocation, by using discontinuous elements, in which the nodes are located within the body of the element, and not at its ends. Collocation on these nodes satisfies the Holder continuity requirements for the hypersingular integral equation, since the shape functions are continuously differentiable at these points.

5.3.1 Evaluation of singular integrals

A semi-analytical technique outlined in Sec. 4.3.4.1 and introduced by [144] to subtract singularity is used here, since it allows straightforward evaluation of enriched terms. Now, we recall Eqn. (4.104) which was implemented to evaluate hypersingular and strongly singular integrals. The expression can be seen to depend on the determination of the nonsingular functions F_{-1} and F_{-2} which evaluated at the source point. These functions can be obtained by utilising Taylor series expansions around the source point ξ'. Consider applying this technique to the enriched hypersingular integral as given by Eqns. (5.13a), this can yield,

$$\begin{aligned}
F(\xi',\xi) &= S_{kij}(x',x(\xi))R_{jq}(\alpha)\psi^{\lambda}_{Iq}(\xi)J^{\bar{n}}(\xi) && \text{(5.16a)}\\
F_{-2}(\xi') &= C_k C_{r2}(\xi')F_0(\xi')R_{jq}(\alpha)\psi^{\lambda}_{Iq0}(\xi') && \text{(5.16b)}\\
F_{-1}(\xi') &= C_k\left\{C_{r2}(\xi')\left[F_0(\xi')R_{jq}(\alpha)\psi^{\lambda}_{Iq1}(\xi')+F_1(\xi')R_{jq}(\alpha)\psi^{\lambda}_{Iq0}(\xi')\right]\right. \\
&+ \left. C_{r1}(\xi')F_0(\xi')R_{jq}(\alpha)\psi^{\lambda}_{Iq0}(\xi')\right\} && \text{(5.16c)}
\end{aligned}$$

where C_k is a constant related to the kernel being integrated, and $C_{r1}(\xi')$, $C_{r2}(\xi')$, $F_0(\xi')$ and $F_1(\xi')$ are obtained from the first and the second terms of the Taylor expansion for $S_{kij}(x',x(\xi))J^{\bar{n}}(\xi)$. In addition, $\psi^{\lambda}_{Iq0}(\xi')$ and $\psi^{\lambda}_{Iq1}(\xi')$ are the first and the second terms of the Taylor expansion of $\psi^{\lambda}_{Iq}(\xi)$. Precisely the same procedures can be used to evaluate the mode II enriched integral given by (5.13a). It should be noted that, the rotation matrix $R_{jq}(\alpha)$ is treated as a constant within the integral since it is not a function of ξ. In the case of an unenriched hypersingular integral given by (5.12a), the procedures are similar, and the integral can be evaluated as,

$$\begin{aligned}
F(\xi',\xi) &= S_{kij}(x',x(\xi))N^{\bar{a}}(\xi)J^{\bar{n}} && \text{(5.17a)}\\
F_{-2}(\xi') &= C_k C_{r2}(\xi')F_0(\xi')N^{\bar{a}}_0(\xi') && \text{(5.17b)}\\
F_{-1}(\xi') &= C_k\left\{C_{r2}(\xi')\left[N^{\bar{a}}_1(\xi')F_0(\xi')+N^{\bar{a}}_0(\xi')F_1(\xi')\right]\right.\\
&+ \left. C_{r1}(\xi')N^{\bar{a}}_0(\xi')F_0(\xi')\right\} && \text{(5.17c)}
\end{aligned}$$

where $N^{\bar{a}}_0(\xi')$, $N^{\bar{a}}_1(\xi')$ are respectively the first and the second terms of the Taylor expansion for the shape function $N^{\bar{a}}(\xi)$. A complete description when obtaining the terms that appear in (5.16) and (5.17) is given in Appendix B.2. Once these terms have been obtained, it is possible to evaluate all the integrals using Eqn. (4.104). Strongly singular integrals can be evaluated in a similar manner; however, because of the lower order of singularity the term $F_{-2}(\xi')$ equals zero.

5.3.2 Enrichment procedure

The proposed method provides no restriction on the number of enriched elements, allowing all elements on the crack surfaces to be enriched. In fact, using more elements for enrichment has been observed to improve accuracy, as will be seen in the results. However, the number of nodes used for the displacement constraint needs to be *ten* or fewer due to the highly oscillating nature of the Lagrangian polynomial near the edge of the interval [145]. This is known as Runge's phenomenon, and implies that an interpolation with a high order polynomial over equidistant points is ill-conditioned, which results in a small variation in the data being able to cause huge variations in the interpolant. This problem can be overcome by using non-equally spaced elements at the crack surface, as presented by [146].

5.3.3 Matrix assembly

The matrices $\boldsymbol{H}$ and $\boldsymbol{G}$ are constructed by collocating at each nodal point in turn, where the integration over each field element yields a 2×6 sub-matrix. In cases when the field element is enriched, an additional 2×2 sub-matrix is generated and collected in columns related to the crack tip. The use of DBEM in the current work implies that the displacement boundary integral equation is used on the outer boundary and on the upper crack surface, whereas the traction boundary integral equation is applied to determine the lower crack surface.

The effect of implementing the current approach on the system matrices is minimised. This can be demonstrated by the system matrices given by (4.65) where no change is made to the right hand side, since traction-free crack surfaces are considered. Whereas, on the left hand side, the additional columns holding the coefficients related to $\tilde{K}_I$ and $\tilde{K}_{II}$ are inserted in the last part of matrix $\boldsymbol{H}$. Moreover, auxiliary equations given by (5.15) are inserted in the last rows in $\boldsymbol{H}$, as shown by Fig. 5.3. It should be noted that each crack tip increases the size of matrix $\boldsymbol{H}$ and vector $\mathbf{u}$ by two; this should not affect the implementation, since it yields a square system.

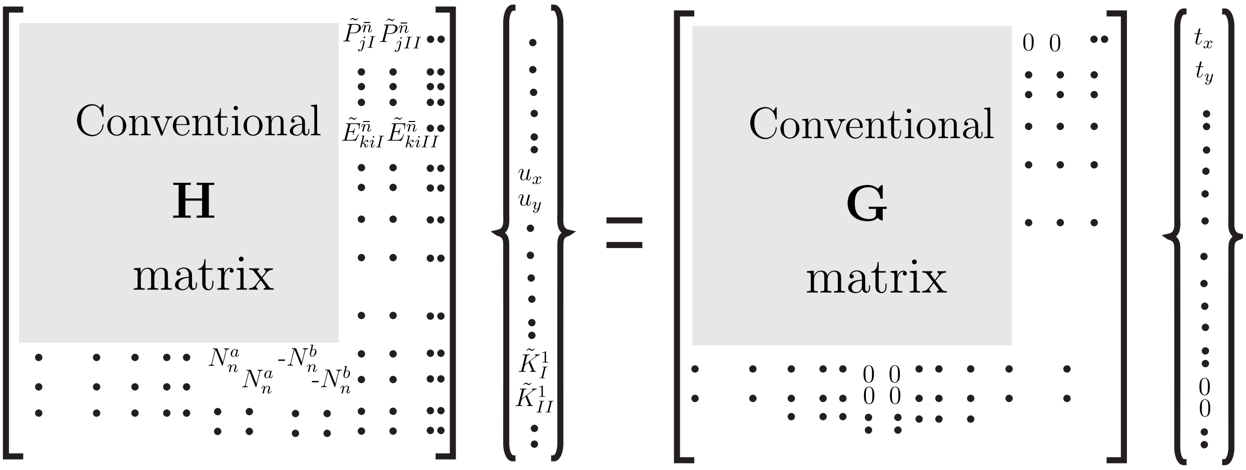

Figure 5.3: Assembly of the system matrices with enrichment terms

Efficient evaluation of the integrals can be obtained by calculating the kernel on one occasion, to be used with the shape functions. In the case of enriched elements the same calculated kernel is used with the enrichment functions. The coefficients of $\tilde{K}_I$ and $\tilde{K}_{II}$ are very small compared to the displacement coefficients in matrix $\boldsymbol{H}$, which affects the system's conditioning number. However, this can be overcome by scaling the affected columns [135].

A code written in MatLab is used to model two-dimensional crack problems in linear elastostatic. Apart from a function that used to generate the Gaussian points and weight [147], the code has not been copied nor translated from any existing codes. The code was tested by solving a problem with a well-known analytical solution of crack in an infinite domain [8]. Fig. 5.4 demonstrates the code constructor; it also shows the main loops and if statements that used within the body of the code. An adaptive method used to accelerate the code by calculating the ratio of r/l (see Sec. 4.3.1) to find the required number of integration points. The evaluation of integrals giving by $P_{ij}^{\bar{n}\bar{a}}$, $Q_{ij}^{\bar{n}\bar{a}}$, $\tilde{P}_{iI}^{\bar{n}\lambda}$, $\tilde{P}_{iII}^{\bar{n}\lambda}$ and $E_{kij}^{\bar{n}\bar{a}}$, $F_{kij}^{\bar{n}\bar{a}}$, $\tilde{E}_{Iij}^{\bar{n}\lambda}$, $\tilde{E}_{IIij}^{\bar{n}\lambda}$ for DBIE and TBIE, respectively, depends on the degree of singularity and can be achieved by appropriate method as illustrated in 5.3.1. The code consists of two loops; the first loop is performed over collocation points, whereas the nested loop is performed over field elements. In a final step, the displacement constraint entries are calculated and added to the appropriate rows in matrix $\boldsymbol{H}$. Using a direct solver, the generated square system of matrices can be solved for all unknowns including $\tilde{K}_I^\lambda$ and $\tilde{K}_{II}^\lambda$.

5.4 Numerical Examples

The implementation requirements for the enriched DBEM have been covered. Therefore, verification of the method, and an evaluation of the ability to yield accurate results is presented in this section. The effect of non-zero crack tip displacement is demonstrated through the presentation of two cases, which are carefully selected in pure mode I. Next, the effects of both the number of enriched elements and the number of nodes used for displacement constraints are presented. The ability to treat various types of crack mode and applied conditions using this method is illustrated through examples, including pure mode II, bending and mixed mode.

5.4.1 Mode I

Two pure mode I cases have been selected to show the effect of crack tip displacement. The first case (**case 1**) is a centre crack in an infinite homogeneous elastic flat plate as shown in Fig. 5.5. This has a well-known exact solution in which the crack tip displacement is zero. The XBEM model is formed from the actual crack surfaces along with a contour, Γ_{ext}, truncating the infinite domain. This contour is formed in such a way that the entire XBEM domain lies close to the crack tip, and so pure mode I applies. Traction-free crack surfaces are prescribed, and on Γ_{ext} calculated displacements using Williams expansions have been used as boundary conditions. The second case (**case 2**) considers an edge crack in a flat plate under uniaxial traction (pull-pull), as shown in Fig. 5.6. The reference solution [5] represented by a ratio of K_I/K_0 has been used as there is no exact solution available. The considered dimensions are $a = h = 0.5W$. Both cases are treated as plane stress.

Case 1 : Fig. 5.7 shows the displaced shape considering (a) the component of the displacement for the crack surface enriched elements associated with the second and the third term of Eqn.(5.6); (b) the component of the displacement represented by the shape

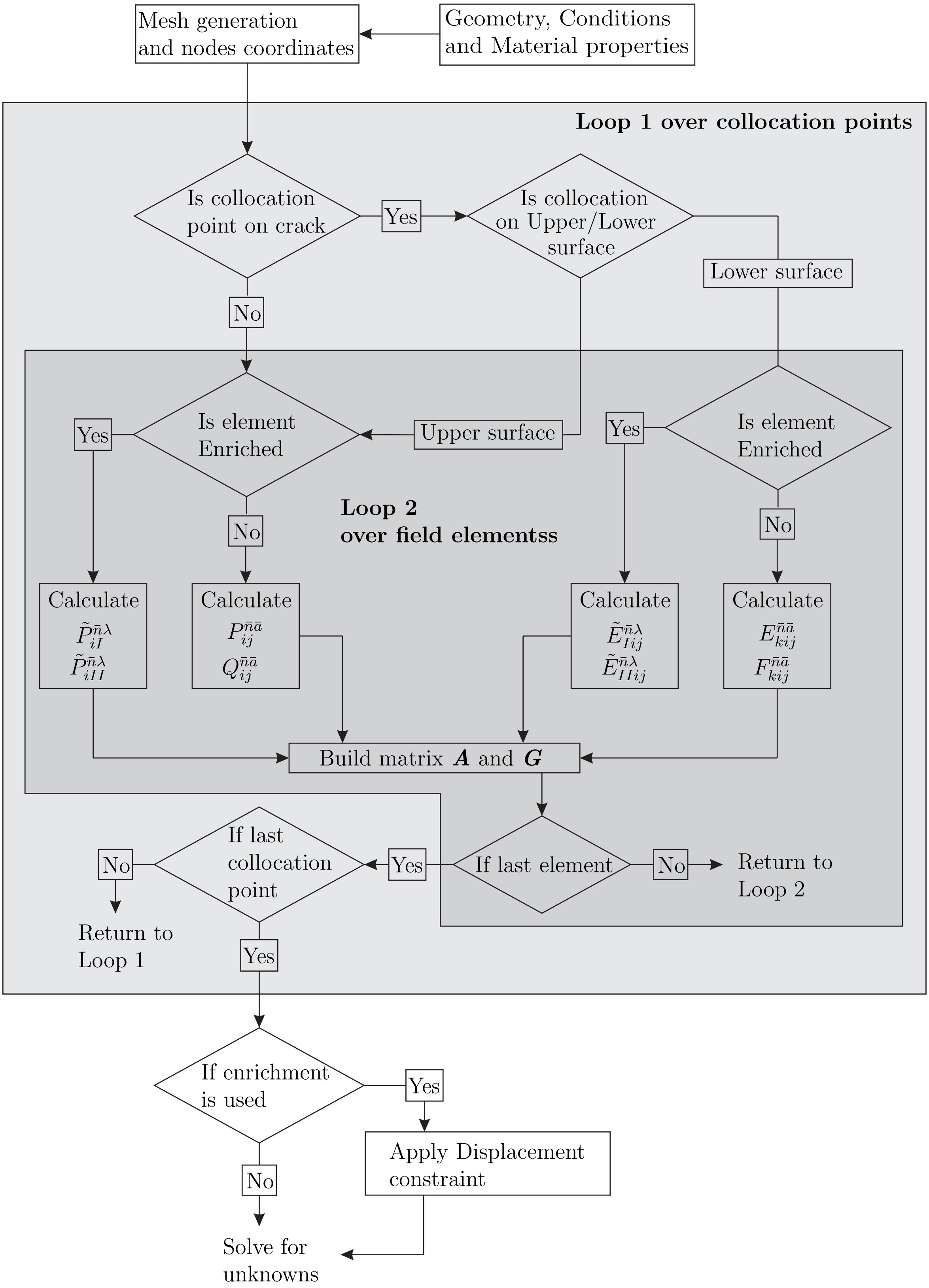

Figure 5.4: Flowchart of the implemented code for enriched DBEM

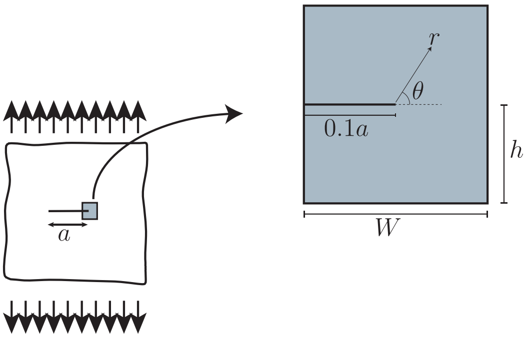

Figure 5.5: Infinite flat plate (case 1)

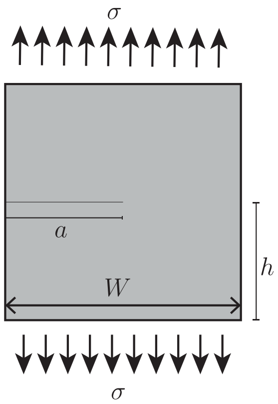

Figure 5.6: Square flate plate under axial tension (case 2)

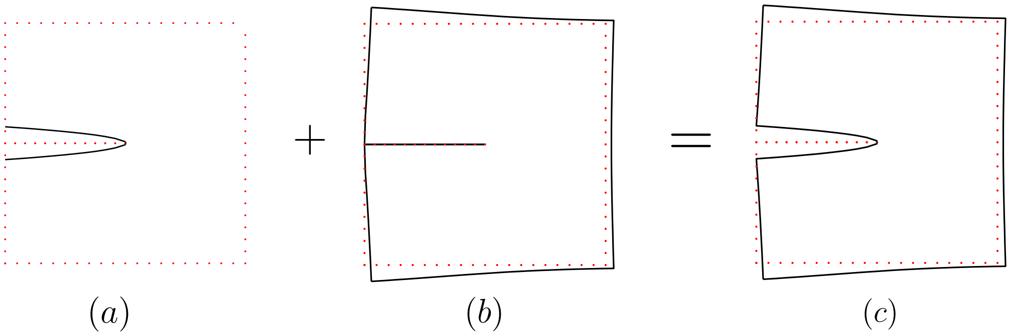

Figure 5.7: Displacment components for case 1

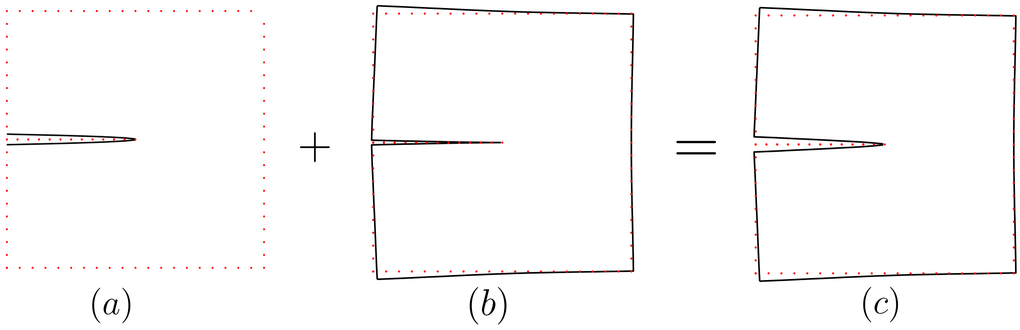

Figure 5.8: Displacment components for case 2

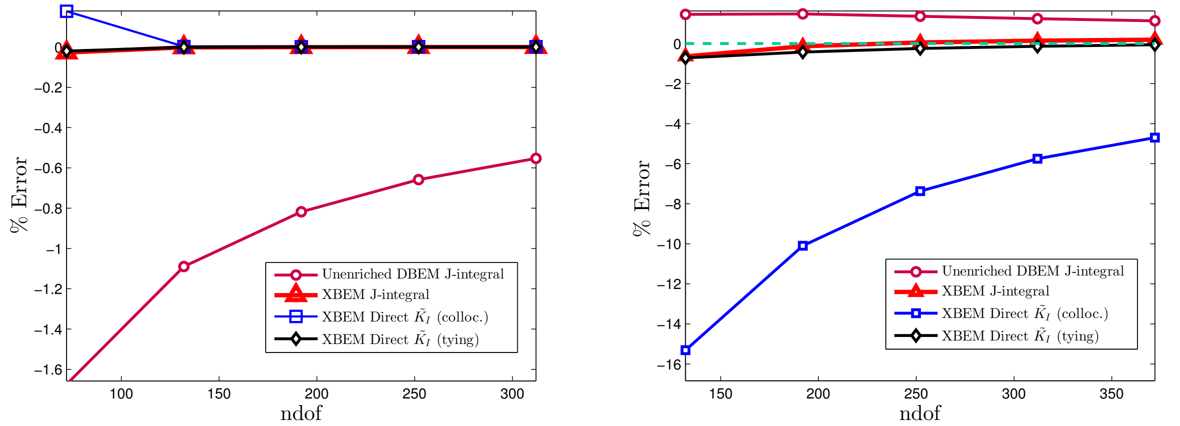

(a) Percentage error of K_I for *case 1*

(b) Percentage error of K_I with respect to [5] for *case 2*

Figure 5.9: Results of K_I for Mode I using various methods

function expansion in the first term of Eqn. (5.6), and (c) the total displacement considering all three terms of (5.6). In this special case the enrichment functions $\psi^{\lambda}_{Iq}, \psi^{\lambda}_{IIb}$ can capture the displacement field over the crack surfaces. Consequently, there is no contribution from the shape functions. In Fig. 5.9a we display the percentage errors in SIF K_I using (i) conventional, unenriched DBEM with the J-integral, (ii) enriched XBEM with the J-integral, (iii) direct $\tilde{K}_I$ from enriched XBEM using extra collocation points to provide the additional integral equations required, and (iv) direct $\tilde{K}_I$ from enriched XBEM using Eqn. (5.15) to enforce the displacement continuity at the crack tip. It is seen that all the enriched methods produce highly accurate SIF results in comparison with the conventional (piecewise polynomial) BEM J-integral solutions. Because the enrichment is ideal, results can be achieved with very small numbers of degrees of freedom. In order to compare the accuracy of the different methods, we focus on the set of results at 312 and 314 degrees of freedom from Fig. 5.9a. Table 5.1 shows the error compared to exact K_I, which can be calculated as $17.7245 MPa\sqrt{m}$. In addition, the complete results that used to calculate the error and to plot Fig. 5.9a are shown in Appendix D.1.

Case 2 : Fig. 5.8 presents the displaced shape for the second case. Fig. 5.8a shows the displacement component represented by the second and the third terms of Eqn.(5.6), Fig. 5.8b shows the displacement contribution by the shape function terms in (5.6), and

Table 5.1: Errors comparison for case 1

Method	**ndof**	K_I $[Pa\sqrt{m}]$	**% Error**
Unenriched DBEM J-integral	312	17626523.75	-0.55299
XBEM J-integral	314	17724524.44	-0.00008
XBEM Direct $\tilde{K}_I$ (colloc.)	314	17724790.96	0.00142
XBEM Direct $\tilde{K}_I$ (Tying)	314	17724564.26	0.000145

Table 5.2: Case 2 results compared to [5]

Method	**ndof**	K_I $[Pa\sqrt{m}]$	**% Error**
Unenriched DBEM J-integral	372	53775818.85	1.1333
XBEM J-integral	374	53299223.93	0.2333
XBEM Direct $\tilde{K}_I$ (colloc.)	374	50677080.10	-4.7000
XBEM Direct $\tilde{K}_I$ (Tying)	374	53142056.71	-0.0667

Fig. 5.8c shows the total displacement considering all three terms of (5.6). Evidence shows that the enrichment functions no longer provide a complete basis for the crack displacement, and that the shape functions are required to compensate, so that the total displacement is approximated accurately. Fig. 5.9b shows convergence of the various methods tested (note that the reference solution is approximate). In Table 5.2 we present the numerical values of K_I/K_o, for the models with 372 and 374 degrees of freedom (the results used to calculate the error and to plot Fig. 5.9b can be found in Appendix D.1). The XBEM with J-integral and the direct method using the tying constraint are both capable of delivering results very close to the reference solution.

By comparing the directly computed $\tilde{K}_I$ from enriched XBEM using extra collocation points for **case 1** and **2** the effect of the displacement discontinuity at the crack tip becomes apparent. It is immediately evident that the use of XBEM enrichment (5.6) without the use of the constraint (5.15) causes a significant deterioration in the ability of $\tilde{K}_I$ to approximate K_I directly; thus, in this case a J-integral is necessary. The injection of the tying constraint, forcing displacement continuity at the crack tip, permits the directly calculated $\tilde{K}_I$ to approximate K_I. Highly accurate results have been achieved showing better accuracy when compared to conventional J-integral BEM approaches.

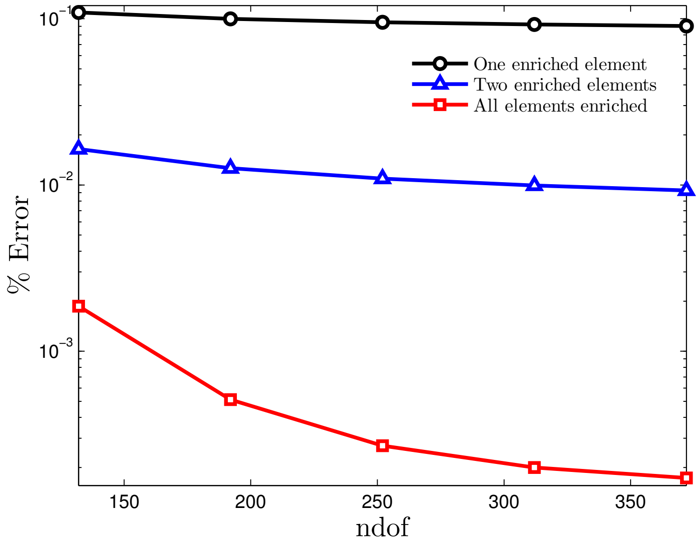

Figure 5.10: Effect of the number of enriched elements (case 1)

5.4.1.1 Number of enriched elements

A useful feature of the new enrichment presented here is that the enrichment functions are not associated with nodal degrees of freedom, as in the Partition of Unity Method. Instead, since the new degrees of freedom $\tilde{K}_I, \tilde{K}_{II}$ are associated with the crack tip, this enrichment technique provides the freedom to increase the number of enriched elements without increasing the DOFs. The enrichment degrees of freedom are limited to two per crack tip. By the term *enriched element* we describe an element (on a crack surface) over which the displacement is approximated by Eqn. (5.6). The number of enriched elements has a significant effect on the results, both when the J-integral is used to determine SIFs and when the directly calculated $\tilde{K}_I, \tilde{K}_{II}$ are used. For example, Fig. 5.10 shows a reduction in error for **case 1** when all crack surface elements are enriched. For this reason, all the results are presented for models in which all the elements on the crack surfaces are enriched. It should be noted that, increasing the number of enriched elements will increase the computational time, since an additional calculation is needed for each enriched element. However, the added computational time is negligible and can be balanced with the required accuracy to achieve the optimum number of enriched elements.

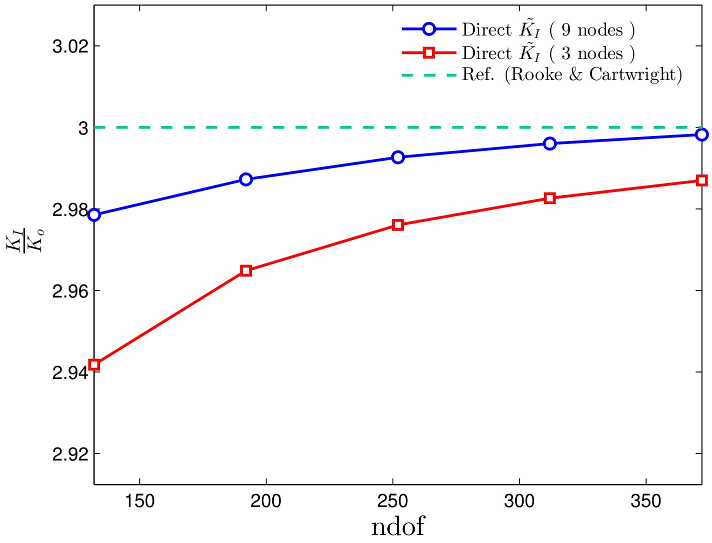

Figure 5.11: Effect of order of displacement extrapolation (case 2)

5.4.1.2 Order of extrapolation for tying constraint

The tying constraint enforces the continuity of displacement at the crack tip, expressed through the equality of the displacements at this point as found by extrapolation of displacements over the upper and lower crack surfaces. The constraint is presented in Eqn. (5.15) by basing the extrapolation on the M nodes of each element touching the crack tip. We use three-noded, quadratic discontinuous elements (i.e. $M = 3$). However, it is possible to use a higher order Lagrangian extrapolation considering nodes on more elements.

This technique has been found to deliver improved accuracy. Fig. 5.11 shows a comparison made (for the problem in **case 2**) of the convergence of SIF results obtained from different orders of extrapolation. It compares results using 3 nodes to extrapolate displacement to those when 9 nodes are used. These are the nearest nine nodes to the crack tip on each crack surface. An improvement can be seen resulting from increasing the order used for extrapolation of the displacement results to the crack tip. It is tempting to suggest using even higher order Lagrangian polynomials; however, this could increase the error due to Rung's phenomenon. Since this difficulty emerges when the distance between nodes is equal [146]; therefore, it can be overcome by employing unequal element size on the crack surface. Consequently, the needs for using certain element size can impose restrictions on the type of implemented mesh which needs to balance with the required accuracy.

5.4.2 Various crack lengths

This example illustrates the accuracy of the direct method when considering various crack lengths. Fig. 5.6 shows the problem configuration, where the ratio of crack length to plate width varies from 0.1 to 0.6. The results have been presented graphically in this example, in contrast with the results provided by [5]. Fig. 5.12 demonstrates the normalised mode I stress intensity factor for the varying crack length. There is excellent agreement between the direct $\tilde{K}_I$ and J-integral with XBEM, as seen where conventional J-integral accuracy lessens as crack length increases. It should be noted that the greatest accuracy afforded by the reference solution is 1%.

The advantage of implementing BEM when modelling varying crack length is the reuse of pre-calculated terms that associated with unchanged nodes. In presented example, the terms related to the nodes on the outer boundaries have been used without change. Whereas, the nodes on the crack surfaces have been re-evaluated after increasing the crack length. This can save valuable computational time when handling a huge number of cracks. In addition, it allows growing cracks with very small steps. Finally, coupling of BEM with the proposed direct evaluation of SIFs can permit the assessment of crack problems in terms of size and accuracy.

5.4.3 Pure Mode II

We also consider a square domain surrounding the tip of a crack in pure mode II. The problem is shown in Fig. 5.13. The dimensions used in the analysis are $h = 0.1a = 0.5W$. We prescribe boundary conditions as follows: The elements on the two crack faces are traction-free, and we apply a displacement boundary condition equal to the pure mode II to the elements on all other parts of the square boundary of the domain. We use the algorithm described for enrichment to determine K_{II}, the exact solution for which

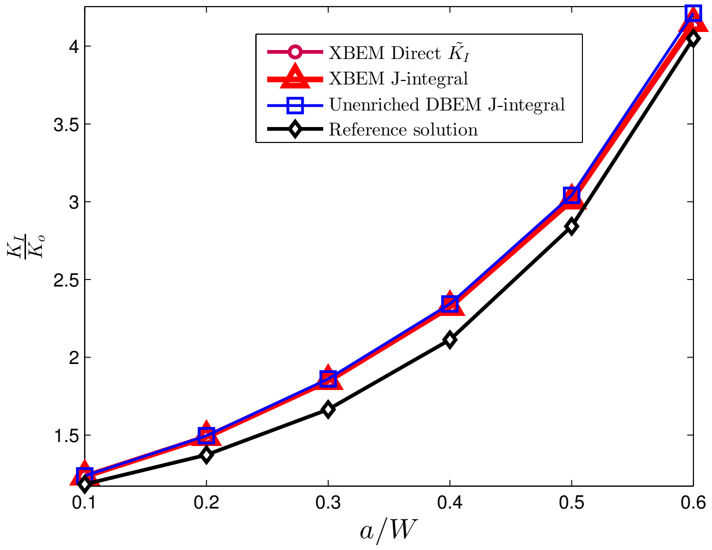

Figure 5.12: Various edge crack length under uniaxial stress

is $K_{II} = \sigma\sqrt{\pi a}$, and compare the errors for the term $\tilde{K}_{II}$ against those from both a conventional BEM solution and an enriched XBEM solution (both using the J-integral). This comparison is shown in Fig. 5.14, and shows both enriched methods to provide highly accurate solutions in comparison with the more slowly converging results of the classical DBEM. As in the mode I (**case 1**) consideration, the enrichment is ideal here leading to very small errors. To clarify further, the exact behaviour is included in the approximation space through (in the mode II case) the third term on the right hand side of Eqn. (5.6). The role of the first term in (5.6) can be viewed as the use of piecewise polynomials to capture the difference between pure mode I and II and the displacements in the case under analysis. The following sections consider cases in which the enrichment is not ideal, i.e. we are not considering pure mode I and II.

Fig. 5.15 shows the deformed shape of the square plate under pure mode II load. The accuracy of the enrichment approach can be demonstrated by analysing displacements obtained at the upper and lower crack faces. Moreover, the displacement for pure mode II is in x-direction whereas there is zero displacement in the y-direction. In this case, the conventional polynomial can be used to capture the displacement on the crack faces, since displacement exhibit linear behaviour. However, singularity emerges in the vicinity of the

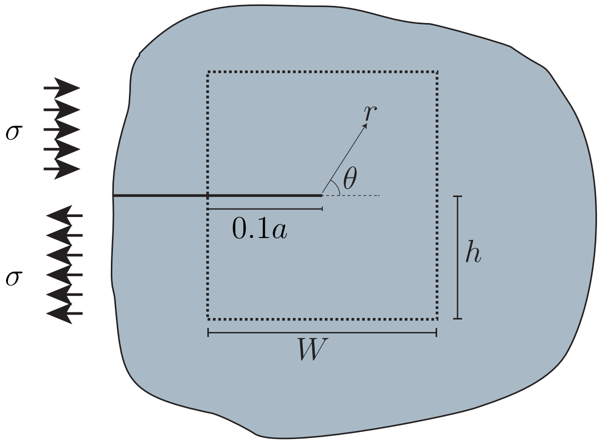

Figure 5.13: A square section sheet subject to shear

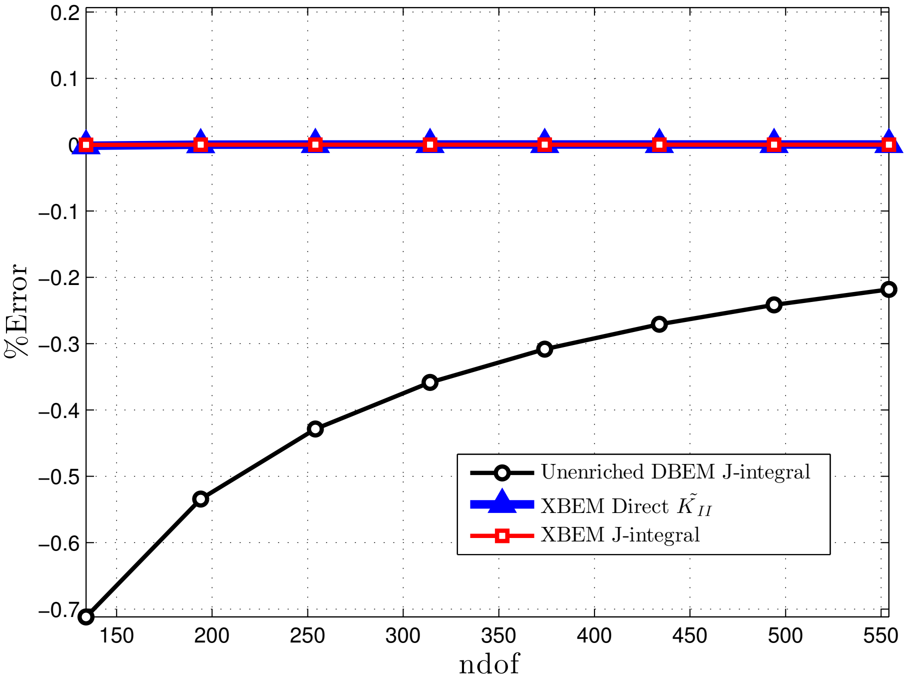

Figure 5.14: Results for pure Mode II

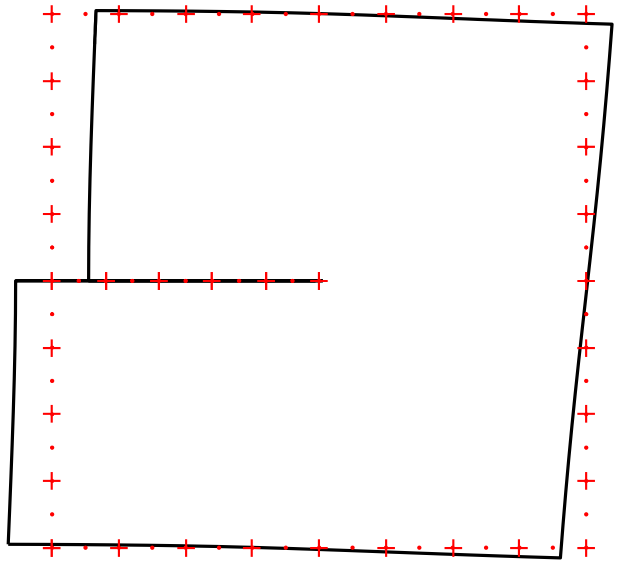

Figure 5.15: The deformed shape of the square plate under pure mode II load

crack tip has an effect on the accuracy of obtained displacement. Therefore, the need for higher accuracy can lead to the implementation of fine mesh. The use of enrichment approach presented here is capable of capturing the displacement while implementing a coarse mesh. In addition, the approach can be utilised to determine SIFs directly without the need for a post-processing method.

5.4.4 Bending

A rectangular plate under bending is considered here, as shown in Fig. 5.16. The plate is subjected to a bending moment, as applied to the upper and lower surfaces, as shown in the figure, and we consider the case $b = 2a$. We compare the convergence of the two enriched formulations, and classical unenriched DBEM in terms of the normalised stress intensity factor K_I/K_o (where $K_o = 6M\sqrt{\pi a}/b^2$). The comparison is presented in Fig. 5.17, and shows smooth convergence toward the reference value from [5](we note the reference solution presented in [5] with an accuracy of 1%, which is rather large in comparison with the errors which have been found). It is important to note that, the XBEM with J-integral is outperforming XBEM with direct K's; which can offer high accuracy via the

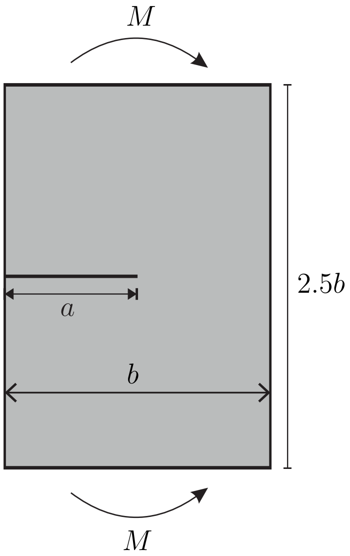

Figure 5.16: Rectangular plate under bending

J-integral or what might be seen as acceptable accuracy from the direct K's. However, the J-integral possibly adds a considerable computational overhead, especially in 3D.

The enrichment approach offers an accurate representation of the displacement at the crack face beside the direct evaluation of the SIFs. Fig. 5.18 shows the deformed shape of the rectangular plate under bending load. The captured displacements on the upper and lower crack faces can be used to demonstrate the accuracy of the proposed enrichment approach. Furthermore, without the utilisation of the enrichment, the conventional polynomial is incapable of capturing the behaviour of the displacement near the crack tip since singularity emerges. The presented crack deformed faces show the $\sqrt{r}$ nature of the displacement. In addition, it can be seen that the use of enrichment reduces the effect of crack tip displacement.

5.4.5 Mixed mode

In this section we apply the proposed enrichment to a mixed mode case for an inclined edge crack in a finite plate under uniaxial tensile loads. For mixed mode cases it is customary to use a decomposition technique (see Sec. 3.2.1.1) when using the J-integral, in order to solve for both K_I and K_{II}. The plate contains an edge inclined crack at an angle described as β, as shown in Fig. 5.19. The problem does not have an exact

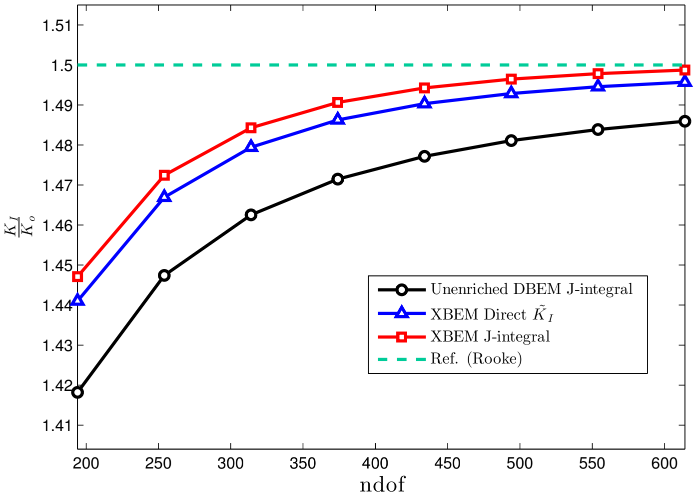

Figure 5.17: A comparison of normalised results for bending plate

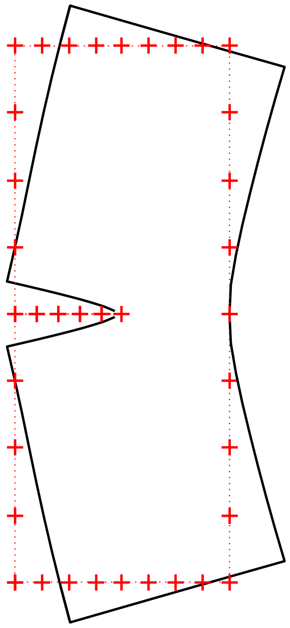

Figure 5.18: Deformation of rectangular plate under bending

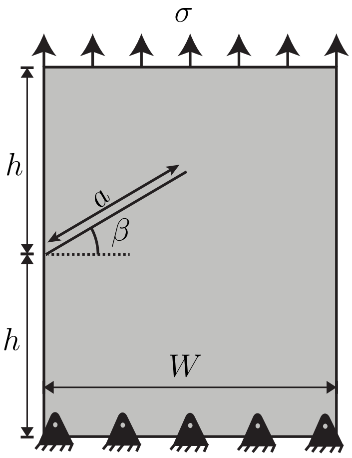

Figure 5.19: Rectangular plate subject to shear [3]

solution; instead, the numerical solution obtained by Xiao *et al.* [4] is used. The plate dimensions are $W = h = 1$, $a = 0.6$ and the angle of inclination β is 30°. We consider Young's modulus and Poisson's ratio as 10^5 and 0.25 respectively. Uniaxial tension $\sigma = 1$ is applied over the top edge of the plate, and zero displacements are prescribed in both directions at the lower edge.

Results for K_I are presented in Fig. 5.20 ; the direct approach, XBEM with the J-integral and DBEM with the J-integral are used to evaluate the SIFs at various model sizes. The reference solution is plotted as a horizontal line for comparison, and the reader is reminded that this is also a numerical approximation and included for the purposes of comparison. In the results it can be seen that the direct method converges smoothly toward the same value as the J-integral methods. It is important to check for any divergent behaviour since the obtained results are converging to a different value from the reference solution. Therefore, a higher number of degrees of freedom is implemented which shows SIFs obtained by direct approach and XBEM with the J-integral are converging to the same value.

Similarly, XBEM and DBEM both with the J-integral and the direct approach are utilised to determine K_{II}. The results for K_{II} are shown in Fig. 5.21, where a various model sizes are used. In addition, the reference solution is plotted as a horizontal line for comparison. The results reveal that the direct method converges smoothly toward the same value as the J-integral method. It is important to recheck the results since they

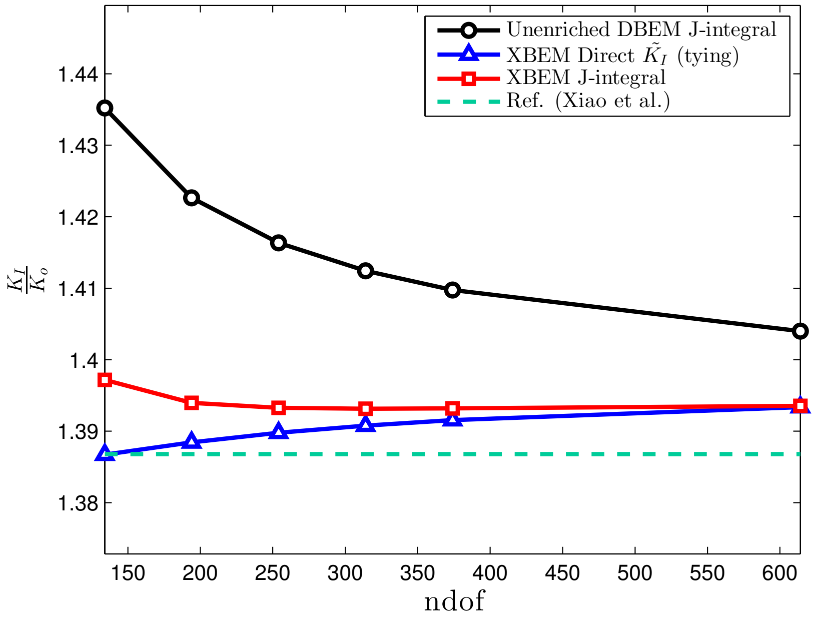

Figure 5.20: K_I for inclined crack results compared to Xiao et al. [4]

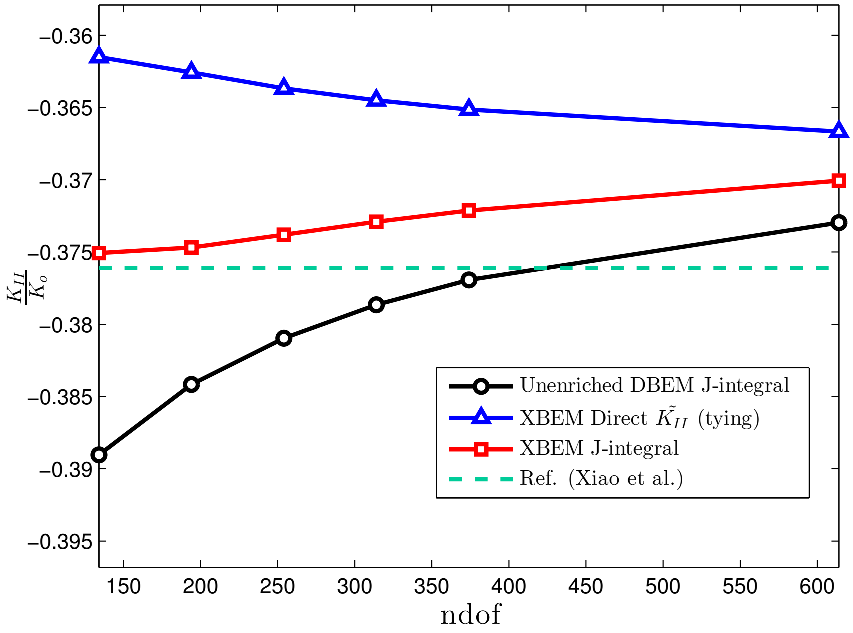

Figure 5.21: K_{II} for inclined crack results compared to Xiao et al. [4]

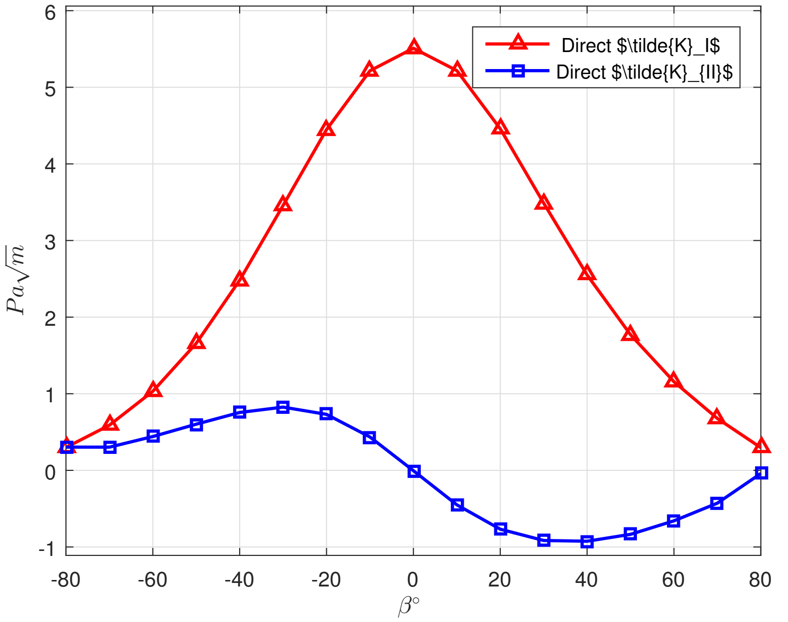

Figure 5.22: Variation of SIF values with respect to the inclination angles

are converging to a different value from the reference solution. Therefore, the number of elements for modelling the problem has been increased. Consequently, the extracted SIF values by the direct approach and XBEM with the J-integral can be noticed to converge to the same value.

5.4.6 Various inclination angles

An inclined edge crack similar to that presented in Fig. 5.19 is analysed to demonstrate the variation of SIF values with respect to the inclination angle. The inclined edge crack is considered in a finite plate under tensile load. The plate is fixed in both directions at the lower edge and stresses are applied to the upper edge in y-direction. The plate dimensions are $W = h = 1$, $a = 0.6$ and the angle of inclination β varies between $-80°$ and $80°$ by step of $10°$. The Young's modulus and the Poisson's ratio are considered as 10^5 and 0.25 respectively. The applied tension is $\sigma = 1$, whereas zero displacements are prescribed in x and y-direction at the lower edge.

Figure 5.22 represents the values of SIFs for mode I and II with respect to various inclination angles. These results are obtained directly by implementing the enrichment approach. The Figure reveals the symmetric behaviour of K_I, whereas the flip in sign can be observed in the case of K_{II}. Furthermore, the maximum value of K_I can be achieved in pure mode I when the crack is horizontal $\beta = 0$. The effect of near singular integrals emerges when the crack is very close to the boundaries at inclination angles of $-80°$ and $80°$. The advantage of using the proposed directly evaluated SIFs can be illustrated when handling cracks near the boundaries. Moreover, the direct evaluation can be utilised regardless how close the crack to the boundaries. Whereas, the use of the J-integral can impose restrictions on the selection of the ideal integration path for the J-integral. In addition, the implementation of DBEM allows the system matrices to be reused by updating the columns and rows associated with crack surface nodes that changed with the inclination angle.

5.5 Conclusion

Herein, a new extended dual boundary element method was presented, in which the enrichment functions are based closely on the stress intensity factors in two-dimensional Linear Elastic Fracture Mechanics. The approach utilises the Williams expansions for displacement to enrich the elements on the crack surfaces. The implementation of enrichment only adds two degrees of freedom per crack tip. The auxiliary equations required, are therefore derived from the enforcement of displacement continuity at the crack tip. The effect of applying enrichment to the system matrices is reduced by inserting additional columns holding the coefficients related to $\tilde{K}_I$ and $\tilde{K}_{II}$ into the last part of matrix $\boldsymbol{H}$. Since crack surfaces are considered traction-free, no enrichment needs to be applied to the terms related to tractions. The implementation of enrichment increases the system's conditioning number which can be then overcome by the use of appropriate scaling factor. However, the use of enrichment has no effect on the degree of singularity. The Guiggiani method [134] is used to evaluate enriched terms. Moreover, the same approach can be used to determine conventional terms that contain strongly singular and hypersingular integrals.

The proposed method can be used to evaluate SIFs directly without any requirement for postprocessing calculations such as the J-integral. The results are improved by increasing the number of enriched elements, since this can be done without increasing the size of the system, and with negligible additional computational cost. In addition, accuracy can be improved further by using high order Lagrangian polynomials (8^{th}) when applying the crack tip tying constraint. This method has been used to model various types of problems, including pure mode I and II, bending, inclined crack and mixed mode. A comparison of two pure mode I problems is used here to illustrate the effect of non-zero crack tip displacement. Moreover, it can be observed that, the SIFs found from the direct method converge to the same values as those from the J-integral, and the method clearly outperforms the use of the piecewise polynomial DBEM. Hence the approach requires minimal changes to be implemented. The next chapter presents an extension of this method, to solve three-dimensional crack problems.

Chapter 6

Enrichment of the 3D Dual Boundary Element Method

6.1 Introduction

In three-dimensional problems, stresses in the vicinity of a crack tip need to be obtained with high accuracy to properly predict crack growth. Three-dimensional cracks can generally be classified into planar and nonplanar cracks. A crack is considered planar if it exists on one plane; however, in LEFM all crack types are subject to the physical singularity at the crack tip. This singularity results in mathematical difficulties affecting the direct use of numerical methods. Therefore, to provide an accurate evaluation of singular stresses many modified BEM and FEM have been submitted (see Sec. 3.1 for additional detail).

In terms of energy approaches, the Griffith theory was extended by [148] to three-dimensional cracks, by the inclusion of a crack in a large sphere and imposing the condition of equilibrium across a spherical surface. Also, the J-integral was applied to three-dimensional cracks, including a line and surface integral for a disk perpendicular to the crack plane and centred at the crack front, where it can be decomposed [129] to determine the value of SIFs for each mode, as illustrated in Sec. 3.2.1.2. However, since the evaluation of the surface integral requires calculation of the first derivative of stress, and the second derivative of displacement field, it is typically neglected. On the other hand, when utilising the symmetric Galerkin method a direct approach [104] is employed to obtain SIFs, although it is mathematically complex and not sufficiently flexible to be added to existing code. The XBEM in 2D, as introduced earlier, was able to evaluate stress intensity factors directly with high accuracy. The application of the same principle to three-dimensional cracks reduces the computational time since SIFs can be evaluated directly especially when considering crack growth.

This chapter extends the two-dimensional enriched boundary element formulation for the applications of linear elastic fracture mechanics to three-dimensional problems. The enrichment approach utilises Williams expansions to enrich the crack surface elements for an accurate and direct evaluation of SIFs. Hartranft and Sih [149] confirmed that the Williams expansions can be used for 3D problems directly if considering a disk perpendicular to the crack plane (see Sec. 2.8). However, they also showed that the application of the Taylor series to Williams expansions permits the evaluation of the off crack local plane stresses and displacements.

When demonstrating the 3D approach, a penny shaped planar crack is considered, and the Williams expansion for plane strain problems used for enrichment. Elements on the crack surfaces have been arranged in a radial pattern to provide nodal information over radial lines for the implementation of displacement continuity constraints. Similar to what was observed in the previous chapter, a complete outline of the formulation and the implementation are presented first. Next, numerical examples have been used to show the accuracy of the direct results in comparison to the J-integral, and illustrating the improvement of the J-integral when the XBEM is used.

6.2 Formulation

The enrichment strategy for three-dimensional cracks is similar to that presented for cracks in two-dimensions. However, attention needs to be directed toward the stress intensity factors, since they are now functions of the location along the crack front. The following sections, introduce the enriched form of displacement first, and then demonstrate the substitution of the enriched displacement into both DBIE and TBIE. In addition, the

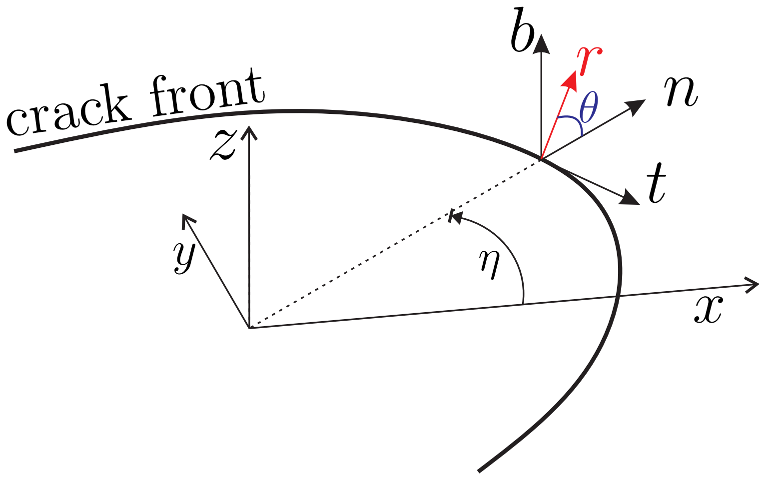

Figure 6.1: Crack local coordinates and global coordinates relationship

displacement constraints at the crack front, and the layout required for the crack surface elements to yield a square system, are described.

6.2.1 Enrichment of displacement

In three-dimensions a penny shaped crack is considered in the formulation of enrichment functions, in order to define a variable that express variation in SIFs along the crack front. Therefore, Williams expansion for near crack tip displacements [12, 13], can be written in terms of K_I, K_{II} and K_{III} as,

$$u_j(\eta) = K_I(\eta)\psi_{Ij}(r,\theta,\eta) + K_{II}(\eta)\psi_{IIj}(r,\theta,\eta) + K_{III}(\eta)\psi_{IIIj}(r,\theta,\eta) \tag{6.1}$$

where r and θ are the usual polar components in the $n-b$ plane as presented in Fig. 6.1, and η is the angle on the crack plane (given by $\eta = \tan^{-1}(y/x)$ in the case of horizontal crack) tracing the crack front, as shown in Fig. 6.1; and $\tilde{K}_I$, $\tilde{K}_{II}$, $\tilde{K}_{III}$ express continuous variation in SIFs with η. Eqn. (6.1) is valid only in the small region around the crack tip where the singular term dominates. However, for remote regions from the crack tip a more general form of the displacement functions can be rewritten as,

$$\{u_j(\eta)\} \quad = \quad [\boldsymbol{u}_j^{\bar{a}}(x)]\{N^{\bar{a}}(\xi_1,\xi_2)\} + [R_{jq}][\boldsymbol{\psi}_{lq}(r,\theta,\eta)]\{\tilde{K}_I(\eta)\ \tilde{K}_{II}(\eta)\ \tilde{K}_{III}(\eta)\}^T \tag{6.2}$$

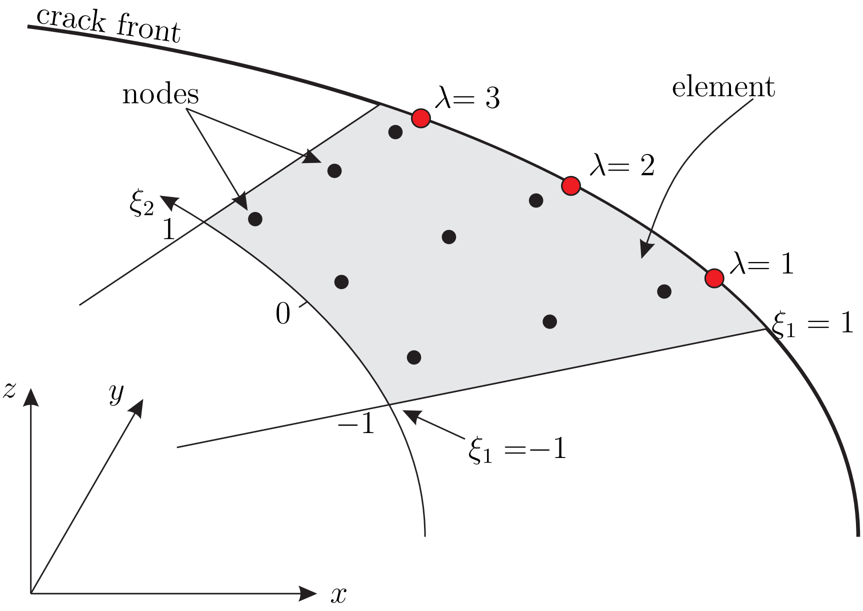

Figure 6.2: Discretisation of SIFs at the crack front

where $\boldsymbol{u}$ is the nodal displacements, N represents the shape functions and R is the required rotation matrix to transfer William expansion local displacements. Before we proceed further, it should be noted that there is a need to express the continuously varying SIFs in a discretised form to proceed with the analysis. Therefore, one dimensional shape functions are used to interpolate the values of $\tilde{K}_I$, $\tilde{K}_{II}$ and $\tilde{K}_{III}$ at points located at the intersection of the crack front, with the radial lines upon which the nodes lie as illustrated in Fig. 6.2. This can be achieved by

$$\tilde{K}_l(\eta) = N^f(\xi_2)\tilde{K}_l^\lambda \qquad \text{where} \quad l = I, II, III \tag{6.3}$$

where the discrete variables $\tilde{K}_l^\lambda$ lie in the solution vector and are found as part of the XBEM solution. The discretised enriched approximation for displacement over an element $\bar{n}$ on a crack surface can be written as,

$$\{u_j^\lambda\} \;=\; R_{jq}(\xi_2)\boldsymbol{\psi}_{lq}^\lambda(r,\theta)\{\tilde{K}_I^\lambda\ \tilde{K}_{II}^\lambda\ \tilde{K}_{III}^\lambda\}^T + \boldsymbol{u}_j^{\bar{n}\bar{a}}(x)\{N^{\bar{a}}(\xi_1,\xi_2)\} \tag{6.4}$$

where $\bar{a}$ denotes the node number and R_{jq} is a rotation that used to transfer displacements from the crack local coordinates (n, b, t) to global coordinates (x, y, z). The nodal displacement matrix $\boldsymbol{u}^{\bar{n}\bar{a}}$ is of size $3 \times m$, where m is the total number of nodes on element $\bar{n}$. The square matrix $\boldsymbol{\psi}^{\lambda}$ is given by

$$\boldsymbol{\psi}^{\lambda}_{lq}(r,\theta) = \begin{bmatrix} \psi^{\lambda}_{In} & \psi^{\lambda}_{IIn} & \psi^{\lambda}_{IIIn} \\ \psi^{\lambda}_{Ib} & \psi^{\lambda}_{IIb} & \psi^{\lambda}_{IIIb} \\ \psi^{\lambda}_{It} & \psi^{\lambda}_{IIt} & \psi^{\lambda}_{IIIt} \end{bmatrix} \tag{6.5}$$

Entries of the matrix $\boldsymbol{\psi}(r,\theta)$ describe the enrichment functions obtained from the first order terms of Williams displacement expansions, and are defined as,

$$\psi^{\lambda}_{In} = \frac{1}{2\mu}\sqrt{\frac{r}{2\pi}}\cos\frac{\theta}{2}\left[\kappa - 1 + 2\sin^2\frac{\theta}{2}\right] \tag{6.6a}$$

$$\psi^{\lambda}_{IIn} = \frac{1}{2\mu}\sqrt{\frac{r}{2\pi}}\sin\frac{\theta}{2}\left[\kappa + 1 + 2\cos^2\frac{\theta}{2}\right] \tag{6.6b}$$

$$\psi^{\lambda}_{Ib} = \frac{1}{2\mu}\sqrt{\frac{r}{2\pi}}\sin\frac{\theta}{2}\left[\kappa + 1 - 2\cos^2\frac{\theta}{2}\right] \tag{6.6c}$$

$$\psi^{\lambda}_{IIb} = \frac{-1}{2\mu}\sqrt{\frac{r}{2\pi}}\cos\frac{\theta}{2}\left[\kappa - 1 - 2\sin^2\frac{\theta}{2}\right] \tag{6.6d}$$

$$\psi^{\lambda}_{IIIt} = \frac{1}{2\mu}\sqrt{\frac{r}{2\pi}}\sin\frac{\theta}{2} \tag{6.6e}$$

$$\psi^{\lambda}_{IIIn} = \psi^{\lambda}_{IIIb} = \psi^{\lambda}_{It} = \psi^{\lambda}_{IIt} = 0 \tag{6.6f}$$

where μ is the shear modulus and κ is the Kosolov constant defined as $\kappa = 3 - 4\nu$ and $\kappa = (3-\nu)/(1+\nu)$ for plane strain and plane stress, respectively. It should be noted that, Eqn. (6.4) is general expression, and can be used to enriched any crack in three-dimensions. However, the variable describing the variation of SIFs along the crack front can differ. In the case of a flat edge crack, global coordinates can be used to present variations in SIFs, as shown in Fig. 6.3.

Enrichment of the crack surface elements is achieved by substituting enriched displacement into the displacement boundary integral equation and the traction boundary integral equation, as will be demonstrated shortly.

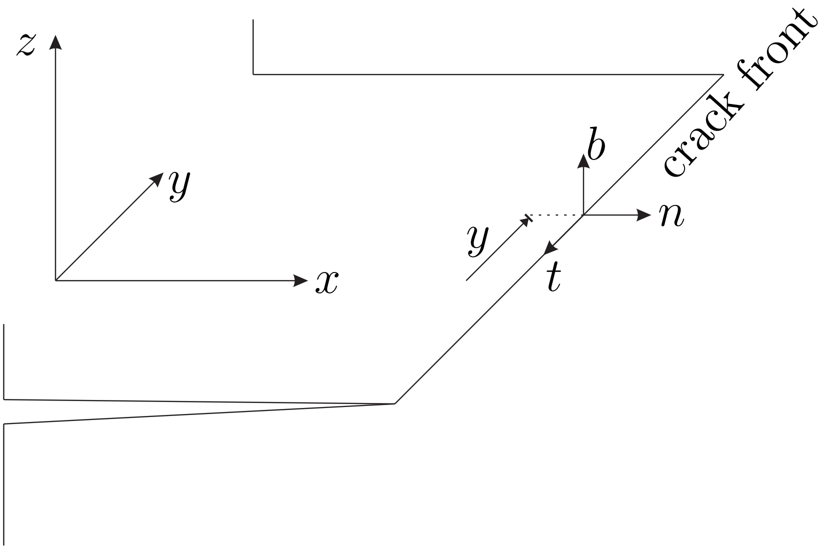

Figure 6.3: The use of global coordinates to define SIFs variation

6.2.2 Extended Dual Boundary Element Method

The previous chapter has demonstrated a direct evaluation of SIFs by enriching the DBEM [94] for two-dimensional crack problems. Therefore, a similar concept can be applied to three-dimensional problems. Enrichment can be achieved by substituting enriched displacement into the DBIE given by (4.81); which can be written in a discretised form as,

$$\begin{aligned} C_{ij}(x')u_j(x') + C_{ij}(\hat{x})u_j(\hat{x}) + \sum_{\bar{n}=1}^{N_e}\sum_{\bar{a}=1}^{m} P_{ij}^{\bar{n}\bar{a}} u_j^{\bar{n}\bar{a}} + \sum_{\bar{n}=1}^{N_e}\sum_{\lambda=1}^{3} \tilde{P}_{iI}^{\bar{n}\lambda}\tilde{K}_I^{\lambda} \\ + \sum_{\bar{n}=1}^{N_e}\sum_{\lambda=1}^{3} \tilde{P}_{iII}^{\bar{n}\lambda}\tilde{K}_{II}^{\lambda} + \sum_{\bar{n}=1}^{N_e}\sum_{\lambda=1}^{3} \tilde{P}_{iIII}^{\bar{n}\lambda}\tilde{K}_{III}^{\lambda} = \sum_{\bar{n}=1}^{N_e}\sum_{\bar{a}=1}^{m} Q_{ij}^{\bar{n}\bar{a}} t_j^{\bar{n}\bar{a}} \end{aligned} \tag{6.7}$$

where C_{ij} denotes the free terms associated with strongly singular integrals of the traction kernel. N_e and m are the total number of elements and the number of nodes per element, respectively; x and x' are the field point and source point in BEM, and $\hat{x}$ is the point coincident with source x' at the opposing crack surface. The integrals $P_{ij}^{\bar{n}\bar{a}}$ and $Q_{ij}^{\bar{n}\bar{a}}$ are given by Eqns. (4.54a) and (4.54b) respectively, and the new terms $\tilde{P}_{iI}^{\bar{n}\lambda}$, $\tilde{P}_{iII}^{\bar{n}\lambda}$ and $\tilde{P}_{iIII}^{\bar{n}\lambda}$

are defined as,

$$\tilde{P}_{iI}^{\bar{n}\lambda} = \int_{-1}^{1}\int_{-1}^{1} T_{ij}\left[x', x(\xi_1,\xi_2)\right] R_{jq}\{\psi_{Iq}^{\lambda}(r,\theta)\} N_{\lambda}^{f}(\xi_2) J^{\bar{n}}(\xi_1,\xi_2) d\xi_1 d\xi_2 \tag{6.8a}$$

$$\tilde{P}_{iII}^{\bar{n}\lambda} = \int_{-1}^{1}\int_{-1}^{1} T_{ij}\left[x', x(\xi_1,\xi_2)\right] R_{jq}\{\psi_{IIq}^{\lambda}(r,\theta)\} N_{\lambda}^{f}(\xi_2) J^{\bar{n}}(\xi_1,\xi_2) d\xi_1 d\xi_2 \tag{6.8b}$$

$$\tilde{P}_{iIII}^{\bar{n}\lambda} = \int_{-1}^{1}\int_{-1}^{1} T_{ij}\left[x', x(\xi_1,\xi_2)\right] R_{jq}\{\psi_{IIIq}^{\lambda}(r,\theta)\} N_{\lambda}^{f}(\xi_2) J^{\bar{n}}(\xi_1,\xi_2) d\xi_1 d\xi_2 \tag{6.8c}$$

where (ξ_1, ξ_2) are local parametric coordinates, $J^n(\xi_1, \xi_2)$ is the Jacobian for coordinate transformation, and T_{ij} is the traction fundamental solutions. In addition, vectors $\{\psi_{Iq}^{\lambda}(r,\theta)\}$, $\{\psi_{IIq}^{\lambda}(r,\theta)\}$ and $\{\psi_{IIq}^{\lambda}(r,\theta)\}$ are the first, second and third column in the matrix $\boldsymbol{\psi}$ given by (6.5). If element $\bar{n}$ is unenriched then $\tilde{P}_{iI}^{\bar{n}\lambda} = 0$, $\tilde{P}_{iII}^{\bar{n}\lambda} = 0$ and $\tilde{P}_{iIII}^{\bar{n}\lambda} = 0$. In reality, enrichment is only applied to elements on the crack surfaces, therefore most displacements can be evaluated using products of shape functions and nodal displacements in the usual way. In cases when the traction boundary integral equation as given by (4.82) is applied to the crack surface, the enriched discretised form for traction-free cracks can be written as,

$$\begin{aligned} n_i(x')\sum_{\bar{n}=1}^{N_e}\sum_{\bar{a}=1}^{m} E_{kij}^{\bar{n}\bar{a}} u_k^{\bar{n}\bar{a}} + n_i(x')\sum_{\bar{n}=1}^{N_e}\sum_{\lambda=1}^{3} \tilde{E}_{Iij}^{\bar{n}\lambda}\tilde{K}_I^{\lambda} + n_i(x')\sum_{\bar{n}=1}^{N_e}\sum_{\lambda=1}^{3} \tilde{E}_{IIij}^{\bar{n}\lambda}\tilde{K}_{II}^{\lambda} \\ + n_i(x')\sum_{\bar{n}=1}^{N_e}\sum_{\lambda=1}^{3} \tilde{E}_{IIIij}^{\bar{n}\lambda}\tilde{K}_{III}^{\lambda} = n_i(x')\sum_{\bar{n}=1}^{N_e}\sum_{\bar{a}=1}^{m} F_{kij}^{\bar{n}\bar{a}} t_k^{\bar{n}\bar{a}} \end{aligned} \tag{6.9}$$

where unenriched integrals $E_{kij}^{\bar{n}\bar{a}}$ and $F_{kij}^{\bar{n}\bar{a}}$ are given by

$$E_{kij}^{\bar{n}\bar{a}} = \int_{-1}^{1}\int_{-1}^{1} N^{\bar{a}}(\xi_1,\xi_2) S_{kij}(x', x(\xi_1,\xi_2)) J^{\bar{n}}(\xi_1,\xi_2) d\xi_1 d\xi_2 \tag{6.10a}$$

$$F_{kij}^{\bar{n}\bar{a}} = \int_{-1}^{1}\int_{-1}^{1} N^{\bar{a}}(\xi_1,\xi_2) D_{kij}(x', x(\xi_1,\xi_2)) J^{\bar{n}}(\xi_1,\xi_2) d\xi_1 d\xi_2 \tag{6.10b}$$

and enriched integrals are expressed as,

$$\tilde{E}^{\bar{n}\lambda}_{Iij} = \int_{-1}^{1}\int_{-1}^{1} S_{kij}\left[x', x(\xi_1,\xi_2)\right] R_{jq}\{\psi^{\lambda}_{Iq}(r,\theta)\} N^{f}_{\lambda}(\xi_2) J^{\bar{n}}(\xi_1,\xi_2) d\xi_1 d\xi_2 \tag{6.11a}$$

$$\tilde{E}^{\bar{n}\lambda}_{IIij} = \int_{-1}^{1}\int_{-1}^{1} S_{kij}\left[x', x(\xi_1,\xi_2)\right] R_{jq}\{\psi^{\lambda}_{IIq}(r,\theta)\} N^{f}_{\lambda}(\xi_2) J^{\bar{n}}(\xi_1,\xi_2) d\xi_1 d\xi_2 \tag{6.11b}$$

$$\tilde{E}^{\bar{n}\lambda}_{IIIij} = \int_{-1}^{1}\int_{-1}^{1} S_{kij}\left[x', x(\xi_1,\xi_2)\right] R_{jq}\{\psi^{\lambda}_{IIIq}(r,\theta)\} N^{f}_{\lambda}(\xi_2) J^{\bar{n}}(\xi_1,\xi_2) d\xi_1 d\xi_2 \tag{6.11c}$$

If the field element $\bar{n}$ is unenriched, then $\tilde{E}^{\bar{n}\lambda}_{Iij} = 0$, $\tilde{E}^{\bar{n}\lambda}_{IIij} = 0$ and $\tilde{E}^{\bar{n}\lambda}_{IIIij} = 0$. It can be seen from Eqns. (6.7) and (6.10), that the enrichment of the DBEM has added a few degrees of freedom to the system. The number of newly added degrees of freedom depends on the number of points at the crack front, where SIFs need to be evaluated. The auxiliary equations required to yield a square system can be derived by enforcing the continuity of displacement at the crack front, as demonstrated below.

6.2.3 Crack front tying constraint

In three-dimensional cracks, the equations required to yield a square system are generated by enforcing the continuity of displacement at the crack front, which can be achieved by following the same procedure as that illustrated in Sec. 5.2.3. However, unlike the two-dimensional cracks, where the number of added degrees of freedom depends on the number of crack tips, the three-dimensional added degrees of freedom depend on the mesh. For instance, the mesh used for a penny shaped crack as shown in Fig. 6.4 has 24×3 degrees of freedom added to the system. In detail, the 24 denotes the black points (see Fig. 6.4) at the crack front where SIFs must be evaluated, and 3 represents mode I, II and III for each point. Therefore, various mesh configurations will generate the different numbers of added degrees of freedom.

It can be seen from Fig. 6.4, that the nodes on the crack surface have been arranged in radial lines, each of which is perpendicular to the crack front. The enforcement of continuity of displacement for each radial line at the crack front yields sufficient equations for a square system. In a similar manner to the two-dimensional case, we define element

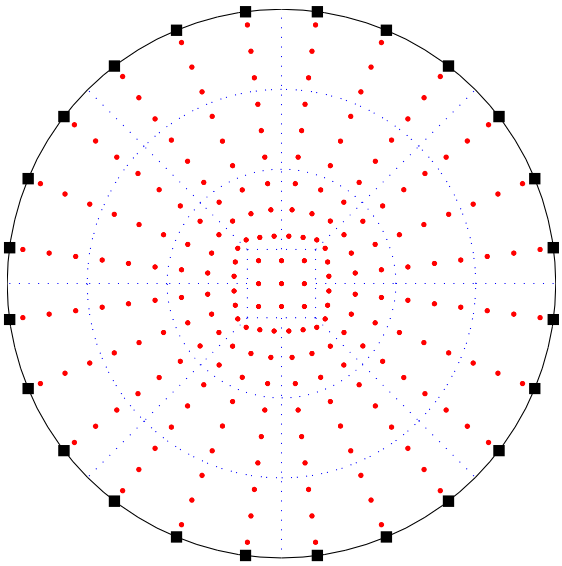

Figure 6.4: Crack surface elements layout for tying constraint

A as adjacent to the crack surface and parameterised by local variable ξ_A. This element has a set of nodes on the upper crack surface and touching the crack tip at $\xi_A = 1$ as shown in Fig. 6.5. On the opposite surface, we define element B, as parameterised by local variable ξ_B and touching the crack tip at $\xi_B = -1$. Applying the expression (6.4) to give the displacement at the crack tip as denoted by point y, and equating the values from elements A and B, yields,

$$\begin{aligned} &\{N^a(1)\}^T\{u_j^a\} + R_{jq}\boldsymbol{\psi}_{lq}(r,\theta)\{\tilde{K}_I\ \tilde{K}_{II}\ \tilde{K}_{III}\}^T \\ &= \{N^b(-1)\}^T\{u_j^b\} + R_{jq}\boldsymbol{\psi}_{lq}(r,\theta)\{\tilde{K}_I\ \tilde{K}_{II}\ \tilde{K}_{III}\}^T \end{aligned} \tag{6.12}$$

where u_j^a and u_j^b are the nodal displacements along elements A and B, respectively. Notice that, the enrichment terms in Eqn. (6.12) vanish at the crack front as $r = 0$, so the constraint equation can be written after rearrangement as,

$$\{N^a(1)\}^T\{u_j^a\} - \{N^b(-1)\}^T\{u_j^b\} = 0 \tag{6.13}$$

Applying Eqn. (6.13) to enforce the displacement continuity in the direction of x, y

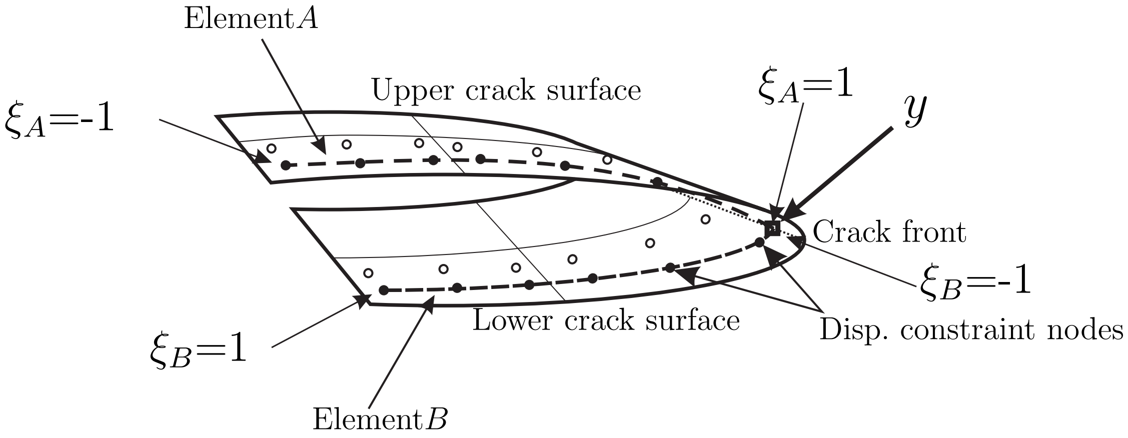

Figure 6.5: Displacement constraint elements on the crack surface

and z, provides three additional equations for each crack front location at which the three SIF unknowns emerge. This makes it possible to accurately obtain unknowns including $\tilde{K}_I^\lambda$, $\tilde{K}_{II}^\lambda$ and $\tilde{K}_{III}^\lambda$ in the solution column.

6.3 Implementation

The use of DBEM for modelling three-dimensional crack problems consists of implementing TBIE and DBIE. In a similar manner to that affecting two-dimensional problems, the focus is given to the evaluation of hypersingular and strongly singular integrals. Although, enrichment functions do not affect the singularity, the use of TBIE requires continuity of C^1 for shape functions at collocation points. This can be achieved by using discontinuous elements, in which the nodes are located within the body of the element. In addition, using discontinuous elements allows the generation of auxiliary equations to solve added degrees of freedom.

6.3.1 Evaluation of singular integrals

The singularity subtraction approach submitted by [144] and demonstrated in Sec. 4.3.4.1 has been utilised in this thesis, since it permits the straightforward inclusion of enriched terms. The evaluation of hypersingular and strongly singular integrals, when using this technique can be achieved by integrating singular terms analytically and regular terms numerically. Recalling Eqn. (4.115), which is suitable for the evaluation of hypersingular and strongly singular integrals, it can be seen that the equation depends on the determination of nonsingular functions $F_{-1}(\phi)$ and $F_{-2}(\phi)$. These functions can be obtained by mapping local coordinates (ξ_1, ξ_2) to a polar system of (ρ, ϕ), and by utilising the Taylor series expansions around the source points (ξ_1', ξ_2') . For instance, applying this technique to the enriched hypersingular integral as given by Eqns. (6.11a) can yield,

$$\begin{aligned}
F(\rho,\phi) &= S_{kij}\left[x', x(\rho,\phi)\right] R_{jq}(\rho,\phi)\{\psi^{\lambda}_{Iq}(r(\rho,\phi),\theta)\} N^f(\rho,\phi) J^{\bar{n}}(\xi_1,\xi_2) && \text{(6.14a)}\\
F_{-2}(\phi) &= C_k C_{r2}(\phi) F_0 R_{jq0}\{\psi^{\lambda}_{Iq0}\} N^f_0 && \text{(6.14b)}\\
F_{-1}(\phi) &= C_k \Big\{ C_{r2}(\phi) \Big[F_0 \Big(R_{jq0}\{\psi^{\lambda}_{Iq1}\}(\phi) N^f_0 + R_{jq0}\{\psi^{\lambda}_{Iq0}\} N^f_1(\phi) + R_{jq1}(\phi)\{\psi^{\lambda}_{Iq0}\} N^f_0 \Big) \\
&+ F_1(\phi) R_{jq0}\{\psi^{\lambda}_{Iq0}\} N^f_0 \Big] + C_{r1}(\phi) F_0 R_{jq0}\{\psi_{Iq0}\} N^f_0 \Big\} && \text{(6.14c)}
\end{aligned}$$

where C_k is the kernel constant, and $C_{r1}(\phi)$, $C_{r2}(\phi)$, $F_0(\phi)$ and $F_1(\phi)$ are obtained from the first and the second terms of the Taylor expansion for $S_{kij}(x', x(\xi_1,\xi_2))J^{\bar{n}}(\xi_1,\xi_2)$. In addition, ψ^{λ}_{Iq0} and $\psi^{\lambda}_{Iq1}(\phi)$ are the first and the second Taylor expansion terms for $\psi^{\lambda}_{Iq}[r(\rho,\phi),\theta]$. It should be noted that in three-dimensions the rotation matrix $R_{jq}(\alpha)$, needs to be expanded by the Taylor series since it is a function of (ξ_1,ξ_2). Likewise, the one-dimensional shape functions $N^f(\rho,\phi)$ should be expanded around the source point by the Taylor series. Similar procedures can be used to evaluate enriched integrals for modes II and III as given by (6.11b) and (6.11c). In cases of an unenriched hypersingular integral such as that given by (5.12a), the procedures are similar, and the integral can be evaluated as,

$$\begin{aligned}
F(\rho,\phi) &= N^{\bar{a}}(\rho,\phi) S_{kij}(x', x(\rho,\phi)) J^{\bar{n}}(\xi_1,\xi_2) && \text{(6.15a)}\\
F_{-2}(\phi) &= C_k C_{r2}(\phi) F_0 N^{\bar{a}}_0 && \text{(6.15b)}\\
F_{-1}(\phi) &= C_k \left\{ C_{r2}(\phi) \left[N^{\bar{a}}_1(\phi) F_0 + N^{\bar{a}}_0 F_1(\phi) \right] + C_{r1}(\phi) N^{\bar{a}}_0 F_0 \right\} && \text{(6.15c)}
\end{aligned}$$

where $N^{\bar{a}}_0$ and $N^{\bar{a}}_1(\phi)$ are the first and the second Taylor expansion terms for $N^{\bar{a}}(\rho,\phi)$, respectively. The derivations of terms appearing in (6.14) and (6.15) are outlined in Appendix B.3. Once these terms have been determined, it is possible to apply Eqn. (4.115) to evaluate all the integrals. In addition, strongly singular integrals can be evaluated in a similar manner. However, because of the lower order of the singularity, the term $F_{-2}(\xi')$ equals zero. It should be noted that the employment of enrichment has not altered the free terms arising from the strongly singular integrals, since these terms cancel out during implementation. The cancellation occurs as the multiplication of the jump terms by the enrichment functions have equal magnitude and opposite sign for upper and lower crack surfaces.

6.3.2 Enrichment procedure

Applying Williams expansions to three-dimensional problems requires more attention than two-dimensional problems, since they are only valid for points located on a plane perpendicular to the crack front, and in the vicinity of the crack front. In addition, it is crucial to classify the problem as plane strain or plane stress, because of the use of two-dimensional enrichment functions. It is worth mentioning that in this thesis only fully embedded cracks are considered, so that it is suitable to use the plane strain form throughout.

In three-dimensional cracks, the number of added degrees of freedom is controlled by the mesh. Consequently, it is important to arrange the nodes on the crack surface to yield sufficient nodes for the displacement constraint. This can be demonstrated by considering the crack mesh, as shown in Fig. 6.4, and comparing it with a refined mesh for the same crack as presented in Fig. 6.6. It is evident that when the number of the crack front points is increased, there are enough nodes for displacement constraint.

Eqn. (6.13) equates the extrapolated values for crack tip displacement using nodes from element A to those found in element B. The three nodes (on a quadratic element) aligned in the radial direction with the particular location on the crack front can be used for displacement constraint. It has been observed that greater accuracy can be gained by including additional nodes in the extrapolation; including those from adjacent elements. However, in the case of when the distance between nodes is equal, only a maximum of 9 nodes are used to apply the continuity constraint [146].

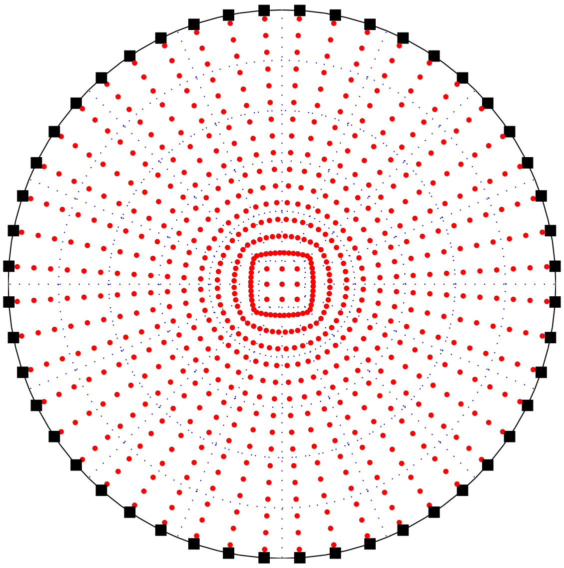

Figure 6.6: Crack surface elements layout with refine mesh for tying constraint

6.3.3 Matrix assembly

The system matrices for three-dimensional crack problems are typically assembled in a similar manner to that demonstrated in Sec. 5.3.3. However, the sub-matrix containing enrichment entries is now 3×3 and can be obtained by computing the enriched integrals. This requires the use of the rotation matrix R to transfer local displacement produced by the enrichment function $\boldsymbol{\psi}^{\lambda}$ (see (6.5)) to global coordinates, which then multiplies by the fundamental solution and shape functions. Since, the value of enrichment sub-matrix entries is very small, it is important to scale system matrices to improve the condition number. However, with the use of proper scaling, the implementation of enrichment has been observed to affect the condition number only mildly of the system by increasing it by approximately one order of magnitude.

The two-dimensional Matlab code is modified to model three-dimensional crack problems. The code was examined by comparing the analytical displacement with the code numerical results for a cube under uniaxial load. A penny shaped central crack is then introduced to the cube where the crack surface displacements are used to verify the accuracy of the code. Fig. 6.7 demonstrates the code constructor; it also shows loops and if statements that used within the body of the code. An adaptive technique used to accelerate the code by calculating the ratio of r/d (see Sec. 4.3.1) to find the optimum number of integration points. The evaluation of integrals depends on the degree of singularity and can be achieved by an appropriate method as illustrated in 6.3.1. The code consists of two loops; the first loop is performed over collocation points, whereas the nested loop is performed over field elements. In order to accelerate the calculations, both loops can be converted into MEX-files. Moreover, the implementation of MEX-files has increased the speed of the code by ×100. In addition, parallel computing can be applied to the first loop, since the rows associated with each source point can be evaluated independently. The employment of the parallel technique to the first loop (see Fig. 6.7) has reduced the computational time, although the achieved reduction depends on the number of used cores. Further improvement can be achieved by reducing the required memory cost by compressing the output matrices $\boldsymbol{H}$ and $\boldsymbol{G}$ into matrix $\boldsymbol{A}$ and vector $\boldsymbol{y}$, as illustrated by Eqn. (4.66). In a final step, the displacement constraint entries are calculated and added to the appropriate rows in matrix $\boldsymbol{A}$. Using a direct solver, the generated square system of matrices can be solved to reveal the SIFs values along the crack front as $\tilde{K}_I^\lambda$, $\tilde{K}_{II}^\lambda$ and $\tilde{K}_{III}^\lambda$.

6.4 Numerical Examples

The previous sections outlined a complete guide to the implementation of enriched DBEM. The method adopted for verification and accuracy assessment is presented in this section. The effect of enrichment implementation on displacement evaluation has been demonstrated by showing the contribution of each term in regard to the enrichment equation (6.4). The ability to treat penny shaped cracks with various orientations is illustrated by examples; including pure mode I, inclined crack and multi cracks.

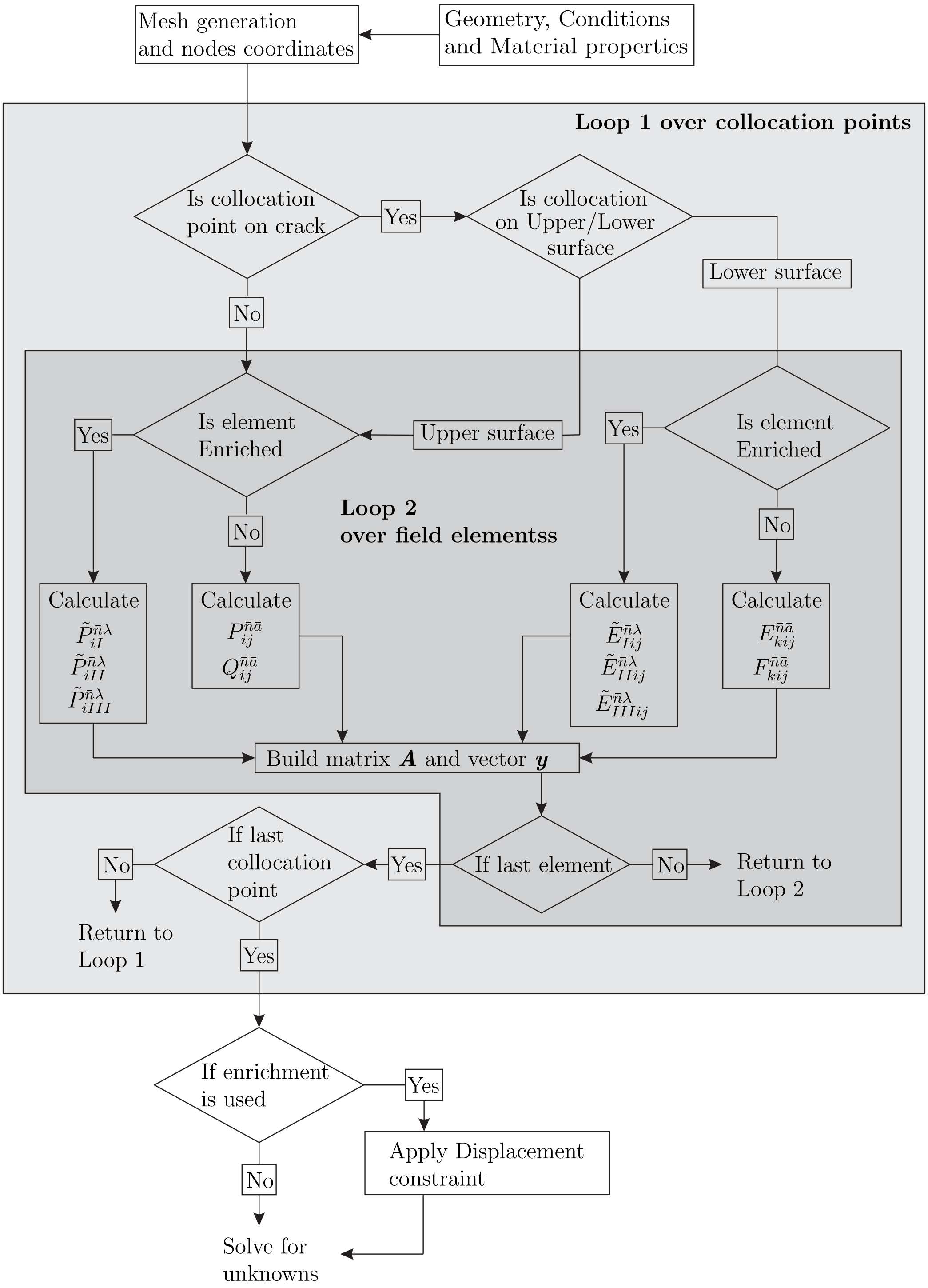

Figure 6.7: Flowchart of the implemented code for enriched DBEM in 3D

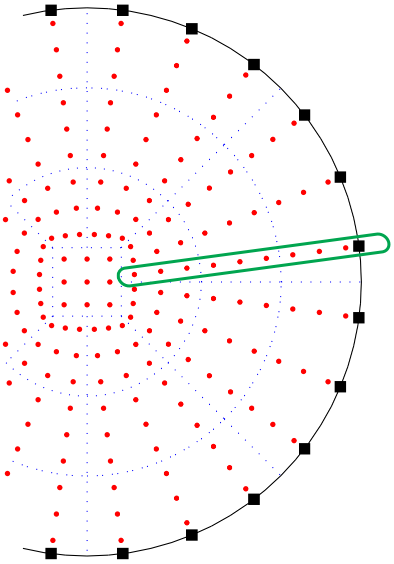

Figure 6.8: A set of aligned nodes perpendicular to the crack front

6.4.1 Effect of enrichment

To demonstrate the effect of enrichment on displacement estimation near the crack front, a set of radially arranged points on the upper crack surface is selected as presented in Fig. 6.8. The displacement of these points is described using the enrichment function given by (6.4). For comparison, a simple traction set of boundary conditions is applied where the results are presented using curves showing: (i) the leading order term in the Williams expansion (enrichment function), (ii) the analytical solution for the crack opening displacement of a penny shaped crack in an infinite domain, and (iii) the difference between (i) and (ii), which is required as the contribution from the shape function terms. Fig. 6.9 shows the contribution from the last term in Eqn. (6.4) is very small near the crack front, and that the displacements are calculated mainly by the first term. However, the last term in Eqn. (6.4) becomes more significant in the calculation of total displacement when moving away from the crack front. This can be explained as the first term of (6.4) is an asymptotic solution giving the best results near the crack front. This example demonstrates the need to include the second term in Eqn. (6.4), as it can capture displacements far from the crack front, and non-zero displacement of the crack tip.

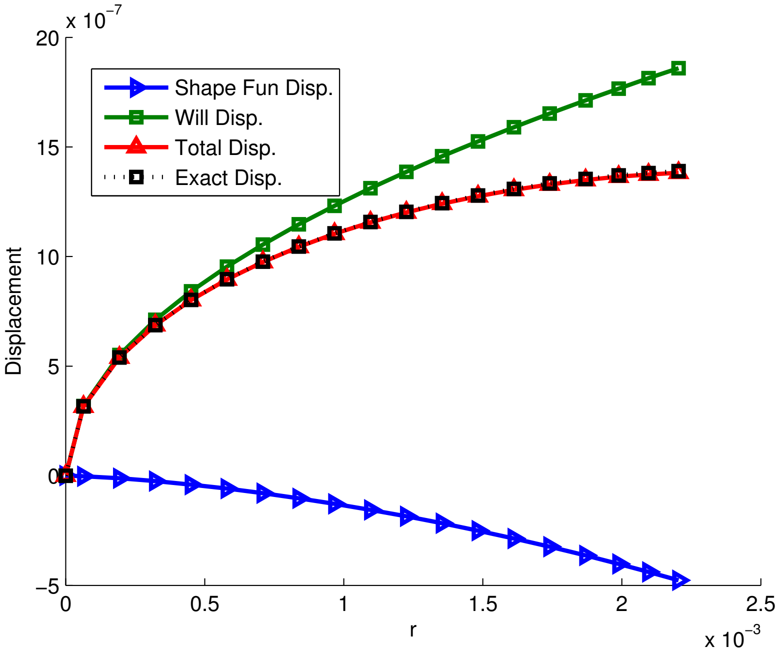

Figure 6.9: Displacement behaviour near the crack front

6.4.2 Pure mode *I*

A cube with a central penny shaped crack can be studied to demonstrate the accuracy of the direct method. Figure 6.10 shows the stresses applied to upper and lower surfaces of the cube; h is the cube side length and a is the radius of the crack where $h/a = 40$. This example does not have an exact solution; however a small crack compared to the cube is considered allowing for the use of the infinite domain solution. The exact solution for an infinite domain as given by [142], can be calculated as $K_{Io} = \frac{2}{\pi}\sigma\sqrt{\pi a}$. Fig. 6.11 presents normalised results showing a very accurate estimation of SIF for mode I when the direct method is used. A slight improvement in error can be noticed when the enriched DBEM is used with the J-integral.

The obtained displacement at the crack surfaces has been studied to demonstrate the effect of the enrichment utilisation on the displacement calculation. Therefore, the nodal displacements at a two-dimensional cross-section at constant y have been considered. Fig. 6.12 shows the determined displacement at the crack surfaces by enrichment implementation. In addition, the figure represents the exact solution for a penny shaped crack in an

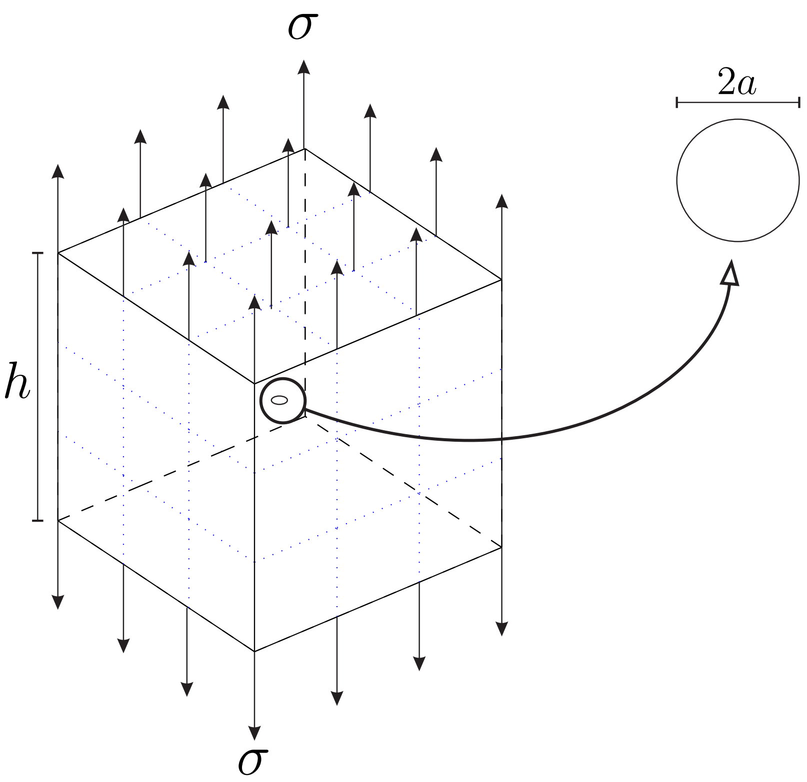

Figure 6.10: Penny shaped crack in large cube

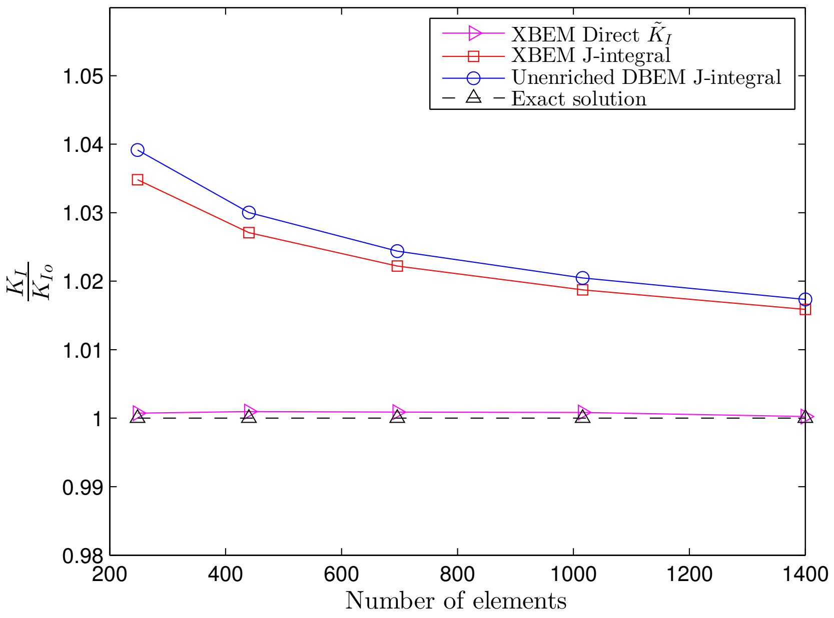

Figure 6.11: A comparison of mode I SIF for penny shaped crack

infinite domain [142] for comparison. The use of enrichment has improved the accuracy of estimated displacements and a good agreement can be seen with the exact displacement. Moreover, by focusing on the last two points at the crack front on the upper and lower crack surfaces, it can be observed that the use of displacement constraint has closed the crack opening displacement which allows for the direct evaluation of SIFs. Furthermore, investigation of the unenriched elements at the centre of the crack shows an improvement in accuracy by just applying the enrichment to elements adjacent to the crack front.

Fig. 6.13 presents the determined displacement at the crack surfaces by conventional DBEM and the exact displacement for comparison. The effect of the crack tip singularity can be noticed on nodal displacements near the crack front, whereas the calculated displacements become close to the exact displacements near the crack centre. Moreover, by focusing on the last two points at the crack front on the upper and lower crack surfaces, the crack opening displacement can be observed. Therefore, the existence of the crack opening displacement prevents the direct evaluation of SIFs and a postprocessing method is required.

6.4.3 Number of enriched elements

Unlike in the Partition of Unity Method, in the enrichment technique presented here the enrichment functions are not associated with nodal degrees of freedom. Moreover, the implemented method provides freedom to increase the number of enriched elements without increasing the DOFs, since the additional degrees of freedom $\tilde{K}_I$, $\tilde{K}_{II}$ and $\tilde{K}_{III}$ are associated with the number of points required at the crack front. Therefore, the new DOFs are limited to three per each point required at the crack front. For these enriched elements (on the crack surfaces), the displacement is approximated by the enriched form of the displacement equation, as given by (6.4). It has been observed that, the number of enriched elements has a significant effect on the results, both when the J-integral is used to determine stress intensity factors and when the directly calculated $\tilde{K}_I$ is used. Hence, a cube with central penny shaped crack similar to the example used in pure mode I (Sec. 6.4.2). In this example, a number of enriched elements have been used to demonstrate

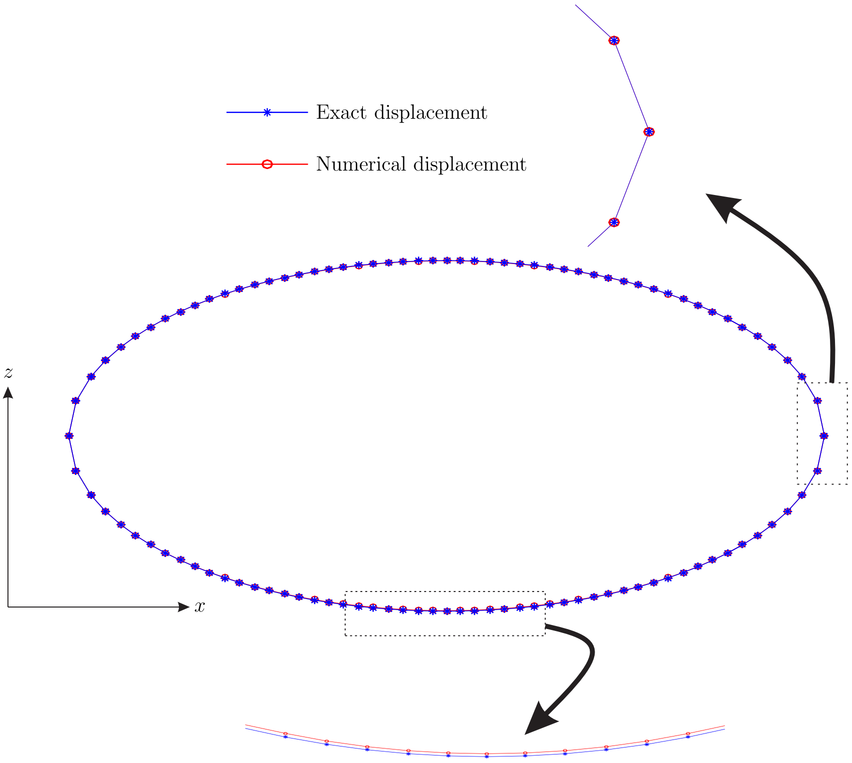

Figure 6.12: A 2D cross-section of the crack surface displacements obtained by enrichment implementation

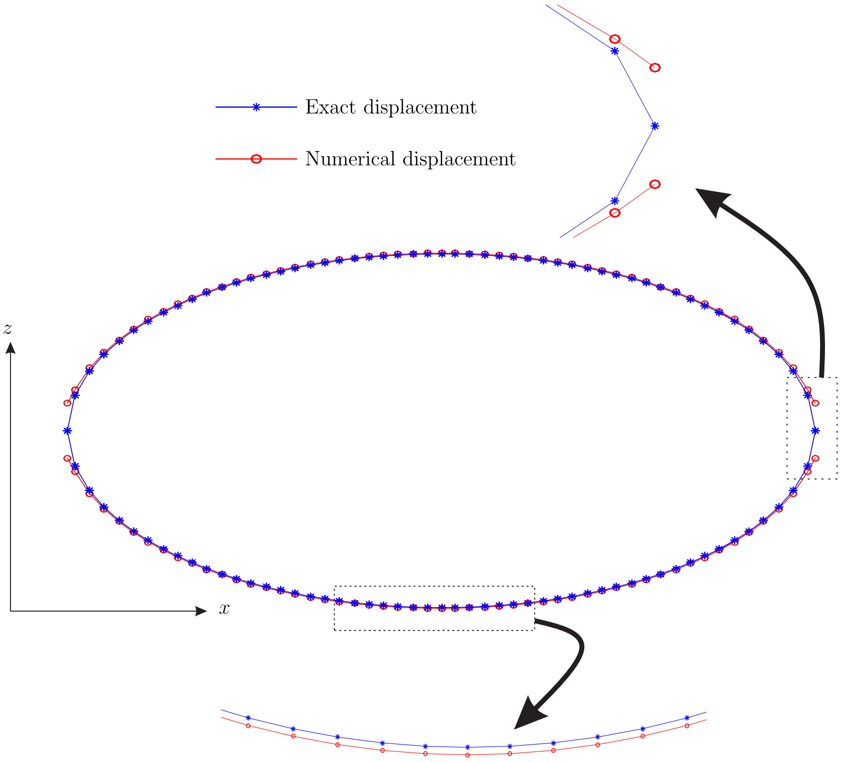

Figure 6.13: A 2D cross-section of the crack surface displacements obtained by conventional DBEM

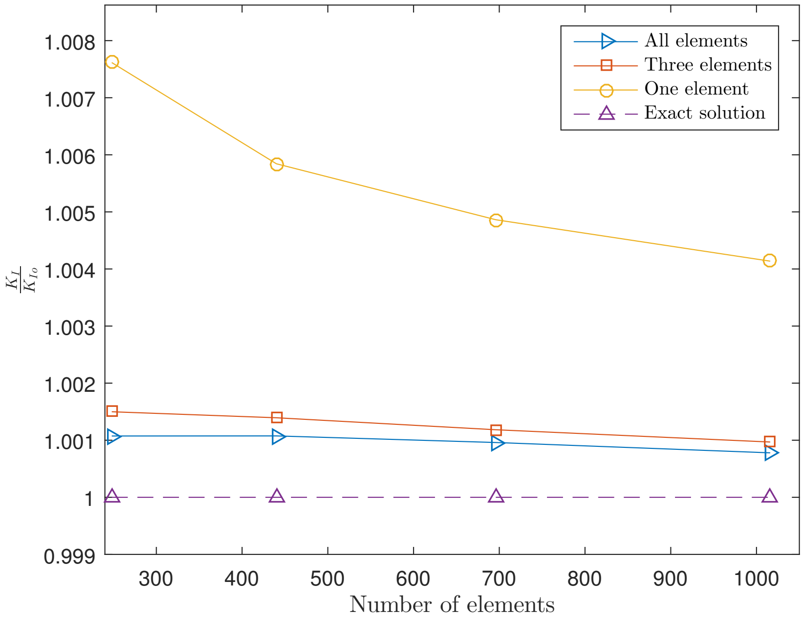

Figure 6.14: A comparison of normalized mode I SIF for different number of enriched elements

the impact on the accuracy of the results. Figure 6.14 shows a reduction in error for cases when a greater number of the elements at the crack surface are enriched. It apparent that optimum accuracy can be achieved by enriching all the elements at crack surface. For this reason, all the results aside from this example, are obtained for models in which all suitable elements (elements with a perpendicular aligned nodes to the crack front) at the crack surfaces are enriched.

6.4.4 Order of extrapolation for the tying constraint

The tying constraint enforces the continuity of displacement at points where SIFs are required at the crack front. It can be expressed through the equality of the displacements at these points as found by extrapolation of valid nodal displacements (nodes located on a virtual line that perpendicular to the crack front) over the upper and lower crack surfaces. Constraint can be achieved by basing the extrapolation equation given by (6.13) on a sufficient number of the nodes on those elements touching the crack front. However, it is possible to use a higher order Lagrangian extrapolation that considers the nodes on adjacent elements. In this example, a cube with a penny shaped crack, as presented in

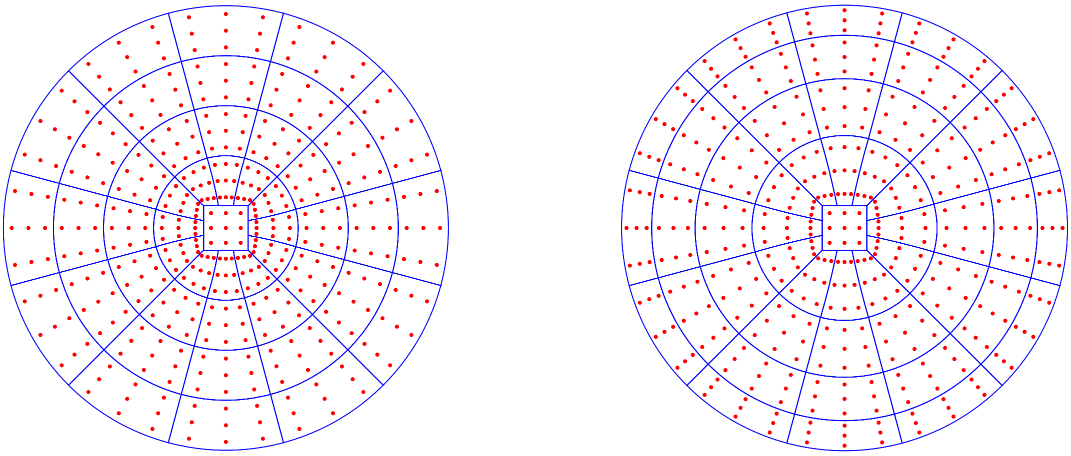

(a) case 1 : uniform mesh (b) case 2 : non-uniform mesh

Figure 6.15: A penny shaped crack with different types of mesh

Fig. 6.10; h is the cube side length and a is the radius of the crack where $h/a = 40$. Whereas, two cases were considered for the crack mesh to show the effect of the number of nodes used for the constraint.

The first case consists of an equal distance between the nodes on the crack surface, as shown in Fig. 6.15a. In this case, the maximum number of nodes that can be used for the constraint is 9, due to the rise of singularity in the extrapolation polynomial. Figure 6.16 compares of the mode I stress intensity factor obtained via different orders of extrapolation. It compares the results using 3 nodes to extrapolate displacement to instances when 9 nodes are used. These will be the 9 nodes nearest to the crack front on each crack surface. Improved results can be seen when increasing the order used for the extrapolation of the displacement results to the crack front. It is tempting to suggest using even higher order Lagrangian polynomials; however, this would then impose restrictions on the distance between the nodes, due to Rung's phenomenon.

In the second case, an non-uniform mesh has been used for elements on the crack surfaces, as presented in Fig. 6.15b. This allows utilization of a higher order Lagrangian extrapolation for displacement constraint. In this case, a number of nodes were used for the displacement constraint, including 3, 9 and 15 nodes on the enriched elements.

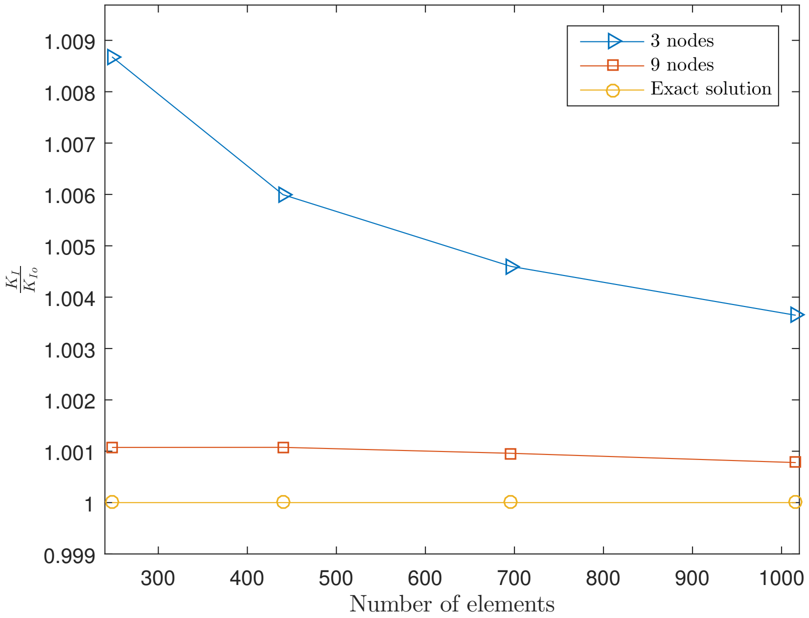

Figure 6.16: Mode I SIF for penny shaped crack with uniform mesh

Figure 6.17 shows the mode I stress intensity factor was obtained from different orders of extrapolation. The results presented in the figure show that an improvement in terms of accuracy arises when increasing the order of the polynomial to extrapolate the displacement. In addition, the effect of mesh refinement on the crack front can be seen when comparing the displacement constraint using 3 and 9 nodes, according to the findings from the two cases. Fig. 6.18 shows normalised mode I stress intensity factor when 9 nodes are used for displacement constraint in both cases.

Improved accuracy can be achieved when increasing the order used for the extrapolation of the displacement, as confirmed by the results of the two cases were examined. However, increasing the number of nodes used for displacement constraint imposes restrictions on the mesh type. In addition, the effect of the non-uniform mesh can be observed on the convergence rate of K_I as shown in Fig. 6.18. Therefore, the effect of the non-uniform mesh needs to be considered when the number of nodes used for displacement constraint is increased. It can be seen from the results a good accuracy can be achieved by using 9 nodes for displacement constraint and without the need for using non-uniform mesh. Finally, the restrictions imposed by the non-uniform mesh must be balanced with obtained

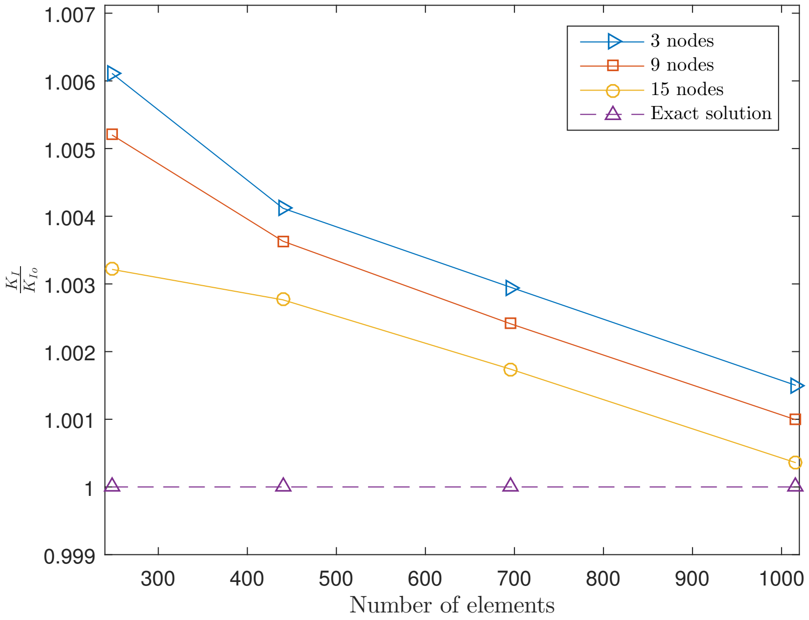

Figure 6.17: Mode *I* SIF for penny shaped crack with non-uniform mesh

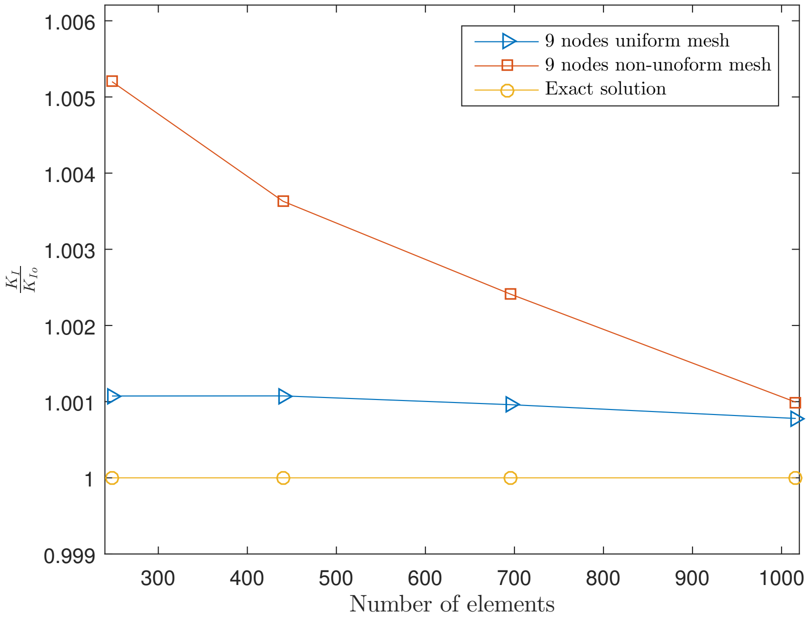

Figure 6.18: A comparison of uniform and non-uniform mesh when 9 nodes are used for the tying

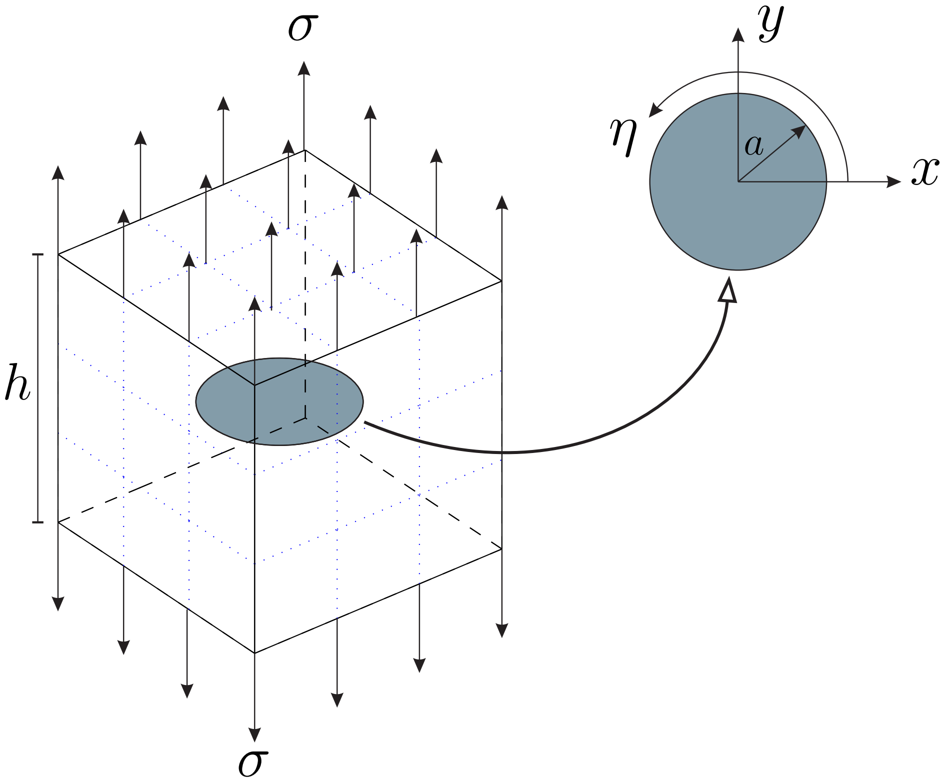

Figure 6.19: A cube with a central penny shaped crack

improvement.

6.4.5 Variation of SIFs along the crack front

Typically, K_I is constant along the crack front when considering an infinite domain. However, in the case of a finite domain, a slight variation is apparent in the value of K_I, which rises because of the geometrical effects. These differences can be captured by increasing the number of points at which SIFs need to be evaluated at the crack front. Two finite geometries have been considered to study the variation of mode I stress intensity factor along the crack front. The first example is a cube, with a central penny shaped crack. Fig. 6.19 shows the stresses applied to the upper and lower surfaces of the cube; a is the radius of the crack and h is the cube side length where $h/a = 4$. In this example, the cube's corners are located at angles $\pi/4$, $3\pi/4$, $-\pi/4$ and $-3\pi/4$. The results presented in Fig. 6.20 show the variation in K_I for different mesh refinements. Clearly, increasing the number of points at the crack front provides a more accurate evaluation of the variations in SIFs.

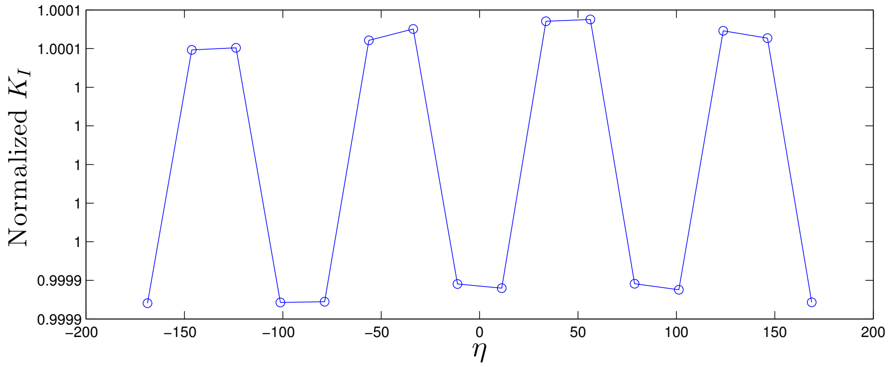

(a) 16 points at the crack front

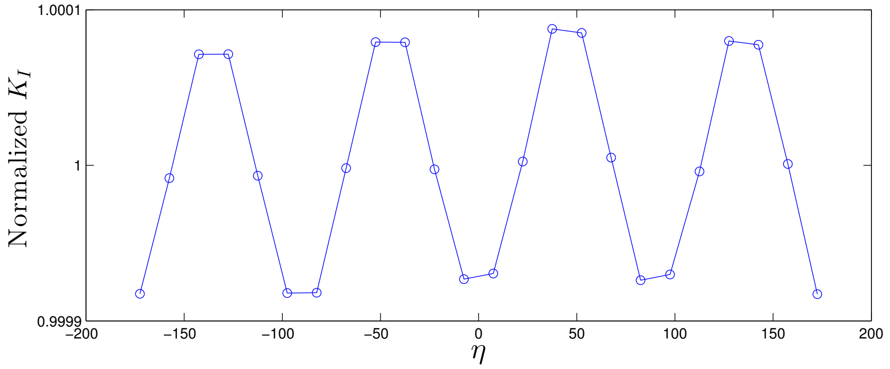

(b) 24 points at the crack front

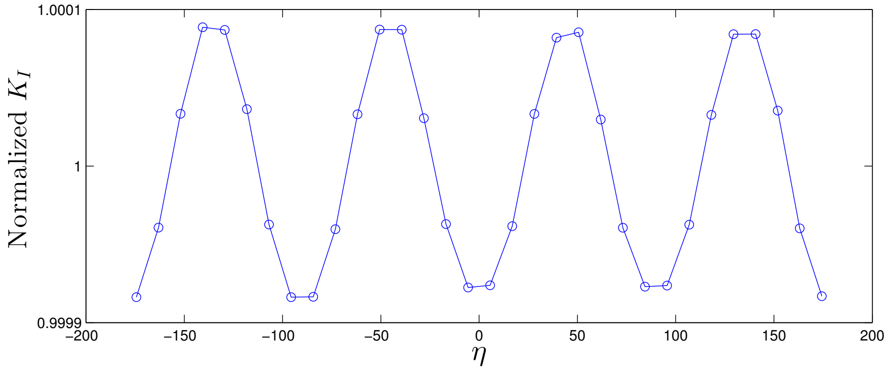

(c) 32 points at the crack front

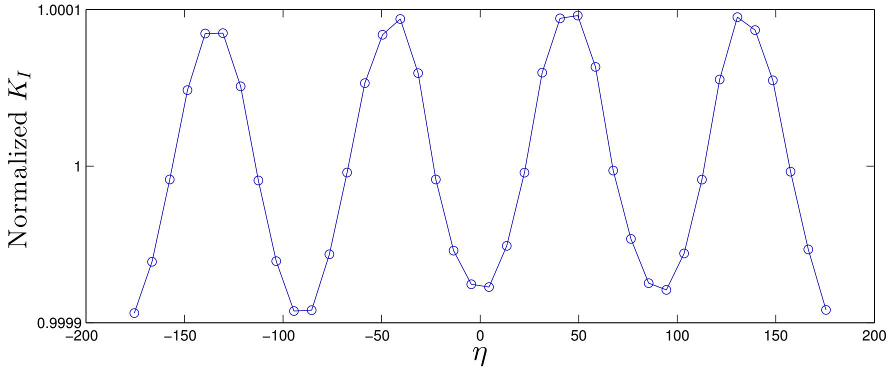

(d) 40 points at the crack front

Figure 6.20: Mode I SIF variation for cube with penny shaped crack

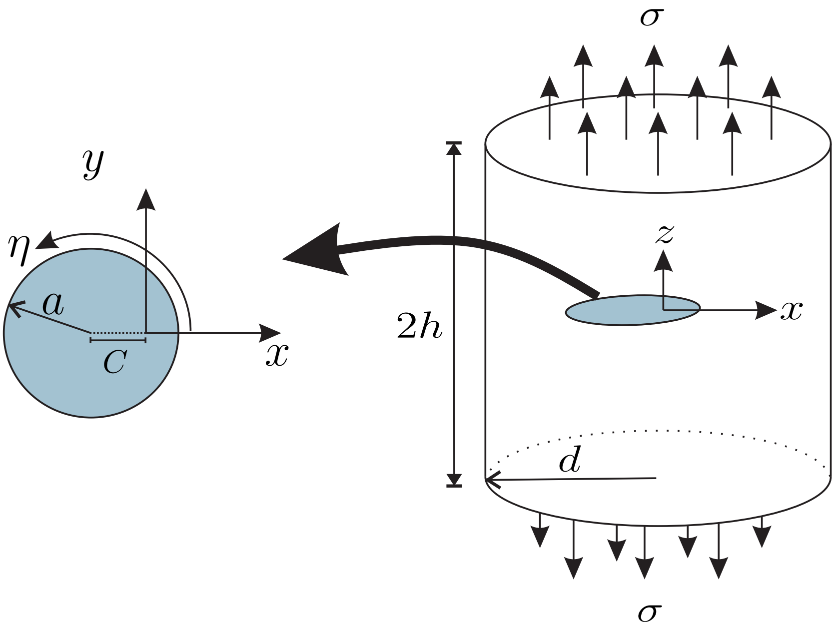

Figure 6.21: A Cylinder with a penny shaped crack

The second example considers a cylinder with a penny shaped crack, as presented in Fig. 6.21. The cylinder has a radius d and height of $2h$, where the height to radius ratio is $h/d = 0.5$. Whereas, the crack length a relates to the cylinder radius d by a ratio of $a/d = 0.25$. In this example, the crack was shifted from the centre by C, where C can be calculated as $C = d/6$. The Poisson ratio is $\nu = 0.3$ and the stress is applied at the cylinder's upper and lower surfaces. Fig. 6.22 represents the variation in the value of K_I along the crack front for a variety of mesh refinements. It can be observed that in cases when non-smooth geometries or when unsymmetrical problems are considered, more points are required at the crack front to capture the variation in the mode I stress intensity factor.

6.4.6 On the computational cost

The computational cost when employing enrichment was also examined. Since the computational cost associated with each element is cumulative, it rises as the number of enriched elements increases. However, sufficient accuracy can be achieved by using fewer elements when employing enrichment. The additional computational costs for evaluating SIFs was calculated. The code has been run on a dual quad-core Intel Xeon platform

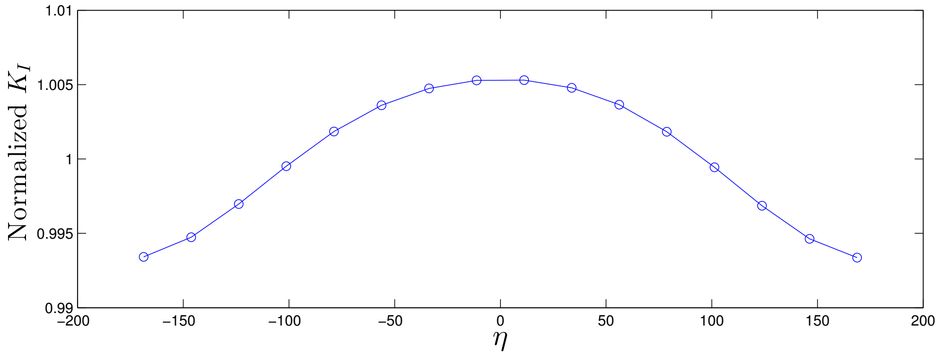

(a) 16 points at the crack front

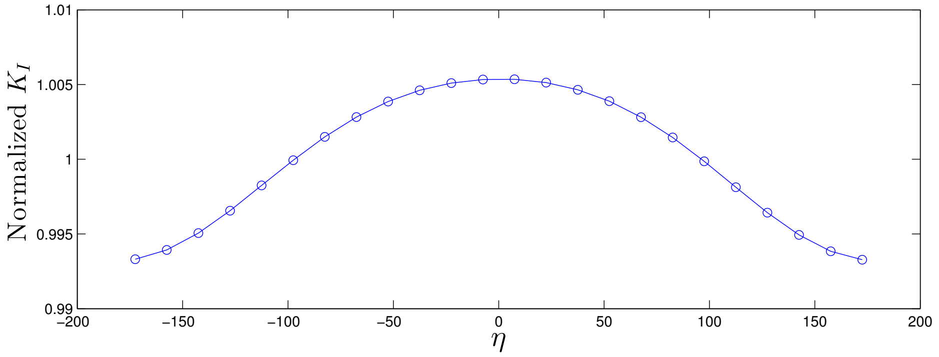

(b) 24 points at the crack front

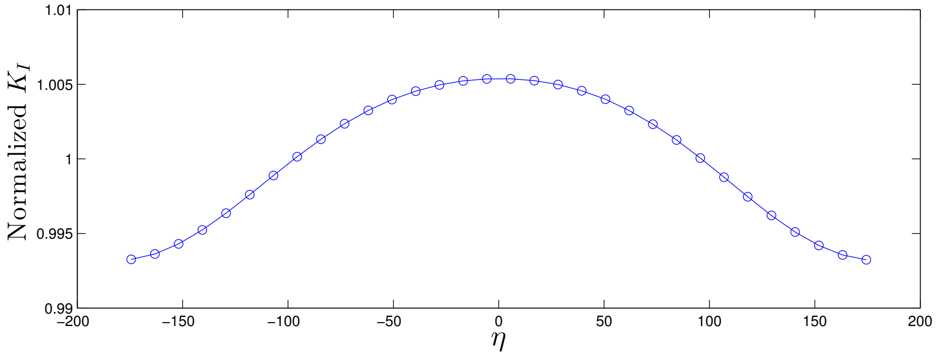

(c) 32 points at the crack front

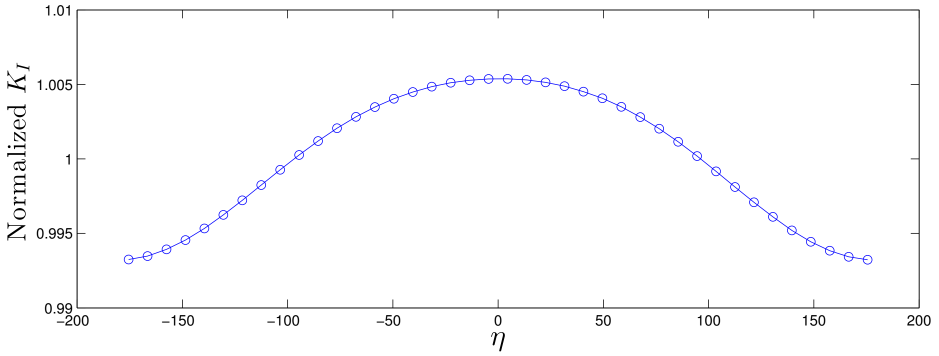

(d) 40 points at the crack front

Figure 6.22: Mode I SIF variation for cylinder with penny shaped crack

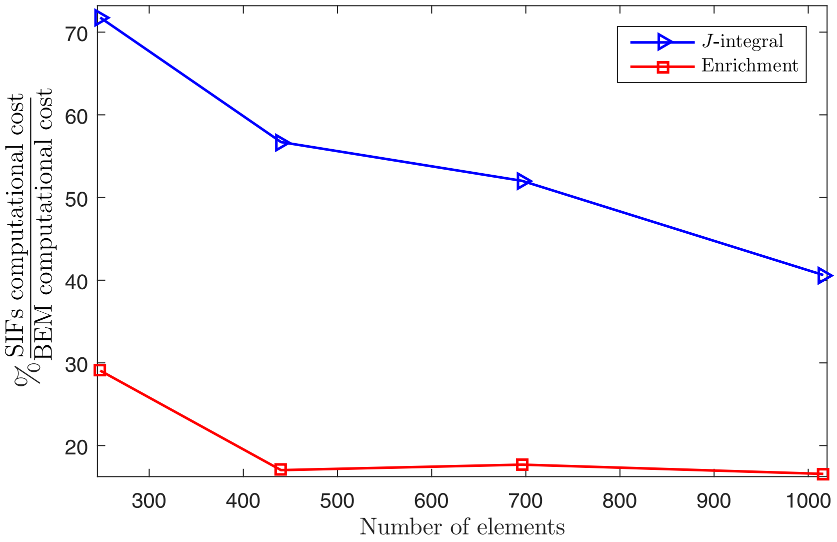

Figure 6.23: A comparison of the required additional computational cost to evaluate SIFs

X5570 @2.93GHz configured with 24 GB of RAM, running under a 64-bit Microsoft operating system. Fig. 6.23 shows the percentage of the additional cost associated with both the J-integral and enrichment when applied to all the crack surface elements. In this example, the number of points used on the J-integral path remains constant and unaffected by the refinement of the mesh on the boundaries. In addition, when the mesh is refined, the J-integral must be evaluated at more locations at the crack front. However, the number of enriched elements increases as a result of the refinement of the mesh on the boundaries. Notably the cost for evaluating SIFs at a specific location at the crack front using enrichment is less than when using the J-integral. Arguably the cost of the J-integral can be reduced by evaluating it at fewer locations at the crack front. However, as mentioned in Sec. 6.4.5 there are instances when the variation of SIFs needs to be captured accurately. Whereas, the number of enriched elements can be reduced by applying enrichment sufficiently to elements adjacent to the crack front while applying the conventional approximation to the remaining elements, with a slight impact on accuracy.

6.5 Conclusion

This chapter presents a three-dimensional extended dual boundary element method, with enrichment functions based on the leading order term in the Williams expansions. The enrichment was applied only to elements on the crack surfaces, while other elements were treated in a conventional fashion. The use of enrichment contributes three degrees of freedom to each location at the crack front, where $\tilde{K}_I^\lambda$, $\tilde{K}_{II}^\lambda$ and $\tilde{K}_{III}^\lambda$ need to be evaluated. It has been confirmed that enforcement of displacement continuity at the crack front provides sufficient auxiliary equations to accommodate the additional degrees of freedom arising because of enrichment. This yields a square system that can be solved to evaluate SIFs directly without any requirement for postprocessing calculations such as the J-integral. The additional columns holding the coefficients related to $\tilde{K}_I$, $\tilde{K}_{II}$ and $\tilde{K}_{III}$ are inserted into the last part of matrix $\boldsymbol{H}$ to reduce the effect on the system matrices when implementing enrichment. Whereas the terms related to traction remain unchanged, since crack surfaces are considered traction-free. An appropriate scaling factor is required as the use of enrichment increases the system's conditioning number. The utilisation of enrichment does not increase the degree of singularity, and a subtraction technique can be used to evaluate enriched terms. Also, a similar approach is used to determine conventional terms that contain strongly singular and hypersingular integrals.

The proposed enrichment approach was used to evaluate SIFs directly without any requirement for postprocessing calculations such as the J-integral. The results were improved by increasing the number of enriched elements which can be achieved without increasing the size of the system, with negligible additional computational costs. In addition, accuracy can be improved by utilising additional nodes when applying the displacement constraint. The method has been successfully used to model a penny shaped central crack under pure mode I conditions. A comparison of the displacements obtained using the enrichment function terms was undertaken to show the important of including the nodal displacement. In addition, the results showed the directly determined SIFs were accurate when compared with the J-integral method, even when using the J-integral with enriched DBEM.

Chapter 7

Conclusion

As outlined in the preceding chapters the need for a tool to provide an accurate evaluation of SIFs, prompted interest in devising numerical methods capable of modelling fracture problems efficiently and accurately. To achieve this goal, this thesis introduced a direct approach to evaluating SIFs for two-dimensional and three-dimensional crack problems in this thesis. Furthermore, by enforcing continuity at the crack tip, a novel auxiliary equation was applied to yield a square system in two-dimensions. In addition, a new formulation was introduced to demonstrate the enrichment of DBEM in 3D, including the implementation of enriched displacements and the treatment of singular integrals. The proposed approach utilised the enrichment of the DBEM, to capture crack tip singularity, using the asymptotic solution near the crack tip in the form of the leading order term in the Williams expansions for displacement. The implementation of this approach can be achieved by applying minor changes to promote easy integration with a conventional DBEM code.

For crack problems in two-dimensions, enrichment functions are introduced to the approximation of displacements for elements on the crack surface. Once an enriched form of displacement is substituted into the DBIE and TBIE, an enriched dual boundary element method is achieved, that can be applied to cracks with coincident crack surfaces. However, the introduction of enrichment functions to the system prompts the need for additional equations to yield a square system that is able to solve the newly added unknowns. The additional equations are produced by forcing the continuity of displacements at the crack tip. These procedures are outlined in Chapter 5 where an enriched displacement approximation and the associated additional degrees of freedom are stated. The method is then applied to various types of cracks to verify accuracy and determine factors that could affect accuracy. Observable remarks for cracks in two-dimensions are listed as key points below:

- Enrichment terms are inserted after the latest column of conventional matrix $\boldsymbol{H}$, whereas the right handed side matrix $\boldsymbol{G}$ is not affected by the enrichment.
- The implicit enrichment technique allows for the direct evaluation of stress intensity factors without the need for a postprocessing method such as the J-integral.
- The use of enrichment introduces only two additional degrees of freedom to the system per crack tip, and is not affected by the number of enriched elements.
- Additional equations can be generated by forcing displacement continuity at the crack tip to yield a square system. These equations are straightforward in implementation and cheap to calculate.
- Enrichment of all crack surface elements shows improvement in the accuracy of SIFs. In addition, further improvements to accuracy can be achieved by increasing the number of nodes used for displacement constraints.
- The use of enriched DBEM with J-integral yields results that are more accurate than direct SIFs. However, this comes at the cost of an additional postprocessing calculation.

A similar concept to that used with two-dimensional problems has been applied to cracks in three-dimensions. the literature confirms that, the crack tip asymptotic solution is valid for cracks in three-dimensions when considering a perpendicular disc to the crack plane. Therefore, the leading order term in the Williams expansions for displacement has been utilised to enrich the displacement approximations for three-dimensional cracks. An outline of how to extend the method to three-dimensions has been presented in Chapter 6. A penny shaped crack has been considered to verify the method accuracy. The observed remarks are listed as key points, as follows:

- The matrix assembly in three-dimension is similar to that used for two dimensions cracks where the enrichment entries are added after the last column of the conventional $\boldsymbol{H}$ matrix.
- The number of added degrees of freedom depends on the number of nodes at the crack front where the stress intensity factor for modes I, II and III needs to be evaluated.
- Additional equations can be generated by forcing displacement continuity at the crack front. However, the displacement constraints in three-dimensions require a sufficient number of nodes to be arranged in a perpendicular way to the crack front.
- Since the displacement calculated by the enrichment function is associated with local coordinates with the origin at the crack tip, a rotation matrix must be used to transfer this displacement to global coordinates.
- For a horizontal crack consisting only of pure mode I, the direct method can evaluate stress intensity factor for mode I with remarkable accuracy without the need for a postprocessing technique.
- The direct evaluation of stress intensity factor can be extended to assess SIFs for mixed mode cracks.

The enrichment approach presented in this thesis can be achieved by applying enriched displacement approximation to elements that are adjacent to the crack tip, which allows for remaining elements to be handled in a conventional manner. This technique provides flexibility, allowing the same code to be employed with enrichment or without enrichment. Moreover, the use of the dual boundary element method enables crack problems with coincident surfaces to be modelled in a single domain. However, the implementation of

DBEM increases the integral singularity degrees that imply the need for an appropriate method to be applied to strongly singular and hypersingular integrals. On the other hand, the enrichment equations do not affect the degree singularity. Although they need to be expanded to subtract the singularity (when considering apply Guiggiani method) since they are functions of the intrinsic coordinates (ξ_1, ξ_2). In addition, it should be noted that a suitable scale factor needs to be applied to the enrichment entries in matrix $\boldsymbol{H}$ since the value of these entries is very small in comparison with the entries associated with conventional terms.

Finally, the presented approach has the potential for further application and improvement, as summarised in the following points:

- Since the direct approach allows SIFs to be evaluated directly without the need for the postprocessing method. It is clear that the application of the method to crack propagation will reduce computational costs, where SIFs need to be updated as cracks advance through the material. In addition, the main advantage of using the boundary element method is to include the newly added elements to the system by each crack propagation step by calculating only rows and columns that correspond to those additional elements.

- For two-dimensional crack problems the approach was extended to anisotropic materials by [102] to investigate enrichment functions embedded into the BEM formulation. The enrichment functions were obtained using the Stroh formalism; a concise formulation that is dependent only on material properties. In further developments, this can be applied to anisotropic materials in three-dimensions.

- The XBEM approach described in this thesis could be further accelerated by using the Fast Multipole Method (FMM) to provide a powerful solution. In addition, the XBEM can be accelerated by Adaptive Cross Approximation (ACA). This allows parts of the system matrix to be approximated without the determination of the fundamental solution.

- It is possible to extend the XBEM in three-dimensions to regions where the cracks break out at the boundary surface. This will require a careful handling of the enrichment at the higher order singularity at the breakout point, and also some enrichment of the elements on the external surface. This latter enrichment for three-dimensional XBEM could look very similar to the enrichment in 2D XFEM.

References

[1] B. R. Swopes, "This day in aviation important dates in aviation history; 28 april 1988." `http://www.thisdayinaviation.com/28-april-1988`. Accessed: 25-06-2015.

[2] S. laboratory, "Charpy v-notch impact rig." `http://www.soetelaboratory.ugent.be/05_a_charpy.shtml`. Accessed: 18-03-2016.

[3] T. Belytschko and T. Black, "Elastic crack growth in finite elements with minimal remeshing," *International Journal of Fracture Mechanics*, vol. 45, pp. 601–620, 1999.

[4] Q. Z. Xiao, B. L. Karihaloo, and X. Y. Liu, "Direct determination of SIF and higher order terms of mixed mode cracks by a hybrid crack element," *International Journal of Fracture*, vol. 125, no. 3-4, pp. 207–225, 2004.

[5] D. P. Rooke and D. J. Carwright, *Compendium of stress intensity factors*. Stationery Office, Great Britain, Ministry of Defence, Procurement Executive, 1976.

[6] A. Zehnder, *Fracture Mechanics*, vol. 62 of *Lecture Notes in Applied and Computational Mechanics*. Dordrecht: Springer Netherlands, 2002.

[7] A. A. Griffith, "The phenomena of rupture and flow in solids," *Philosophical Transactions of the Royal Society A: Mathematical, Physical and Engineering Sciences*, vol. 221, no. 582-593, pp. 163–198, 1920.

[8] G. R. Irwin, "Fracture dynamics in fracturing of metals," *American Society for Metals*, pp. 147–166, 1948.

[9] V. Jr, "The finite element method for prediction of crack behavior," *Nuclear Engineering and Design*, vol. 11, no. 2, pp. 323–332, 1970.

[10] D. Owen and A. Fawkes, *Engineering Fracture Mechanics: Numerical Methods and Applications.* Pineridge Press Limited, 1983.

[11] J. M. Melenk and I. Babuška, "The partition of unity finite element method: Basic theory and applications," *Computer Methods in Applied Mechanics and Engineering*, vol. 139, pp. 289–314, 1996.

[12] M. L. William, "On the stress distribution at the base of a stationary crack," *Journal of Applied Mechanics*, vol. 24, pp. 109–111, 1957.

[13] S. E. Benzley, "Representation of singularities with isoparametric finite elements," *International Journal for Numerical Methods in Engineering*, vol. 8, pp. 537–545, 1974.

[14] R. Simpson and J. Trevelyan, "A partition of unity enriched dual boundary element method for accurate computations in fracture mechanics," *Computer Methods in Applied Mechanics and Engineering*, vol. 200, no. 1, pp. 1–10, 2011.

[15] E. Kirsch, "Die theorie der elastizität und die bedürfnisse der festigkeitslehre," *Zeitschrift des Vereins deutscher Ingenieure*, vol. 42, no. 28, pp. 797–807, 1898.

[16] C. E. Inglis, "Stresses in a plate due to the presnce of cracks and sharp corners," *Trans. I.N.A.*, vol. XLIV, p. 15, 1913.

[17] G. R. Irwin, "Analysis of stresses and strains near the end of cracking traversing a plate," *Journal of Applied Mechanics*, vol. 24, pp. 361 – 364, 1957.

[18] H. M. Westergaard, "Bearing and cracks," *Journal of Applied Mechanics*, vol. B9, pp. A49–A53, 1939.

[19] N. I. Muskhelishvili, *Some basic problems of the mathematical theory of elasticity.* Springer Science + Business Media, 1977.

[20] G. C. Sih, “Stress distribution near internal crack tips for longitudinal shear problems,” *Journal of Applied Mechanics*, vol. 32, p. 51, 1965.

[21] R. J. Hartranft and G. C. Sih, “The use of eigenfunction expansions in the general solution of three-dimensional crack problems,” *Journal of Mathematics and Mechanics*, vol. 19, pp. 123–138, 1969.

[22] I. N. Sneddon, “The distribution of stress in the neighbourhood of a crack in an elastic solid,” *Proceedings of the Royal Society of London. Series A, Mathematical and Physical Sciences*, vol. 187, no. 1009, pp. 229–260, 1946.

[23] H. Tada, P. C. Paris, and G. R. Irwin, *The Stress Analysis of Cracks - Handbook*. Paris Productions Inc., St Louis, MO, 1985.

[24] P. Paris and F. Erdogan, “A critical analysis of crack propagation laws,” *Journal of Basic Engineering*, vol. 85, no. 4, p. 528, 1963.

[25] M. Szata and G. Lesiuk, “Algorithms for the estimation of fatigue crack growth using energy method,” *Archives of Civil and Mechanical Engineering*, vol. 9, no. 1, pp. 119–134, 2009.

[26] N. Pugno, M. Ciavarella, P. Cornetti, and A. Carpinteri, “A generalized paris’ law for fatigue crack growth,” *Journal of the Mechanics and Physics of Solids*, vol. 54, no. 7, pp. 1333–1349, 2006.

[27] A. Hrennikoff, “Solution of problems of elasticity by the frame-work method,” *Applied Scientific Research*, vol. A8, no. 4, pp. 169–175, 1941.

[28] D. Mchenry, “A lattice analogy for the solution of stress problems,” *Journal of the ICE*, vol. 21, no. 2, pp. 59–82, 1943.

[29] R. Courant, “Variational methods for the solution of problems of equilibrium and vibrations,” *Bulletin of the American Mathematical Society*, vol. 49, no. 1, pp. 1–24, 1943.

[30] S. Levy, “Structural analysis and influence coefficients for delta wings,” *Journal of the Aeronautical Sciences*, vol. 20, no. 7, pp. 449–454, 1953.

[31] J. H. Argyris and S. Kelsey, *Energy Theorems and Structural Analysis*, vol. 26. Boston, MA: Springer US, 1960.

[32] C. V. Nielsen, W. Zhang, L. M. Alves, N. Bay, and P. A. F. Martins, *Modeling of Thermo-Electro-Mechanical Manufacturing Processes.* Springer London, 2013.

[33] D. Hutton, *Fundamentals of Finite Element Analysis.* McGraw-Hill series in mechanical engineering, McGraw-Hill, 2004.

[34] M. Kuna, *Finite Elements in Fracture Mechanics.* Springer Netherlands, 2013.

[35] R. D. Henshell and K. G. Shaw, “Crack tip finite elements are unnecessary,” *International Journal for Numerical Methods in Engineering*, vol. 9, pp. 495–507, 1975.

[36] R. S. Barsoum, “On the use of isoparametric finite elements in linear fracture mechanics,” *International Journal for Numerical Methods in Engineering*, vol. 10, no. 1, pp. 25–37, 1976.

[37] L. Banks-Sills, “Application of the finite element method to linear elastic fracture mechanics,” *Applied Mechanics Reviews*, vol. 44, no. 10, p. 447, 1991.

[38] L. Banks-Sills, “Update: Application of the finite element method to linear elastic fracture mechanics,” *Applied Mechanics Reviews*, vol. 63, no. 2, p. 020803, 2010.

[39] J. Dolbow and T. Belytschko, “A finite element method for crack growth without remeshing,” *International Journal for Numerical Methods in Engineering*, vol. 46, pp. 131–150, 1999.

[40] J. Dolbow, N. Moës, and T. Belytschko, “Discontinuous enrichment in finite elements with a partition of unity method,” *Finite Elements in Analysis and Design*, vol. 46, pp. 235–260, 2000.

[41] N. Sukumar, N. Moës, B. Moran, and T. Belytschko, “Extended finite element method for three-dimensional crack modeling,” *International Journal for Numerical Methods in Engineering*, vol. 48, pp. 1549–1570, 2000.

[42] N. Sukumar, D. J. Srolovitz, T. J. Baker, and J. H. Prevost, “Brittle fracture in polycrystalline microstructures with the extended finite element method,” *International Journal for Numerical Methods in Engineering*, vol. 59, pp. 2015–2037, 2003.

[43] R. Huang, N. Sukumar, and J. H. Prévost, “Modeling quasi-static crack growth with the extended finite element method, part II: Numerical applications,” *International Journal of Solids and Structures*, vol. 40, pp. 7539–7552, 2003.

[44] X. Y. Liu, Q. Z. Xiao, and B. L. Karihaloo, “XFEM for direct evaluation of mixed mode SIFs in homogeneous and bi-materials,” *International Journal for Numerical Methods in Engineering*, vol. 59, pp. 1103–1118, 2004.

[45] A. Legay, H. W. Wang, and T. Belytschko, “Strong and weak arbitrary discontinuities in spectral finite elements,” *International Journal for Numerical Methods in Engineering*, vol. 64, pp. 991–1008, 2005.

[46] L. Wu, L. X. Zhang, and Y. K. Guo, “A review of the extended finite element for fracture analysis of structures,” *AMM*, vol. 444-445, pp. 96–102, oct 2013.

[47] R. Spatschek, E. Brener, and A. Karma, “Phase field modeling of crack propagation,” *Philosophical Magazine*, vol. 91, no. 1, pp. 75–95, 2011.

[48] M. Ambati, T. Gerasimov, and L. De Lorenzis, “A review on phase-field models of brittle fracture and a new fast hybrid formulation,” *Computational Mechanics*, vol. 55, no. 2, pp. 383–405, 2015.

[49] B. Bourdin, G. A. Francfort, and J. J. Marigo, “Numerical experiments in revisited brittle fracture,” *Journal of the Mechanics and Physics of Solids*, vol. 48, no. 4, pp. 797–826, 2000.

[50] G. A. Francfort and J. J. Marigo, “Revisiting brittle fracture as an energy minimization problem,” *Journal of the Mechanics and Physics of Solids*, vol. 46, no. 8, pp. 1319–1342, 1998.

[51] H. Amor, J. J. Marigo, and C. Maurini, “Regularized formulation of the variational brittle fracture with unilateral contact: Numerical experiments,” *Journal of the Mechanics and Physics of Solids*, vol. 57, no. 8, pp. 1209–1229, 2009.

[52] A. Takezawa and M. Kitamura, “Phase field method to optimize dielectric devices for electromagnetic wave propagation,” *Journal of Computational Physics*, vol. 257, pp. 216–240, 2014.

[53] M. Asta, C. Beckermann, A. Karma, W. Kurz, R. Napolitano, M. Plapp, G. Purdy, M. Rappaz, and R. Trivedi, “Solidification microstructures and solid-state parallels: Recent developments, future directions,” *Acta Materialia*, vol. 57, no. 4, pp. 941–971, 2009.

[54] A. Abdollahi and I. Arias, “Phase-field simulation of anisotropic crack propagation in ferroelectric single crystals: effect of microstructure on the fracture process,” *Modelling and Simulation in Materials Science and Engineering*, vol. 19, no. 7, p. 74010, 2011.

[55] R. D. M. Travasso, M. Castro, and J. C. R. E. Oliveira, “The phase-field model in tumor growth,” *Philosophical Magazine*, vol. 91, no. 1, pp. 183–206, 2011.

[56] H. Henry and M. Adda-Bedia, “Fractographic aspects of crack branching instability using a phase-field model,” *Physical Review E*, vol. 88, no. 6, p. 60401, 2013.

[57] J. D. Eshelby, “The force on an elastic singularity,” *Philosophical Transactions of the Royal Society A: Mathematical, Physical & Engineering Sciences*, vol. 224, pp. 87–112, 1951.

[58] J. D. Eshelby, “Energy relations and the energy-momentum tensor in continuum mechanics,” in *Inelastic behaviour of soilds* (M. F. Kanninen, ed.), 1970.

[59] B. D. Coleman and W. Noll, "The thermodynamics of elastic materials with heat conduction and viscosity," *Archive for Rational Mechanics and Analysis*, vol. 13, no. 1, pp. 167–178, 1963.

[60] M. Gurtin, "The nature of configurational forces," *Archive for Rational Mechanics and Analysis*, vol. 131, no. 1, pp. 67–100, 1995.

[61] G. Dal Maso and R. Toader, "A model for the quasi-static growth of brittle fracture: existence and approximation results," *Archives for Rational Mechanics and Analysis*, vol. 162, pp. 101–135, 2002.

[62] P. Steinmann, D. Ackermann, and F. J. Barth, "Application of material forces to hyperelastostatic fracture mechanics. II. computational setting," *International Journal of Solids and Structures*, vol. 38, pp. 5509–5526, 2001.

[63] R. Denzer, F. J. Barth, and P. Steinmann, "Studies in elastic fracture mechanics based on the material force method," *International Journal for Numerical Methods in Engineering*, vol. 58, pp. 1817–1835, 2003.

[64] R. Mueller, S. Kolling, and D. Gross, "On configurational forces in the context of the finite element method," *International Journal for Numerical Methods in Engineering*, vol. 53, no. 7, pp. 1557–1574, 2002.

[65] P. Heintz, F. Larsson, P. Hansbo, and K. Runesson, "Adaptive strategies and error control for computing material forces in fracture mechanics," *International Journal for Numerical Methods in Engineering*, vol. 60, no. 7, pp. 1287–1299, 2004.

[66] E. Gürses and C. Miehe, "A computational framework of three-dimensional configurational-force-driven brittle crack propagation," *Computer Methods in Applied Mechanics and Engineering*, vol. 198, no. 15, pp. 1413–1428, 2009.

[67] R. Mueller and G. A. Maugin, "On material forces and finite element discretizations," *Computational Mechanics*, vol. 29, no. 1, pp. 52–60, 2002.

[68] R. Larsson and M. Fagerström, "A framework for fracture modelling based on the material forces concept with XFEM kinematics," *International Journal for Numerical Methods in Engineering*, vol. 62, no. 13, pp. 1763–1788, 2005.

[69] P. Heintz, "On the numerical modelling of quasi-static crack growth in linear elastic fracture mechanics," *International Journal for Numerical Methods in Engineering*, vol. 65, no. 2, pp. 174–189, 2006.

[70] Ł. Kaczmarczyk, M. M. Nezhad, and C. Pearce, "Three-dimensional brittle fracture: configurational-force-driven crack propagation," *International Journal for Numerical Methods in Engineering*, vol. 97, no. 7, pp. 531–550, 2014.

[71] C. Miehe, E. Gürses, and M. Birkle, "A computational framework of configurational-force-driven brittle fracture based on incremental energy minimization," *International Journal of Fracture*, vol. 145, no. 4, pp. 245–259, 2007.

[72] V. P. Nguyen, T. Rabczuk, S. Bordas, and M. Duflot, "Meshless methods: A review and computer implementation aspects," *Mathematics and Computers in Simulation*, vol. 79, pp. 763–813, dec 2008.

[73] G. R. Liu and B. Liu, *Smoothed Particle Hydrodynamics: A Meshfree Particle Method*. World Scientific, 2003.

[74] L. B. Lucy, "A numerical approach to the testing of the fission hypothesis," *The astronomical journal*, vol. 82, pp. 1013–1024, 1977.

[75] R. A. Gingold and J. J. Monaghan, "Smoothed particle hydrodynamics: Theory and application to non-spherical stars," *Monthly notices of the royal astronomical society*, vol. 181, p. 375, 1977.

[76] T. Belytschko, Y. Y. Lu, and L. Gu, "Element-free Galerkin methods," *International Journal for Numerical Methods in Engineering*, vol. 37, no. 2, pp. 229–256, 1994.

[77] D. Organ, M. Fleming, T. Terry, and T. Belytschko, “Continuous meshless approximations for nonconvex bodies by diffraction and transparency,” *Computational mechanics*, vol. 18, no. 3, pp. 225–235, 1996.

[78] T. Belytschko, L. Gu, and Y. Y. Lu, “Fracture and crack growth by element-free Galerkin methods,” *Modelling and Simulation in Materials Science and Engineering*, vol. 2, no. 3A, pp. 519–534, 1994.

[79] T. Belytschko and M. Fleming, “Smoothing, enrichment and contact in the element-free Galerkin method,” *Computers & Structures*, vol. 71, no. 2, pp. 173–195, 1999.

[80] M. Fleming, Y. Chu, B. Moran, T. Belytschko, Y. Lu, and L. Gu, “Enriched element-free Galerkin methods for crack tip fields,” *International Journal for Numerical Methods in Engineering*, vol. 40, no. 8, pp. 1483–1504, 1997.

[81] B. N. Rao and S. Rahman, “Mesh-free analysis of cracks in isotropic functionally graded materials,” *Engineering Fracture Mechanics*, vol. 70, no. 1, pp. 1–27, 2003.

[82] B. Nayroles, G. Touzot, and P. Villon, “Generalizing the finite element method: Diffuse approximation and diffuse elements,” *Computational Mechanics*, vol. 10, no. 5, pp. 307–318, 1992.

[83] B. N. Rao and S. Rahman, “An efficient meshless method for fracture analysis of cracks,” *Computational Mechanics*, vol. 26, pp. 398–408, oct 2000.

[84] S. N. Atluri and T. Zhu, “A new meshless local petrov-galerkin (MLPG) approach in computational mechanics,” *Computational Mechanics*, vol. 22, pp. 117–127, aug 1998.

[85] P. Xia and K. X. Wei, “Application of the meshless local petrov-galerkin method in the elasto-plastic fracture problem of moderately thick plate,” *AMM*, vol. 155-156, pp. 485–490, feb 2012.

[86] S. D. Daxini and J. M. Prajapati, “A review on recent contribution of meshfree methods to structure and fracture mechanics applications,” *The Scientific World Journal*, vol. 2014, pp. 1–13, 2014.

[87] G. Green, “An essay on the application on mathematical analysis to the theories of electricity and magnetism,” *Nottingham*, 1828.

[88] M. A. Jaswon, “Integral equation methods in potential theory. I,” *Proceedings of the Royal Society of London A: Mathematical, Physical and Engineering Sciences*, vol. A275, pp. 23–32, 1963.

[89] F. J. Rizzo, “An integral equation approach to boundary value problems of classical elastostatics,” *Quarterly of Applied Mathematics*, vol. 25, pp. 83–95, 1967.

[90] T. A. Cruse, “Numerical solutions in three dimensional elastostatics,” *International Jornal of solids and structure*, vol. 5, pp. 1259–1274, 1969.

[91] M. H. Aliabadi, “Boundary element formulations in fracture mechanics,” *Applied Mechanics Reviews*, vol. 50, no. 2, pp. 83–96, 1997.

[92] T. Cruse, “Two-dimensional BIE fracture mechanics analysis,” *Applied Mathematical Modelling*, vol. 2, no. 4, pp. 287–293, 1978.

[93] G. E. Blandford, A. R. Ingraffea, and J. A. Liggett, “Two-dimensional stress intensity factor computations using the boundary element method,” *International Journal for Numerical Methods in Engineering*, vol. 17, no. 3, pp. 387–404, 1981.

[94] A. Portela, M. H. Aliabadi, and D. P. Rooke, “The dual boundary element method: Effective implementation for crack problems,” *International Journal for Numerical Methods in Engineering*, vol. 33, pp. 1269–1287, 1992.

[95] Y. Mi and M. H. Aliabadi, “Dual boundary element method for three-dimensional fracture mechanics analysis,” *Engineering Analysis with Boundary Elements*, vol. 10, no. 2, pp. 161–171, 1992.

[96] J. T. Chen and H. K. Hong, "Review of dual boundary element methods with emphasis on hypersingular integrals and divergent series," *Applied Mechanics Reviews*, vol. 52, pp. 17–33, 1999.

[97] A. Portela, M. H. Aliabadi, and D. P. Rooke, "Efficient boundary element analysis of sharp notched plates," *International Journal for Numerical Methods in Engineering*, vol. 32, pp. 445–470, 1991.

[98] M. Aliabadi, "BEM for crack dynamics," in *Boundary Element Methods for Soil-Structure Interaction* (W. Hall and G. Oliveto, eds.), pp. 297–314, Springer Netherlands, 2003.

[99] J. Watson, "Singular boundary elements for the analysis of cracks in plane strain," *International journal for numerical methods in engineering*, vol. 38, pp. 2389–2411, 1995.

[100] R. Simpson and J. Trevelyan, "Evaluation of J_1 and J_2 integrals for curved cracks using an enriched boundary element method," *Engineering Fracture Mechanics*, vol. 78, no. 4, pp. 623–637, 2011.

[101] J. R. Rice, "A path independent integral and the approximate analysis of strain concentration by notches and cracks," *Journal of applied mechanics*, vol. 35, pp. 379–386, 1968.

[102] G. Hattori, I. A. Alatawi, and J. Trevelyan, "An impliit enrihment approach in the boundary element method framework for stress intensity fators calculation in anisotropic materials," *Manuscript submitted for publication*, 2015.

[103] Z. Suo, "Singularities, interfaces and cracks in dissimilar anisotropic media," *Proceedings of the Royal Society A: Mathematical, Physical and Engineering Sciences*, vol. 427, pp. 331–358, feb 1990.

[104] S. Li, M. E. Mear, and L. Xiao, "Symmetric weak-form integral equation method

for three-dimensional fracture analysis," *Computer Methods in Applied Mechanics and Engineering*, vol. 151, no. 3, pp. 435–459, 1998.

[105] I. Alatawi and J. Trevelyan, "A direct evaluation of stress intensity factors using the extended dual boundary element method," *Engineering Analysis with Boundary Elements*, vol. 52, pp. 56 – 63, 2015.

[106] P. Tong, T. H. Pian, and S. J. Lasry, "A hybrid-element approach to crack problems in plane elasticity," *International Journal for Numerical Methods in Engineering*, vol. 7, pp. 297–308, 1973.

[107] R. K. L. Su and S. L. Fok, "Determination of coefficients of the crack tip asymptotic field by fractal hybrid finite elements," *Engineering Fracture Mechanics*, vol. 74, pp. 1649–1664, 2007.

[108] M. Treifi and S. O. Oyadiji, "Evaluation of mode III stress intensity factors for bi-material notched bodies using the fractal-like finite element method," *Computers & Structures*, vol. 129, pp. 99–110, 2013.

[109] A. Y. T. Leung and R. K. L. Su, "Mode I crack problems by fractal two level finite element methods," *Engineering Fracture Mechanics*, vol. 48, pp. 847–856, 1994.

[110] A. Y. T. Leung and R. K. L. Su, "Mixed-mode two-dimensional crack problem by fractal two level finite element method," *Engineering Fracture Mechanics*, vol. 51, pp. 889–895, 1995.

[111] J. Klusák, T. Profant, and M. Kotoul, "A comparison of two direct methods of generalized stress intensity factor calculations of bi-material notches," in *Key Engineering Materials*, vol. 385, pp. 409–412, Trans Tech Publ, 2008.

[112] C. Song, F. Tin-Loi, and W. Gao, "A definition and evaluation procedure of generalized stress intensity factors at cracks and multi-material wedges," *Engineering Fracture Mechanics*, vol. 77, no. 12, pp. 2316–2336, 2010.

[113] N. Ioakimidis, “A remark on the direct numerical determination of stress intensity factors at crack tips,” *International Journal for Numerical Methods in Engineering*, vol. 18, no. 9, pp. 1416–1419, 1982.

[114] T. A. Cruse, “Boundary-integral equation formulation and solution,” in *Mechanics: Computational Mechanics*, pp. 17–44, Springer Science + Business Media, 1988.

[115] N. G. Zamani and W. Sun, “A direct method for calculating the stress intensity factor in BEM,” *Engineering analysis with boundary elements*, vol. 11, no. 4, pp. 285–292, 1993.

[116] C. R. Langlois, A. Gravouil, M. C. Baietto, and J. Réthoré, “Three-dimensional simulation of crack with curved front with direct estimation of stress intensity factors,” *International Journal for Numerical Methods in Engineering*, vol. 101, no. 8, pp. 635–652, 2015.

[117] E. Shields, T. Srivatsan, and J. Padovan, “Analytical methods for evaluation of stress intensity factors and fatigue crack growth,” *Engineering fracture mechanics*, vol. 42, no. 1, pp. 1–26, 1992.

[118] R. H. Dodds and D. T. Read, “Experimental and numerical studies of the J-integral for a surface flaw,” *International Journal of Fracture*, vol. 43, no. 1, pp. 47–67, 1990.

[119] T. Murakami and T. Sato, “Three-dimensional J-integral calculations of part-through surface crack problems,” *Computers & Structures*, vol. 17, no. 5, pp. 731–736, 1983.

[120] H. G. DeLorenzi, “On the energy release rate and the J-integral for 3-D crack configurations,” *International Journal of Fracture*, vol. 19, no. 3, pp. 183–193, 1982.

[121] N. Miyazaki, T. Ikeda, T. Soda, and T. Munakata, “Stress intensity factor analysis of interface crack using boundary element method–application of contour-integral method,” *Engineering Fracture Mechanics*, vol. 45, no. 5, pp. 599–610, 1993.

[122] P. Wen, M. Aliabadi, and D. Rooke, “A contour integral for the evaluation of stress intensity factors,” *Applied Mathematical Modelling*, vol. 19, no. 8, pp. 450–455, 1995.

[123] M. Stern, E. Becker, and R. Dunham, “A contour integral computation of mixed-mode stress intensity factors,” *International Journal of Fracture*, vol. 12, no. 3, pp. 359–368, 1976.

[124] H. Ishikawa, H. Kitagawa, and H. Okamura, “J-integral of a mixed mode crack and its application,” in *Mechanical Behaviour of Materials*, pp. 447–455, Elsevier BV, 1980.

[125] G. P. Nikishkov and S. N. Atluri, “Calculation of fracture mechanics parameters for an arbitrary three-dimensional crack, by the equivalent domain integral method,” *International Journal for Numerical Methods in Engineering*, vol. 24, no. 9, pp. 1801–1821, 1987.

[126] R. H. Rigby and M. H. Aliabadi, “Mixed-mode J-integral method for analysis of 3D fracture problems using BEM,” *Engineering Analysis with Boundary Elements*, vol. 11, no. 3, pp. 239–256, 1993.

[127] O. Huber, J. Nickel, and G. Kuhn, “On the decomposition of the J-integral for 3D crack problems,” *International Journal of Fracture*, vol. 64, no. 4, pp. 339–348, 1993.

[128] K. N. Shivakumar and I. S. Raju, “An equivalent domain integral method for three-dimensional mixed-mode fracture problems,” *Engineering Fracture Mechanics*, vol. 42, no. 6, pp. 935–959, 1992.

[129] R. Rigby and M. Aliabadi, “Decomposition of the mixed-mode J-integral – revisited,” *International Journal of Solids and Structures*, vol. 35, no. 17, pp. 2073–2099, 1998.

[130] A. H. D. Cheng and D. T. Cheng, “Heritage and early history of the boundary

element method," *Engineering Analysis with Boundary Elements*, vol. 29, no. 3, pp. 268–302, 2005.

[131] H. Aliabadi, *The Boundary Element Method, Applications in Solids and Structures.* The Boundary Element Method, John Wiley & Sons, 2002.

[132] "Fundamental solution," in *Encyclopedia of Thermal Stresses*, pp. 1893–1893, Springer Science + Business Media, 2014.

[133] L. Kelvin and W. Thomson, "Note on the integration of the equation of equilbrium of an elastic solid," in *Mathematical and Physical Papers*, pp. 97–99, Cambridge University Press (CUP), 2011.

[134] M. Guiggiani and A. Gigante, "A general algorithm of multidimensional cauchy principal value integrals in the boundary element method," *American Society of Mechanical Engineers*, vol. 57, pp. 906–915, 1990.

[135] A. Becker, *The Boundary Element Method in Engineering: A Complete Course.* McGraw-Hill, 1992.

[136] H. Hong and J. Chen, "Derivations of integral equations of elasticity," *J. Eng. Mech*, vol. 114, pp. 1028–1044, 1988.

[137] X. W. Gao and T. G. Davies, "Adaptive integration in elasto-plastic boundary element analysis," *Journal of the Chinese Institute of Engineers*, vol. 23, no. 3, pp. 349–356, 2000.

[138] J. C. F. Telles and C. A. Brebbia, "On the application of the boundary element method to plasticity," *Applied Mathematical Modeling*, vol. 3, pp. 466–470, 1979.

[139] J. C. F. Telles, "A self-adaptive coordinate transformation for efficient numerical evaluation of general boundary integrals," *International Journal for Numerical Methods in Engineering*, vol. 24, pp. 959–973, 1987.

[140] J. C. Lachat and J. O. Watson, "Effective numerical treatment of boundary integral equations: A formulation for three-dimensional elastostatics," *International Journal for Numerical Methods in Engineering*, vol. 10, pp. 991–1005, 1976.

[141] M. Guiggiani and P. Casalini, "Direct computation of cauchy principal value integrals in advanced boundary element," *International Journal for Numerical Methods in Engineering*, vol. 24, pp. 1711–1716, 1987.

[142] T. A. Cruse, "Numerical evaluation of elastic stress intensity factors by the boundary-integral equation method," *The surface Crack: Physical and Computational Solutions*, pp. 153–170, 1972.

[143] R. Simpson, *Enrichment of the Boundary Element Method through the Partition of Unity Method for Fracture Analysis using Local and Global Formulations.* Doctoral thesis, Durham University, 2010.

[144] M. Guiggiani, G. Krishnasamy, T. J. Rudolphi, F. J. Rizzo, T. J. R. M. Guiggiani G. Krishnasamy, and F. J. Rizzo, "A general algorithm for the numerical solution of hypersingular boundary integral equations," *ASME Jornal of Applied Mechanics*, vol. 59, pp. 604–614, 1992.

[145] G. Dahlquist and Å. Björck, *Numerical Methods.* Dover Books on Mathematics, Dover Publications, 2003.

[146] C. Runge, "Über empirische funktionen und die interpolation zwischen äquidistanten ordinaten," *Zeitschrift für Mathematik und Physik*, vol. 46, pp. 224–243, 1901.

[147] J. Trevelyan, "Concept Analyst." `http://www.conceptanalyst.com/`. Accessed: 25-04-2016.

[148] M. K. Kassir and G. C. Sih, "Griffith's theory of brittle fracture in three dimensions," *International Journal of Engineering Science*, vol. 5, no. 12, pp. 899–918, 1967.

[149] R. J. Hartranft and G. C. Sih, “Stress singularity for a crack with an arbitrarily curved front,” *Engineering Fracture Mechanics*, vol. 9, no. 3, pp. 705–718, 1977.

[150] G. B. Airy, “On the strains in the interior of beams,” *Philosophical Transactions of the Royal Society of London*, vol. 153, pp. 49–79, 1863.

[151] S. Timoshenko, *Theory of elasticity.* Engineering societies monographs, McGraw-Hill, 1951.

Appendix A

Elastic Analysis

A.1 Basic equations of elasticity

Consider an element volume of a loaded body under equilibrium conditions in a three-dimensional domain, as presented in Fig. A.1. Here, the stress acting on the element can be defined by six stress components, which can be represented in tensor notation as σ_{ij} where $i, j = x, y, z$. Such that, σ_{ij} is expressing a stress in j direction, which is acting on a surface defined by a normal in i direction. It is convenient to note that, the stresses are symmetry as $\sigma_{ij} = \sigma_{ji}$. The equilibrium equation for a body subjected to external forces and body forces can be written in tensor form as,

$$\frac{\partial \sigma_{ii}}{\partial x_i} + \frac{\partial \sigma_{ij}}{\partial x_j} + \frac{\partial \sigma_{ik}}{\partial x_k} + b_i = 0 \tag{A.1.1}$$

where b_i denotes body forces. The equation (A.1.1) can be written in compact form to describe $i \neq j \neq k$ as,

$$\sigma_{ij,j} + b_i = 0 \tag{A.1.2}$$

To introduce strain, we must consider a small deformation where strain ϵ_{ij} is defined in terms of displacements as,

$$\epsilon_{ij} = \frac{1}{2}\left(\frac{\partial u_i}{\partial x_j} + \frac{\partial u_j}{\partial x_i}\right) \tag{A.1.3}$$

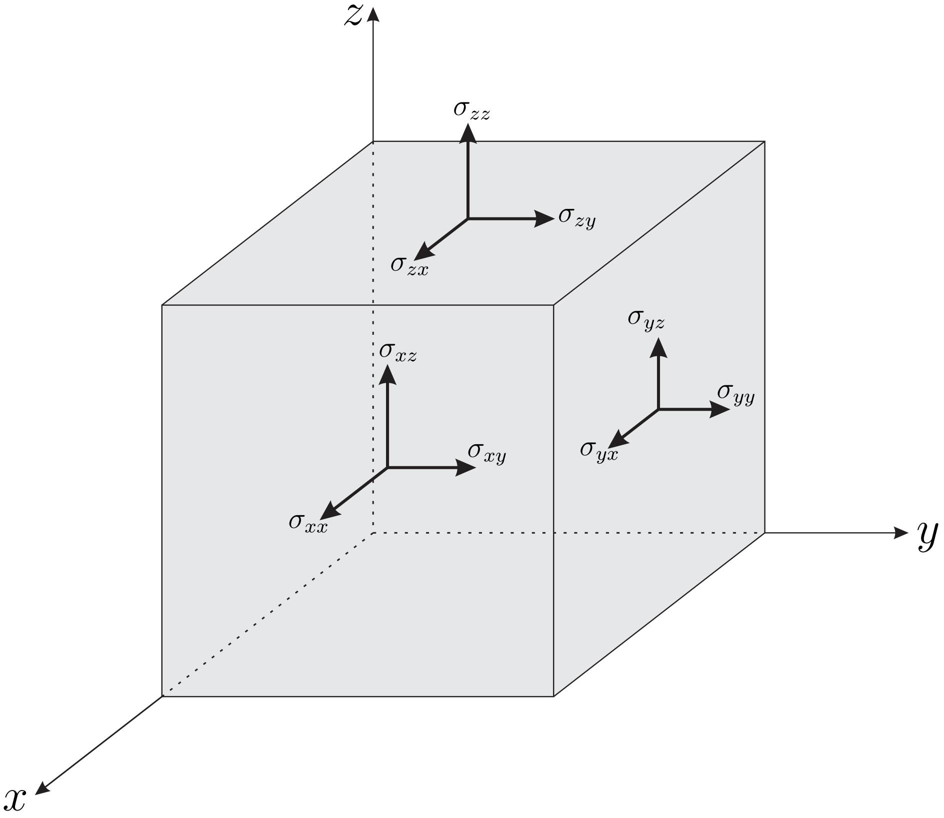

Figure A.1: Stress components on an infinitesimal element

where u_i is the displacement in i direction. The compatibility equations of strain can be expressed as,

$$\frac{\partial^2 \epsilon_{ii}}{\partial x_j^2} + \frac{\partial^2 \epsilon_{jj}}{\partial x_i^2} - 2\frac{\partial^2 \epsilon_{ij}}{\partial x_i \partial x_j} = 0 \tag{A.1.4a}$$

$$\frac{\partial \epsilon_{ij}}{\partial x_j \partial x_k} - \frac{\partial}{\partial x_i}\left(-\frac{\partial \epsilon_{jk}}{\partial x_i} + \frac{\partial \epsilon_{ik}}{\partial x_j} + \frac{\partial \epsilon_{ij}}{\partial x_k}\right) = 0 \quad \text{where} \quad i \neq j \neq k \tag{A.1.4b}$$

Strains and stresses relationship is defined by Hooke's law and can be expressed for an elastic and isotropic material as,

$$\begin{aligned} \epsilon_{xx} &= \frac{1}{E}\left(\sigma_{xx} - \nu(\sigma_{yy} + \sigma_{zz})\right), & \epsilon_{xy} &= \frac{1+\nu}{E}\sigma_{xy} \\ \epsilon_{yy} &= \frac{1}{E}\left(\sigma_{yy} - \nu(\sigma_{xx} + \sigma_{zz})\right), & \epsilon_{yz} &= \frac{1+\nu}{E}\sigma_{yz} \\ \epsilon_{zz} &= \frac{1}{E}\left(\sigma_{zz} - \nu(\sigma_{xx} + \sigma_{yy})\right), & \epsilon_{zx} &= \frac{1+\nu}{E}\sigma_{zx} \end{aligned} \tag{A.1.5}$$

where E is the Young's modulus and ν is the Poisson's ratio. Similarly, stresses can be expressed in terms of strain as,

$$\begin{aligned} \sigma_{xx} &= \lambda e + 2\mu\epsilon_{xx} \ , \qquad \sigma_{xy} = 2\mu\epsilon_{xy} \\ \sigma_{yy} &= \lambda e + 2\mu\epsilon_{yy} \ , \qquad \sigma_{yz} = 2\mu\epsilon_{yz} \\ \sigma_{zz} &= \lambda e + 2\mu\epsilon_{zz} \ , \qquad \sigma_{zx} = 2\mu\epsilon_{zx} \end{aligned} \tag{A.1.6}$$

where the shear modulus μ is defined as,

$$\mu = \frac{E}{2(1+\nu)} \tag{A.1.7}$$

the Lamé constant is given by,

$$\lambda = \frac{2\mu\nu}{2(1-2\nu)} \tag{A.1.8}$$

and the volumetric strain e is defined as,

$$e = \epsilon_{xx} + \epsilon_{yy} + \epsilon_{zz} \tag{A.1.9}$$

Further simplification of the elasticity equations can be made by considering two-dimensional plane strain or plane stress. The plane strain state is applicable to thick plates since geometry and loading do not change significantly in the z direction. Furthermore, displacement u_z is zero, which impose the strain components in z direction as zero, such that $\epsilon_{zz} = \epsilon_{zx} = \epsilon_{zy} = 0$. When applying these assumptions, the strains for plane strain are given by,

$$\begin{aligned} \epsilon_{xx} &= \frac{1-\nu^2}{E}\left(\sigma_{xx} - \frac{\nu}{1-\nu}\sigma_{yy}\right) \\ \epsilon_{yy} &= \frac{1-\nu^2}{E}\left(\sigma_{yy} - \frac{\nu}{1-\nu}\sigma_{xx}\right) \\ \epsilon_{xy} &= \frac{1+\nu}{E}\sigma_{xy} \end{aligned} \tag{A.1.10}$$

The plane stress states can be applied to a thin plate, where stresses in the z direction do not reach any significant value. Consequently, the stresses components in z direction are assumed to be zero, such that $\sigma_{zz} = \sigma_{zx} = \sigma_{zy} = 0$. For plane stress strain components are given by,

$$\begin{aligned} \epsilon_{xx} &= \frac{1}{E}\left(\sigma_{xx} - \nu\sigma_{yy}\right) \\ \epsilon_{yy} &= \frac{1}{E}\left(\sigma_{yy} - \nu\sigma_{xx}\right) \\ \epsilon_{xy} &= \frac{1+\nu}{E}\sigma_{xy} \\ \epsilon_{zz} &= -\frac{\nu}{1-\nu}(\epsilon_{xx} + \epsilon_{yy}) \end{aligned} \tag{A.1.11}$$

Commonly plane strain is considered a general case and Young's modulus, and Poisson's ratio are modified for the case of plane stress. The modified Young's modulus is defined as,

$$\begin{aligned} E' &= E && \text{plane strain} \\ E' &= \frac{E(1+2\nu)}{(1+\nu)^2} && \text{plane stress} \end{aligned} \tag{A.1.12}$$

where E' denotes the modified Young's modulus. Similarly, modified Poisson's ratio is expressed as,

$$\begin{aligned} \nu' &= \nu && \text{plane strain} \\ \nu' &= \frac{\nu}{1+\nu} && \text{plane stress} \end{aligned} \tag{A.1.13}$$

where ν' represents the modified Poisson's ratio.

It is convenient to illustrate how stresses are related to traction in this section. Consider a body subjected to stress and under equilibrium conditions; if we cut through to create a surface (see Fig. A.2) defined by the normal n; then, by state of equilibrium, the tractions relate to the stresses by,

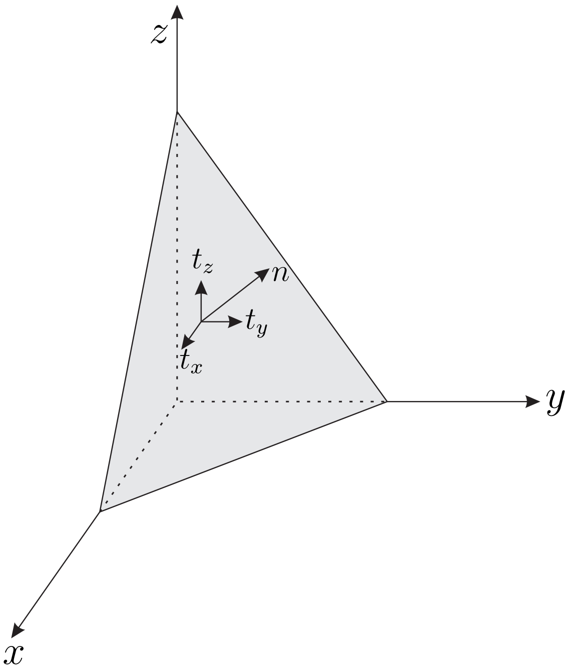

Figure A.2: Traction components acting on the surface of an element

$$\begin{aligned} t_x &= \sigma_{xx} n_x + \sigma_{xy} n_y + \sigma_{xz} n_z \\ t_y &= \sigma_{yx} n_x + \sigma_{yy} n_y + \sigma_{yz} n_z \\ t_z &= \sigma_{zx} n_x + \sigma_{zy} n_y + \sigma_{zz} n_z \end{aligned} \tag{A.1.14}$$

and in tensor form as,

$$t_i = \sigma_{ij} n_j \tag{A.1.15}$$

where t_i is traction in i direction, and n_j is the unit normal in j direction.

A.2 Airy stress functions

Several solutions to plane stress and plane strain problems can be resolved by utilising a particular stress function technique. The Airy stress function is a widely employed technique to reduce the general formulation of a problem to a single governing equation which can be expressed by a single unknown. Furthermore, Airy [150] combines Eqns. (A.1.2),(A.1.3) and (A.1.10) into one function, well known as the Airy stress function. Consider, a cartesian coordinate (x, y), the relationships of the Airy stress function Φ and stresses can be expressed as,

$$\sigma_{xx} = \frac{\partial^2 \Phi}{\partial y^2}\ , \qquad \sigma_{yy} = \frac{\partial^2 \Phi}{\partial x^2}\ , \qquad \sigma_{xy} = -\frac{\partial^2 \Phi}{\partial x \partial y} \tag{A.2.16}$$

Similarly, a polar cordinate (r, θ) can be expressed as,

$$\sigma_r = \frac{1}{r}\frac{\partial \Phi}{\partial r} + \frac{1}{r^2}\frac{\partial^2 \Phi}{\partial \theta^2}\ , \qquad \sigma_\theta = \frac{\partial^2 \Phi}{\partial r^2}\ , \qquad \sigma_{r\theta} = -\frac{\partial}{\partial r}\left[\frac{1}{r}\frac{\partial \Phi}{\partial \theta}\right] \tag{A.2.17}$$

where σ_r , σ_θ denote radial stress and tangential stress respectively, and $\sigma_{r\theta}$ is the in-plane shearing stress. The substitution of equation (A.2.16) into equations (A.1.4a), will result in a differential equation, which can be written as,

$$\frac{\partial^4 \Phi}{\partial x^4} + 2\frac{\partial^4 \Phi}{\partial x^2 \partial y^2} + \frac{\partial^4 \Phi}{\partial y^4} \tag{A.2.18}$$

Now, we introduce the harmonic operator, which can be defined as,

$$\nabla^2 = \frac{\partial^2}{\partial x^2} + \frac{\partial^2}{\partial y^2} \tag{A.2.19}$$

Likewise in polar coordinates, this can be written as,

$$\nabla^2 = \frac{\partial^2}{\partial r^2} + \frac{1}{r}\frac{\partial}{\partial r} + \frac{1}{r^2}\frac{\partial^2}{\partial \theta^2} \tag{A.2.20}$$

Finally, the differential equation (A.2.18) can be found as,

$$\nabla^4 \Phi = 0 \tag{A.2.21}$$

Equation (A.2.21) is a recognised form of bi-harmonic equation.

A.3 2D rotation matrix

In general, the rotation of a coordinate system into another can be achieved using an orthogonal matrix. In two-dimensions, the basic rotation matrix around the z-axis, relates components of a vector in one coordinate frame and that in another frame. Therefore, the displacement components expressed by Williams expansion in the (n, b) local system are related to nodal displacements in the (x, y) global system by

$$R = \begin{bmatrix} \cos\alpha & -\sin\alpha \\ \sin\alpha & \cos\alpha \end{bmatrix} \tag{A.3.22}$$

where R is the so-called rotation matrix and α is the angle between the two frames as defined in Fig. 5.1. It should be noted that angle α is determined by the right hand rule. Hence, α is positive if local axes (n, b) are rotated counterclockwise, and negative if the local axes are rotated clockwise.

A.4 3D rotation matrix

In three-dimensional cracks, displacements are calculated by Williams expansions with respect to local coordinates (n, b, t) can be transformed to global coordinates (x, y, z) by using an appropriate rotation matrix. The rotation matrix for α about the z-axis can be written as,

$$R_z(\alpha) = \begin{bmatrix} \cos\alpha & -\sin\alpha & 0 \\ \sin\alpha & \cos\alpha & 0 \\ 0 & 0 & 1 \end{bmatrix} \tag{A.4.23}$$

and the rotation matrix for ω about the y-axis can be expressed as,

$$R_y(\omega) = \begin{bmatrix} \cos\omega & 0 & \sin\omega \\ 0 & 1 & 0 \\ -\sin\omega & 0 & \cos\omega \end{bmatrix} \tag{A.4.24}$$

similarly, the rotation matrix for φ about the x-axis can be expressed as,

$$R_x(\varphi) = \begin{bmatrix} 1 & 0 & 0 \\ 0 & \cos\varphi & -\sin\varphi \\ 0 & \sin\varphi & \cos\varphi \end{bmatrix} \tag{A.4.25}$$

Finally, the rotation matrix around z, y and x can be achieved by

$$R = R_z R_y R_x \tag{A.4.26}$$

It is important to note that, the local system (n, b, t) is left handed, whereas the global system (x, y, z) is right handed. Consequently, the coordinate frame (n, b, t) must be flipped before the application of any rotational operations.

Appendix B

BEM Supplementary Material

B.1 Limiting process for the kernel T_{ij}

In this section, the jump term α_{ij} which associated with the singularity exhibited in the kernel T_{ij} for two-dimensional and three-dimensional problems are obtained. If we consider a smooth 2D boundary as illustrated in Fig. B.1, and the distance between the source point x' and the field point x on the arc S_ϵ^* is defined as $r = |x' - x|$, This can be presented in a polar coordinate system as,

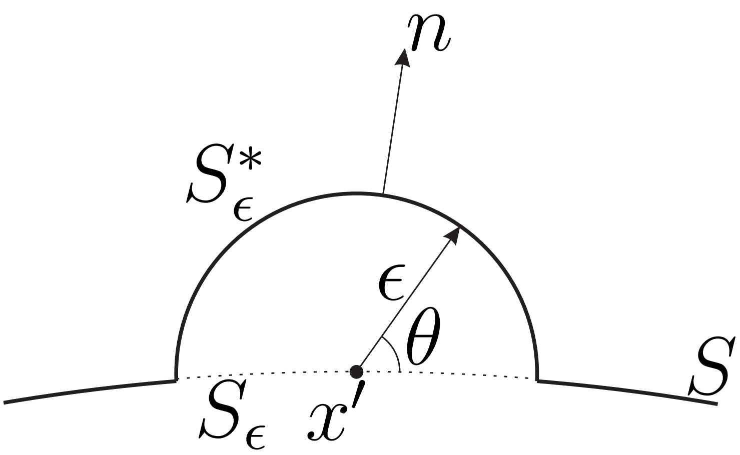

Figure B.1: Semi-circular arc defined on the boundary for limiting process.

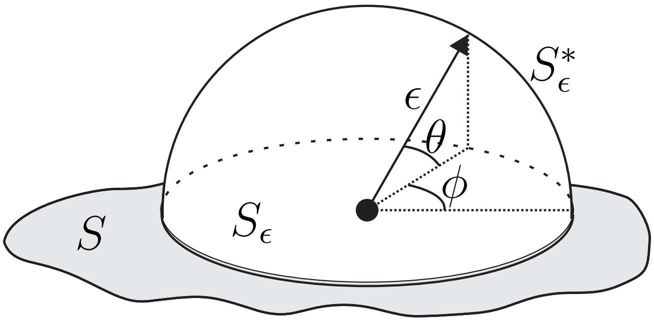

Figure B.2: Hemisphere surface defined on the boundary for limiting processes.

$$\begin{aligned} r &= \epsilon\cos\theta + \epsilon\sin\theta \\ dS_\epsilon^* &= \epsilon d\theta \\ \frac{\partial r}{\partial n} &= 1 \\ r_{,x} &= \cos\theta\ , \qquad r_{,y} = \sin\theta \end{aligned} \tag{B.1.1}$$

When utilising the relations in Eqns. (B.1.1), the constant α_{xx} can be determined as,

$$\begin{aligned} \alpha_{xx} &= \frac{-1}{4\pi(1-\nu)} \lim_{\epsilon\to 0} \int_{S_\epsilon^*} \frac{1}{\epsilon}[(1-2\nu) + 2r_{,x}r_{,x}]\epsilon d\theta \\ &= \frac{-1}{4\pi(1-\nu)} \int_0^\pi [(1-2\nu) + 2\cos^2\theta]d\theta = -\frac{1}{2} \end{aligned} \tag{B.1.2}$$

and in a similar manner α_{xy}, α_{yx} and α_{yy} can be obtain as,

$$\alpha_{xy} = \frac{-1}{4\pi(1-\nu)} \int_0^\pi 2\sin\theta\cos\theta d\theta = 0 \tag{B.1.3}$$

$$\alpha_{yx} = \frac{-1}{4\pi(1-\nu)} \int_0^\pi 2\cos\theta\sin\theta d\theta = 0 \tag{B.1.4}$$

$$\alpha_{yy} = \frac{-1}{4\pi(1-\nu)} \int_0^\pi [(1-2\nu) + 2\sin^2\theta]d\theta = -\frac{1}{2} \tag{B.1.5}$$

Whereas, the three-dimensional problem integral is considered over a hemisphere centred at point x' as shown in Fig. B.2. this can be presented in a spherical coordinate system as,

$$\begin{aligned}
r &= \epsilon\cos\phi\cos\theta + \epsilon\sin\phi\cos\theta + \epsilon\sin\theta \\
dS^*_\epsilon &= \epsilon^2 \sin\theta d\theta d\phi \\
\frac{\partial r}{\partial n} &= 1 \\
r_{,x} &= \cos\phi\cos\theta \ , \qquad r_{,y} = \sin\phi\cos\theta \ , \qquad r_{,z} = \sin\theta
\end{aligned} \tag{B.1.6}$$

Using the relations in Eqns. (B.1.6), the constant α_{xx} can be obtained as,

$$\begin{aligned}
\alpha_{xx} &= \frac{-1}{4\pi(1-\nu)} \int_0^{2\pi} \int_0^{\pi/2} \frac{1}{\epsilon^2}[(1-2\nu) + 3\cos^2\phi\cos^2\theta]\epsilon^2 \sin\theta d\theta d\phi \\
&= -\frac{1}{2}
\end{aligned} \tag{B.1.7}$$

and in similar manner to the α_{xx}, we can obtain α_{xy}, α_{yx} and α_{yy}, and in general $\alpha_{ij} = -\delta/2$ as confirmed by the two-dimensional solutions.

B.2 Expansion of 2D singular integrals

The method proposed by [134] is used in this thesis to evaluate strongly singular and hypersingular integrals; since, it allows the inclusion of enriched terms without adding complexity to the integrals. It can be seen that, all hypersingular integrals involving the multiplication of the kernel and the Jacobian of transformation. In the case of enriched integrals, these terms are multiplied by enrichment functions, whereas for unenriched elements the terms are multiplied by the shape functions. However, all the terms required to determine enriched and unenriched integrals, and which are given by Eqns. (5.16) and Eqns. (5.17) respectively , are presented in this section.

If we allow the components of the source and field points to be denoted as x'_i and x_i respectively, then the Taylor series expansion about the singular point ξ' can be expressed as,

$$\begin{aligned} x_i - x_i' &= \left.\frac{dx_i}{d\xi}\right|_{\xi=\xi'} (\xi-\xi') + \left.\frac{d^2x_i}{d\xi^2}\right|_{\xi=\xi'} \frac{(\xi-\xi')^2}{2} + \cdots \\ &= A_i\delta + B_i\delta^2 + O(\delta^3) \end{aligned} \tag{B.2.8}$$

where the derivative of x_i with respect to the local coordinate ξ can be achieved by taking the derivative of the shape functions given by (B.4.42), which yield,

$$\frac{dx_i}{d\xi} = \frac{dN^{\bar{a}}}{d\xi} x_i^{\bar{a}} \tag{B.2.9a}$$

$$\frac{d^2x_i}{d\xi^2} = \frac{d^2N^{\bar{a}}}{d\xi^2} x_i^{\bar{a}} \tag{B.2.9b}$$

Using similar notations to those given in source [134], the constants A and C are expressed as,

$$A = \sqrt{\sum_{i=1}^{2} A_i^2} \tag{B.2.10a}$$

$$C = \sum_{i=1}^{2} A_i B_i \tag{B.2.10b}$$

The derivative $r_{,i}$ is given by,

$$\begin{aligned} r_{,i} &= \frac{A_i}{A} + \left(\frac{B_i}{A} - \frac{A_i C}{A^3}\right)\delta + O(\delta^2) \\ &= d_{i0} + d_{i1}\delta + O(\delta^2) \end{aligned} \tag{B.2.11}$$

and the term $1/r^2$ is expressed as,

$$\begin{aligned} \frac{1}{r^2} &= \frac{1}{A^2\delta^2} - \frac{2C}{A^4\delta} + O(\delta^2) \\ &= \frac{C_{r2}}{\delta^2} + \frac{C_{r1}}{\delta} \end{aligned} \tag{B.2.12}$$

The Jacobian of transformation is given by $J(\xi) = \sqrt{J_x^2(\xi) + J_y^2(\xi)}$. However, it is useful to also have the Jacobian expressed in terms of its components as,

$$J_x = n_x J = A_y + 2B_y\delta + O(\delta^2) \tag{B.2.13a}$$

$$J_y = n_y J = A_x + 2B_x\delta + O(\delta^2) \tag{B.2.13b}$$

which can also be written in general form as,

$$J_i = J_{i0} + J_{i1}\delta + O(\delta^2) \tag{B.2.14}$$

The constant C_k can be written in the case of the kernel S_{kij} as,

$$C_k = \frac{\mu}{2\pi(1-\nu)} \tag{B.2.15}$$

Since, the required components for expanding the terms $S_{kij}J(\xi)$ are obtained, it can be written as,

$$S_{kij}(x', x(\xi))J(\xi) = C_k \left[\frac{C_{r2}}{\delta^2} + \frac{C_{r1}}{\delta}\right](F_0 + F_1\delta) \tag{B.2.16}$$

where F_0 is given by,

$$\begin{aligned} F_0(\xi') &= 2\nu(J_{i0}d_{j0}d_{k0} + J_{j0}d_{i0}d_{k0}) + (1-2\nu)(2J_{k0}d_{i0}d_{j0} + \delta_{ik}J_{j0} + \delta_{jk}J_{i0}) \\ &- (1-4\nu)\delta_{ij}J_{k0} \end{aligned} \tag{B.2.17}$$

and F_1 can be written as,

$$\begin{aligned} F_1(\xi') &= 2M\left[(1-2\nu)\delta_{ij}d_{k0} + \nu(\delta_{ik}d_{j0} + \delta_{jk}d_{i0}) - 4d_{i0}d_{j0}d_{k0}\right] \\ &+ 2\nu\left[J_{i0}(d_{j0}d_{k1} + d_{j1}d_{k0}) + J_{i1}d_{j0}d_{k0} + J_{j0}(d_{i0}d_{k1} + d_{i1}d_{k0}) + J_{j1}d_{i0}d_{k0}\right] \\ &+ (1-2\nu)\left[2(J_{k0}(d_{i0}d_{j1} + d_{i1}d_{j0}) + J_{k1}d_{i0}d_{j0}) + \delta_{ik}J_{j1} + \delta_{jk}J_{i1}\right] \\ &- (1-4\nu)\delta_{ij}J_{k1} \end{aligned} \tag{B.2.18}$$

where M is defined as,

$$M = d_{x0}J_{x1} + d_{y0}J_{y1} + J_{x0}d_{x1} + J_{y0}d_{y1} \tag{B.2.19}$$

The remaining terms in the case of enriched integral, are enrichment functions which can be expanded as,

$$\begin{aligned} R_{jq}(\alpha)\psi^{\lambda}_{Iq}(\xi) &= R_{jq}(\alpha)\psi^{\lambda}_{Iq}(\xi') + R_{jq}(\alpha)\left.\frac{d\psi^{\lambda}_{Iq}}{d\xi}\right|_{\xi=\xi'}(\xi-\xi') + \cdots && \text{(B.2.20)} \\ &= R_{jq}(\alpha)\psi^{\lambda}_{Iq0}(\xi') + R_{jq}(\alpha)\psi^{\lambda}_{Iq1}(\xi')\delta + O(\delta^2) && \text{(B.2.21)} \end{aligned}$$

whereas in the case of an unenriched integral, the remaining terms are the shape functions which can be written as,

$$\begin{aligned} N^{\bar{a}} &= N^{\bar{a}}(\xi') + \left.\frac{dN^{\bar{a}}}{d\xi}\right|_{\xi=\xi'}(\xi-\xi') + \cdots && \text{(B.2.22)} \\ &= N^{\bar{a}}_0(\xi') + N^{\bar{a}}_1(\xi')\delta + O(\delta^2) && \text{(B.2.23)} \end{aligned}$$

The substitution of the necessary terms given by (B.2.12), (B.2.15), (B.2.17), (B.2.18), (B.2.21) and (B.2.23) into equations (5.16) and (5.17) allow the evaluation of hypersingular integrals for both enriched and unenriched elements.

B.3 Expansion of 3D singular integrals

In a similar manner, three-dimensional singular integrals are expanded using the Taylor series to enable the subtraction of singular terms. Therefore, all the terms required to evaluate enriched and unenriched integrals, as given by (6.14) and (6.15) are illustrated here. If the components of the field and the source point locations are expressed as $x_i$and

x_i' then:

$$\begin{aligned} x_i - x_i' = \rho & \left[\left. \frac{\partial x_i}{\partial \xi_1} \right|_{\xi_1 = \xi_1'} \cos\phi + \left. \frac{\partial x_i}{\partial \xi_2} \right|_{\xi_2 = \xi_2'} \sin\phi \right] \\ & + \rho^2 \left[\left. \frac{\partial^2 x_i}{\partial \xi_1^2} \right|_{\xi_1 = \xi_1'} \frac{\cos^2\phi}{2} + \left. \frac{\partial^2 x_i}{\partial \xi_1 \partial \xi_2} \right|_{\xi = \xi'} \cos\phi \sin\phi \right. \\ & \left. + \left. \frac{\partial^2 x_i}{\partial \xi_2^2} \right|_{\xi_2 = \xi_2'} \frac{\sin^2\phi}{2} \right] + \cdots \\ & = \rho A_i(\phi) + \rho^2 B_i(\phi) + O(\rho^3) \end{aligned} \tag{B.3.24}$$

where the derivative of x_i with respect to the local coordinates ξ_1 and ξ_2 are given by

$$\begin{aligned} \frac{\partial x_i}{d\xi} &= \frac{\partial N^{\bar{a}}}{\partial \xi} x_i^{\bar{a}} \\ \frac{\partial^2 x_i}{d\xi^2} &= \frac{\partial^2 N^{\bar{a}}}{\partial \xi^2} x_i^{\bar{a}} \\ \frac{\partial^2 x_i}{\partial \xi_1 \partial \xi_2} &= \frac{\partial^2 N^{\bar{a}}}{\partial \xi_1 \partial \xi_2} x_i^{\bar{a}} \end{aligned} \tag{B.3.25}$$

where the shape function derivatives are presented in Sec. B.4. Additionally, the constants A and C in the three-dimensions are defined as,

$$A = \sqrt{\sum_{i=1}^{3} (A_i)^2} \tag{B.3.26a}$$

$$C = \sum_{i=1}^{3} A_i B_i \tag{B.3.26b}$$

Using Eqn. (B.3.24), the derivative of r in i direction can be expressed using the Tailor series as,

$$\begin{aligned} r_{,i} &= \frac{A_i}{A} + \rho \left(\frac{B_i}{A} - \frac{A_i C}{A^3} \right) + \cdots \\ &= d_{i0}(\phi) + \rho d_{i1}(\phi) + O(\rho^2) \end{aligned} \tag{B.3.27}$$

in a similar way, the term r^{-3} is given by

$$\begin{aligned} \frac{1}{r^3} &= \frac{1}{A^3\rho^3} - \frac{3C}{A^5\rho^2} + O\left(\frac{1}{\rho}\right) \\ &= \frac{C_{r2}}{\rho^3} + \frac{C_{r1}}{\rho^2} + O\left(\frac{1}{\rho}\right) \end{aligned} \tag{B.3.28}$$

If the relationship between the Jacobian of transformation and normals (where $J_i = n_i J$) is considered, then the Jacobian components can be written as,

$$\begin{aligned} J_i = J_i(\zeta) \; &+ \rho\left[\left.\frac{\partial J_i}{\partial \xi_1}\right|_{\xi_1=\xi_1'} \cos\phi + \left.\frac{\partial J_i}{\partial \xi_2}\right|_{\xi_2=\xi_2'} \sin\phi\right] + \cdots \\ = J_{i0} + \rho J_{i1}(\phi) + O(\rho^2) \end{aligned} \tag{B.3.29}$$

At this point, the derivative of r in normal diction can be expressed as,

$$\begin{aligned} \frac{dr}{dn} &= d_0 \cdot J_0 + \rho(d_1 \cdot J_0 + d_0 \cdot J_1) \\ &= M_0 + \rho M_1(\phi) + O(\rho^2) \end{aligned} \tag{B.3.30}$$

where $M_0 = 0$, since $A_i J_{i0} \equiv 0$. The constant C_k for the fundamental solution S_{kij}, as given by (4.33), can be expressed as,

$$C_k = \frac{\mu}{4\pi(1-\nu)} \tag{B.3.31}$$

By utilising Eqns. (B.3.31), (B.3.29), (B.3.28) and (B.3.27), the terms $S_{kij}J(\xi_1, \xi_2)$ can be expressed as,

$$S_{kij}(x', x(\xi))J(\xi) = C_k\left[\frac{C_{r2}}{\rho^2} + \frac{C_{r1}}{\rho}\right](F_0 + \rho F_1) \tag{B.3.32}$$

where F_0 is defined as,

$$\begin{aligned} F_0(\phi) &= 3\nu(J_{i0}d_{j0}d_{k0} + J_{j0}d_{i0}d_{k0}) + (1-2\nu)(3J_{k0}d_{i0}d_{j0} + \delta_{ik}J_{j0} + \delta_{jk}J_{i0}) \\ &- (1-4\nu)\delta_{ij}J_{k0} \end{aligned} \tag{B.3.33}$$

and F_1 can be written as,

$$\begin{aligned} F_1(\phi) &= 3M_1\left[(1-2\nu)\delta_{ij}d_{k0} + \nu(\delta_{ik}d_{j0} + \delta_{jk}d_{i0}) - 5d_{i0}d_{j0}d_{k0}\right] \\ &+ 3\nu\left[J_{i0}(d_{j0}d_{k1} + d_{j1}d_{k0}) + J_{i1}d_{j0}d_{k0} + J_{j0}(d_{i0}d_{k1} + d_{i1}d_{k0}) + J_{j1}d_{i0}d_{k0}\right] \\ &+ (1-2\nu)\left[3(J_{k0}(d_{i0}d_{j1} + d_{i1}d_{j0}) + J_{k1}d_{i0}d_{j0}) + \delta_{ik}J_{j1} + \delta_{jk}J_{i1}\right] \\ &- (1-4\nu)\delta_{ij}J_{k1} \end{aligned} \tag{B.3.34}$$

In cases where is an enriched element, the enrichment function can be expressed in Taylor series form as,

$$\psi^{\lambda}_{Iq}\left[r(\xi_1,\xi_2),\theta\right] = \psi^{\lambda}_{Iq}(\xi_1',\xi_2') + \rho\left[\left.\frac{\partial\psi^{\lambda}_{Iq}}{\partial\xi_1}\right|_{\xi_1=\xi_1'} + \left.\frac{\partial\psi^{\lambda}_{Iq}}{\partial\xi_2}\right|_{\xi_2=\xi_2'}\right] + \cdots \tag{B.3.35}$$

$$= \psi^{\lambda}_{Iq0} + \rho\psi^{\lambda}_{Iq1}(\phi) + O(\delta^2) \tag{B.3.36}$$

It should be noted that the one-dimensional shape functions used for the interpolation of SIFs and the rotation matrix are a function of ξ_2 only (e.g. flat crack is considered). Therefore, the rotation matrix can be expanded as,

$$R_{jq} = R_{jq}(\xi_2') + \rho\left[\left.\frac{\partial R_{jq}}{\partial\xi_2}\right|_{\xi_2=\xi_2'}\sin\phi\right] + \cdots \tag{B.3.37}$$

$$= R_{jq0} + \rho R_{jq1}(\phi) + O(\rho^2) \tag{B.3.38}$$

Similarly the one-dimensional shape functions are given by

$$\begin{aligned} N^f &= N^f(\xi_2') + \rho\left[\left.\frac{\partial N^f}{\partial\xi_2}\right|_{\xi_2=\xi_2'}\sin\phi\right] + \cdots \\ &= N^f_0 + \rho N^f_1(\phi) + O(\rho^2) \end{aligned} \tag{B.3.39}$$

Finally, the three-dimensional shape functions are expanded around the source point as,

$$\begin{aligned} N^{\bar{a}} &= N^{\bar{a}}(\xi_1', \xi_2') + \rho \left[\left. \frac{\partial N^{\bar{a}}}{\partial \xi_1} \right|_{\xi_1=\xi_1'} \cos\phi + \left. \frac{\partial N^{\bar{a}}}{\partial \xi_2} \right|_{\xi_2=\xi_2'} \sin\phi \right] + \cdots \\ &= N_0^{\bar{a}} + \rho N_1^{\bar{a}}(\phi) + O(\rho^2) \end{aligned} \tag{B.3.40}$$

B.4 Shape functions

In BEM, elements are defined by shape functions and nodes. Moreover, the shape functions exhibit a Kronecker delta property and change according to the positions of the nodes on the element. In the case of a one-dimensional quadratic discontinuous element the shape functions are given by

$$\begin{aligned} N^1 &= \frac{9}{8}\xi(\xi - \frac{3}{2}) \\ N^2 &= (1 - \frac{3}{2}\xi)(1 + \frac{3}{2}\xi) \\ N^3 &= \frac{9}{8}\xi(\xi + \frac{3}{2}); \end{aligned} \tag{B.4.41}$$

and the first derivative of the shape functions can be expressed as,

$$\begin{aligned} \frac{dN^1}{d\xi} &= \frac{9}{4}\xi - \frac{3}{2} \\ \frac{dN^2}{d\xi} &= -\frac{9}{2}\xi \\ \frac{dN^3}{d\xi} &= \frac{9}{4}\xi + \frac{3}{2} \end{aligned} \tag{B.4.42}$$

In the case of 9-node two-dimensional quadrature element the shape functions can be written as,

$$
\begin{aligned}
N^1 &= \frac{1}{4s^4}\xi_1(\xi_1 - s)\xi_2(\xi_2 - s) \\
N^2 &= \frac{1}{4s^4}\xi_1(\xi_1 + s)\xi_2(\xi_2 - s) \\
N^3 &= \frac{1}{4s^4}\xi_1(\xi_1 + s)\xi_2(\xi_2 + s) \\
N^4 &= \frac{1}{4s^4}\xi_1(\xi_1 - s)\xi_2(\xi_2 + s) \\
N^5 &= \frac{1}{2s^4}(s^2 - \xi_1^2)\xi_2(\xi_2 - s) \\
N^6 &= \frac{1}{2s^4}\xi_1(\xi_1 + s)(s^2 - \xi_2^2) \\
N^7 &= \frac{1}{2s^4}(s^2 - \xi_1^2)\xi_2(\xi_2 + s) \\
N^8 &= \frac{1}{2s^4}\xi_1(\xi_1 - s)(d^2 - \xi_2^2) \\
N^9 &= \frac{1}{s^4}(s^2 - \xi_1^2)(s^2 - \xi_2^2)
\end{aligned}
\tag{B.4.43}
$$

where s is a parameter defining the position of the node as presented in Fig. B.3, which equals $2/3$ for discontinuous elements and 1 for continuous elements. The first derivative

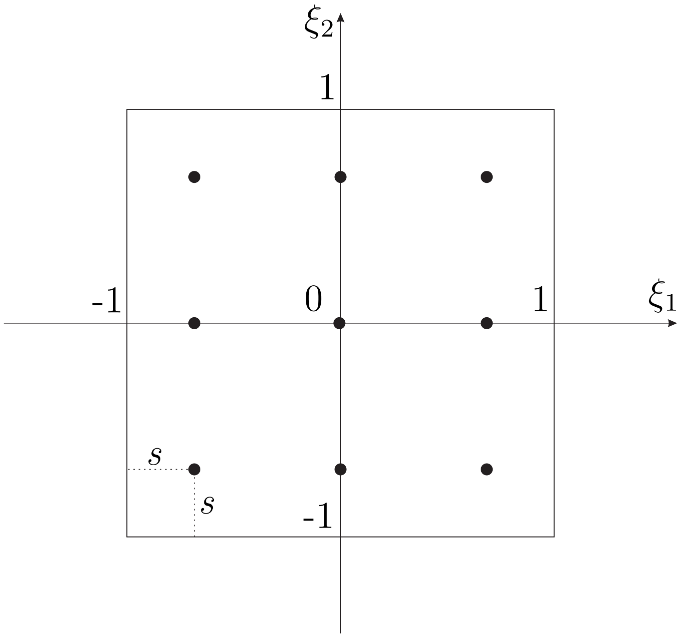

Figure B.3: 9-nodes two-dimensional quadrature element

of the shape functions with respect to ξ_1 can be written as,

$$\begin{aligned}
\frac{\partial N^1}{\partial \xi_1} &= \frac{1}{4s^4}(s-2\xi_1)\xi_2(s-\xi_2)\\
\frac{\partial N^2}{\partial \xi_1} &= \frac{1}{4s^4}(s+2\xi_1)\xi_2(-s+\xi_2)\\
\frac{\partial N^3}{\partial \xi_1} &= \frac{1}{4s^4}(s+2\xi_1)\xi_2(s+\xi_2)\\
\frac{\partial N^4}{\partial \xi_1} &= -\frac{1}{4s^4}(s-2\xi_1)\xi_2(s+\xi_2)\\
\frac{\partial N^5}{\partial \xi_1} &= -2\frac{1}{2s^4}\xi_1\xi_2(-s+\xi_2)\\
\frac{\partial N^6}{\partial \xi_1} &= \frac{1}{2s^4}(s+2\xi_1)(s^2-\xi_2^2)\\
\frac{\partial N^7}{\partial \xi_1} &= -2\frac{1}{2s^4}\xi_1\xi_2(s+\xi_2)\\
\frac{\partial N^8}{\partial \xi_1} &= -\frac{1}{2s^4}(s-2\xi_1)(s^2-\xi_2^2)\\
\frac{\partial N^9}{\partial \xi_1} &= -2/s^4\xi_1(s^2-\xi_2^2)
\end{aligned} \tag{B.4.44}$$

Similarly, the first derivative with respect to ξ_2 can be expressed as,

$$
\begin{aligned}
\frac{\partial N^1}{\partial \xi_2} &= -\frac{1}{4s^4}\xi_1(-s+\xi_1)(s-2\xi_2)\\
\frac{\partial N^2}{\partial \xi_2} &= -\frac{1}{4s^4}\xi_1(s+\xi_1)(s-2\xi_2)\\
\frac{\partial N^3}{\partial \xi_2} &= \frac{1}{4s^4}\xi_1(s+\xi_1)(s+2\xi_2)\\
\frac{\partial N^4}{\partial \xi_2} &= \frac{1}{4s^4}\xi_1(-s+\xi_1)(s+2\xi_2)\\
\frac{\partial N^5}{\partial \xi_2} &= -\frac{1}{2s^4}(s^2-\xi_1^2)(s-2\xi_2)\\
\frac{\partial N^6}{\partial \xi_2} &= -2\frac{1}{2s^4}\xi_1\xi_2(s+\xi_1)\\
\frac{\partial N^7}{\partial \xi_2} &= \frac{1}{2s^4}(s^2-\xi_1^2)(s+2\xi_2)\\
\frac{\partial N^8}{\partial \xi_2} &= -2\frac{1}{2s^4}\xi_1\xi_2(-s+\xi_1)\\
\frac{\partial N^9}{\partial \xi_2} &= \frac{-2}{s^4}\xi_2(s^2-\xi_1^2)
\end{aligned}
\tag{B.4.45}
$$

The second derivative can be obtained by deriving Eqn. (B.4.44) once more with respect to ξ_1, which can be written as,

$$\begin{aligned}
\frac{\partial^2 N^1}{\partial \xi_1^2} &= 2\frac{1}{4s^4}\xi_2(-s+\xi_2) \\
\frac{\partial^2 N^2}{\partial \xi_1^2} &= 2\frac{1}{4s^4}\xi_2(-s+\xi_2) \\
\frac{\partial^2 N^3}{\partial \xi_1^2} &= 2\frac{1}{4s^4}\xi_2(s+\xi_2) \\
\frac{\partial^2 N^4}{\partial \xi_1^2} &= 2\frac{1}{4s^4}\xi_2(s+\xi_2) \\
\frac{\partial^2 N^5}{\partial \xi_1^2} &= -2\frac{1}{2s^4}\xi_2(-s+\xi_2) \\
\frac{\partial^2 N^6}{\partial \xi_1^2} &= 2\frac{1}{2s^4}(s^2-\xi_2^2) \\
\frac{\partial^2 N^7}{\partial \xi_1^2} &= -2\frac{1}{2s^4}\xi_2(s+\xi_2) \\
\frac{\partial^2 N^8}{\partial \xi_1^2} &= 2\frac{1}{2s^4}(s^2-\xi_2^2) \\
\frac{\partial^2 N^9}{\partial \xi_1^2} &= -\frac{2}{s^4}(s^2-\xi_2^2)
\end{aligned} \tag{B.4.46}$$

and deriving Eqn. (B.4.45) once more with respect to ξ_2, gives,

$$\begin{aligned}
\frac{\partial^2 N^1}{\partial \xi_2^2} &= 2\frac{1}{4s^4}\xi_1(-s+\xi_1) \\
\frac{\partial^2 N^2}{\partial \xi_2^2} &= 2\frac{1}{4s^4}\xi_1(s+\xi_1) \\
\frac{\partial^2 N^3}{\partial \xi_2^2} &= 2\frac{1}{4s^4}\xi_1(s+\xi_1) \\
\frac{\partial^2 N^4}{\partial \xi_2^2} &= 2\frac{1}{4s^4}\xi_1(-s+\xi_1) \\
\frac{\partial^2 N^5}{\partial \xi_2^2} &= 2\frac{1}{2s^4}(s^2-\xi_1^2) \\
\frac{\partial^2 N^6}{\partial \xi_2^2} &= -2\frac{1}{2s^4}\xi_1(s+\xi_1) \\
\frac{\partial^2 N^7}{\partial \xi_2^2} &= 2\frac{1}{2s^4}(s^2-\xi_1^2) \\
\frac{\partial^2 N^8}{\partial \xi_2^2} &= -2\frac{1}{2s^4}\xi_1(-s+\xi_1) \\
\frac{\partial^2 N^9}{\partial \xi_2^2} &= -\frac{2}{s^4}(s^2-\xi_1^2)
\end{aligned} \tag{B.4.47}$$

Next, deriving Eqn. (B.4.44) with respect to ξ_2 or Eqn. (B.4.45) with respect to ξ_1, yields similar results, which can be written as,

$$\begin{aligned}
\frac{\partial^2 N^1}{\partial\xi_1\partial\xi_2} &= \frac{1}{4s^4}(s-2\xi_1)(s-2\xi_2)\\
\frac{\partial^2 N^2}{\partial\xi_1\partial\xi_2} &= -\frac{1}{4s^4}(s+2\xi_1)(s-2\xi_2)\\
\frac{\partial^2 N^3}{\partial\xi_1\partial\xi_2} &= \frac{1}{4s^4}(s+2\xi_1)(s+2\xi_2)\\
\frac{\partial^2 N^4}{\partial\xi_1\partial\xi_2} &= -\frac{1}{4s^4}(s-2\xi_1)(s+2\xi_2)\\
\frac{\partial^2 N^5}{\partial\xi_1\partial\xi_2} &= 2\frac{1}{2s^4}\xi_1(s-2\xi_2)\\
\frac{\partial^2 N^6}{\partial\xi_1\partial\xi_2} &= -2\frac{1}{2s^4}\xi_2(s+2\xi_1)\\
\frac{\partial^2 N^7}{\partial\xi_1\partial\xi_2} &= -2\frac{1}{2s^4}\xi_1(s+2\xi_2)\\
\frac{\partial^2 N^8}{\partial\xi_1\partial\xi_2} &= 2\frac{1}{2s^4}\xi_2(s-2\xi_1)\\
\frac{\partial^2 N^9}{\partial\xi_1\partial\xi_2} &= \frac{4}{s^4}\xi_1\xi_2
\end{aligned} \tag{B.4.48}$$

The above derivatives are essential for the treatment of singular integrals.

Appendix C

Fracture Mechanics Supplementary Material

C.1 Crack Closure Proof

Let us consider a crack with an initial length of $a + \Delta a$ and subjected to a load in Mode I, as illustrated in figure C.1. In this case, it is appropriate to place the origin at a distance of Δa from the tip of the crack.

Considering the plate has unit thickness; we can force the crack to close by applying a sufficient magnitude of stresses to the crack surfaces, with the length of Δa from the crack tip. The work required to close the tip of the crack relates to the energy release

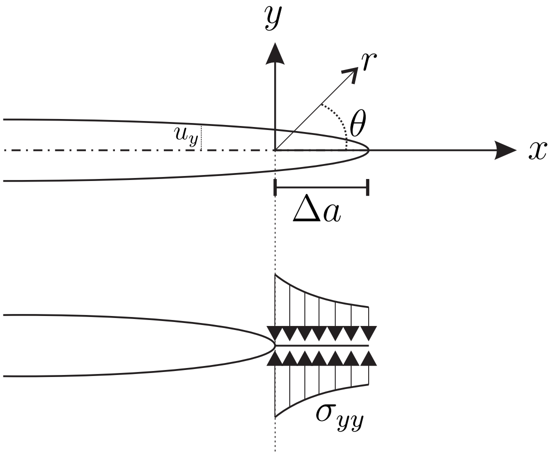

Figure C.1: Stress applied to close a crack tip rate as,

$$\mathcal{G} = \lim_{\Delta a \to 0} \left(\frac{\Delta W}{\Delta a} \right) \tag{C.1.1}$$

where ΔW is the work of crack closure, and is equivalent to the sum of contribution to work from $x = 0$ to $x = \Delta a$; so that,

$$\Delta W = \int_{x=0}^{x=\Delta a} \sigma_{yy} u_y(x) dx = \int_{x=0}^{x=\Delta a} 2\frac{1}{2} F_y(x) u_y(x) dx \tag{C.1.2}$$

where $u_y(x)$ is the displacement in y direction, as shown in Fig. C.1. F_y and σ_{yy} are the force and the stress in y direction, respectively. A factor of 2 is included because both crack surfaces are considered in the absolute distance of $u_y(x)$. The displacement for mode I in y direction can be calculated as,

$$u_y = \frac{K_I}{2\mu} \sqrt{\frac{r}{2\pi}} \sin\left(\frac{\theta}{2}\right) \left[\kappa + 1 - 2\cos^2\left(\frac{\theta}{2}\right) \right] \tag{C.1.3}$$

Equation(C.1.3) can be simplified further by considering $\theta = \pi$,

$$u_y = \frac{(\kappa + 1) K_I(a + \Delta a)}{2\mu} \sqrt{\frac{\Delta a - x}{2\pi}} \tag{C.1.4}$$

Here, the stress intensity factor at the original of the crack tip is presented by $K_I(a + \Delta a)$. For the shortened crack, the normal stress needed to close the crack relates to K_I as,

$$\sigma_{yy} = \frac{K_I(a)}{\sqrt{2\pi x}} \tag{C.1.5}$$

Substitution of equation (C.1.1) to (C.1.5) gives,

$$\begin{aligned}\mathcal{G}_I &= \lim_{\Delta a \to 0} \frac{(\kappa+1)K_I(a)K_I(a+\Delta a)}{4\pi\mu\Delta a}\int_0^{\Delta a}\sqrt{\frac{\Delta a - x}{x}}dx \\ &= \frac{(\kappa+1)K_I^2}{8\mu} = \frac{K_I^2}{E'} \end{aligned} \tag{C.1.6}$$

Equation (2.11) is a general equation for mode I. The same steps described above can also be used for other modes. In the case of mode II, relevant displacement and closure stress are u_x and τ_{xy}, and that for mode III is τ_{yz} and u_z. A combination of three loading modes is used to present the energy release rates,

$$\mathcal{G} = \mathcal{G}_I + \mathcal{G}_{II} + \mathcal{G}_{III} = \frac{K_I^2}{E'} + \frac{K_{II}^2}{E'} + \frac{K_{III}^2}{2\mu} \tag{C.1.7}$$

The energy release rate is a scalar quantity. Hence, stress intensity factors are additive. However, equation (C.1.7) assumes that the crack is planar and grows in a consistent shape, whereas mixed-mode cracks do not.

C.2 Williams Expansions Derivation

Since the crack is a special case of Williams problem, as mention in Sec. 2.6. Therefore, in order to solve this special problem Williams utilised the Airy stress function as $\Phi(r,\theta)$, defined in polar coordinates as,

$$\Phi(r,\theta) = r^{\lambda+1}.F(\theta) \tag{C.2.8}$$

where r and θ are the polar coordinates system as defined in Fig. 2.7, and λ and $F(\theta)$ are unknowns as yet unresolved. As shown by [151] the governing equation of linear elasticity problems is the two-dimensional biharmonic equation in terms of function $\Phi(r,\theta)$. Accordingly, the differential equation (see Eqn. (A.2.21)) is expressed as,

$$\nabla^4\Phi(r,\theta) = \nabla^2\nabla^2\Phi(r,\theta) = 0 \tag{C.2.9}$$

where the Laplace operator ∇^2 for the case of polar coordinates is defined in Eqn. (A.2.20). The substitution of Eqn. (C.2.8) into Eqn. (C.2.9) yields the following ordinary differential equation,

$$\left[\frac{d^2}{d\theta^2} + (\lambda+1)^2\right]\left[\frac{d^2}{d\theta^2} + (\lambda-1)^2\right]F(\theta) = 0 \tag{C.2.10}$$

Equation (C.2.10) has a general solution for $F(\theta)$, which can be written as,

$$F(\theta) = C_1\cos(\lambda-1)\theta + C_2\sin(\lambda-1)\theta + C_3\cos(\lambda+1)\theta + C_4\sin(\lambda+1)\theta \tag{C.2.11}$$

C_1, C_2, C_3 and C_4 are arbitrary constants to be determined later by consideration of the applied boundary conditions at the edges.

The relationship between the stresses and the Airy stress function is given by Eqn. (A.2.17). Now, the substitution of (C.2.8) into (A.2.17) yields,

$$\sigma_{rr} = r^{\lambda-1}[(\lambda+1)F(\theta) + F''(\theta)] \tag{C.2.12a}$$

$$\sigma_{\theta\theta} = r^{\lambda-1}[\lambda(\lambda+1)F(\theta)] \tag{C.2.12b}$$

$$\sigma_{r\theta} = -r^{\lambda-1}[\lambda F'(\theta)] \tag{C.2.12c}$$

where $'$ denotes the derivative of a function. The imposed boundary conditions for traction free faces of the wedge require the following conditions,

$$\sigma_{\theta\theta} = 0, \quad \sigma_{r\theta} = 0 \quad \text{for} \quad \theta = \pm\alpha, \quad r \geqslant 0 \tag{C.2.13}$$

Respectively, the restrictions on $F(\theta)$ can be written as,

$$F(\alpha) = F(-\alpha) = 0 \tag{C.2.14a}$$

$$F'(\alpha) = F'(-\alpha) = 0 \tag{C.2.14b}$$

By assuming $\lambda \neq 0$ the conditions (C.2.14) are naturally satisfied by equations (C.2.12b) and (C.2.12c). Now, the characteristic equation for the problem needs to be determined.

A system of four simultaneous equations can be generated by applying boundary conditions (C.2.14) into the general form of $F(\theta)$, as exhibited in (C.2.11), yielding,

$$C_1\cos(\lambda-1)\alpha+C_2\sin(\lambda-1)\alpha+C_3\cos(\lambda+1)\alpha+C_4\sin(\lambda+1)\alpha = 0 \tag{C.2.15a}$$

$$C_1\cos(\lambda-1)\alpha-C_2\sin(\lambda-1)\alpha+C_3\cos(\lambda+1)\alpha-C_4\sin(\lambda+1)\alpha = 0 \tag{C.2.15b}$$

$$\begin{aligned}(\lambda-1)[-C_1\sin(\lambda-1)\alpha+C_2\cos(\lambda-1)\alpha]&\\ +(\lambda+1)[-C_3\sin(\lambda+1)\alpha+C_4\cos(\lambda+1)\alpha] &= 0\end{aligned} \tag{C.2.15c}$$

$$\begin{aligned}(\lambda-1)[C_1\sin(\lambda-1)\alpha+C_2\cos(\lambda-1)\alpha]&\\ +(\lambda+1)[C_3\sin(\lambda+1)\alpha+C_4\cos(\lambda+1)\alpha] &= 0\end{aligned} \tag{C.2.15d}$$

Elementary algebraic operations can be used to separate these equations into two independent groups of equations, each containing two constants. When the subequations in (C.2.15) are added then the following results are obtained,

$$C_1\cos(\lambda-1)\alpha+C_3\cos(\lambda+1)\alpha = 0 \tag{C.2.16a}$$

$$C_2(\lambda-1)\cos(\lambda-1)\alpha+C_4(\lambda+1)\cos(\lambda+1)\alpha = 0 \tag{C.2.16b}$$

Conversely, subtraction of the subequations in (C.2.15) gives,

$$C_2\sin(\lambda-1)\alpha+C_4\sin(\lambda+1)\alpha = 0 \tag{C.2.17a}$$

$$C_1(\lambda-1)\sin(\lambda-1)\alpha+C_3(\lambda+1)\sin(\lambda+1)\alpha = 0 \tag{C.2.17b}$$

Equations (C.2.16) and (C.2.17) can be presented in a simpler matrix form as,

$$\begin{bmatrix}\cos(\lambda-1)\alpha & \cos(\lambda+1)\alpha\\ (\lambda-1)\sin(\lambda-1)\alpha & (\lambda+1)\sin(\lambda+1)\alpha\end{bmatrix}\begin{Bmatrix}C_1\\ C_2\end{Bmatrix}=\begin{Bmatrix}0\\ 0\end{Bmatrix} \tag{C.2.18a}$$

$$\begin{bmatrix}\sin(\lambda-1)\alpha & \sin(\lambda+1)\alpha\\ (\lambda-1)\cos(\lambda-1)\alpha & (\lambda+1)\cos(\lambda+1)\alpha\end{bmatrix}\begin{Bmatrix}C_3\\ C_4\end{Bmatrix}=\begin{Bmatrix}0\\ 0\end{Bmatrix} \tag{C.2.18b}$$

The determinants of the coefficient matrices in (C.2.18) must be equal to zero in order to obtain a meaningful solution. After simplification this gives,

$$\sin 2\lambda\alpha = 0 \tag{C.2.19a}$$

$$\lambda \sin 2\alpha = 0 \tag{C.2.19b}$$

Equations (C.2.19) yield the non-trivial solutions to the problem of free-free boundary conditions at the radial edge of a wedge. Hence, a wedge with apex angle $\alpha = \pi$ is a special limiting case, Eqn. (C.2.19) becomes,

$$\sin(2\pi\lambda) = 0 \tag{C.2.20}$$

where the roots of (C.2.20) are given by

$$\lambda = \frac{n}{2}; \quad n = 0, \pm1, \pm2, \pm3, ... \tag{C.2.21}$$

However, some of these roots must be excluded, as they yield unacceptable physical results regarding the crack problems. Thus, the possible nature of this problem field needs to be discussed in greater detail. The displacements are unbounded at the origin when $r = 0$ for any $n < 0$, therefore n must have only positive values. Furthermore, an infinite amount of strain energy is stored in a finite volume in the case of $n = 0$; hence $n = 0$ is also rejected. Considering these conditions, the sum of all the terms contains acceptable eigenvalues when $\lambda = n/2$ and $n > 0$ are included in the general solution. From Eqn. (C.2.18) a relationship can be established between C_1 and C_3 also C_2 and C_4. It is essential to note that, not all the constants C_1, C_2, C_3 and C_4 are independent. Substituting $\lambda = n/2$ and $\alpha = \pi$ in equation (C.2.18), can provide the results for all values of n when,

$$\left.\begin{aligned} C_3 &= -\tfrac{n-2}{n+2} C_1 \\ C_4 &= -C_2 \end{aligned}\right\} ; n = 1, 3, 5, ... \tag{C.2.22}$$

and also,

$$\left.\begin{array}{r} C_3 = -C_1 \\ C_4 = -\frac{n-2}{n+2} C_2 \end{array}\right\} ; n = 2, 4, 6, ... \tag{C.2.23}$$

Substitution of (C.2.22) and (C.2.23) into the general solution (C.2.11) by setting $\lambda = n/2$, and then into the Airy stress function (C.2.8); yields,

$$\begin{aligned} \Phi(r,\theta) &= \sum_{n=1,3,5,...}^{\infty} r^{1+\frac{n}{2}} \left[C_1 \left(\cos\left[\frac{n-2}{2}\theta\right] - \frac{n-2}{n+2} + \cos\left[\frac{n-2}{2}\theta\right] \right) \right. \\ &+ \left. C_2 \left(\sin\left[\frac{n-2}{2}\theta\right] - \sin\left[\frac{n-2}{2}\theta\right] \right) \right] \\ &+ \sum_{n=2,4,6,...}^{\infty} r^{1+\frac{n}{2}} \left[C_1 \left(\cos\left[\frac{n-2}{2}\theta\right] - \frac{n-2}{n+2} + \cos\left[\frac{n-2}{2}\theta\right] \right) \right. \\ &+ \left. C_2 \left(\sin\left[\frac{n-2}{2}\theta\right] - \sin\left[\frac{n-2}{2}\theta\right] \right) \right] \end{aligned} \tag{C.2.24}$$

The symmetric stress field with respect to the crack plane (mode I) can be obtained by multiplying the even terms by C_1. Similarly, the antisymmetric stress field (mode II) is produced by odd terms involving C_2. However, these two types of stress field can be uncoupled and treated independently according to the principle of superposition. In order to make use of Eqn. (C.2.24) we recall the relationship between an Airy stress function and stresses, as expressed in Eqn. (A.2.16). Therefore, expressions for crack tip stresses can be obtained by substituting Eqn.(C.2.24) into Eqns. (A.2.16) to give,

$$\begin{aligned} \sigma_{nn} &= \sum_{n=}^{\infty} \frac{n}{2} r^{\frac{n}{2}-1} \left\{ C_{1n} \left[\left(2+\frac{n}{2}+(-1)^n\right) \cos\left(\frac{n}{2}-1\right)\theta + \left(\frac{n}{2}-1\right) \cos\left(\frac{n}{2}-3\right)\theta \right] \right. \\ &- \left. C_{2n} \left[\left(2+\frac{n}{2}-(-1)^n\right) \sin\left(\frac{n}{2}-1\right)\theta - \left(\frac{n}{2}-1\right) \sin\left(\frac{n}{2}-3\right)\theta \right] \right\} \end{aligned} \tag{C.2.25a}$$

$$\begin{aligned} \sigma_{bb} &= \sum_{n=}^{\infty} \frac{n}{2} r^{\frac{n}{2}-1} \left\{ C_{1n} \left[\left(2-\frac{n}{2}-(-1)^n\right) \cos\left(\frac{n}{2}-1\right)\theta + \left(\frac{n}{2}-1\right) \cos\left(\frac{n}{2}-3\right)\theta \right] \right. \\ &- \left. C_{2n} \left[\left(2-\frac{n}{2}+(-1)^n\right) \sin\left(\frac{n}{2}-1\right)\theta + \left(\frac{n}{2}-1\right) \sin\left(\frac{n}{2}-3\right)\theta \right] \right\} \end{aligned} \tag{C.2.25b}$$

$$\begin{aligned} \sigma_{nb} &= \sum_{n=}^{\infty} \frac{n}{2} r^{\frac{n}{2}-1} \left\{ C_{1n} \left[\left(\frac{n}{2}-1\right) \sin\left(\frac{n}{2}-3\right)\theta + \left(\frac{n}{2}+(-1)^n\right) \sin\left(\frac{n}{2}-1\right)\theta \right] \right. \\ &+ \left. C_{2n} \left[\left(\frac{n}{2}-1\right) \cos\left(\frac{n}{2}-3\right)\theta - \left(\frac{n}{2}-(-1)^n\right) \cos\left(\frac{n}{2}-1\right)\theta \right] \right\} \end{aligned} \tag{C.2.25c}$$

where n and b denote the local coordinates with the origin at the crack tip. It has been noticed that including more terms of Eqns. C.2.25, when evaluating stresses near the crack tips can lead to more accurate results.

Appendix D

Supplementary results

D.1 Pure mode I in two-dimensions

In Sec. 5.4.1, the pure mode I SIFs were studied for case 1 and 2 of an edge crack in an infinite plate and a finite plate, respectively. The results used to plot Fig. 5.9a and Fig. 5.9b are presented in this section. The SIFs for case 1 are shown in Table D.1. In addition, the exact SIF value can be calculated using $K_I = \sigma\sqrt{\pi a} = 1.772453850905516 \times 10^8 Pa\sqrt{m}$.

Table D.1: SIFs for infinite plate (**case 1**)

ndof	**Unenriched DBEM J-integral**	**ndof**	**XBEM J-integral**	**XBEM Direct $\tilde{K}_I$ (colloc.)**	**XBEM Direct $\tilde{K}_I$ (Tying)**
72	1742789905.83	74	1772029158.93	1775593310.28	1771588498.46
132	1753146120.45	134	1772421452.43	1772497708.45	1772431322.75
192	1757957719.29	194	1772446626.50	1772477692.93	1772450806.70
252	1760787045.25	254	1772451154.21	1772478576.89	1772455148.24
312	1762652375.22	314	1772452444.37	1772479096.26	1772456426.92

The SIFs values for a finite plate under tensile load (case 2) which have been used to plot Fig. 5.9b are shown in Table D.2. The problem considered in case 2 does not have an exact solution. Therefore, a numerical solution by [5] is used for comparison and to calculate the errors. The reference numerical solution accurate within 1% and can be calculated as;

Table D.2: SIFs for finite plate under tensile load (**case 2**)

ndof	**Unenriched DBEM** **J-integral**	**ndof**	**XBEM** **J-integral**	**XBEM Direct $\tilde{K_I}$ (colloc.)**	**XBEM Direct $\tilde{K_I}$ (Tying)**
132	53589319.84	134	52999752.18	45031591.82	52793286.99
192	53961286.35	194	53186644.01	47805323.36	52947518.19
252	53899227.78	254	53254300.98	49253347.32	53043363.38
312	53833299.46	314	53284118.03	50113915.05	53102663.92
372	53775818.89	374	53299223.94	50677080.10	53142056.72

$$\frac{K_I}{K_o} = 1.12 - 0.23\frac{a}{W} + 10.6\left(\frac{a}{W}\right)^2 - 21.7\left(\frac{a}{W}\right)^3 + 30.4\left(\frac{a}{W}\right)^4 \tag{D.1.1}$$

where, a and W are the crack length and the plate width, respectively. In addition, K_o can be calculated as $K_o = \sigma\sqrt{\pi a}$. The stress intensity factor value that been used to calculate the error found to be $K_I = 53173615.53Pa\sqrt{m}$